THE UNIVERSITY OF CHICAGO

POLYMER-GRAFTED CELLULOSE NANOCRYSTALS: STRUCTURE, PROPERTIES, AND INTERFACES

A DISSERTATION SUBMITTED TO

THE FACULTY OF THE PRITZKER SCHOOL OF MOLECULAR ENGINEERING

IN CANDIDACY FOR THE DEGREE OF

DOCTOR OF PHILOSOPHY

BY

JAMES H. LETTOW

CHICAGO, ILLINOIS

DECEMBER 2021

It is the glory of God to conceal things, but the glory of kings is to search things out.

-Proverbs 25:2

[Jesus] is the radiance of the glory of God and the exact imprint of his nature, and he upholds the universe by the word of his power.

-Hebrews 1:3a

Table of Contents

List of Figures

List of Schemes

List of Tables

Acknowledgements

Although a thesis is attributable to one person, the work herein is indebted to many. Completing a PhD has been like venturing through a high mountain pass, needing counsel for the route, friends to journey together, and the occasional final push up the last incline.

First and foremost, I thank my advisors, Drs. Stuart Rowan and Paul Nealey, for their gracious support and for being willing to mentor and guide me through this vast unknown. You have both provided me breadth of insight into both the content and method of research as well as the tools and encouragement to achieve it. I would also like to thank my coworkers spanning both research groups, whom I have learned from and trained up, growing with every step together.

My deepest gratitude goes to my family. My parents have offered immense support and trust. I am grateful for the many experiences that have formed character and hope. I thank my sister as well. Finally, I thank my wife, Victoria, for your deep, deep love. I look forward to spending the rest of our lives together.

Finally, I thank the Lord, my Creator and Savior, Father and King. You have made all from planets to polymer chains and have formed in me a mind capable to enjoy research and the difficulties of academia, all while finding great joy in Your Personhood. All the glory to God.

Abstract

Polymer nanocomposites, due to combining constituent properties, can fulfil a wide variety of applications, ranging from structural materials to filtration membranes to battery separators. However, nanofiller aggregation can pose detrimental to best maximizing the nanocomposite properties. Polymer-grafted nanoparticles, which when cast into films without additional matrix material, limit nanofiller aggregation due to the covalent bonding between nanofiller and polymer matrix, and although the class of materials has seen increasing study, gaps remain particularly in anisotropic nanofiller and ionically conductive matrices. This dissertation will focus on investigating polymer-grafted cellulose nanocrystals to establish structure/property relationships, particularly between the grafted polymer conformation and composite mechanical properties, ion conductivity enhancement in hydrated, polyelectrolyte grafted systems, as well as explore the rationale for ion conductivity enhancement at their interfaces. To this end polystyrene-grafted cellulose nanocrystals will be used as a model system to investigate the polymer graft conformation and its impact on the thermally dependent elastic modulus and material fracture toughness. Hydrated, poly(2-vinylpyridine)-grafted cellulose nanocrystals treated with iodomethane will then be used to probe the ionic conductivity enhancement (compared to ungrafted polymer) by altering the polymer molecular weight, grafting density, and architecture. Finally, the interfacial contribution to ionic conductivity will be explored using thin film, model polymer brushes on interdigitated electrodes to differentiate competing hypotheses of surface hydrophilicity and functional group content.

Chapter 1

Introduction

1.1 INTRODUCTION

Nanocomposites are composed of a nanofiller embedded in a polymer matrix and are used in a wide array of applications,[1,2] particularly when improvement are needed in the polymer's materials properties, whether mechanical,[3–5] electronic,[6–8] water impurity rejection or transport,[9,10] etc. Improvement in the properties of interest is often controlled by the ratio of polymer to nanofiller. However, such two-component nanocomposites often suffer from demixing/phase separation of the matrix and filler, particularly at high nanofiller content or if there is significant incompatability between nanofiller and matrix. Ultimately, demixing can lead to a reduction in the materials properties, restrict possible processing techniques, and ultimately limit the loading of the nanofiller material.[11] One way to address these issues is to attach the polymer matrix to the nanoparticle filler by covalent bonds to make polymer grafted nanoparticles (PGNs)[12] which can either be integrated into nanocomposites to improve compatibility between or be processed into films solely consisting of PGNs, which have been termed one-component nanocomposites (OCNs).[12] Such OCNs can allow access to materials that exhibit enhanced mechanical properties such as modulus and toughness or electronic properties such as ionic conductivity relative to two-component nanocomposite of similar composition.[13–15] Furthermore, on account of the covalent bond between the polymer and nanofiller, these materials do not suffer from demixing, permitting melting processing and much higher loadings of nanoparticles beyond that of traditional nanocomposites.[16,17] As a result, beneficial interfacial interactions can be maximized, such as the ability to enhance ion transport, forming materials with the possibility for greatly enhanced conductivity.

This thesis will investigate nanorod based PGN films composed of polymer, either polystyrene (PS), poly(2-vinylpyridine) (PV), or their diblock copolymers, grafted to cellulose

nanocrystals (CNCs). The mechanical properties and polymer graft conformation of nanorod based OCNs will be investigated by altering the polymer molecular weight and grafting density of the PS grafted CNCs, which begins understanding the structure-property relationships and indicates how to optimize mechanical properties (Chapter 2). Next, the ionic conductivity will be investigated and beneficial polymer/CNC interface will be studied by similarly altering the polymer molecular weight and grafting density of the PV grafted CNCs as well as using diblock copolymers to isolate the CNC surface as the principal cause of conductivity enhancement (Chapter 3-4). Finally, the interface-based conductivity enhancement will be studied using model polymer brushes on interdigitated electrodes (IDEs) by altering both the hydrophilicity and alcohol functional content to discern which has a greater impact on the conductivity enhancement (Chapter 5).

This introduction will work to provide the foundation from which to discuss the mechanical and ionic conductivity properties of polymer grafted to cellulose nanocrystals as well as to describe the role interfaces play in conductivity enhancement within these systems. First, the structure-property relationships of OCNs will be presented, focusing principally on the impact of grafted polymer conformation on mechanical properties of the well-studied nanosphere based OCNs but also presenting what is known about nanorod based OCNs. Literature examples will be examined that probe the ionic conductivity of PGNs and their films to provide context for the field of study Next, cellulose nanocrystals will be introduced as mechanically robust and easily functionalizable nanorod useful for studying the structure-property relationships of nanorod based OCNs as well as interesting nanofiller for ionically conductive nanocomposites (and thus PGN films). Finally, mechanisms of ionic conductivity will be presented, with particular focus on the impact of interfaces and grafted polymer, as well as potential methods of study.

1.2 POLYMER BRUSHES

To begin understanding the structure-property relations of OCNs, the grafted polymer brush structure will first be discussed as it is the fundamental distinction between standard 2-component nanocomposites and OCNs. Grafted polymer brushes have been theorized upon for more than 40 years,[18,19] and yet their applications and experimental study are still of active investigation.[20–22] As a polymer is end-grafted to a flat surface, the monomer distribution and structure of the polymer brush change as a function of the grafting density and polymer length, which controls the radius of gyration (R_g). Below a critical grafting density, there is no interaction between polymer chains, which occurs when the grafting density (σ) is less than $1/(\pi R_g^2)$. This results in the polymer coil adopting what is termed the mushroom regime. As the grafting density increases (thus more interaction between the polymer chains), the elastic entropy and excluded volume contributions of the polymer chains are in conflict, resulting in an extension of the polymer chains, forming a polymer brush. At low to intermediate grafting densities, the brush resides in the semidilute polymer brush (SDPB) regime, which is less constrained, relying more upon pairwise intermonomer interactions and following a brush thickness (h) scaling behavior of $h \sim N\ \sigma^{1/3}$. At higher grafting densities, the brush resides in the concentrated polymer brush (CPB) regime, a more extended brush relying upon higher order intermonomer interactions and following a different scaling behavior of $h \sim N\ \sigma^{1/2}$. From a fundamental understanding of the polymer physics and conformation come scaling behaviors for the polymer brushes.

However, as these brushes are attached to curved as opposed to flat surfaces in OCNs, their behavior changes.[23,24] While the same polymer brush regimes (mushroom, SDPB, CPB) exist, the scaling behaviors are altered. First developed by Daoud and Cotton in 1982 for star shaped polymers,[25] the termed Daoud-Cotton model predicted that at a critical polymer length, the

polymer conformation would change from a concentrated polymer brush to a semidilute polymer brush due to the curvature introduced in the star polymer, resulting in an outer corona of SDPB and inner CPB core, termed CPB/SDPB as seen in **Figure 1.1**. Now, the brush height dependences change, with the concentrated polymer brush regime following a dependence of h~N and the outer SDPB following a dependence of $h \sim N^{3/5}$. This was then expanded by Ohno *et al.* to include an inner spherical particle, with grafted outer polymer following the same dependences.[26,27]

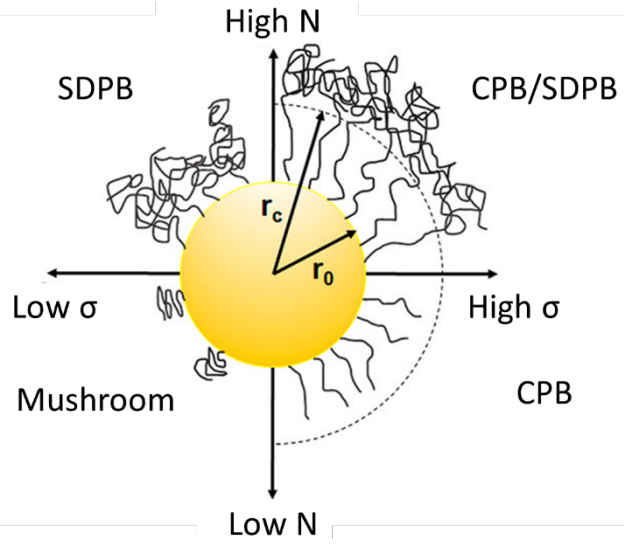

Figure 1.1: Chain conformation of polymer grafted nanoparticles (PGN) as a function of chain grafting density, σ, and degree of polymerization, N, at a given particle radius, r_0. The polymer conformations include mushroom (bottom left), concentrated polymer brush (CPB) (bottom right), semidilute polymer brush (SDPB) (top left), and mixed CPB/SDPB (top right) with a transition at a critical radius, r_c. Adapted from Vaia and coworkers.[17]

1.3 DEVELOPMENTS FOR EXPERIMENTALLY INVESTIGATING ONE-COMPONENT NANOCOMPOSITES

As controlled radical polymerization (CRP) developed, the ability to synthetically access polymer grafted surfaces greatly expanded the polymer chemistries and architectures available for study and making polymer grafted nanoparticles (and thus OCNs) more accessible. Although anionically grown star polymers have been studied since the 60s and 70s,[28,29] the ability to attach polymers to surfaces either through "graft from" via CRP (most used) or to prepare polymers and then "graft to" has provided the literature with excellent studies and examples.[20,21,30,31] For example, Husseman *et al.* used silane chemistry to graft nitroxide initiators to a silica surface to grow controlled polystyrene brushes via nitroxide mediated polymerization (NMP).[32] Baum *et al*. used reversible addition fragmentation chain transfer (RAFT) polymerization to produce polymer brushes of polystyrene and poly(methyl methacrylate) from silica surfaces modified surface-immobilized azo initiators, which thermolytically produced free radicals that in the presence of monomer and chain transfer agents grew polymer.[33] Matyjaszewski and coworkers produced dense brushes of polystyrene and polyacrylates, as well as block copolymers, on silica surfaces by using silane chemistry to attach an initiator such as 11-(2- Bromo-2-methyl)propionyloxyundecenyltrichlorosilane to initiate atom transfer radical polymerization (ATRP).[31,34] From this accessible grafting from chemistry, various polymer grafted nanoparticles (PGNs) have been synthesized and has enabled further investigation into the behavior of not only the PGNs themselves, but also their assemblies into OCNs.[12,30,31]

In 2012, Matyjaszewski and coworkers synthesized OCNs based on polystyrene and poly(methyl methacrylate) grafted from silica particles to investigate both the structure and mechanical properties.[13] The materials synthesized range in molecular weight from 1 kg/mol to

1600 kg/mol with grafting densities from 0.25 to 0.67 chains/nm^2. In analyzing the brush thickness by transmission electron microscopy (d) and dynamic light scattering (R_H-R_0), the particle surface-to-surface distance and the brush height are found to scale with the degree of polymerization as $d \sim N^{0.8}$ and R_H-$R_0 \sim N^{0.98}$ (in CPB regime) and $d \sim N^{0.52}$ and R_H-$R_0 \sim N^{0.58}$ (in SDPB regime), respectively, in good agreement with theory, which predicted that the CPB regime should have the brush thickness scale as $N^{1.0}$, while the SDPB regime scales as $N^{0.5}$ (**Figure 1.2a)**. Additionally, the elastic modulus and fracture toughness were probed using nanoindentation. For modulus, low molecular weight samples (in CPB) showed moduli below that of the associated homopolymer, which with increasing molecular weight approached the homopolymer modulus at the CPB to SDPB transition. For the fracture toughness, samples monotonically increased so that at the highest molecular weights, the samples approximated the homopolymer results (**Figure 1.2b)**. The authors describe this as a transition from 'hard-sphere-like' to 'polymer-like' mechanical characteristics of particle solids. Additionally, TEM images showed crazing behavior in SDPB samples which permitted an analysis of the fragile to crazing transition (**Figure 1.2c-d)**. Offering a solid foundation for analyzing OCNs, this work provides the first steps toward analyzing the behavior and comparing it to theoretical predictions.

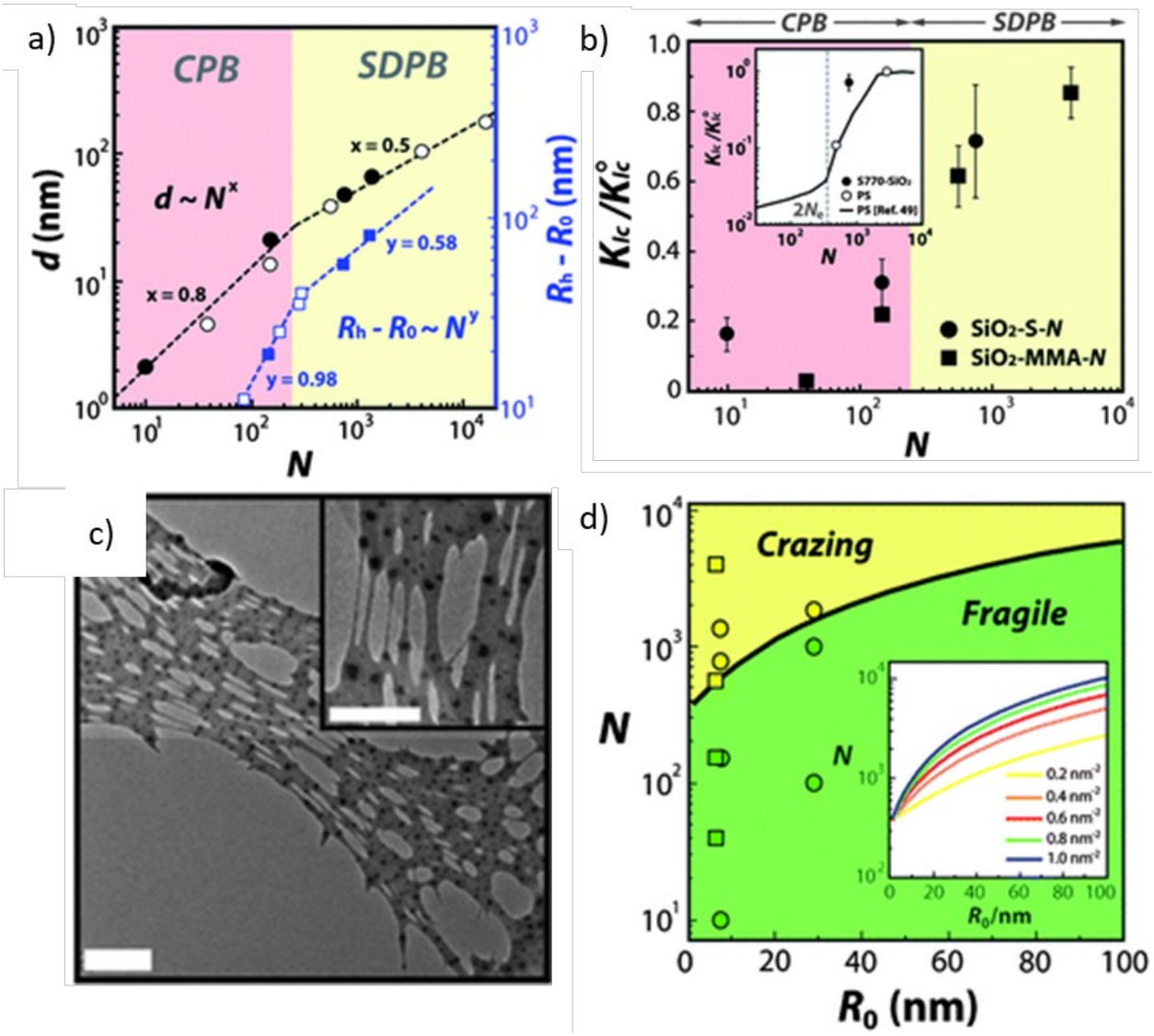

Figure 1.2: a) The dependence of the particle surface-to-surface distance d and brush height $R_h - R_0$ on the degree of polymerization N of surface-grafted chains. Filled circles (SiO_2-SN) and open circles (SiO_2-MMAN) represent d determined by TEM of particle monolayers shown in panels a–h; blue squares (SiO_2-SN) and open circles (SiO_2-SN) represent $R_h - R_0$ determined by DLS in toluene solution. b) Dependence of normalized fracture toughness KIc/K_{Ic}° on the degree of polymerization of polymer grafts in the CPB and SDPB regimes. K_{Ic}° denotes the measured toughness of linear polymer analogues with high molecular weight, c) Electron micrograph

Figure 1.2 continued: revealing the formation of craze in the thin film of SiO_2-MMA570, d) Predicted dependence of the threshold degree of polymerization to facilitate entanglement formation of grafted chains on the particle core size. Adapted from ref [13]

Although Matyjaszewski and coworkers focused principally on high molecular weight, high grafting density samples, Vaia and coworkers analyzed high molecular weight and low grafting density samples, focusing on the impact on crazing behavior.[17] In this work, Fe_3O_4−PS PGNs were synthesized by surface-initiated RAFT polymerization and probed using dynamic light scattering and thin film wrinkling−cracking method. The materials synthesized range in molecular weight from 35 kg/mol to 369 kg/mol with grafting densities from 0.04 to 0.14 chains/nm^2. The corona height of the PGNs in toluene showed a molecular weight dependence of $N^{0.65}$ for samples with predominantly predicted SDPB conformations (**Figure 1.3a**). The measured modulus followed good agreement with effective medium theory, representing the properties following the volume percent of nanofiller. Finally, similar to pure PS, a transition from brittle fracture to crazing occurs for grafts >110 kg/mol, and stable craze extension is seen above 200 kg/mol, which was used to deduce critical length scales for craze microstructure formation (**Figure 1.3b**). This work both confirmed the brush conformation predictions of Matyjaszewski and coworkers[13] and expanded the types of OCNs studied establishing further structure-property relationships.

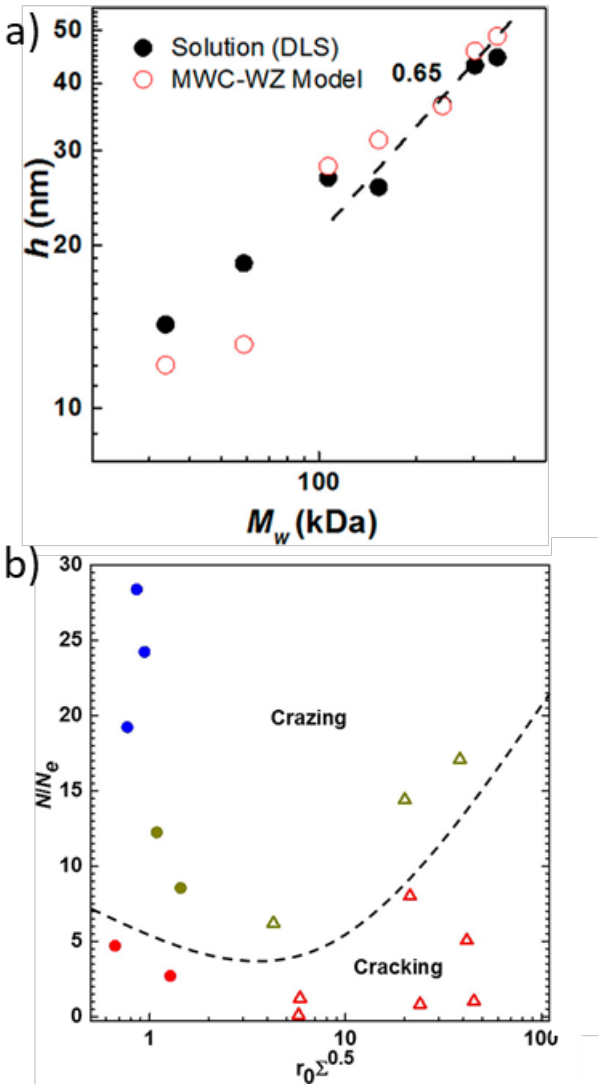

Figure 1.3: a) Corona height (h) in toluene (DLS, solid black circles; MWC–WZ model, open red circles). The dashed line (R^2 = 0.97) shows the line of best fit (slope = 0.65) between log(h) and log(MW) for DLS corona height with MW > 100 kg/mol b) Deformability relative to 267 kg/mol PS of low graft density Fe_3O_4-PS PGNs and high graft density SiO2-PS PGNs. Adapted from ref [17]

Ultimately, the structure/property relationship of nanosphere-based OCNs have been well investigated. Specifically, the theoretical predictions and experimental results of grafted polymer

conformation have been reconciled which permits the further connection between the conformation and the mechanical properties. Through several studies, high molecular weight grafted polymers in the semidilute polymer brush regime have shown increasing toughness, both in fracture toughness and crazing behavior with moduli showing good agreement with effective medium theory. However, a clear gap in the literature exists in probing the impact of nanoparticle geometry on the polymer brush structure and mechanical properties of OCNs, with Chapter 2 of this thesis focusing on filling that gap.

1.4 IONICALLY CONDUCTIVE NANOCOMPOSITES: STANDARD TWO-COMPONENT NANOCOMPOSITE

Having established what is currently known about the mechanical structure-property relationships in OCNs, the focus turns toward the ionic conductivity properties of nanocomposites. As there has been relatively little work investigating the behavior of polyelectrolyte grafted nanoparticle (PEGN) films, discussion will begin looking at the impact of nanofiller in ionically conductive matrices. Although this field is broad and well-trodden, with much work in the literature,[2,6,35–41] the aim is to give an overview of important works within ionically conductive nanocomposites before working towards polymer grafted nanoparticles in ionically conductive nanocomposites, finally discussing what work has been done in ionically conductive PGN films.

To begin with a particularly seminal example, in 1998 Croce *et al.* introduced 13 nm diameter TiO_2 and 5.8 nm diameter Al_2O_3 at 10wt% into PEO with 8:1 ratio $LiClO_4$.[42] From 20-110 °C, the materials showed an order of magnitude enhancement in ion conductivity compared to a homopolymer sample, which was attributed to the ceramic filler promoting enhanced Li+ transport via a surface mechanism and reducing crystallization of the PEO. Similar enhancement in ionic conductivity can be seen in hydrated polyelectrolyte systems such as Nafion based nanocomposites. Yin *et al.* introduced 3-6 nm diameter SiO_2 and TiO_2 nanoparticles at 5 wt% into Nafion membranes.[43] In this work, both samples showed increased proton conductivity comparted to Nafion, with TiO_2 showing higher conductivity than the SiO_2. Further investigation concluded that the nanoparticles enhanced water uptake and conductivity due to the formation of extra ionic-water cluster phases around the nanofiller.

Although generally nanospheres have been studied in the ionically conductive nanocomposite literature, Cui and coworkers have produced a number of papers investigating different geometries of $Li_{0.33}La_{0.557}TiO_3$ nanoparticles in poly(acrylonitrile) (PAN) (**Figure 1.4a**).[44–46] All investigated nanospheres, nanorods, and nanowires showed up to 3 orders of magnitude increases in conductivity (**Figure 1.4b**). Specifically, nanospheres performed the worst, with additives of up to 15wt% showing a maximizing of the conductivity, as opposed to nanowires overtaking the nanospheres at all loadings.[44,45] Finally, nanowires were aligned parallel and perpendicular to the applied electric field, with the parallel samples performing the best with 3 orders of magnitude increase in conductivity compared to the homopolymer while perpendicularly aligned nanowires approximating the conductivity of the filler-free material.[46] This investigation into the LLTO material's enhancement originates from the positive- charged oxygen vacancies on the surfaces of the nanowires that could associate with anions and then release more Li ions, with the extended surfaces of the nanorods and nanowires allowing for easy percolation throughout the bulk of the material. However, it should be noted that the nanofiller loading was limited at up to 15% in order to not encounter phase segregation within the materials, a common theme in these ionically conductive nanocomposites with beneficial surface interfaces. Ultimately, the nanoparticle aspect ratio is shown to greatly impact the ionic conductivity properties of the nanocomposite, providing substantial impetus towards the study of nanorod based PGN films that ionically conduct through the grafted polymer matrix.

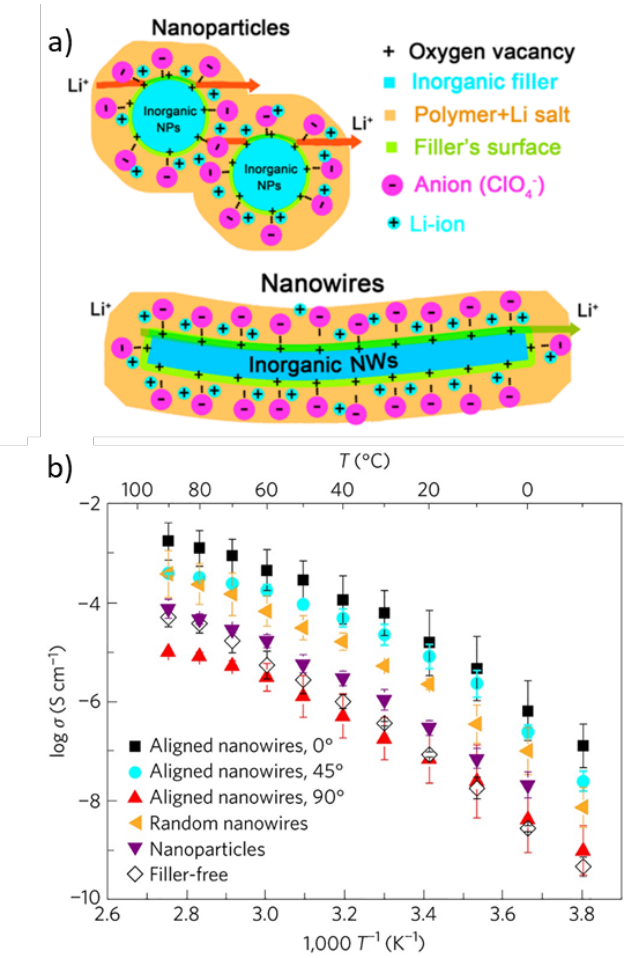

Figure 1.4: a) Cartoon illustrating ion conduction through nanocomposites consisting of either nanoparticles or nanowires. b) Arrhenius plots of the composite polymer electrolytes with aligned nanowire arrays at various orientations, together with the data for the composite electrolyte with randomly dispersed nanowires and the filler-free electrolyte. Adapted from refs [44,45]

One route to overcome the phase segregation of nanofiller within nanocomposites is to graft compatiblizing polymer to the surface of the nanofiller.[12] As discussed previously, many synthetic routes have been used to attach polymer to the surfaces of nanoparticles.[20,21,30,31] Here, however, the principle goal is to choose conductive graft polymer for the purpose of better/more compatible inclusion into a conductive matrix, whereby the beneficial interfacial interactions can

be best magnified at high nanofiller loadings. Surprisingly, few works have explicitly looked at ionically conductive polymer grafted nanoparticles included in ionically conductive polymer matrices as nanocomposites with this aim in mind.

To this end, Villaluenga *et al.* introduced poly(ethylene glycol) polyhedral oligomeric silsesquioxane nanoparticles (POSS) into 70k-74k PS-PEO block copolymer with LiTFSI at R=0.085 for all samples ranging between 2 and 10 wt% POSS addition. Structural characterization (scanning transmission electron microscopy) showed that the POSS resides in the PEO regime with small angle x-ray scattering showing lamellar-to-bicontinuous phase transition at POSS loadings above 2 wt%. Electrical impedance measurements of these materials yielded conductivity of the materials maximizing at 2 wt% POSS inclusion, with conductivities of the block copolymer system being 94% of the homopolymer conductivity with similar POSS and LiTFSI loadings, attributed to better conducting diblock copolymer morphology.[47]Similarly, O'Reilly and Winey introduced 10-15 nm diameter SiO_2 nanoparticles with 5000 g/mol grafted PEO using silane condensation and nucleophilic substitution. These nanoparticles, along with unfunctionalized SiO_2 nanoparticles, were introduced 600 g/mol single-ion conducting PEO/sulfoisophthalate ionomer neutralized with lithium. DC conductivity measurements of the system show that increasing quantities of the grafted nanoparticles (up to 35wt%) showed increases in conductivity as compared to the homopolymer, while ungrafted SiO_2 nanoparticles showed monotonically decreasing conductivity up to 35 wt%. The increase of the grafted nanoparticles was attributed to plasticization of the ionomer, supported by DSC and viscosity measurements of the system.[48] Neither of these examples used nanofiller known to provide beneficial polyelectrolyte/interface interactions, although the grafted poly(ethylene glycol) from Villaluenga *et al.* possibly could

inhibit matrix crystallization. Not surprisingly, neither example demonstrates enhancement in nanocomposite conductivity.

1.5 IONICALLY CONDUCTIVE NANOCOMPOSITES: POLYMER GRAFTED NANOPARTICLE FILMS

As discussed previously, by casting polymer grafted nanoparticles into films, higher loadings of nanofiller can be attained, which directly works to maximize the beneficial interfaces of the nanofiller. These films are distinct from the ionically conductive nanocomposites in the previous section as no additional polymer matrix is added to the system. Even so, nearly all examples of PGN film-based nanocomposites rely upon additional added components, whether water vapor, solvent, or additional ionic liquid or salt. Although technically not one-component nanocomposites, these materials still attempt to maximize the added nanofiller, to varying degrees of success.

Within the context of anhydrous systems, Lithium bis(trifluoromethanesulfonyl)imide (LiTFSI) is often added is used to provide ionic conductivity, particularly in poly(ethylene glycol) (PEG) based systems. In work by Agrawal *et al*, 10 and 25 nm silica nanospheres were functionalized with poly(ethylene glycol) (500 g/mol) by grafting to and yielded a grafting density of and 1.5 and 1.3 chains/nm^2 respectively.[49] The PEGNs were then mixed together in propylene carbonate ranging from 0.1 to 0.5 vol% and imbibed with LiTFSI at 1M, which showed a maximum conductivity (although still less than a control sample) when the core volumes of both nanoparticle types (so volume percent silica of both the 10 nm and 25 nm samples) were equal. This observed maximum conductivity at equal core volumes was attributed to the ability mixture of particle sizes to produce disordering of the suspension by lowering correlation among the polydisperse particles. Rheological measurements show solid mechanical behavior at loadings above 0.2 vol%. With increasing fractions of nanoparticles maintaining the equal core volume composition, the ionic conductivity measured decreased from 1.6 mS/cm or 80% of a similar

mixture of ungrafted PEG, propylene carbonate and LiTFSI to 0.4 mS/cm. In work by Nugent *et al*, 8 and 18 nm diameter SiO_2 and 15 nm diameter TiO_2 nanospheres were grafted with 550-5000 g/mol PEG with inorganic nanosphere loadings up to 55wt% and imbibed with 1 M LiTFSI.[50] Compared to 500 g/mol PEG with 1 M LiTFSI, the polyelectrolyte grafted nanoparticle samples imbibed with 1 M LiTFSI showed reduced conductivity, with the lower molecular weight grafted samples showing the highest conductivity (ca. half that of the homopolymer). All grafted samples showed higher conductivity than the 2000 g/mol homopolymer up to 60 °C (melting point of PEG) whereupon at higher temperatures the 2000 g/mol homopolymer surpassed the grafted system conductivity.[50] Although TiO_2 nanospheres have shown enhancements in conductivity in two-component nanocomposites,[42] all of the above samples only showed enhancement below the melting point of PEG (for the solventless system by Nugent *et al*.) or none at all.

For hydrated PGN films, water helps to both disassociate backbone ions as well as to plasticize the polymer. In work by Wang et al, 16 nm SiO_2 nanospheres were functionalized with a poly (ionic liquid), poly((*p*-vinyl-benzyl) trimethylammonium tetrafluoroborate), via a grafting from method.[51] In this system, the molecular weight was estimated using a sacrificial initiator yielding a 4 kg/mol polymer at 4 hours and 17 kg/mol at 24 hours. Due to selecting a hydrophilic monomer, the ionic liquid nature of the polymer permitted ionic conductivity with water uptake, although the measurements were taken at ambient conditions. The measured ionic conductivity of the samples increased up to the 12 kg/mol PGN (0.104 mS/cm) and decreased at higher reaction times. This was compared to a 12 kg/mol homopolymer sample which had a conductivity of 0.0185 mS/cm, with the increased conductivity being attributed to better ion transport channels. Another hydrated example by Jiao et al., examined 6 nm diameter Fe_3O_4 nanospheres were functionalized with poly(styrene-*b*-trioctylammonium *p*-styrenesulfonate) block copolymer (100kg/mol and

grafting density of 0.059 chains/nm^2).[52] The samples were imbibed with ionic liquid (1-Hexyl-3-methylimidazolium bis-(trifluoromethylsulfonyl)imide) at 30 wt% and the ionic conductivity increased with sulfonate content from 0.05 mS/cm to 5 mS/cm peaking at 3 mol% sulfonate, yet decreasing after to 0.1 mS/cm. The work did not compare their conductivity values to that of similar polymer compositions. Rather, this result was compared to poly(styrenesulfonate-*b*-methylbutylene) with 17 mol% 2-ethyl-4-methyl imidazole bis-(trifluoromethylsulfonyl)imide which showed a conductivity of 70 mS/cm. Both examples were done at ambient conditions with little comment as to the effect of water content on material properties. Even so, work by *Wang et al*. did seem to show conductivity enhancement even using SiO_2, although the mechanism of enhancement was postulated to be ion conducting channels rather than interface related enhancement.

Taken together, ionically conductive nanocomposites have shown promise in enhancing the material conductivity, although no works have successfully used nanospheres with beneficial interfaces in PGN geometries and successfully showed enhancement. As a result, further work towards both successful integration and investigation into the structure/property relationships of this class of materials is untapped potential for the field. Although a couple examples exist looking at the effect of nanoparticle geometry on the nanocomposite ionic properties (showing enhancement relative to nanospheres),[44–46] only one recent example from the Rowan group has investigated the ionic conductivity of nanorod based PGNs, which will be described more in depth shortly.[15] Chapters 3 and 4 of this thesis will focus on filling this gap of investigating ionically conductive, nanorod based PGN films.

1.6 CELLULOSE NANOCRYSTALS AS NANORODS FOR OCN STUDY

Nanorods have distinct advantages over nanospheres, particularly in their ability percolate through a given nanocomposite at low nanofiller loadings.[53,54] By establishing percolating networks, a wide variety of properties can be easily enhanced such as mechanical strengthening,[4,55] electronic and thermal conductivity,[56–59] and water transport.[60] Specifically, percolation onset occurs at critical concertation, Φ_{cr}, corresponding to the aspect ratio, A, of the nanofiller, such that $\Phi_{cr} = 0.7/A$ with even the onset of percolation affecting the electronic properties.[59] However, two principle models for mechanical property improvement are used for anisotropic nanofiller: Haplin-Kardos and Percolation theory.[55,61] Halpin-Kardos model assumes homogeneously dispersed anisotropic nanofiller in a polymer matrix that does not display pronounced filler-filler interactions representative of a mixing behavior while percolation model relies upon the nanofiller having strong nanoparticle-nanoparticle interactions to share induced stress upon the nanofiller across the network, although both show mechanical property enhancement over spherical nanofiller. As mentioned previously in work by Cui and coworkers, even without full percolation established, anisotropic nanofiller has shown enhancement in ionic conductivity by inducing long channels of continuous interface based enhancement.[44,45] Thus, when incorporating nanorods into OCNs, the easily formed percolation networks can be advantageous toward both mechanical properties (even if only Halpin-Kardos reinforcement) as well as ionic conductivities.

In this work, cellulose nanocrystals (CNCs) were chosen as ideal nanorods for study as they provide a unique blend of well-studied surface chemistry and functionalization, mechanical reinforcement, and interesting ionic conductivity enhancement hypothesized to be due to the material interface. Clearly, other interesting ceramic materials (such as those described above),

carbon nanotubes, or metals could provide interesting cases for study in developing nanorod based OCNs, particularly if electronic properties are of interest. Below, work on CNCs will be summarized, as well as important examples of CNC based nanocomposites, OCNs, and PGN films.

The modification of the CNC surface has seen extensive investigation, particularly in order to improve solution processing and integration into nanocomposites. One particular challenge with CNCs is their tendency toward self-aggregation due to extensive hydrogen bonding, but the readily available cellulose chains allow for both functionalization to reduce aggregation and to attach polymer. Beginning with a cellulose biosource, as shown in **Figure 1.5**, CNC isolation begins with grinding, base treatment, and bleaching to remove lignin and hemi-cellulose to form cellulose nanofibers.[62] After acid hydrolysis, CNCs can be obtained from the nanofibers through degradation of the amorphous cellulose and access the crystalline domains. However, the choice of acid alters the surface chemistry of the CNCs: using sulfuric acid yields CNCs with sulfate half-esters (and surface alcohols) and using hydrochloric acid yields CNCs with only surface alcohols.[62,63] Naturally, the hydrochloric acid treated CNCs tend to agglomerate due to hydrogen bonding. However, the anionic surface charges of the sulfonated CNCs aid in repelling the CNCs and allowing formation of stable dispersions necessary for creating robust polymer nanocomposites. Hydrochloric acid treated CNCs are capable of similar anionic repulsion by undergoing TEMPO mediated oxidation or ammonium persulfate oxidation to yield carboxylic acid CNCs.[64,65] Thus, by either functionalizing CNCs with a surface charge, they can be better dispersed in solution and thus polymer nanocomposites. Chemistries that utilize the carboxylic acid moieties at the surface such as amide coupling can be employed, providing a facile route to OCNs, as will be described in this thesis.

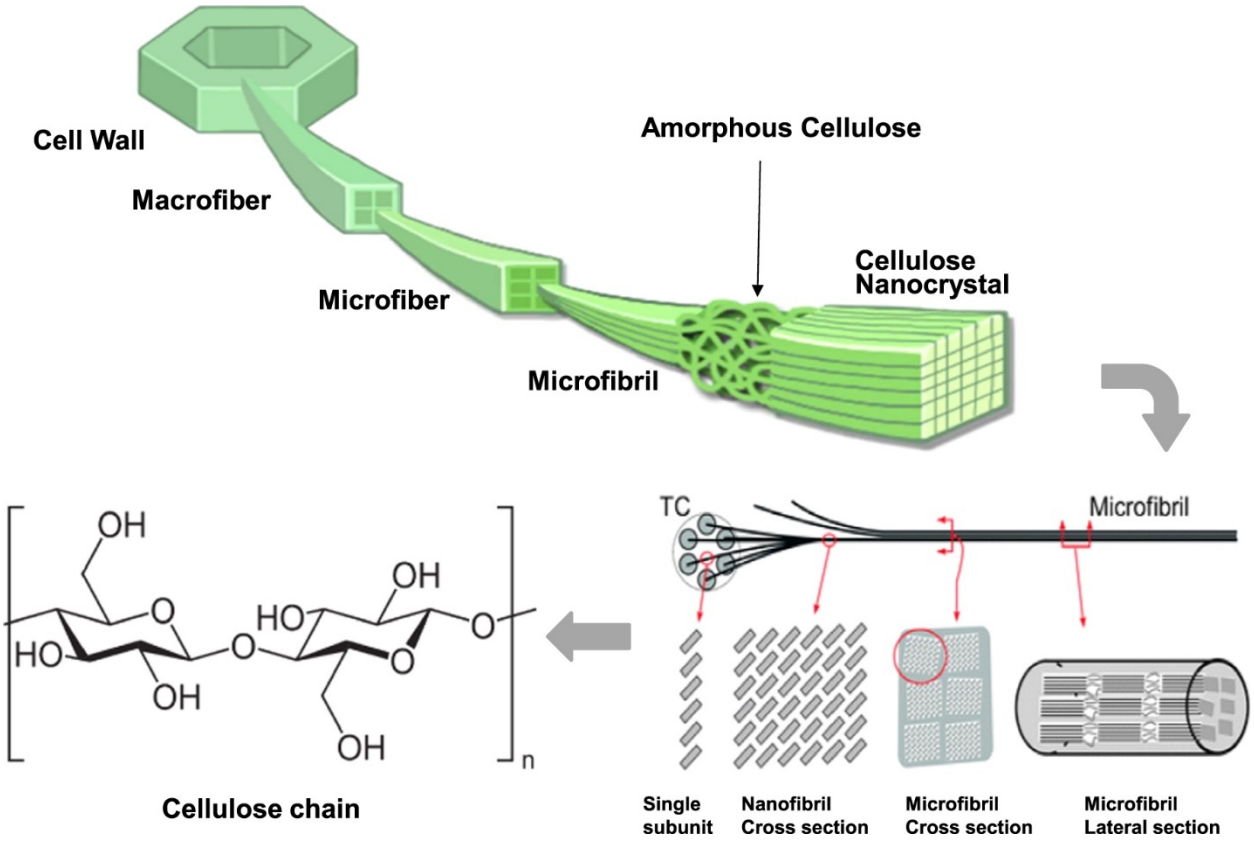

Figure 1.5: Hierarchical structure of cellulose showing the fibril packing, cellulose nanocrystals, and cellulose chain stacking. Adapted from Kim *et al*.[36]

The isolated CNCs are fundamentally composed of cellulose polymer chains aligning into nanofibrils which make up the nanorods, held together by hydrogen bonding and forming the highly crystalline domains of the CNCs.[66] In addition to the internal hydrogen bonding, the external surface of the CNC contains exposed primary and secondary alcohols which act as sites for the aforementioned chemical modification. Depending on the biosource of cellulose and processing method, the size and aspect ratio of the CNCs can be altered, ranging in length from 200-2000 nm and diameter from 5-30 nm.[67,68] CNCs derived from cotton, wood pulp, tunicates, and *Miscanthus x. Giganteus* (MxG) are common examples of academically used sources.[62,69] As mentioned previously, the high aspect ratio permits CNCs to achieve percolation throughout a

material at low concentration, on the order of 1-10%, which stress transfer along the stiff nanorods and is critical for interface based transport enhancement possible for OCNs.[70–72] For example, CNCs isolated from tunicates have been shown to exhibit the highest stiffness (on-axis tensile modulus ~143 GPa)[73] and aspect ratio (~85 with dimensions of ca. 25 nm × 2.2 μm), while CNCs isolated from wood (w-CNCs) or cotton (c-CNCs) have a lower aspect ratio (~10-20) and stiffness (~105 GPa).[74] *MxG*-CNCs used in this thesis are known to have an aspect ratio of 70,[62] yet although the stiffness hasn't been measured, wood offers a useful comparison.

On account of the mechanical stiffness and ease of percolation, combined with the surface functionalization to either induce surface charge or graft polymer, CNCs have been introduced into a wide variety of nanocomposites, generally for the purpose of reinforcement. Some of the polymer matrices used for nanocomposite formation have been poly(vinyl acetate),[61,71,75] poly(ethylene oxide-*co*-epichlorohydrin),[61] poly(styrene-*co*-butadiene),[76] polyurethane,[70,77] polyethylene,[78,79] and epoxy resins,[80] to name a few. Methods to access these materials include solution-casting, templating,[80,81] and melt-mixing of CNCs with polar polymers.[75,78,82] Additionally, in order to increase CNC loading (important for mechanical properties) and aid integration into polymer matrices, polymer grafted CNCs can be used.[1,21,30,83] Examples of polymer grafted CNCs include polyurethanes,[84] polystyrene[85], poly(ethylene oxide),[86] poly(*N*-isopropylacrylamide- co-acrylic acid)[87], and poly(lactic acid),[88] among others. Even so, until recently the mechanical properties and structure-property relationships of OCNs based on nanorods, and CNCs in particular, have seen little investigation.

Recently theoretical and computational work has been applied to CNC-based OCNs, permitting better polymer regime and mechanical property predictions. Specifically, computational work by Keten and coworkers using coarse-grained and molecular dynamics

approaches, when combined with metamodels, have probed various design parameters (polymer chain length, grafting density, polymer−nanoparticle interaction strength, and the nanoparticle edge length) and their effects on the polymer brushes (**Figure 1.6a**).[89] Based on this work, predictions were made on the polymer conformation transition point from CPB to CPB/SDPB as a function of polymer length and grafting density, with further work extending this to a wide array of polymers (**Figure 1.6b**).[90] This work indicated that modulus is maximized at low grafting density and degree of polymerization (i.e. higher volume fractions of CNCs) while toughness is maximized at relatively low grafting density but high degree of polymerization. The computational studies suggested that in order to maximize both modulus and toughness the grafted polymers should be in the SDPB regime and the OCN should have a CNC wt% of ca. 60 %. The models within this work will be discussed at length in Chapter 2 of this thesis.

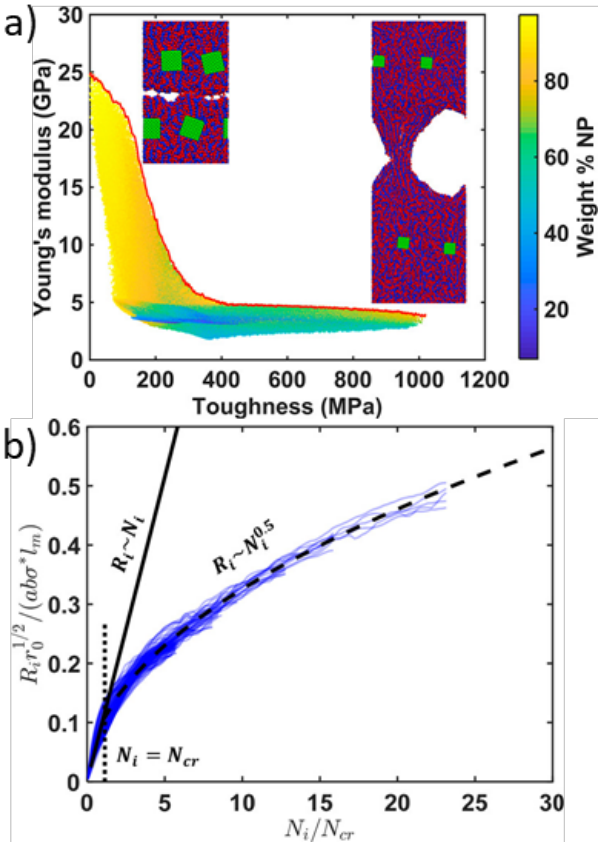

Figure 1.6: a) Young's modulus vs toughness plot with points color coded with respect to the weight percentage of CNC obtained from a set of input parameters.[89] b) Monomer position index N_i is normalized with N_{cr} and the radial distance (R_i) is normalized with material design parameters.[90]

Only recently have the mechanical properties CNC-based OCNs begun to be investigated, although leaving a clear opening for more fundamental studies. Weder and coworkers reported CNC-based OCNs with high molecular polymer grafts (100-400 kg/mol) and moderate grafting density (0.04-0.15 chains/nm^2) and demonstrated toughness and elastic modulus enhancement consistent with previous spherical nanofiller based OCNs.[91] OCNs containing up to 20 wt% CNC with grafted high glass transition temperature (T_g) poly(methyl methacrylate) display enhanced

toughening while maintaining similar levels of elastic modulus as compared to a mixed, 2-component nanocomposites (**Figure 1.7a**). Additionally, OCNs consisting of low T_g poly(hexyl methacrylate) show similar toughness but higher modulus as compared to a mixed, 2-component nanocomposites (**Figure 1.7b**). Even so, this work did not relate their findings back to polymer conformation or investigate a range of grafted polymer molecular weights and grafting densities to more fully understand the structure property relationships, although it offers a tantalizing introduction into the possibilities for this class of materials.

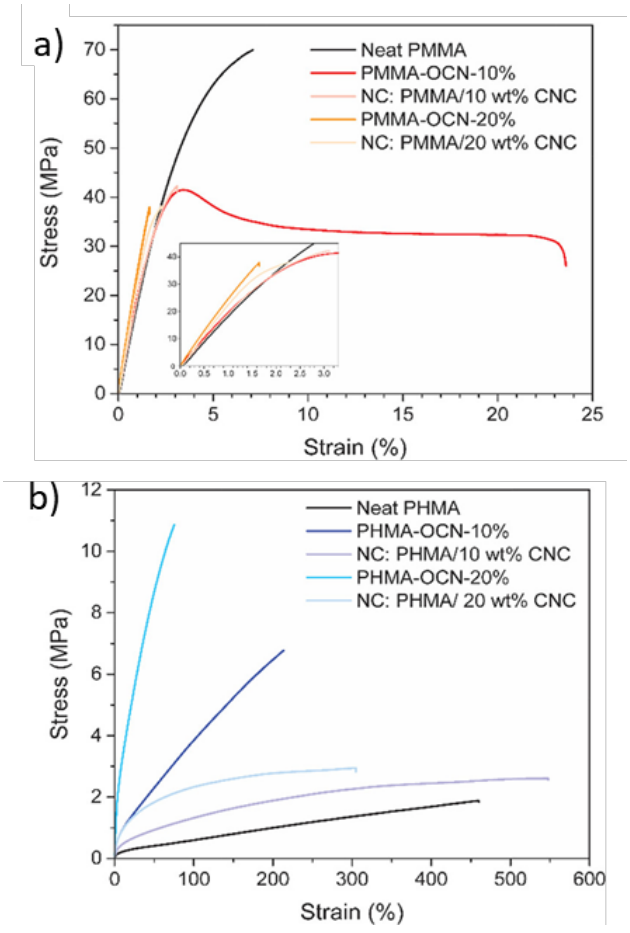

Figure 1.7: Stress-strain curves of OCNs and two-component nanocomposites with grafted polymers of a) poly(methyl methacrylate) and b) poly(hexyl methacrylate) grafted from cellulose nanocrystals. Adapted from ref [91]

Cellulose nanocrystals (CNCs) have also been introduced into ionically conductive nanocomposite,[7,92–95] with several examples showing enhancement in conductivity. Cheng *et al*. synthesized CNCs with quaternary ammonium groups functionalized on the surface (QCNC) and incorporated them into a poly(phenylene oxide) matrix functionalized with similar quaternary ammonium groups (QPPO).[96] Transmission electron micrographs show subtle agglomeration at loadings above 2 wt% (**Figure 1.8a**). When immersed in water the resulting materials showed a 60% higher ionic conductivity than the homopolymer (60 vs 38 mS/cm) at 80 °C peaking at a 2 wt.% CNC loading (**Figure 1.8b**). In addition, the fuel cell performance confirmed a higher peak power density using this anion exchange membrane (**Figure 1.8c**). Rincón-Iglesias *et al*. prepared nanocomposites of CNCs in ι-carrageenan, a marine sulfated polysaccharide isolated from red algae (*Rhodophyta*), and measured the mechanical properties and dielectric response of the bio-sourced nanocomposite membrane at ambient conditions.[94] The ionic conductivity of the composite material peaked at 10 wt.% CNCs with roughly a 3-fold improvement in conductivity. Both examples highlight the conductivity enhancement of CNCs in ionically conductive matrices, yet they also indicate that at too high a loading (2 wt% and 10 wt % respectively) causes phase segregation occurs which limits the amount of enhancing filler that can ultimately be added. As a reminder, this is not a polymer grafted nanoparticle system,

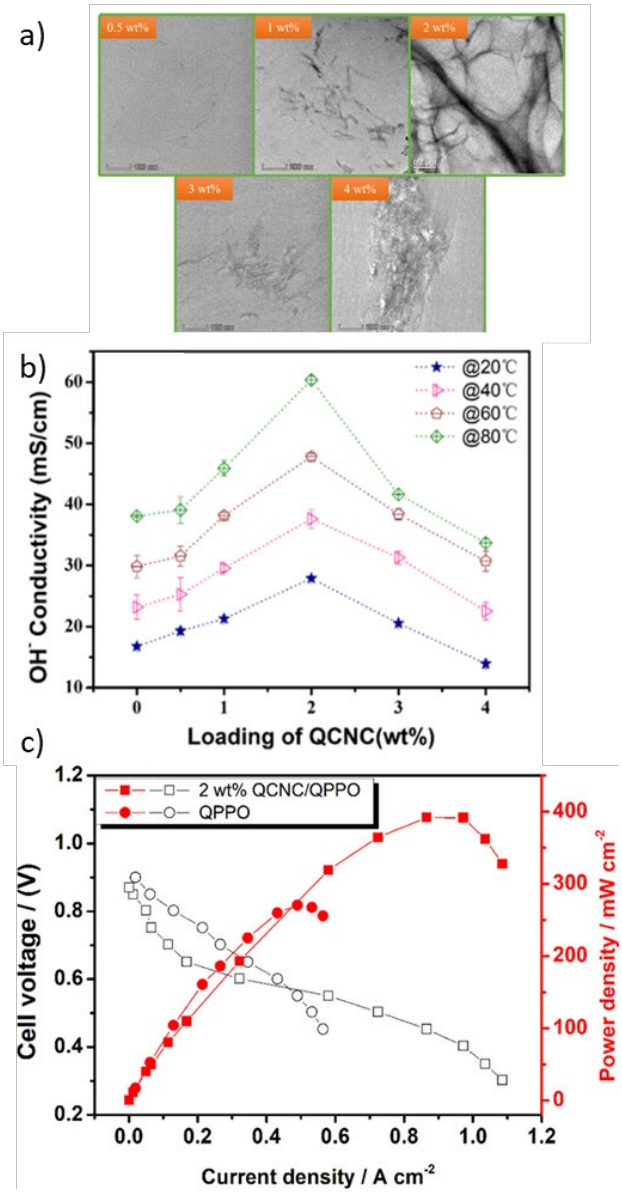

Figure 1.8: a) Transmission electron micrographs of QCNC/QPPO composites at various percent of filler. b) hydroxide conductivity as a function of percent of filler, c) H_2/O_2 fuel cell performance at 60 °C without back pressure. Solid square and hollow square are the power density and cell voltage of 2 wt % QCNC/QPPO-based anion exchange membrane, respectively; solid circle and hollow circle are the power density and cell voltage of neat QPPO-based anion exchange membrane, respectively. Adapted from ref [96]

More recently, the mechanical properties and ion conductivity of films of PGNs composed of uncharged poly(2-phenylethyl methacrylate) (PPMA) grafted to *MxG*-CNCs imbibed with ionic liquid (IL) have been reported.[15] Here, the PPMA polymer was synthesized via ATRP with a phthalimide functionalized initiator which is convertible into a primary amine. The primary amine was then reacted with the carboxylic acid surface of the *MxG*-CNC thus forming PGNs with variable molecular weights (6 kg/mol, 10 kg/mol, and 20 kg/mol) yet similar weight percent polymer (~70 wt%). The PGNs were the cast into films and imbibed with different ionic liquids chosen to either induces a lower critical solution temperature (LCST) transition (1-ethyl-3-methylimidazolium bis(trifluoromethylsulfonyl)imide ([EMIM][TFSI])) or used as a control (1-hexyl-3- methylimidazolium bis(trifluoromethylsulfonyl)imide ([HMIM][TFSI]) (**Figure 1.9a**). In terms of mechanical properties, these IL-imbibed OCN films (30 wt% IL) exhibited a 70-fold increase in tensile strength and 25-fold increase in toughness relative to an ionic liquid imbibed 2-component nanocomposite (**Figure 1.9b**). Additionally, the use of the LCST causing [EMIM][TFSI] worked as expected, displaying a clear drop in ionic conductivity around 60°C. Note that these measurements were done in an anhydrous environment. Interestingly, when using [HMIM][TFSI], the films displayed higher ionic conductivity relative to the ionic liquid imbibed homopolymer or the ionic liquid containing multi-component composite prepared from the unfunctionalized CNC embedded in a poly(2-phenylethyl methacrylate) matrix (**Figure 1.10c**). This later study also showed that the IL-imbibed CNC-based PGNs exhibit a slight enhancement in conductivity relative to the IL-imbibed polymer, suggesting that the CNCs maybe playing a beneficial role on the ion conductivity in these films.

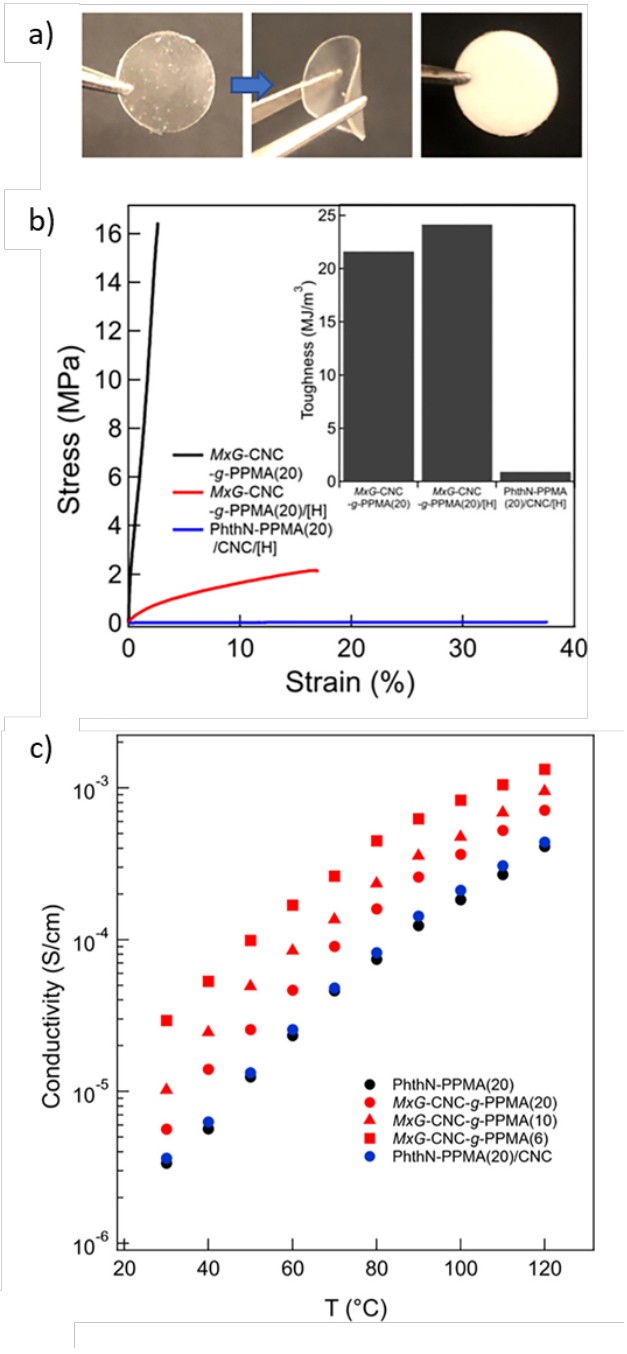

Figure 1.9: (a) Photographs of films of *MxG*-CNC-*g*-PPMA(20)/[H] (right) and PhthN-PPMA(20)/CNC/[H] (left). (b) Stress–strain curves and toughness values (inset) of the composite films with or without 30 wt % [HMIM][TFSI] (H), and c) Temperature-dependent conductivity

Figure 1.9 Continued: and thermal-responsive behavior of ionic-liquid-containing films containing 30 wt % [HMIM][TFSI]. Adapted from ref [15]

1.7 INTERFACES AND THEIR IMPACT ON CONDUCTIVE NANOCOMPOSITES

In analyzing a wide variety of nanocomposites, whether organic or inorganic, the added nanofiller has been shown to have a nontrivial impact on ionic conductivity and mechanical properties, whether based on nanofiller without polymer grafting, polymer grafted nanoparticles embedded in a matrix, or polymer grafted nanoparticle films. The mechanical properties of nanocomposites generally follow well understood models, whether Halpin psai,[61] percolation,[97] or effective medium theory.[17] Even so, nanoparticle loading can be increased by tailoring interfaces either by the nanoparticle surface chemistry or grafted polymer which directly impacts the mechanical properties through the aforementioned models. The electronic properties can be positively impacted by nanoparticle inclusion, but to fully apply the electronic property advantages and realize the potential of these solid electrolyte materials, a deeper understanding is required of the interfacial phenomena driving ion transport within the electrolyte material and also at the electrode/solid-electrolyte interface. Specifically, polymer grafted nanoparticle (PGN) films can attain high nanofiller loading and thus surface area. With additional surface area, beneficial interfacial interactions can be better magnified throughout a material. However, taking advantage of the beneficial interfacial interactions requires understanding the transport at this grafted polymer interface. In this section, polyelectrolyte ion transport mechanisms will be discussed, and interdigitated electrodes and their ability to successfully provide ideal platforms to investigate interfacial impacts on ionic conductivity will be presented.

In order to more broadly discuss the impact of interfaces on ionic conductivity, particularly in hydrated systems as will be presented in this thesis, the interactions of water and ions must be investigated. To this end, new spectroscopic[98–100] and computational methods[101–106] have been studied to better understand these relatively simple interactions between water and ions. Using 2-

dimensional infrared spectroscopy, Tokmakoff and coworkers have managed to investigate the ultrafast proton transfer kinetics in water and associated effects of added salt on the salt-water structure.[99,100] When combining this with molecular dynamics simulation work anomalous nonmonotonic dependences on the dynamics of salt concentration can be teased out highlighting the electrostatic and nonelectrostatic effects in the vibrational dynamics unexplainable through electrostatic fields alone.[98] First principles work on aqueous systems by Galli and coworkers has highlighted the importance of molecular polarizability in aqueous systems and the dependence of the ion and water interactions at high pressures and temperatures, analyzing the average structural and vibrational properties of water.[102,103] Finally, Voth and coworkers investigated proton transport in sub-2 nm hydrophobic nanopores using molecular dynamics simulations to identify the spatial distribution of water molecules and their structure to tease out mechanism for proton enhancement under confinement.[106] Ultimately, investigations such as these into the structure and dynamics of water and ions offer an important starting place for further understanding the impact of interfaces on transport.

1.8 IONIC CONDUCTIVITY THROUGH POLYELECTROLYTES

Understanding the mechanism of ion transport in polyelectrolytes provides the principal foundation for discussing the potential impact of interfaces. **Figure 1.10a** shows the proposed ion transport mechanism in the anhydrous PEO matrix, which demonstrates that lithium ions are coordinated by the ether oxygen atoms on a segmental PEO chain in a similar way to their complexation by organic carbonates.[107] With the processes of breaking/forming lithium–oxygen (Li–O) bonds, ion transport occurs by intrachain or interchain hooping in the PEO-based electrolyte.[108,109] The interchain and intrachain hopping can either occur in solitary lithium ions or ion pairs, yet fundamentally involves solvation site creation by the flexible PEO chain.[101] As water is added into the polyelectrolyte, the complexity of the system increases, resulting in a wider variety of mechanism such that the transport of anions through hydrated, ionically conductive polymer membranes are governed by three transport mechanisms: surface site hopping, vehicular, and Grotthuss.[110] Surface site hopping permits anions to hop between solvation sites without the aid of water molecules is correlated with the segmental mobility of polymer chain. When polymer is exposed to humidified environment, vehicular and Grotthuss mechanisms begin to dominate the overall anion transport as shown in **Figure 1.10b**. Water molecules will first participate the solvation of anions and as more water molecules added to the system, anions will be fully dissociated from the positively charged groups. The co-diffusion of anions with unbound water molecules is recognized as vehicular mechanism, and diffusion of the hydroxide ion through the static network of free water molecules by the formation and cleavage of the hydrogen bond is recognized as Grotthuss mechanism. For hydroxide ion transport in anion exchange membranes, both vehicular and Grotthuss mechanism substantially contribute to the overall conductivity.[111]

larger ion transport (such as iodide in chapters 3, 4 and 5 of this thesis) generally follow site hopping, with some vehicular transport.

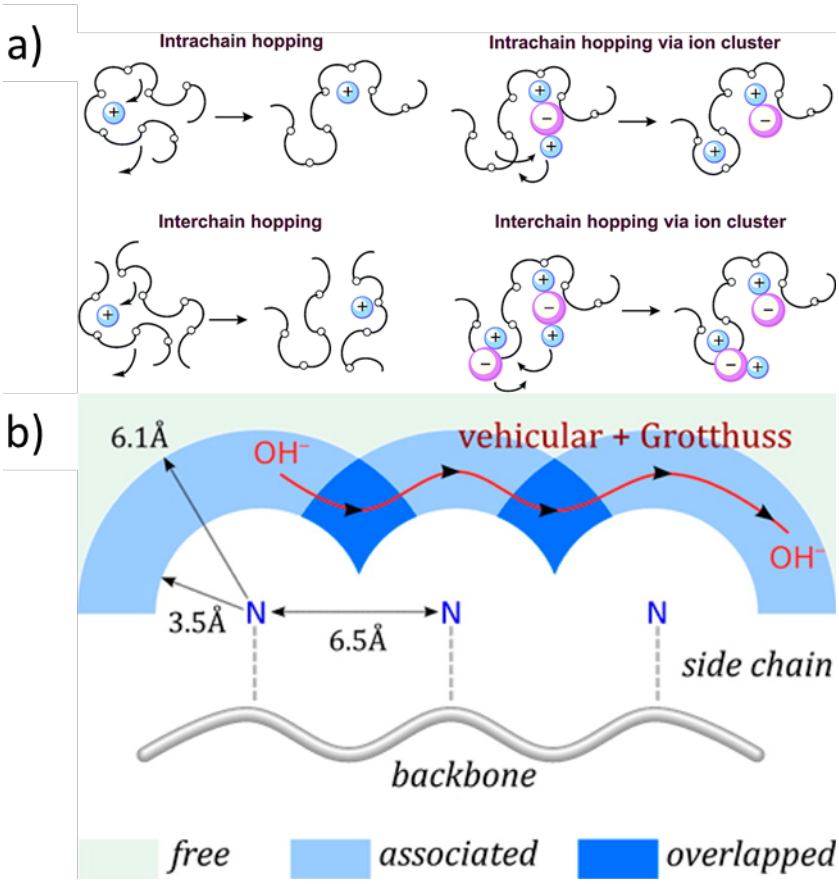

Figure 1.10: a) Ion transport mechanism of LiTFSI in poly(ethylene oxide) adapted from ref[107]. b) Ion transport mechanism of hydroxide in quaternary amine including polymer membrane adapted from ref[111].

In a recent example of analyzing the impact of solvation and transport mechanism on ionic conductivity, Bennington *et al.*[112] investigated LiTFSI transport in poly(ethylene oxide) (PEO), a ubiquitously studied solid polymer electrolyte, and poly[(oligo(ethylene oxide)) methyl ether methacrylate] (POEM) materials of different sidechain lengths, essentially sidechain PEO with a methacrylate backbone. In measuring the conductivity, it was shown that an order of magnitude

difference can be seen between side chain lengths of 9 PEO units (highest) to 3 PEO units (lowest) (**Figure 1.11a**). Furthermore, the conductivity of these materials fell by a factor of 3 compared to PEO itself. In analyzing the coordination state of the lithium, ether units furthest from the backbone were most likely to coordinate with lithium which suggests an outsized effect on the formation of solvation sites, the principal mechanism of lithium travel, and as a result in facilitating ionic motion. Most importantly, however, the further ether oxygen units exhibited faster dynamics than those near the methacrylate backbone, although the differences determined via molecular dynamics simulations and vibrational spectroscopy were not evident in T_g discrepancies of the material (**Figure 1.11b**). Thus, how the ethylene oxide segments participate in bonding the lithium, in forming solvation sites, and their dynamics were shown to be the critical factor in material conductivity.

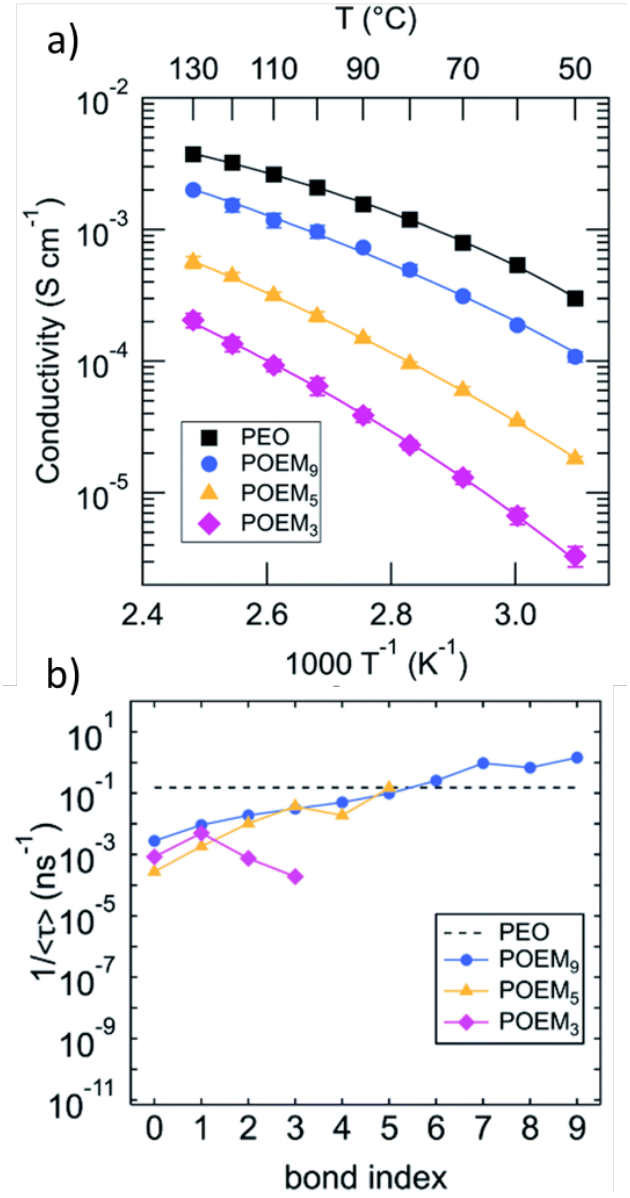

Figure 1.11: a) Experimentally determined temperature dependent ionic conductivity for r = 0.05 polymer electrolytes with solid lines representing the fits to the Vogel–Tammann–Fulcher (VTF) equation, b) Inverse mean relaxation time ($1/\langle\tau\rangle$) of different bonds along the polymer chains at T − Tg = 150 K derived from the bond vector autocorrelation function. $1/\langle\tau\rangle$ serves as an indicator of local segmental mobility. Adapted from ref [112]

Recent work by Chu *et al.*[105] examined the complicating inclusion of water into polyelectrolytes with charged polymer species, with particular relevance to this thesis as it is looking at identical polyelectrolytes in thesis chapters 3-5. In investigating the conductivity of iodide ions through poly (2-vinylpyridine-co-2-vinyl-1-methylpyridinium iodide) (mP2VP) at different relative humidities, the water uptake in the mP2VP was shown to greatly control conductivity over 5 orders of magnitude. Experimental and molecular dynamics simulation results were consistent in showing that increasing water decreased the T_g and thus impacting the conductivity. However, the relative impact of the polymer-ion bond disassociation and increase in polymer dynamics via plasticization was not well understood. Simulation analysis, however, yields the mechanism of iodide transport, with water being more important to facilitate the motion of iodide from solvation site to solvation site rather than its ability to enhance polymer dynamics; simulations at higher temperatures but lower water content yielded little iodide motion. Thus, water's coordination with iodide is irrefutably linked to its transport within the polymer, principally in moving between solvation sites. As a result, even in the relatively simply system of iodide transport, water functions to both permit site hopping mechanisms and coordinated, vehicular transport.

1.9 STRUCTURE OF WATER AT INTERFACES

In attempting to study the impact of interfaces on ion conductivity, difficulties arise at even the most fundamental of sources: understanding the position and interactions of constituents.[113,114] The conductivities of these systems depend upon the relative interactions between the interface, polymer, ions, and any solvating water or plasticizing solvent present. Understanding these most basic interactions is critical. However, even to begin probing these nuanced interactions, the nature of the interface must first be thoroughly explored. Beginning with water at interfaces, a solid material surface impacts the local structure of water surrounding it.[114,115] The subtle interactions of hydrogen bonding between molecular water and the different dielectric, metallic, or organic surfaces further impact water structure such as through double layer formation. Double layer formation involves a monolayer of water orienting itself at the interface, with the orientation extending over the course of several molecular units and eventually yielding to bulk water structure (**Figure 1.12**). Due to the molecularly thin interface, even generating sufficient data from the scant material present impedes the study of interfaces. Additional interactions and material types complicate interfacial study through solvated ions, polymer, organics at the interface.[116–120] Much of this fundamental interaction is still of active research, for example even the ubiquity of bilayer like structure being called into question.[113]

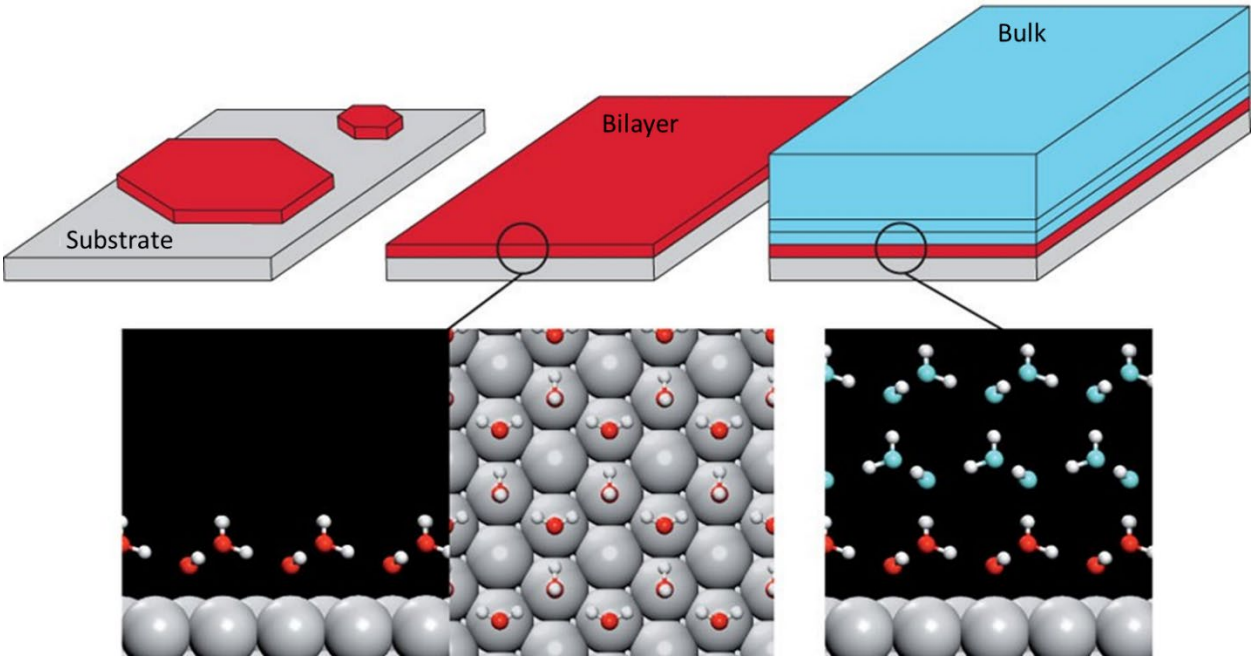

Figure 1.12: Cartoon displaying differentiation of interfacial and bulk alignment of water after formation of a bilayer. Adapted from ref [113]

1.10 FUNDAMENTAL STUDY OF INTERFACES VIA INTERDIGITATED ELECTRODES

The interfacial impacts of inorganic, solid materials on conductivity of grafted polymers offers another perspective worthy of investigation. As indicated previously, many inorganic nanoparticle inclusions into polyelectrolytes have shown both increases and decreases in conductivity, sometimes from the same material composition. Although much work has been done to tailor this organic-inorganic interface for enhanced conduction,[121–124] with grafted polymer playing a critical role, depth of fundamental investigation is lacking. Even so, great strides have been made recently through the use of interdigitated electrodes (IDEs).[125] IDEs enable the study of thin film materials by vastly increasing the surface area studied through use of the interdigitation. By either changing the IDE geometry (distance between electrodes, amount of overlap or electrodes, number of electrodes) and film geometry (thickness, different layered materials), a side range of material types can be studied. Although IDEs had been used previously to study material conductivity, Sharon *et al*. thoroughly investigated how to optimize the measurement of the electrochemical impedance (which enables conductivity measurements) of polymer electrolyte thin films.[125] Relevant to this discussion, different types and thickness of dielectric layers were applied by plasma enhanced atomic layer deposition. The dielectric layers had a number of effects, ranging from altering the surface energy to prevent dewetting to removing direct contact to the electrodes (preventing electrochemistry from occurring) to altering the measured electrochemical impedance spectrums. Specifically, layers with higher dielectric constants or thicker layers negatively impacted the ability to measure the impedance, but thin layers of polarizable oxides provide the correct frequency bandwidth to extract the film resistance. Additionally, the ideal models were investigated for inferring the film resistance and, with the film

geometry information, the material conductivity. Ultimately, the ability to add different surfaces to the IDEs enables them to probe a wide variety of surface interfaces experimentally, whether inorganic materials or polymer brushes.

Diblock copolymer offer an intriguing step towards grafted polymer systems due to the relatively "soft" polymer-polymer interface as compared to ceramic particles with grafted polymer, which has been shown to greatly impact ion conductivity. Diblock copolymers have long been seen as an ideal way to combine the structural properties of one polymer with the properties of a non-structurally sound but functional second block through the microphase separation and subsequent phase structure of these bound blocks. Specifically, by covalently bonding the two blocks, essentially creating a grafted interface, with sufficient immiscibility between blocks, the material can form structured phases from spheres, to rods, to lamellae, a well-established field of polymer physics.[126–129] By using polystyrene-block-poly(ethylene oxide) (PS-b-PEO) with imbibed LiTFSI, researchers have long hoped to combine the structural polystyrene properties with the ionic conductivity of PEO with LITFSI, forming an ideal solid polymer electrolyte.[130–132] Even so, these materials have always shown lower conductivity than their conductive homopolymer counterparts,[38] even accounting for the portion of non-conducting block. Termed effective medium theory, much work has then gone into investigating specifically what portion of the loss in conductivity can be accounted for by the non-conducting block under ideal, perfectly assembled situations and what must be accounted for by interfacial interactions at this grafted interconnection, while also accounting for the random orientation of the block copolymer phase grains.[133,134] Recent work on perfectly aligned lamella of PS-*b*-mP2VP via directed self-assembly on IDEs, whereupon either the microphase separated domains were aligned perpendicular to, randomly, or parallel to electrodes allowed for further insight into the conduction of these

materials.[135] Specifically, the parallel, or unaligned sample, showed a 4 order of magnitude decrease in conduction compared to the aligned ample, and yet even in this defect free material, the diblock conductivity did not homopolymer conductivity accounting perfectly for non-conducting material.

Recent work by Sharon *et al*. deeply probed the polymer physics rationale for the discrepancy in diblock copolymer conductivity in the PS-PEO system using both experimental and computational techniques.[136] This fundamental study assembled PS-PEO diblock copolymer with added LiTFSI salt parallel to applied electric field, with results in defect free assembly of the PEO+LiTFSI domains parallel the applied electric field. This enables measurement of the conductivity of the diblock copolymer and the homopolymer. By controlling the amount of added salt (r, the molar ratio of lithium to ethylene oxide repeat units), and the temperature, and comparing the conductivity of the PS-PEO vs PEO, the amount of inactive PEO in the PS-PEO block copolymer can be determined to be between 20%-50%. By using mean-field theory simulations of the structure with and without salt, the PEO/PS interface was modeled indicating an inactive region of intermixed PS and PEO, as would be expected in low Chi (interaction parameter) diblock copolymers. However, the quantity of intermixed interface agrees well with the quantity of inactive PEO in the conductivity measurements. Although this block copolymer interface and its dependence on Chi and block copolymer length has been studied extensively,[128,137–139] applying the field's insights into the polyelectrolyte conundrum of reduced conductivity in this material beautifully merges the polymer physics with the applicable polymer engineering. Finally, the lack of temperature dependence indicated that disrupted solvation site connectivity, rather than reduced segmental mobility, was the predominant factor in the reduced conductivity.

Dong *et al.* investigated PEO with LiTFSI, where 10 kg/mol hydroxy terminated PEO was grafted to the IDE surface and subsequently 20 kg/mol PEO layers of varying thickness (ca. 10 to 250 nm) were added on top of the initial grafting.[140] The measured conductivity decreased as the added PEO layer decreased in thickness, even as the ratio of PEO to LiTFSI remained constant (**Figure 1.13a**). Additionally, using methoxy terminated PEO, which would not graft to the SiO2 surface, instead of the initial hydroxy terminated PEO did not show the same drop in ionic conductivity. Taken together, it was concluded that the grafted PEO layer forms an immobile interfacial zone that leads to deviation from the bulk conductivity. Indeed, the thickness of this immobile interfacial zone could be modeled simply by assuming a parallel structure where a layer nearest the IDE surface exhibited no conductivity while the remaining polymer film exhibits the conductivity of bulk PEO with LiTFSI (**Figure 1.13b**). This immobile interfacial layer was estimated to be between 3nm to 10 nm as a function of the lithium to ethylene oxide ratio, r, ranging from 0.15 to 0.01 respectively. Although the work demurs as to the specific cause of the immobile interfacial layer, hypotheses are given such as reduced segmental mobility or uneven distribution of the LiTFSI salt due to the dense polymer grafts, although the grafted polymer clearly impedes the ionic conductivity.

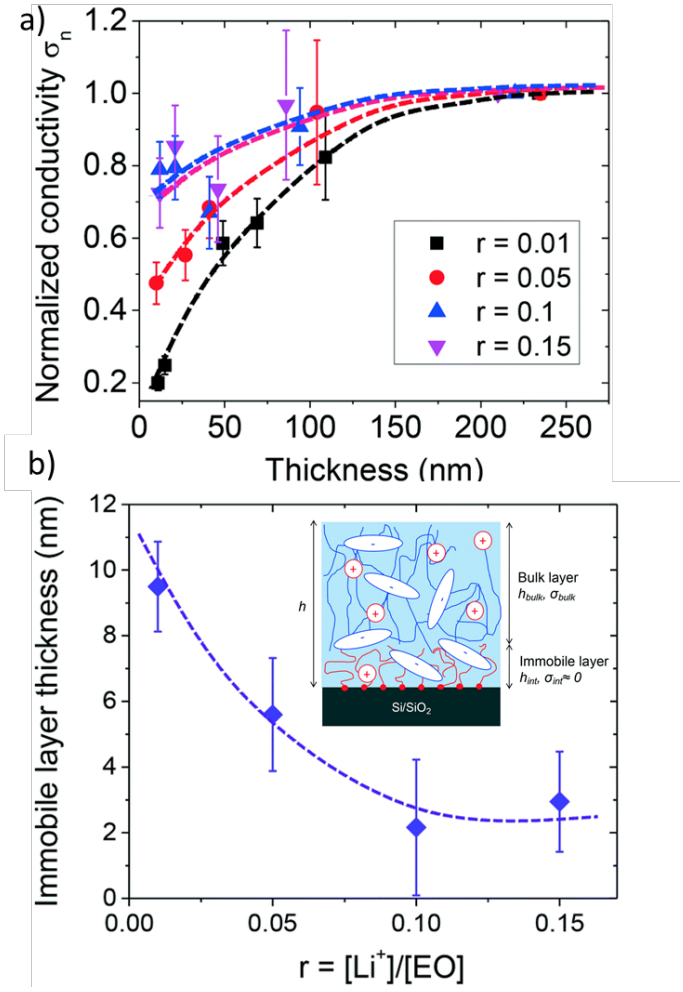

Figure 1.13: a) Normalized thickness dependence ionic conductivity of PEO–LiTFSI nanothin film on PEO-grafted substrates at different salt concentrations, *r*. b) Extracted immobile interfacial layer thickness h_{int} as a function of *r*.

Arges *et al.* investigated two hydrated polyelectrolyte brushes, sulfonated polystyrene (hydronium counter ion) (**Figure 1.14a)** and poly(2-vinyl n-methylpyridinium iodide) (**Figure 1.14b)** prepared by the selective sulfonation of a polystyrene brush and methylation via iodomethane of a poly(2-vinylpyridine) brush.[141] Specifically, the ionic conductivity of these brushes was investigated with as grafted to the planar IDEs or in grafted to a lithographically

defined, nanoconfined domain where the ionic conductivities of the nanoconfined samples were slightly (5-20%) less than the unconfined samples. However, the measured conductivities were on par with ungrafted conductivities of the same polymers, but this was not the principle focus of the work. Rather, the effects of confinement and counterion condensation were investigated and compared to molecular dynamics simulations. In actuality, the measured nanoconfined samples did not take into account the volume fraction of nonconducting polymer samples as the in-plane resistances were about the same even though the nanoconfined samples had half the volume fraction available for transport which was attributed to the counterion condensation in the materials.

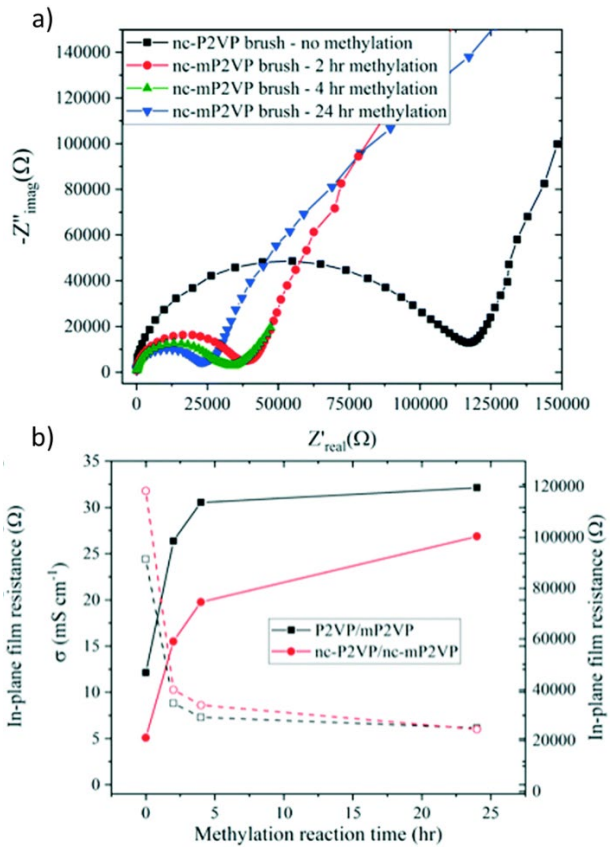

Figure 1.14: Nyquist plots of a) nc-P2VP and nc-mP2VP films with different exposure times to MeI. The determined in-plane resistance (dashed lines) and ionic conductivity (solid lines) for b) nc-P2VP, nc-mP2VP, P2VP, and mP2VP films with different exposure times to MeI.

As a result, IDEs provide the ideal platform for investigating surface interfacial effects, particularly of grafted polymer brushes, with the fundamental investigations having wide ranging impacts on the development of new polymer electrolyte nanocomposites. Understanding the role of interfaces on ionic conductivity is still an active field of investigation as the complex interplay of ions, polymers, interfaces and any additional components yields its insights slowly, but with great reward.

1.11 DISSERTATION SCOPE

The remaining chapters will focus on polymer grafted nanoparticle films based on cellulose nanocrystal nanorods and their structural, mechanical and ionic properties. Additionally, the rationale will be investigated for interesting interface driven ionic conductivity enhancement of model polymer systems. The overall goal is to establish structure/property relationships for these nanorod based polymer grafted nanoparticle films, both for mechanical and ionic conductivity properties.

Chapter 2 will focus on the structural and mechanical properties of polystyrene (PS) grafted cellulose nanocrystal OCNs. In particular the impact of polymer brush conformation on the toughness, modulus, and T_g will be explored.

Chapter 3 will focus on the ionic conductivity properties of poly(2-vinylpyridine) (PV) grafted CNCs after methylation with iodomethane. In analyzing the film structure, as well as polymer molecular weight, grafting density, and architecture, the variables regarding conductivity enhancement in this system will be investigated.

Chapter 4 will focus on the measured anisotropy in conductivity of the methylated PV grafted CNCs, with particular investigation as to how measuring anisotropicically conductive materials renders interesting electrochemical spectra.

Chapter 5 will focus on the fundamental impact of surface alcohol moiety and hydrophilicity on the ionic conductivity of hydrated, polymer electrolytes. This understanding will be applied to the methylated PV grafted CNC system.

1.12 REFERENCES

(1) Kumar, S. K.; Benicewicz, B. C.; Vaia, R. A.; Winey, K. I. 50th Anniversary Perspective: Are Polymer Nanocomposites Practical for Applications? *Macromolecules* **2017**, *50* (3), 714–731. https://doi.org/10.1021/acs.macromol.6b02330.

(2) Bet-Moushoul, E.; Mansourpanah, Y.; Farhadi, K.; Tabatabaei, M. TiO2 Nanocomposite Based Polymeric Membranes: A Review on Performance Improvement for Various Applications in Chemical Engineering Processes. *Chem. Eng. J.* **2016**, *283*, 29–46. https://doi.org/10.1016/j.cej.2015.06.124.

(3) Crosby, A. J.; Lee, J. Y. Polymer Nanocomposites: The "Nano" Effect on Mechanical Properties. *Polym. Rev.* **2007**, *47* (2), 217–229. https://doi.org/10.1080/15583720701271278.

(4) Cammarata, R. C. Mechanical Properties of Nanocomposite Thin Films. *Thin Solid Films* **1994**, *240*, 82–87. https://doi.org/10.1016/j.surfcoat.2008.06.131.

(5) Kumar, A.; Sharma, K.; Dixit, A. R. A Review of the Mechanical and Thermal Properties of Graphene and Its Hybrid Polymer Nanocomposites for Structural Applications. *J. Mater. Sci.* **2019**, *54* (8), 5992–6026. https://doi.org/10.1007/s10853-018-03244-3.

(6) Kim, D. J.; Jo, M. J.; Nam, S. Y. A Review of Polymer-Nanocomposite Electrolyte Membranes for Fuel Cell Application. *J. Ind. Eng. Chem.* **2015**, *21*, 36–52. https://doi.org/10.1016/j.jiec.2014.04.030.

(7) Gadim, T. D. O.; Vilela, C.; Loureiro, F. J. A.; Silvestre, A. J. D.; Freire, C. S. R.; Figueiredo, F. M. L. Nafion® and Nanocellulose: A Partnership for Greener Polymer Electrolyte Membranes. *Ind. Crops Prod.* **2016**, *93*, 212–218. https://doi.org/10.1016/j.indcrop.2016.01.028.

(8) Demirocak, D. E.; Srinivasan, S. S.; Stefanakos, E. K. A Review on Nanocomposite Materials for Rechargeable Li-Ion Batteries. *Appl. Sci.* **2017**, *7* (7), 1–26. https://doi.org/10.3390/app7070731.

(9) Ashraf, S.; Siddiqa, A.; Shahida, S.; Qaisar, S. Titanium-Based Nanocomposite Materials for Arsenic Removal from Water: A Review. *Heliyon* **2019**, *5* (5), e01577. https://doi.org/10.1016/j.heliyon.2019.e01577.

(10) Bassyouni, M.; Abdel-Aziz, M. H.; Zoromba, M. S.; Abdel-Hamid, S. M. S.; Drioli, E. A Review of Polymeric Nanocomposite Membranes for Water Purification. *J. Ind. Eng. Chem.* **2019**, *73*, 19–46. https://doi.org/10.1016/j.jiec.2019.01.045.

(11) Fernandes, N. J.; Koerner, H.; Giannelis, E. P.; Vaia, R. A. Hairy Nanoparticle Assemblies as One-Component Functional Polymer Nanocomposites: Opportunities and Challenges. *MRS Commun.* **2013**, *3* (01), 13–29. https://doi.org/10.1557/mrc.2013.9.

(12) Fernandes, N. J.; Koerner, H.; Giannelis, E. P.; Vaia, R. A. Hairy Nanoparticle Assemblies

as One-Component Functional Polymer Nanocomposites: Opportunities and Challenges. *MRS Commun.* **2013**, *3* (1), 13–29. https://doi.org/10.1557/mrc.2013.9.

(13) Choi, J.; Hui, C. M.; Pietrasik, J.; Dong, H.; Matyjaszewski, K.; Bockstaller, M. R. Toughening Fragile Matter: Mechanical Properties of Particle Solids Assembled from Polymer-Grafted Hybrid Particles Synthesized by ATRP. *Soft Matter* **2012**, *8* (15), 4072. https://doi.org/10.1039/c2sm06915f.

(14) Schmitt, M.; Choi, J.; Min Hui, C.; Chen, B.; Korkmaz, E.; Yan, J.; Margel, S.; Burak Ozdoganlar, O.; Matyjaszewski, K.; Bockstaller, M. R. Processing Fragile Matter: Effect of Polymer Graft Modification on the Mechanical Properties and Processibility of (Nano-) Particulate Solids. *Soft Matter* **2016**, *12* (15), 3527–3537. https://doi.org/10.1039/C6SM00095A.

(15) Kato, R.; Lettow, J. H.; Patel, S. N.; Rowan, S. J. Ion-Conducting Thermoresponsive Films Based on Polymer-Grafted Cellulose Nanocrystals. *ACS Appl. Mater. Interfaces* **2020**, *12*, 54083–54093. https://doi.org/10.1021/acsami.0c16059.

(16) Schmitt, M.; Choi, J.; Min Hui, C.; Chen, B.; Korkmaz, E.; Yan, J.; Margel, S.; Burak Ozdoganlar, O.; Matyjaszewski, K.; Bockstaller, M. R. Processing Fragile Matter: Effect of Polymer Graft Modification on the Mechanical Properties and Processibility of (Nano-) Particulate Solids. *Soft Matter* **2016**, *12* (15), 3527–3537. https://doi.org/10.1039/C6SM00095A.

(17) Jiao, Y.; Tibbits, A.; Gillman, A.; Hsiao, M. S.; Buskohl, P.; Drummy, L. F.; Vaia, R. A. Deformation Behavior of Polystyrene-Grafted Nanoparticle Assemblies with Low Grafting Density. *Macromolecules* **2018**, *51* (18), 7257–7265. https://doi.org/10.1021/acs.macromol.8b01524.

(18) de Gennes, P. G. Conformations of Polymers Attached to an Interface. *Macromolecules* **1980**, *13* (5), 1069–1075. https://doi.org/10.1021/ma60077a009.

(19) Milner, S. T.; Witten, T. A.; Cates, M. E. Theory of the Grafted Polymer Brush. *Macromolecules* **1988**, *21* (8), 2610–2619. https://doi.org/10.1021/ma00186a051.

(20) Hore, M. J. A.; Korley, L. S. T. J.; Kumar, S. K. Polymer-Grafted Nanoparticles. *J. Appl. Phys.* **2020**, *128* (3). https://doi.org/10.1063/5.0019326.

(21) Kumar, S. K.; Jouault, N.; Benicewicz, B.; Neely, T. Nanocomposites with Polymer Grafted Nanoparticles. *Macromolecules* **2013**, *46* (9), 3199–3214. https://doi.org/10.1021/ma4001385.

(22) Dukes, D.; Li, Y.; Lewis, S.; Benicewicz, B.; Schadler, L.; Kumar, S. K. Conformational Transitions of Spherical Polymer Brushes: Synthesis, Characterization, and Theory. *Macromolecules* **2010**, *43* (3), 1564–1570. https://doi.org/10.1021/ma901228t.

(23) Dan, N.; Tirrell, M. Polymers Tethered to Curved Interfaces. A Self-Consistent-Field Analysis. *Macromolecules* **1992**, *25* (11), 2890–2895. https://doi.org/10.1021/ma00037a016.

(24) Halperin, A.; Tirrell, M.; Lodge, T. P. Tethered Chains in Polymer Microstructures. *Adv. Polym. Sci.* **1991**, *100*, 30–71. https://doi.org/10.1007/bfb0051635.

(25) Daoud, M.; Cotton, J. P. Star Shaped Polymers: A Model for the Conformation and Its Concentration Dependence. *J. Phys. Paris* **1982**, *43* (3), 531–538. https://doi.org/10.1051/jphys:01982004303053100.

(26) Ohno, K.; Morinaga, T.; Koh, K.; Tsujii, Y.; Fukuda, T. Synthesis of Monodisperse Silica Particles Coated with Well-Defined, High-Density Polymer Brushes by Surface-Initiated Atom Transfer Radical Polymerization. *Macromolecules* **2005**, *38* (6), 2137–2142. https://doi.org/10.1021/ma048011q.

(27) Ohno, K.; Morinaga, T.; Takeno, S.; Tsujii, Y.; Fukuda, T. Suspensions of Silica Particles Grafted with Concentrated Polymer Brush: Effects of Graft Chain Length on Brush Layer Thickness and Colloidal Crystallization. *Macromolecules* **2007**, *40* (25), 9143–9150. https://doi.org/10.1021/ma071770z.

(28) Roovers, J. E. L.; Bywater, S. Preparation and Characterization of Four-Branched Star Polystyrene. *Macromolecules* **1972**, *5* (4), 384–388.

(29) Morton, M.; Helminiak, T. E.; Gadkary, S. D.; Bueche, F. Preparation and Properties of Monodisperse Branched Polystyrene. *J. Polym. Sci.* **1962**, *57* (165), 471–482. https://doi.org/10.1002/pol.1962.1205716537.

(30) Wohlhauser, S.; Delepierre, G.; Labet, M.; Morandi, G.; Thielemans, W.; Weder, C.; Zoppe, J. O. Grafting Polymers from Cellulose Nanocrystals: Synthesis, Properties, and Applications. *Macromolecules* **2018**, *51* (16), 6157–6189. https://doi.org/10.1021/acs.macromol.8b00733.

(31) Pyun, J.; Matyjaszewski, K.; Kowalewski, T.; Savin, D.; Patterson, G.; Kickelbick, G.; Huesing, N. Synthesis of Well-Defined Block Copolymers Tethered to Polysilsesquioxane Nanoparticles and Their Nanoscale Morphology on Surfaces [2]. *Journal of the American Chemical Society*. 2001, pp 9445–9446. https://doi.org/10.1021/ja010241m.

(32) Husseman, M.; Malmström, E. E.; McNamara, M.; Mate, M.; Mecerreyes, D.; Benoit, D. G.; Hedrick, J. L.; Mansky, P.; Huang, E.; Russell, T. P.; Hawker, C. J. Controlled Synthesis of Polymer Brushes by "Living" Free Radical Polymerization Techniques. *Macromolecules* **1999**, *32* (5), 1424–1431. https://doi.org/10.1021/ma981290v.

(33) Baum, M.; Brittain, W. J. Synthesis of Polymer Brushes on Silicate Substrates via Reversible Addition Fragmentation Chain Transfer Technique. *Macromolecules* **2002**, *35* (3), 610–615. https://doi.org/10.1021/ma0112467.

(34) Matyjaszewski, K.; Miller, P. J.; Shukla, N.; Immaraporn, B.; Gelman, A.; Luokala, B. B.; Siclovan, T. M.; Kickelbick, G.; Valiant, T.; Hoffmann, H.; Pakula, T. Polymers at Interfaces: Using Atom Transfer Radical Polymerization in the Controlled Growth of Homopolymers and Block Copolymers from Silicon Surfaces in the Absence of Untethered Sacrificial Initiator. *Macromolecules* **1999**, *32* (26), 8716–8724. https://doi.org/10.1021/ma991146p.

(35) Placke, T.; Kloepsch, R.; Dühnen, S.; Winter, M. Lithium Ion, Lithium Metal, and Alternative Rechargeable Battery Technologies: The Odyssey for High Energy Density. *J. Solid State Electrochem.* **2017**, *21* (7), 1939–1964. https://doi.org/10.1007/s10008-017-3610-7.

(36) Kim, H. C.; Mun, S.; Ko, H. U.; Zhai, L.; Kafy, A.; Kim, J. Renewable Smart Materials. *Smart Mater. Struct.* **2016**, *25* (7). https://doi.org/10.1088/0964-1726/25/7/073001.

(37) Ellabban, O.; Abu-Rub, H.; Blaabjerg, F. Renewable Energy Resources: Current Status, Future Prospects and Their Enabling Technology. *Renew. Sustain. Energy Rev.* **2014**, *39*, 748–764. https://doi.org/10.1016/j.rser.2014.07.113.

(38) Hallinan, D. T.; Balsara, N. P. Polymer Electrolytes. *Annu. Rev. Mater. Res.* **2013**, *43*, 503–525. https://doi.org/10.1146/annurev-matsci-071312-121705.

(39) Shi, Y.; Eze, C.; Xiong, B.; He, W.; Zhang, H.; Lim, T. M.; Ukil, A.; Zhao, J. Recent Development of Membrane for Vanadium Redox Flow Battery Applications: A Review. *Appl. Energy* **2019**, *238* (December 2018), 202–224. https://doi.org/10.1016/j.apenergy.2018.12.087.

(40) Manuel Stephan, A.; Nahm, K. S. Review on Composite Polymer Electrolytes for Lithium Batteries. *Polymer (Guildf).* **2006**, *47* (16), 5952–5964. https://doi.org/10.1016/j.polymer.2006.05.069.

(41) Boaretto, N.; Meabe, L.; Martinez-Ibañez, M.; Armand, M.; Zhang, H. Review—Polymer Electrolytes for Rechargeable Batteries: From Nanocomposite to Nanohybrid. *J. Electrochem. Soc.* **2020**, *167* (7), 070524. https://doi.org/10.1149/1945-7111/ab7221.

(42) Croce, F.; Appetecchi, G. B.; Persi, L.; Scrosati, B. (Al2O3, TiO2) Nanocomposite Polymer Electrolytes for Lithium Batteries, F. Croce, B. Scrosati, Nature (1998). *Nat. Lett.* **1998**, *394* (July), 456–458.

(43) Yin, C.; Li, J.; Zhou, Y.; Zhang, H.; Fang, P.; He, C. Phase Separation and Development of Proton Transport Pathways in Metal Oxide Nanoparticle/Nafion Composite Membranes during Water Uptake. *J. Phys. Chem. C* **2018**, *122* (17), 9710–9717. https://doi.org/10.1021/acs.jpcc.8b02535.

(44) Liu, W.; Liu, N.; Sun, J.; Hsu, P. C.; Li, Y.; Lee, H. W.; Cui, Y. Ionic Conductivity Enhancement of Polymer Electrolytes with Ceramic Nanowire Fillers. *Nano Lett.* **2015**, *15* (4), 2740–2745. https://doi.org/10.1021/acs.nanolett.5b00600.

(45) Liu, W.; Lin, D.; Sun, J.; Zhou, G.; Cui, Y. Improved Lithium Ionic Conductivity in Composite Polymer Electrolytes with Oxide-Ion Conducting Nanowires. *ACS Nano* **2016**, *10* (12), 11407–11413. https://doi.org/10.1021/acsnano.6b06797.

(46) Liu, W.; Lee, S. W.; Lin, D.; Shi, F.; Wang, S.; Sendek, A. D.; Cui, Y. Enhancing Ionic Conductivity in Composite Polymer Electrolytes with Well-Aligned Ceramic Nanowires. *Nat. Energy* **2017**, *2* (5), 1–7. https://doi.org/10.1038/nenergy.2017.35.

(47) Villaluenga, I.; Chen, X. C.; Devaux, D.; Hallinan, D. T.; Balsara, N. P. Nanoparticle-Driven Assembly of Highly Conducting Hybrid Block Copolymer Electrolytes. *Macromolecules* **2015**, *48* (2), 358–364. https://doi.org/10.1021/ma502234y.

(48) O'Reilly, M. V.; Winey, K. I. Silica Nanoparticles Densely Grafted with PEO for Ionomer Plasticization. *RSC Adv.* **2015**, *5* (25), 19570–19580. https://doi.org/10.1039/c4ra15178j.

(49) Agrawal, A.; Choudhury, S.; Archer, L. A. A Highly Conductive, Non-Flammable Polymer-Nanoparticle Hybrid Electrolyte. *RSC Adv.* **2015**, *5* (27), 20800–20809. https://doi.org/10.1039/c5ra01031d.

(50) Nugent, J. L.; Moganty, S. S.; Archer, L. A. Nanoscale Organic Hybrid Electrolytes. *Adv. Mater.* **2010**, *22* (33), 3677–3680. https://doi.org/10.1002/adma.201000898.

(51) Wang, P.; Zhou, Y. N.; Luo, J. S.; Luo, Z. H. Poly(Ionic Liquid)s-Based Nanocomposite Polyelectrolytes with Tunable Ionic Conductivity Prepared via SI-ATRP. *Polym. Chem.* **2014**, *5* (3), 882–891. https://doi.org/10.1039/c3py01025b.

(52) Jiao, Y.; Chou, T.; Akcora, P. Design of Ion-Containing Polymer-Grafted Nanoparticles for Conductive Membranes. *Macromolecules* **2015**, *48* (14), 4910–4917. https://doi.org/10.1021/acs.macromol.5b00758.

(53) Hore, M. J. A.; Composto, R. J. Functional Polymer Nanocomposites Enhanced by Nanorods. *Macromolecules* **2014**, *47* (3), 875–887. https://doi.org/10.1021/ma402179w.

(54) Lin, C. C.; Cargnello, M.; Murray, C. B.; Clarke, N.; Winey, K. I.; Riggleman, R. A.; Composto, R. J. Nanorod Mobility Influences Polymer Diffusion in Polymer Nanocomposites. *ACS Macro Lett.* **2017**, *6* (8), 869–874. https://doi.org/10.1021/acsmacrolett.7b00533.

(55) Mendez, J.; Annamalai, P. K.; Eichhorn, S. J.; Rusli, R.; Rowan, S. J.; Foster, E. J.; Weder, C. Bioinspired Mechanically Adaptive Polymer Nanocomposites with Water-Activated Shape-Memory Effect. *Macromolecules* **2011**, *44* (17), 6827–6835. https://doi.org/10.1021/ma201502k.

(56) Salehiyan, R.; Ray, S. S. Tuning the Conductivity of Nanocomposites through Nanoparticle Migration and Interface Crossing in Immiscible Polymer Blends: A Review on Fundamental Understanding. *Macromol. Mater. Eng.* **2019**, *304* (2), 1–33. https://doi.org/10.1002/mame.201800431.

(57) Zhang, G.; Xia, Y.; Wang, H.; Tao, Y.; Tao, G.; Tu, S.; Wu, H. A Percolation Model of Thermal Conductivity for Filled Polymer Composites. *J. Compos. Mater.* **2010**, *44* (8), 963–970. https://doi.org/10.1177/0021998309349690.

(58) Bonnet, P.; Sireude, D.; Garnier, B.; Chauvet, O. Thermal Properties and Percolation in Carbon Nanotube-Polymer Composites. *Appl. Phys. Lett.* **2007**, *91* (20), 2005–2008. https://doi.org/10.1063/1.2813625.

(59) Last, B. J.; Thouless, D. J. Percolation Theory and Electrical Conductivity. *Phys. Rev. Lett.*

1971, *27* (25), 1719–1721. https://doi.org/10.1103/PhysRevLett.27.1719.

(60) Follain, N.; Belbekhouche, S.; Bras, J.; Siqueira, G.; Marais, S.; Dufresne, A. Water Transport Properties of Bio-Nanocomposites Reinforced by Luffa Cylindrica Cellulose Nanocrystals. *J. Memb. Sci.* **2013**, *427*, 218–229. https://doi.org/10.1016/j.memsci.2012.09.048.

(61) Nanocomposites, S. P.; Capadona, J. R.; Shanmuganathan, K.; Tyler, D. J.; Rowan, S. J.; Weder, C.; J, S. Stimuli-Responsive Polymer Nanocomposites Inspired by the Sea Cucumber Dermis. *Science (80-.).* **2008**, No. March, 1370–1375. https://doi.org/10.1126/science.1153307.

(62) Cudjoe, E.; Hunsen, M.; Xue, Z.; Way, A. E.; Barrios, E.; Olson, R. A.; Hore, M. J. A.; Rowan, S. J. Miscanthus Giganteus: A Commercially Viable Sustainable Source of Cellulose Nanocrystals. *Carbohydr. Polym.* **2017**, *155*, 230–241. https://doi.org/10.1016/j.carbpol.2016.08.049.

(63) Zhao, Y.; Moser, C.; Lindström, M. E.; Henriksson, G.; Li, J. Cellulose Nanofibers from Softwood, Hardwood, and Tunicate: Preparation-Structure-Film Performance Interrelation. *ACS Appl. Mater. Interfaces* **2017**, *9* (15), 13508–13519. https://doi.org/10.1021/acsami.7b01738.

(64) Fraschini, C.; Chauve, G.; Bouchard, J. TEMPO-Mediated Surface Oxidation of Cellulose Nanocrystals (CNCs). *Cellulose* **2017**, *24* (7), 2775–2790. https://doi.org/10.1007/s10570-017-1319-5.

(65) Yang, H.; Zhang, Y.; Kato, R.; Rowan, S. J. Preparation of Cellulose Nanofibers from Miscanthus x. Giganteus by Ammonium Persulfate Oxidation. *Carbohydr. Polym.* **2019**, *212* (February), 30–39. https://doi.org/10.1016/j.carbpol.2019.02.008.

(66) Moon, R. J.; Martini, A.; Nairn, J.; Simonsen, J.; Youngblood, J. *Cellulose Nanomaterials Review: Structure, Properties and Nanocomposites*; 2011; Vol. 40. https://doi.org/10.1039/c0cs00108b.

(67) Eichhorn, S. J.; Dufresne, A.; Aranguren, M.; Marcovich, N. E.; Capadona, J. R.; Rowan, S. J.; Weder, C.; Thielemans, W.; Roman, M.; Renneckar, S.; Gindl, W.; Veigel, S.; Keckes, J.; Yano, H.; Abe, K.; Nogi, M.; Nakagaito, A. N.; Mangalam, A.; Simonsen, J.; Benight, A. S.; Bismarck, A.; Berglund, L. A.; Peijs, T. Review: Current International Research into Cellulose Nanofibres and Nanocomposites. *J. Mater. Sci.* **2010**, *45* (1), 1–33. https://doi.org/10.1007/s10853-009-3874-0.

(68) Eyley, S.; Thielemans, W. Surface Modification of Cellulose Nanocrystals. *Nanoscale* **2014**, *6* (14), 7764–7779. https://doi.org/10.1039/c4nr01756k.

(69) Moon, R. J.; Martini, A.; Nairn, J.; Simonsen, J.; Youngblood, J. *Cellulose Nanomaterials Review: Structure, Properties and Nanocomposites*; 2011; Vol. 40. https://doi.org/10.1039/c0cs00108b.

(70) Mendez, J.; Annamalai, P. K.; Eichhorn, S. J.; Rusli, R.; Rowan, S. J.; Foster, E. J.; Weder,

C. Bioinspired Mechanically Adaptive Polymer Nanocomposites with Water-Activated Shape-Memory Effect. *Macromolecules* **2011**, *44* (17), 6827–6835. https://doi.org/10.1021/ma201502k.

(71) Nguyen, J. K.; Park, D. J.; Skousen, J. L.; Hess-Dunning, A. E.; Tyler, D. J.; Rowan, S. J.; Weder, C.; Capadona, J. R. Mechanically-Compliant Intracortical Implants Reduce the Neuroinflammatory Response. *J. Neural Eng.* **2014**, *11* (5). https://doi.org/10.1088/1741-2560/11/5/056014.

(72) Padalkar, S.; Capadona, J. R.; Rowan, S. J.; Weder, C.; Won, Y. H.; Stanciu, L. A.; Moon, R. J. Natural Biopolymers: Novel Templates for the Synthesis of Nanostructures. *Langmuir* **2010**, *26* (11), 8497–8502. https://doi.org/10.1021/la904439p.

(73) Šturcová, A.; Davies, G. R.; Eichhorn, S. J. Elastic Modulus and Stress-Transfer Properties of Tunicate Cellulose Whiskers. *Biomacromolecules* **2005**, *6* (2), 1055–1061. https://doi.org/10.1021/bm049291k.

(74) Rusli, R.; Eichhorn, S. J. Determination of the Stiffness of Cellulose Nanowhiskers and the Fiber-Matrix Interface in a Nanocomposite Using Raman Spectroscopy. *Appl. Phys. Lett.* **2008**, *93* (3), 91–94. https://doi.org/10.1063/1.2963491.

(75) Sapkota, J.; Kumar, S.; Weder, C.; Foster, E. J. Influence of Processing Conditions on Properties of Poly (Vinyl Acetate)/Cellulose Nanocrystal Nanocomposites. *Macromol. Mater. Eng.* **2015**, *300* (5), 562–571. https://doi.org/10.1002/mame.201400313.

(76) Dagnon, K. L.; Shanmuganathan, K.; Weder, C.; Rowan, S. J. Water-Triggered Modulus Changes of Cellulose Nanofiber Nanocomposites with Hydrophobic Polymer Matrices. *Macromolecules* **2012**, *45* (11), 4707–4715. https://doi.org/10.1021/ma300463y.

(77) Nicharat, A.; Shirole, A.; Foster, E. J.; Weder, C. Thermally Activated Shape Memory Behavior of Melt-Mixed Polyurethane/Cellulose Nanocrystal Composites. *J. Appl. Polym. Sci.* **2017**, *134* (27), 1–10. https://doi.org/10.1002/app.45033.

(78) Sapkota, J.; Natterodt, J. C.; Shirole, A.; Foster, E. J.; Weder, C. Fabrication and Properties of Polyethylene/Cellulose Nanocrystal Composites. *Macromol. Mater. Eng.* **2017**, *302* (1), 1–6. https://doi.org/10.1002/mame.201600300.

(79) Sapkota, J.; Jorfi, M.; Weder, C.; Foster, E. J. Reinforcing Poly (Ethylene) with Cellulose Nanocrystals. *Macromol. Rapid Commun.* **2014**, *35* (20), 1747–1753. https://doi.org/10.1002/marc.201400382.

(80) Tang, L.; Weder, C. Cellulose Whisker/Epoxy Resin Nanocomposites. *ACS Appl. Mater. Interfaces* **2010**, *2* (4), 1073–1080. https://doi.org/10.1021/am900830h.

(81) Capadona, J. R.; Van Den Berg, O.; Capadona, L. A.; Schroeter, M.; Rowan, S. J.; Tyler, D. J.; Weder, C. A Versatile Approach for the Processing of Polymer Nanocomposites with Self-Assembled Nanofibre Templates. *Nat. Nanotechnol.* **2007**, *2* (12), 765–769. https://doi.org/10.1038/nnano.2007.379.

(82) Nicharat, A.; Sapkota, J.; Weder, C.; Johan Foster, E. Melt Processing of Polyamide 12 and Cellulose Nanocrystals Nanocomposites. *J. Appl. Polym. Sci.* **2015**, *132* (45), 1–10. https://doi.org/10.1002/app.42752.

(83) Hore, M. J. A. Polymers on Nanoparticles: Structure & Dynamics. *Soft Matter* **2019**, *15* (6), 1120–1134. https://doi.org/10.1039/c8sm02110d.

(84) Cao, X.; Habibi, Y.; Lucia, L. A. One-Pot Polymerization, Surface Grafting, and Processing of Waterborne Polyurethane-Cellulose Nanocrystal Nanocomposites. *J. Mater. Chem.* **2009**, *19* (38), 7137. https://doi.org/10.1039/b910517d.

(85) Harrisson, S.; Drisko, G. L.; Malmström, E.; Hult, A.; Wooley, K. L. Hybrid Rigid/Soft and Biologic/Synthetic Materials: Polymers Grafted onto Cellulose Microcrystals. *Biomacromolecules* **2011**, *12* (4), 1214–1223. https://doi.org/10.1021/bm101506j.

(86) Kloser, E.; Gray, D. G. Surface Grafting of Cellulose Nanocrystals with Poly(Ethylene Oxide) in Aqueous Media. *Langmuir* **2010**, *26* (16), 13450–13456. https://doi.org/10.1021/la101795s.

(87) Zeinali, E.; Haddadi-asl, V.; Roghani-mamaqani, H. Synthesis of Dual Thermo- and PH-Sensitive Poly (N-Isopropylacrylamide-Co-Acrylic Acid)-Grafted Cellulose Nanocrystals by Reversible Addition-Fragmentation Chain Transfer Polymerization. *J. Biomed. Mater. Res. Part A* **2017**, 1–13. https://doi.org/10.1002/jbm.a.36230.

(88) Dhar, P.; Tarafder, D.; Kumar, A.; Katiyar, V. Thermally Recyclable Polylactic Acid/Cellulose Nanocrystal Films through Reactive Extrusion Process. *Polym. (United Kingdom)* **2016**, *87*, 268–282. https://doi.org/10.1016/j.polymer.2016.02.004.

(89) Hansoge, N. K.; Huang, T.; Sinko, R.; Xia, W.; Chen, W.; Keten, S. Materials by Design for Stiff and Tough Hairy Nanoparticle Assemblies. *ACS Nano* **2018**, *12* (8), 7946–7958. https://doi.org/10.1021/acsnano.8b02454.

(90) Hansoge, N. K.; Keten, S. Effect of Polymer Chemistry on Chain Conformations in Hairy Nanoparticle Assemblies. *ACS Macro Lett.* **2019**, 1209–1215. https://doi.org/10.1021/acsmacrolett.9b00526.

(91) Wohlhauser, S.; Kuhnt, T.; Meesorn, W.; Montero De Espinosa, L.; Zoppe, J. O.; Weder, C. One-Component Nanocomposites Based on Polymer-Grafted Cellulose Nanocrystals. *Macromolecules* **2020**, *53*, 821–834. https://doi.org/10.1021/acs.macromol.9b01612.

(92) Tayeb, P.; H. Tayeb, A. Nanocellulose Applications in Sustainable Electrochemical and Piezoelectric Systems: A Review. *Carbohydr. Polym.* **2019**, *224* (July), 115149. https://doi.org/10.1016/j.carbpol.2019.115149.

(93) Muhd Julkapli, N.; Bagheri, S. Nanocellulose as a Green and Sustainable Emerging Material in Energy Applications: A Review. *Polym. Adv. Technol.* **2017**, *28* (12), 1583–1594. https://doi.org/10.1002/pat.4074.

(94) Rincón-Iglesias, M.; Lizundia, E.; Costa, C. M.; Lanceros-Méndez, S. Tailoring Electrical

and Mechanical Properties of All-Natural Polymer Composites for Environmentally Friendlier Electronics. *ACS Appl. Polym. Mater.* **2020**, *2* (4), 1448–1457. https://doi.org/10.1021/acsapm.9b01098.

(95) Jabbour, L.; Bongiovanni, R.; Beneventi, D. Cellulose-Based Li-Ion Batteries : A Review. *Cellulose* **2013**, No. 20, 1523–1545. https://doi.org/10.1007/s10570-013-9973-8.

(96) Cheng, X.; Wang, J.; Liao, Y.; Li, C.; Wei, Z. Enhanced Conductivity of Anion-Exchange Membrane by Incorporation of Quaternized Cellulose Nanocrystal. *ACS Appl. Mater. Interfaces* **2018**, *10* (28), 23774–23782. https://doi.org/10.1021/acsami.8b05298.

(97) Fujisawa, S.; Ikeuchi, T.; Takeuchi, M.; Saito, T.; Isogai, A. Superior Reinforcement Effect of TEMPO-Oxidized Cellulose Nanofibrils in Polystyrene Matrix: Optical, Thermal, and Mechanical Studies. *Biomacromolecules* **2012**, *13* (7), 2188–2194. https://doi.org/10.1021/bm300609c.

(98) Lewis, N. H. C.; Iscen, A.; Felts, A.; Dereka, B.; Schatz, G. C.; Tokmakoff, A. Vibrational Probe of Aqueous Electrolytes: The Field Is Not Enough. *J. Phys. Chem. B* **2020**, *124* (32), 7013–7026. https://doi.org/10.1021/acs.jpcb.0c05510.

(99) Carpenter, W. B.; Lewis, N. H. C.; Fournier, J. A.; Tokmakoff, A. Entropic Barriers in the Kinetics of Aqueous Proton Transfer. *J. Chem. Phys.* **2019**, *151* (3). https://doi.org/10.1063/1.5108907.

(100) Carpenter, W. B.; Fournier, J. A.; Lewis, N. H. C.; Tokmakoff, A. Picosecond Proton Transfer Kinetics in Water Revealed with Ultrafast IR Spectroscopy. *J. Phys. Chem. B* **2018**, *122* (10), 2792–2802. https://doi.org/10.1021/acs.jpcb.8b00118.

(101) Sharon, D.; Bennington, P.; Webb, M. A.; Deng, C.; De Pablo, J. J.; Patel, S. N.; Nealey, P. F. Molecular Level Differences in Ionic Solvation and Transport Behavior in Ethylene Oxide-Based Homopolymer and Block Copolymer Electrolytes. *J. Am. Chem. Soc.* **2021**, *143* (8), 3180–3190. https://doi.org/10.1021/jacs.0c12538.

(102) Rozsa, V.; Galli, G. Solvation of Simple Ions in Water at Extreme Conditions. *J. Chem. Phys.* **2021**, *154* (14), 15–17. https://doi.org/10.1063/5.0046193.

(103) Galli, G.; Rozsa, V. F. Molecular Polarizabilities in Aqueous Systems from First-Principles. *J. Phys. Chem. B* **2021**, *125* (9), 2183–2192. https://doi.org/10.1021/acs.jpcb.0c10732.

(104) Rozsa, V.; Pham, T. A.; Galli, G. Molecular Polarizabilities as Fingerprints of Perturbations to Water by Ions and Confinement. *J. Chem. Phys.* **2020**, *152* (12). https://doi.org/10.1063/1.5143317.

(105) Chu, W.; Webb, M. A.; Deng, C.; Colon, Y. J.; Kambe, Y.; Krishnan, S.; Nealey, P. F.; de Pablo, J. J. Understanding Ion Mobility in P2VP/NMP+I − Polymer Electrolytes: A Combined Simulation and Experimental Study. *Macromolecules* **2020**, *53* (8), 2783–2792. https://doi.org/10.1021/acs.macromol.9b02329.

(106) Ma, X.; Li, C.; Martinson, A. B. F.; Voth, G. A. Water-Assisted Proton Transport in

Confined Nanochannels. *J. Phys. Chem. C* **2020**, *124* (29), 16186–16201. https://doi.org/10.1021/acs.jpcc.0c04493.

(107) Xue, Z.; He, D.; Xie, X. Poly(Ethylene Oxide)-Based Electrolytes for Lithium-Ion Batteries. *J. Mater. Chem. A* **2015**, *3* (38), 19218–19253. https://doi.org/10.1039/c5ta03471j.

(108) Stephan, A. M. Review on Gel Polymer Electrolytes for Lithium Batteries. *Eur. Polym. J.* **2006**, *42* (1), 21–42. https://doi.org/10.1016/j.eurpolymj.2005.09.017.

(109) Xu, K. Nonaqueous Liquid Electrolytes for Lithium-Based Rechargeable Batteries. *Chem. Rev.* **2004**, *104* (10), 4303–4417. https://doi.org/10.1021/cr030203g.

(110) Salvatore, D. A.; Gabardo, C. M.; Reyes, A.; O'Brien, C. P.; Holdcroft, S.; Pintauro, P.; Bahar, B.; Hickner, M.; Bae, C.; Sinton, D.; Sargent, E. H.; Berlinguette, C. P. Designing Anion Exchange Membranes for CO2 Electrolysers. *Nat. Energy* **2021**, *6* (4), 339–348. https://doi.org/10.1038/s41560-020-00761-x.

(111) Chen, C.; Tse, Y. L. S.; Lindberg, G. E.; Knight, C.; Voth, G. A. Hydroxide Solvation and Transport in Anion Exchange Membranes. *J. Am. Chem. Soc.* **2016**, *138* (3), 991–1000. https://doi.org/10.1021/jacs.5b11951.

(112) Bennington, P.; Deng, C.; Sharon, D.; Webb, M. A.; de Pablo, J. J.; Nealey, P. F.; Patel, S. N. Role of Solvation Site Segmental Dynamics on Ion Transport in Ethylene-Oxide Based Side-Chain Polymer Electrolytes. *J. Mater. Chem. A* **2021**, *9* (15), 9937–9951. https://doi.org/10.1039/d1ta00899d.

(113) Carrasco, J.; Hodgson, A.; Michaelides, A. A Molecular Perspective of Water at Metal Interfaces. *Nat. Mater.* **2012**, *11* (8), 667–674. https://doi.org/10.1038/nmat3354.

(114) Thiel, P. A.; Madey, T. E. The Interaction of Water with Solid Surfaces: Fundamental Aspects. *Surf. Sci. Rep.* **1987**, *7* (6–8), 211–385. https://doi.org/10.1016/0167-5729(87)90001-X.

(115) Hodgson, A.; Haq, S. Water Adsorption and the Wetting of Metal Surfaces. *Surf. Sci. Rep.* **2009**, *64* (9), 381–451. https://doi.org/10.1016/j.surfrep.2009.07.001.

(116) Granseth, E.; Von Heijne, G.; Elofsson, A. A Study of the Membrane-Water Interface Region of Membrane Proteins. *J. Mol. Biol.* **2005**, *346* (1), 377–385. https://doi.org/10.1016/j.jmb.2004.11.036.

(117) Kim, J.; Kim, G.; Cremer, P. S. Investigations of Water Structure at the Solid/Liquid Interface in the Presence of Supported Lipid Bilayers by Vibrational Sum Frequency Spectroscopy. *Langmuir* **2001**, *17* (23), 7255–7260. https://doi.org/10.1021/la0017274.

(118) Rehl, B.; Gibbs, J. M. Role of Ions on the Surface-Bound Water Structure at the Silica/Water Interface: Identifying the Spectral Signature of Stability. *J. Phys. Chem. Lett.* **2021**, *12* (11), 2854–2864. https://doi.org/10.1021/acs.jpclett.0c03565.

(119) Scatena, L. F.; Richmond, G. L. Orientation, Hydrogen Bonding, and Penetration of Water

at the Organic/Water Interface. *J. Phys. Chem. B* **2001**, *105* (45), 11240–11250. https://doi.org/10.1021/jp0132174.

(120) Hosseinpour, S.; Tang, F.; Wang, F.; Livingstone, R. A.; Schlegel, S. J.; Ohto, T.; Bonn, M.; Nagata, Y.; Backus, E. H. G. Chemisorbed and Physisorbed Water at the TiO2/Water Interface. *J. Phys. Chem. Lett.* **2017**, *8* (10), 2195–2199. https://doi.org/10.1021/acs.jpclett.7b00564.

(121) Wu, S. L.; Liu, F.; Yang, H. C.; Darling, S. B. Recent Progress in Molecular Engineering to Tailor Organic-Inorganic Interfaces in Composite Membranes. *Mol. Syst. Des. Eng.* **2020**, *5* (2), 433–444. https://doi.org/10.1039/c9me00154a.

(122) Yang, H. C.; Waldman, R. Z.; Chen, Z.; Darling, S. B. Atomic Layer Deposition for Membrane Interface Engineering. *Nanoscale* **2018**, *10* (44), 20505–20513. https://doi.org/10.1039/c8nr08114j.

(123) Wenderott, J. K.; Dong, B. X.; Amonoo, J. A.; Green, P. F. Quantification of Interactions at the Polymer–Substrate Interface: Implications for Nanoscale Behavior. *Macromolecules* **2021**. https://doi.org/10.1021/acs.macromol.1c00517.

(124) Kango, S.; Kalia, S.; Celli, A.; Njuguna, J.; Habibi, Y.; Kumar, R. Surface Modification of Inorganic Nanoparticles for Development of Organic-Inorganic Nanocomposites - A Review. *Prog. Polym. Sci.* **2013**, *38* (8), 1232–1261. https://doi.org/10.1016/j.progpolymsci.2013.02.003.

(125) Sharon, D.; Bennington, P.; Liu, C.; Kambe, Y.; Dong, B. X.; Burnett, V. F.; Dolejsi, M.; Grocke, G.; Patel, S. N.; Nealey, P. F. Interrogation of Electrochemical Properties of Polymer Electrolyte Thin Films with Interdigitated Electrodes. *J. Electrochem. Soc.* **2018**, *165* (16), H1028–H1039. https://doi.org/10.1149/2.0291816jes.

(126) Fredrickson, G. H.; Bates, F. S. Dynamics of Block Copolymers: Theory and Experiment. *Annu. Rev. Mater. Sci.* **1996**, *26*, 501–550. https://doi.org/10.1146/annurev.ms.26.080196.002441.

(127) Bates, F. S.; Hillmyer, M. A.; Lodge, T. P.; Bates, C. M.; Delaney, K. T.; Fredrickson, G. H. Multiblock Polymers: Panacea or Dandora's Box? *Science* **2012**, *336* (6080), 434–440. https://doi.org/10.1126/science.1215368.

(128) Bates, F. S.; Fredrickson, G. H. Block Copolymers—Designer Soft Materials. *Phys. Today* **1999**, *52* (2), 32. https://doi.org/10.1063/1.882522.

(129) Bates, F. S. Polymer- Polymer Phase Behavior. *Science (80-.).* **1991**, *251* (4996), 898–905.

(130) Epps, T. H.; Bailey, T. S.; Waletzko, R.; Bates, F. S. Phase Behavior and Block Sequence Effects in Lithium Perchlorate-Doped Poly(Isoprene-b-Styrene-b-Ethylene Oxide) and Poly(Styrene-b-Isoprene-b-Ethylene Oxide) Triblock Copolymers. *Macromolecules* **2003**, *36* (8), 2873–2881. https://doi.org/10.1021/ma021231o.

(131) Teran, A. A.; Tang, M. H.; Mullin, S. A.; Balsara, N. P. Effect of Molecular Weight on

Conductivity of Polymer Electrolytes. *Solid State Ionics* **2011**, *203* (1), 18–21. https://doi.org/10.1016/j.ssi.2011.09.021.

(132) Soo, P. P.; Huang, B.; Jang, Y.; Chiang, Y.; Sadoway, D. R.; Mayes, A. M. Rubbery Block Copolymer Electrolytes for Solid-State Rechargeable Lithium Batteries. *J. Electrochem. Soc.* **1999**, *146* (1), 32–37. https://doi.org/10.1149/1.1391560.

(133) Kambe, Y.; Arges, C. G.; Patel, S. N.; Stoykovich, M. P.; Nealey, P. F. Ion Conduction in Microphase-Separated Block Copolymer Electrolytes. *Electrochem. Soc. Interface* **2017**, *26* (1). https://doi.org/10.1149/2.F07171if.

(134) Arges, C. G.; Kambe, Y.; Suh, H. S.; Ocola, L. E.; Nealey, P. F. Perpendicularly Aligned, Anion Conducting Nanochannels in Block Copolymer Electrolyte Films. *Chem. Mater.* **2016**, *28* (5), 1377–1389. https://doi.org/10.1021/acs.chemmater.5b04452.

(135) Kambe, Y.; Arges, C. G.; Czaplewski, D. A.; Dolejsi, M.; Krishnan, S.; Stoykovich, M. P.; De Pablo, J. J.; Nealey, P. F. Role of Defects in Ion Transport in Block Copolymer Electrolytes. *Nano Lett.* **2019**, *19* (7), 4684–4691. https://doi.org/10.1021/acs.nanolett.9b01758.

(136) Sharon, D.; Bennington, P.; Dolejsi, M.; Webb, M. A.; Dong, B. X.; De Pablo, J. J.; Nealey, P. F.; Patel, S. N. Intrinsic Ion Transport Properties of Block Copolymer Electrolytes. *ACS Nano* **2020**, *14* (7), 8902–8914. https://doi.org/10.1021/acsnano.0c03713.

(137) Gartner, T. E.; Morris, M. A.; Shelton, C. K.; Dura, J. A.; Epps, T. H. Quantifying Lithium Salt and Polymer Density Distributions in Nanostructured Ion-Conducting Block Polymers. *Macromolecules* **2018**, *51* (5), 1917–1926. https://doi.org/10.1021/acs.macromol.7b02600.

(138) Lee, S.; Gillard, T. M.; Bates, F. S. Fluctuations, Order, and Disorder in Short Diblock Copolymers. *AIChE J.* **2013**, *59* (9). https://doi.org/10.1002/aic.14023.

(139) Seo, Y.; Brown, J. R.; Hall, L. M. Effect of Tapering on Morphology and Interfacial Behavior of Diblock Copolymers from Molecular Dynamics Simulations. *Macromolecules* **2015**, *48* (14), 4974–4982. https://doi.org/10.1021/ma502309h.

(140) Dong, B. X.; Bennington, P.; Kambe, Y.; Sharon, D.; Dolejsi, M.; Strzalka, J.; Burnett, V. F.; Nealey, P. F.; Patel, S. N. Nanothin Film Conductivity Measurements Reveal Interfacial Influence on Ion Transport in Polymer Electrolytes. *Mol. Syst. Des. Eng.* **2019**, *4* (3), 597–608. https://doi.org/10.1039/c9me00011a.

(141) Arges, C. G.; Li, K.; Zhang, L.; Kambe, Y.; Wu, G.-P.; Lwoya, B.; Albert, J. N. L.; Nealey, P. F.; Kumar, R. Ionic Conductivity and Counterion Condensation in Nanoconfined Polycation and Polyanion Brushes Prepared from Block Copolymer Templates. *Mol. Syst. Des. Eng* **2019**, *4*, 365. https://doi.org/10.1039/c8me00081f.

Chapter 2

Effect of Graft Molecular Weight and Density on the Mechanical Properties of Polystyrene-grafted Cellulose Nanocrystal Films

2.1 ABSTRACT

Polymer grafted nanoparticle (PGN) films were prepared from polystyrene (PS)-grafted to rod-like cellulose nanocrystals (***MxG*-CNC-*g*-PS**) with controllable grafting density (0.03-0.25 chains/nm^2) and molecular weight (5-60 kg/mol). These nanorod-based PGNs are solution and melt processible permitting access to one-component composite films with high nanofiller loadings (with up to 55 wt%). The impact of both grafted polymer density and molecular weight on the mechanical properties of the films was investigated and related to the polymer brush conformation; concentrated polymer brush (CPB), semidilute polymer brush (SDPB) or CPB core with SDPB corona (CPB/SDPB). The rubbery regime storage modulus (above T_g) showed a 2 order of magnitude increase, maximizing at low degree of polymerization (N) and low grafting density (σ). Fracture toughness was maximized in samples with the grafted polymer in the SDPB or CPD/SDPB (higher N and relatively low σ) regime and showed enhancement relative to PS of molecular weight similar to the graft. In line with prior computation predictions, optimizing for both rubbery modulus and fracture toughness in such nanorod-based PGN films requires the polymers in the SDPB regime and CNC loading levels (ca. 50-60 wt.%) that are difficult to attain in more traditional two-component CNC composites.

2.2 INTRODUCTION

Nanocomposites, in which a nanofiller is embedded in a polymer matrix, are used in wide array of applications[1,2] in which an improvement in the polymer's materials properties, for example, mechanical,[3–5] electronic,[6–8] water transport/purification,[9,10] etc, are required. The properties are often controlled by the ratio of polymer to nanofiller; however, such two-component nanocomposites often suffer from demixing/phase separation of the matrix and filler, which can lead to a reduction in the materials properties, restrict possible processing techniques, and ultimately limit the loading of the nanofiller material. One way to address these issues is to covalently bond the polymer matrix to the nanoparticle filler, creating polymer grafted nanoparticles (PGNs)[11] which can be processed into films solely consisting of PGNs, also known as one-component nanocomposites (OCNs).[12] Such OCNs can allow access to materials that exhibit enhanced toughness and modulus when compared to two-component nanocomposites of similar composition.[13,14] Furthermore, on account of the covalent bond between the polymer and nanofiller, these materials do not suffer from demixing, permitting melt processing and much higher loadings of nanoparticles beyond that of traditional nanocomposites.

The mechanical structure-property relationships of nanosphere based OCNs has been studied in detail and is controlled by the graft polymer conformation.[13–16] In line with traditional brush literature on planar surfaces,[17,18] radius of gyration (R_g) and polymer grafting density control the polymer brush conformation of OCNs based on spherical nanoparticles (**Figure 2.1a**), in which the polymer brush conformation falls into three regimes, mushroom, semidilute polymer brush (SDPB), and concentrated polymer brush (CPB) (**Figure 2.1b**).[12] The mushroom regime, where the grafted polymer exists in a loose coil conformation with little interactions between grafted

chains, occurs when the polymer grafting density is less than R_g^{-2}. At slightly higher grafting densities (and/or higher molecular weights) the polymer brushes move into the SDPB regime in which the polymer chain conformations are still generally relaxed but now there are soft inter-graft interactions and chain penetration. PGNs in which the polymer is in the CPB regime, on the other hand, are more akin to hard particles. On account of curvature of the nanoparticle an inner corona of CPB with an outer layer of SDPB, termed CPB/SDPB, is generally formed if the molecular weight of the polymer graft is large enough. Previous work[13–16] has confirmed densely packed brushes on spherical PGNs transition from CPB to CPB/SDPB at critical polymer lengths and grafting densities following predictions by Daoud-Cotton models applied to nanoparticles.[19–21] Additionally, the mechanical properties of spherical PGNs show increasing stiffness (elastic modulus) with increasing molecular weight and increasing toughening behavior (via crazing) when polymer grafts reside in the CPB/SDPB regime with sufficient molecular weight to entangle.[13,15] Thus, the mechanical properties of OCNs are determined by the graft polymer conformation, which in turn is controlled by the polymer grafting density and radius of gyration. However, while much work has been done on nanosphere based OCNs, much less work has investigated nanorod geometries (**Figure 2.1c**).

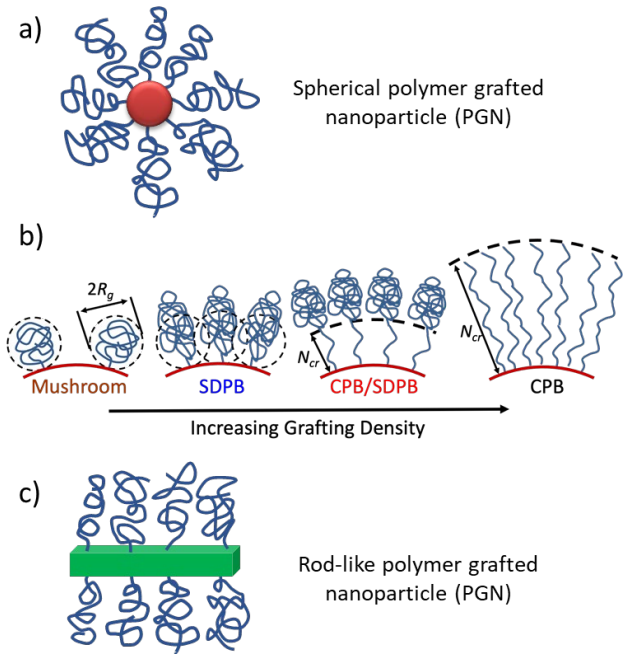

Figure 2.1: Schematic of (a) a spherical polymer grafted nanoparticle, b) a representation of the various polymer brush conformations on a curved surface upon increasing polymer grafting density (mushroom, semidilute polymer brush (SDPB), concentrated polymer brush/semidilute polymer brush (CPB/SDPB), and concentrated polymer brush (CPB)) and c) a rod-like polymer grafted nanoparticle.

Cellulose nanocrystals (CNCs), are organic, biorenewable nanorods with a high degree of crystallinity and easily functionalizable surfaces, and have been investigated as green nanofillers.[22–26] CNCs are commonly prepared by acid hydrolysis, such as hydrochloric acid, hydrobromic acid, sulfuric acid, phosphoric acid, of natural cellulose at elevated temperatures.[27,28] The width of the CNCs is between 3 and 20 nm, and their length can be 100-1000 nm depending on both the bioresource, e.g. wood, cotton, tunicate or *Miscanthus x. Giganteus* (*MxG*) and isolation procedures.[29,30] In addition to being bioavailable, CNCs offer a number of advantages, that include low coefficient of thermal expansion, high elastic modulus, and

biocompatibility.[23,27,31] making them attractive nanoparticles for composites materials. Indeed, while there are only a few reported studies on OCN films of polymer grafted CNCs, there are a number of examples in the literature of polymer grafted CNCs, whether for study in solution or for integration into nanocomposites for enhancing mechanical properties.[32–38]

Recently, Weder and coworkers reported CNC-based OCNs with high molecular polymer grafts (100-400 kg/mol) and moderate grafting density (0.04-0.15 chains/nm^2) and demonstrated toughness and elastic modulus enhancement consistent with previous spherical nanofiller based OCNs.[39] OCNs containing up to 20 wt% CNC with grafted high glass transition temperature (T_g) poly(methyl methacrylate) display enhanced toughening while retaining a similar elastic modulus to the 2-component nanocomposite of similar composition. Additionally, OCNs consisting of low T_g poly(hexyl methacrylate) show similar toughness but higher modulus as compared to a mixed, 2-component nanocomposites. More recently, PGN films consisting of CNCs grafted with poly(2-phenylethyl methacrylate) imbibed with ionic liquid were prepared and their mechanical properties and ion conductivity measured.[40] These imbibed PGN films (30 wt% ionic liquid) exhibited an increase in both tensile strength and ionic conductivity relative to the mixed CNC, polymer and ionic liquid nanocomposites. These materials probed relatively low molecular weights (6-20 kg/mol) and moderate to high grafting densities (0.10-0.43), and the grafted polymers were predicted to reside in the CPB or CPB/SDPB regimes. In neither of these studies was the effect of molecular weight nor grafting density explored. Interestingly, Lettow et al. showed that both degree of polymerization and grafting density impact the ion conductivity of hydrated PGN films of polyelectrolyte grafted CNCs with a relatively high density of short polymer chains resulting in the highest conductivity, although no detail mechanical studies were performed on these thin films.[41]

Recently theoretical and computational work has been applied to CNC-based OCNs, permitting better polymer regime and mechanical property predictions. Specifically, computational work by Keten and coworkers using coarse-grained and molecular dynamics approaches, when combined with metamodels, have probed various design parameters (polymer chain length, grafting density, polymer−nanoparticle interaction strength, and the nanoparticle edge length) and their effects on the poly(methyl methacrylate) polymer brushes.[42] Based on the simulations, predictions were made on the polymer conformation transition point from CPB to CPB/SDPB as a function of polymer length and grafting density, which was extended in further work to a wide array of polymers including polystyrene.[43] Additionally, modeling indicated that the modulus is maximized at low grafting density and degree of polymerization (i.e. higher volume fractions of CNCs) while toughness is maximized at relatively low grafting density but high degree of polymerization. The computational studies suggested that in order have both modulus and toughness maximized, the grafted polymer should be in the SDPB regime and the OCN should have a CNC content of ~60 wt.%. While the initial experimental work on CNC-based OCNs discussed above have shown they can exhibit interesting properties, to date no work has been done to explore the effect that degree of polymerization and polymer chain density have on mechanical properties in support of these computational studies. To this end, reported herein are studies with the goal of synthesizing and studying polystyrene-grafted CNC-based OCNs in order to probe experimentally the impact that polymer grafting density and degree of polymerization have on the grafted polymer conformation and mechanical properties of their films.

2.3 EXPERIMENTAL METHODS

2.3.1 Instrumentation

Nuclear Magnetic Resonance Spectroscopy. The ^{1}H NMR and ^{13}C NMR spectra were recorded on a Bruker Ascend Advance II+ 500 MHz spectrometer at 25 °C using $CDCl_3$ as solvent. All NMR spectra were processed by MestReNova software.

Gel Permeation Chromatography-Multiangle Light Scattering and UV-VIS Spectrometry. Polymer molecular weight and dispersity and their UV-VIS spectra were determined by gel permeation chromatography-multi-angle light scattering (GPC-MALS) with in-line UV-VIS spectrometry, measured on a Shimadzu Prominence LC system with PL gel Mixed-D columns with Wyatt Dawn Heleos MALS (658 nm laser), Wyatt Optilab T-rEX refractive index (RI) detectors, and Shimadzu SPD-M30A Photodiode Array detector (200-800 nm). HPLC grade tetrahydrofuran (THF) as the eluent (1mL/min) at 25 °C. The data were processed by Wyatt Astra software.

Conductometric titration. The amount of surface carboxylic acid groups on the CNCs was determined by conductometric titrations using a Accumet XL benchtop pH/conductivity meter (Fisher Scientific). In a typical run, 25 mg of CNC was dispersed in DI water (80 mL) by sonication, before addition of 15 µL of HCl (33 wt.%) to adjust the pH to around 3. 0.01 M NaOH was then titrated into the CNC dispersion and the conductivity measured until the pH was around about 11.

Thermal gravimetric analysis (TGA). TGA experiments were carried out on a thermogravimetric analyzer (TA Instrument Discovery). The samples were heated from 30 °C to 650 °C under nitrogen atmosphere with a heating rate of 10 °C/min.

Electrospray Mass Spectroscopy. Electrospray mass spectroscopy (ESI-MS) experiments were conducted using an Agilent 6135 quadrupole LC/MS system equipped with a 50 x 4.6 mm Poroshell 120 EC-C18 column (Agilent). A gradient elution of 10-100% acetonitrile in H_2O (+0.1% TFA) was conducted over 10 min and then held at 100% acetonitrile for 2.5 min, and absorbance was measured at 220 nm.

Wide Angle X-ray Scattering (WAXS). The degree of crystallinity was determined by Synchrotron WAXS experiments were performed at the DND-CAT 5-ID-D beamline of the Advanced Photon S3 Source (Argonne National Laboratory, Argonne, IL) using a triple detector system for simultaneous data collection SAXS and WAXS regimes. Two-dimensional (2D) data were collected on Rayonix CCD area detectors using an exposure time of ca. 0.1 s. Gaussian deconvolution and crystallinity index analysis followed literature precedent.[31]

Fourier transform infrared spectroscopy (FTIR). FTIR spectrometer were collected on a Shimadzu FTIR instrument. Solid samples were placed directly on the ATR crystal, and then the spectra were averaged from 46 scans from 550 to 4000 cm^{-1} with a resolution of 4 cm^{-1}.

Atomic force microscopy (AFM). The dimensions of ***MxG*-CNC-COOH** and ***MxG*-CNC-*g*-PS** were investigated by Asylum Research Oxford Instruments Cypher ES AFM. A drop of CNCs suspension (0.01 wt%) was placed on a freshly cleaved mica surface which was pretreated with poly-l-lysine solution, and then rinsed off after five minutes. The images were acquired using AC Tapping mode. The sizes of nanoparticles were analyzed by Gwyddion software.

Scanning electron microscope (SEM). SEM images of the cast films were taken with the Carl Zeiss−Merlin field emission scanning electron microscope. The acceleration voltage was 1.0 kV with a working distance of 2 to 3 mm using an in-lens detector. Two nanometers of Pt/Pd was

sputtered onto the surface of the device using the Cressington 108 Auto Sputter Coater to reduce electron beam charging and improve the image quality.

Differential scanning calorimetry (DSC) analysis. DSC experiments were performed on a TA Instruments Discovery DSC 2500. Samples (5-10 mg) were hermetically crimped in Tzero aluminum pans. Sequential heating, cooling and reheating ramps were conducted from -50 to 200 °C at a rate of 10 °C min^{-1}.

Dynamic mechanical analysis (DMA). DMA experiments were conducted in tension mode at a fixed frequency of 1 Hz using an RSA-G2 solids analyzer (TA Instruments). The CNCs films were cut into a rectangular shape with about 4 mm in width and 10 mm in length. The temperature scan was performed between 20 to 200 °C with a heating rate of 3 °C/min.

Nanoindentation. Nanoindentation experiments were performed on a Hysitron Triboindenter using a Berkovich indenter. Samples were indented using displacement control to 1000 nm at a rate of 200 nm/s. AFM images of indentations were acquired using the same instrument.

Shear Rheology. Rheology was performed using the TA Instruments RSA-G2 ARES with Forced Convection oven (20 °C – 200 °C) running TA Trios Software with a heating rate of 3 °C/min. An 8 mm parallel plate was used for all tests.

2.3.2 Material Synthesis

Materials. Miscanthus x. Giganteus (ground stalks) were donated by Aloterra Energy LLC, Conneaut, Ohio. Styrene was purchased from Sigma-Aldrich and passed through a basic alumina column immediately prior to usage. Hydrochloric acid (HCl), and sodium hydroxide (NaOH) were purchased from Fisher Scientific. All other reagents were purchased from Sigma-Aldrich and used as received.

Synthesis of α-phthalimidomethyl-ω-butyltrithiocarbonatepoly(styrene) by RAFT. Phthalimidomethyl butyl trithiocarbonate (0.12 g) and styrene (16.6 g) were transferred to a 150 mL flask, underwent three freeze-pump-thaw cycles, and then heated at 110 °C for 24 h, followed by rapid quenching to room temperature. The mixture was diluted with THF (~5 mL) and the polymer was precipitated into methanol (100 mL), collected by filtration and dried in a vacuum oven at 40 °C for 24 h forming α-phthalimidomethyl-ω-butyltrithiocarbonatepoly(styrene) (**PS-x**, where **x** denotes the molecular weight in kg/mol as determined by GPC-MALS). Two further precipitations from THF to methanol were used to remove unreacted monomer yield the desired polymer (70% yield) ^{1}H NMR (500 MHz, $CDCl_3$); δ ppm: 7.8 (2H, Ar**H**, phthalimide), 7.7 (2H, Ar**H**, phthalimide), 7.2-6.3 (br PS) 3.4 (2H, N-CH_2-), 3.3 (2H, S-CH_2-), 2.2-1.2 (br PS), 1.0 (3H, -CH_3) (**Figure S2.1**). GPC-MALS (THF) PS-x series were measured (Mn=5, 8, 12, 27, 34, 60 kg/mol, $Đ$<1.1) (**Figure S2.2**). UV-Vis (THF) λ_{max} = 310 nm (trithiocarbonate endgroup) (**Figure S2.3**).

Synthesis of α-aminomethyl-poly(styrene). α-aminomethyl-poly(styrene) was synthesized following literature precedent.[42] α-phthalimidomethyl-ω-butyltrithiocarbonatepoly(styrene) (1 g) was placed in a 150 ml beaker and the polymer was heated at 250 °C under vacuum for 4 hours.

The polymer was dissolved in THF and precipitated into methanol three times, collected by filtration, then dried in a vacuum oven at 40 °C for 24 hours to yield 0.9 g (90% yield). ^{1}H NMR and UV-Vis confirmed removal of the trithiocarbonate endgroup via reduction of peaks at 1.0 and 3.3 ppm, and 310 nm, respectively (**Figures S2.1,2.3**). A peak in ^{1}H NMR at 6.0 ppm is indicative of the double bond formation at the PS endgroup. Additionally, TGA of low molecular weight PS confirmed endgroup removal by comparing weight loss (**Figure S2.4**). The resulting α-phthalimidomethyl-poly(styrene) was dissolved in THF (50 mL) and then hydrazine hydrate (5 mL) was added. The mixture was refluxed for 2 hours, cooled to room temperature, and left overnight for precipitation. The liquid phase was then precipitated by pouring into methanol, collected by filtration, and dried in a vacuum oven at 40 °C for 24 hours. Deprotection to form α-aminomethyl poly(styrene) (**PS-NH$_2$-x**, where **x** denotes the molecular weight in kg/mol as determined by GPC-MALS) was confirmed using a Kaiser test, GPC-MALS, and H^{1} NMR. GPC-MALS (THF) confirms similar molecular weight after thermolysis, with all **PS-NH$_2$-x** samples shown in **Figure S2.5** (5, 8, 12, 27, 34, 60 kg/mol, $Đ$<1.1). ^{1}H NMR (500 MHz, $CDCl_3$) δ ppm: 7.2-6.3 (br PS), 6.0 (1H, C=C-H), 3.4 (2H, N-CH_2-), 2.2-1.2 (br PS) (**Figure S2.1, 2.6**). UV-Vis (THF) shows full reduction of the 310 nm peak (**Figure S2.3**)

Preparation of *MxG*-CNCs. *MxG*-CNCs were isolated from *Miscanthus x. Giganteus* stalks by hydrochloric acid hydrolysis, and then were further oxidized to obtain ***MxG*-CNC-COOH** by TEMPO oxidation according to previously published methods.[30] Conductivity titration was performed to determine surface charge density and functionalization quantity, with ***MxG*-CNC-COOH** having surface charge density of 1000 mmol/kg. Thermal gravimetric analysis (TGA), wide angle x-ray scattering (WAXS) and atomic force microscopy confirm thermal decomposition, crystallinity index, and size respectively (**Figures S2.7-2.9**).

Preparation of CNCs/DMF suspension by solvent exchange. ***MxG*-CNC-COOH** were first dispersed in 40 mL water with a concentration of 2.5 wt% by ultrasonication and 1 ml of saturated NaCl was added. The gel was collected by centrifugation (5 min, 8000 rpm), and the supernatant removed and collected. The remaining gel was resoaked in 40 mL of methanol for 2 h with constantly shaking, then separated by centrifugation. The same procedure was repeated two more times with methanol and then two times with DMF. The concentration of ***MxG*-CNC-COOH** suspension was determined by thermal gravimetric analysis and shown to be ca. 0.25 wt%.

Preparation of DMTMMBF$_4$. To prepare **DMTMMBF$_4$**, n-methylmorpholine (2.4 mL) was added dropwise to a vigorously stirred solution of 2-chloro-4,6-dimethoxy-1,3,5-triazine (3.68 g in 40 mL H_2O), and kept stirring at 20 °C for 0.5 h. Then a 30 mL of sodium tetrafluoroborate (10 mmol) solution was added and stirred for another 2 h. The precipitate was collected by filtration and dried at room temperature to yield **DMTMMBF$_4$** in 75%. ^{1}H NMR (500 MHz, d_6-DMSO) δ ppm: 3.47 (s, 3H), 3.78 (m, 2H), 3.89, (m, 2H), 4.02 (m, 2H), 4.12 (s, 6H), 4.36 (m, 2H),^{13}C NMR (125 MHz, d_6-DMSO); δ ppm: 53.1, 55.7, 57.2, 60.0, 61.8, 63.9, 170.6, 173.8, and ESI-MS (241, [M]+H-BF_4), agreeing well with literature (**Scheme S2.1**, **Figures S2.10-2.11**).[43]

Example Synthesis of *MxG*-CNC-*g*-PS-5-45. DMTMMBF$_4$ (0.28 g) was added to a 40 mL suspension of ***MxG*-CNC-COOH** in DMF (0.25 wt%, 100mg), obtained using the solvent exchange process, and the suspension was stirred at room temperature for 10 min. **PS-NH$_2$-5** (0.5 g for 5 kg/mol polymer) was dissolved in 10 mL of DMF and then added to the CNCs suspension, and the reaction mixture was continuously stirred at room temperature for 24 h. The mole ratio of **DMTMMBF$_4$** : **PS-NH$_2$-5** : -COOH on CNCs was kept at 1:1:1. The resulting mixture was precipitated into methanol, to yield a white precipitate. To remove any unreacted polymer, the precipitate was collected by centrifugation and redispersed in acetone by sonication, followed by

further centrifugation to separate the precipitant and the supernatant. This was repeated 3 times, or until a negative Kaiser test on the supernatant was obtained. ***MxG*-CNC-*g*-PS** was characterized with TGA and were shown to yield ***MxG*-CNC-*g*-PS-5-45**, where 5 refers to the molecular weight (5 kg/mol) and 45 refers to the weight percent of grafted PS. The same procedure using reduced equivalents of polymer enabled access to PGNs with a lower amount percent of grafted polymer. Specifically, 0.25 eq of **PS-NH_2-34** yielded ***MxG*-CNC-*g*-PS-34-80** and **PS-NH_2-60** yielded ***MxG*-CNC-*g*-PS-60-90**, while 0.04 eq was used of **PS-NH_2-34** to access ***MxG*-CNC-*g*-PS-34-55**.

Film formation: The ***MxG*-CNC-*g*-PS** samples were dissolved in THF and sonicated in a Branson CPX sonication bath before being cast into Teflon dishes. Solvent was allowed to evaporate at RT for 2 days followed by 1 day at 140℃ in a vacuum oven. After casting, films were melt-pressed at 140℃ for 30 minutes under 70 MPa.

2.4 RESULTS AND DISCUSSION

In order to synthesize poly(styrene) grafted CNCs, amide chemistry was utilized to graft amine capped poly(styrene) (**PS-NH$_2$**) to carboxylic acid CNCs (***MxG*-CNC-COOH**). RAFT polymerization of styrene with phthalimidomethyl butyl trithiocarbonate[44] as the chain transfer agent (CTA) was used to produce the CTA-endcapped polystyrene, which after thermal removal of the trithiocarbonate endgroup and subsequent deprotection of the amine yielded the targeted **PS-NH$_2$** (**Scheme 2.1**). A series of different molecular weight **PS-NH$_2$** (5, 8, 12, 27, 34, 60 kg/mol, dispersity, $Đ$ <1.1, termed **PS-NH$_2$-x**, where x is the molecular weight in kg/mol) was prepared to range from 0.5 to 6 times the PS entanglement molecular weight (~10 kg/mol) by simply varying the monomer to CTA ratio. The polymers were characterized by gel permeation chromatography multi-angle light scattering (GPC-MALS), nuclear magnetic resonance spectroscopy (^{1}H NMR), and UV-Vis spectroscopy. ^{1}H NMR confirmed endgroup removal (both trithiocarbonate and phthalimide) (**Figures S2.1, 2.6**). GPC-MALS measured the molecular weights and confirmed similar values before and after thermolytic cleavage of the trithiocarbonate moiety (**Figure S2.2, 2.5, Table S2.1**). UV-VIS showed reduction in the 310 nm peak corresponding to the trithiocarbonate moiety (**Figure 2.3**). Thermal gravimetric analysis confirmed the thermal removal of the trithiocarbonate moiety when held at 250℃ for 4 hours (**Figure S2.5)**.

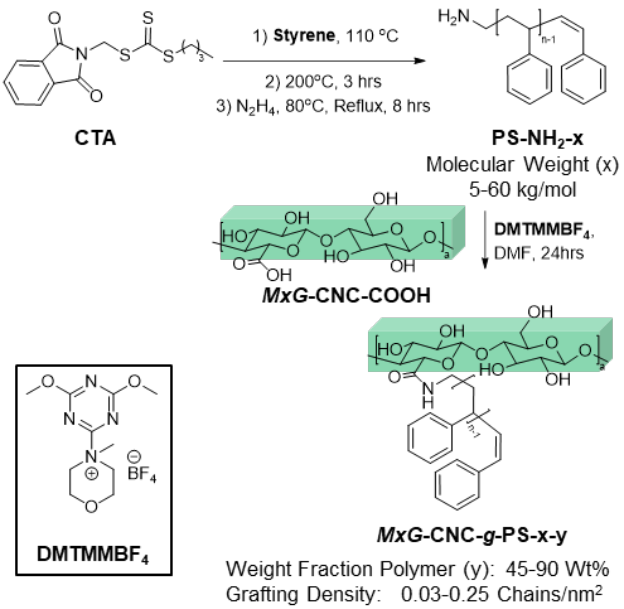

Scheme 2.1. Synthesis of polystyrene-grafted CNCs (***MxG*-CNC-*g*-PS-x-y**), where x is the molecular weight (in kg/mol) and y is the percent weight fraction of the grafted polymer. The amine-end capped poly(styrene) (**PS-NH₂-x**) was prepared via RAFT polymerization and grafted to carboxylic acid-functionalized CNCs (***MxG*-CNC-COOH**) via peptide coupling chemistry before being cast into films via evaporation and pressed at 140°C for 30 minutes under 70 MPa.

Coupling of the **PS-NH₂** to the CNCs via amide chemistry requires the use of the carboxylic acid functionalized CNCs, which were obtained from *Miscanthus x. Giganteus* (via hydrochloric acid hydrolysis and TEMPO-mediated oxidation) using literature procedures.[30] The resulting ***MxG*-CNC-COOHs** have a crystallinity index of 85% (determined by wide angle x-ray scattering, **Figure S2.8**) and carboxylic acid density of ca. 1000 mmol/kg, as determined via conductometric titration. The dimensions of the ***MxG*-CNC-COOHs** agrees with literature (from AFM, height = 2.2±0.5 nm, length = 290±60 nm for ***MxG*-CNC-COOH**, respectively (n=20), **Figure S2.9**). The ***MxG*-CNC-COOH** were dispersed in water using ultrasonication followed by solvent exchange into methanol from the the aqueous dispersion and subsequent solvent exchange

into DMF. DMF was chosen as the solvent for the coupling reaction as it readily dissolves the polymer and disperses the CNCs. Various amide coupling reagents (DIC/NHS, DIC/ HOBT, EDC/NHS) and reaction conditions (with direct mixing of CNCs in DMF or with CNCs in DMF prepared by solvent exchange) were explored (**Scheme S2.1-2.2**), and 4-(4,6-dimethoxy-1,3,5-triazin-2-yl)-4-methylmorpholinium tetrafluoroborate (**DMTMMBF$_4$**)[45] with CNCs dispersed using a solvent exchange process (**Figure S2.10-2.11**) was found to yield the highest grafting efficiency (**Figure S2.12, Table S2.2**).

Thus, **DMTMMBF$_4$** was used to attach the different molecular weight (5-60 kg/mol) amine-endcapped **PS-NH$_2$-x** (x = 5, 8, 12, 27, 34, 60) onto the surface carboxylic acid groups of ***MxG*-CNC-COOH**. After purifying the samples to remove the ungrafted polymer via three cycles of centrifugation, decanting, and redispersion using acetone, the final samples were subjected to a Kaiser test to confirm that most of the free (ungrafted) polymer had been removed following previously published literature procedures.[40] An identical purification method was also shown efficacious in removing free, ungrafted polymer.[41] The sensitivity of the Kaiser test allows confirmation that the 60 kg/mol grafted samples contain less than 6 wt.% free polymer, while the 12 kg/mol and 5 kg/mol grafted samples have less than 1.2 wt.% and 0.5 wt.% of ungrafted, free polymer, respectively. FTIR was used to confirm the presence of the new -CONH- bond (at 1650 cm^{-1}) in these PGNs (**Figure S2.13**).

AFM height images (**Figure 2.2a-b**) and the height profile (**Figure 2.2c**) of the ***MxG*-CNC-COOHs** and the ***MxG*-CNC-*g*-PS-8-y** PGN (grafted with **PS-NH$_2$-8**) shows a height increase from 2.2±0.5 nm to 4.5±0.4 nm upon attachment of the polymer to the CNCs. See **Figure S2.14-2.15** for AFM images of all the ***MxG*-CNC-*g*-PS** materials prepared. Thermogravimetric

analysis (TGA) was used to calculate the weight percent of grafted polymer the PGN. In the TGA the PGNs (**Figure 2.1d** for ***MxG*-CNC-*g*-PS-8-y**) show two clear regimes that correspond to the degradation of the CNC and PS. Comparing the mass loss from 220 - 360 °C (predominantly CNC degradation) to that of 360 - 450 °C (predominantly PS degradation) the weight percent of grafted polymer can be estimated. After determining the weight percent of polymer ***MxG*-CNC-*g*-PS-8-y** is now termed ***MxG*-CNC-*g*-PS-8-49**, where the 8 is the molecular weight of the grafted polymer in kg/mol and the 49 is the weight percentage of polymer. **Table 2.1** shows the data on all the ***MxG*-CNC-*g*-PS** materials prepared along with their calculated grafting density (obtained from the polymer molecular weight and wt.%) following literature procedure (See SI for more details on page 108).[41]

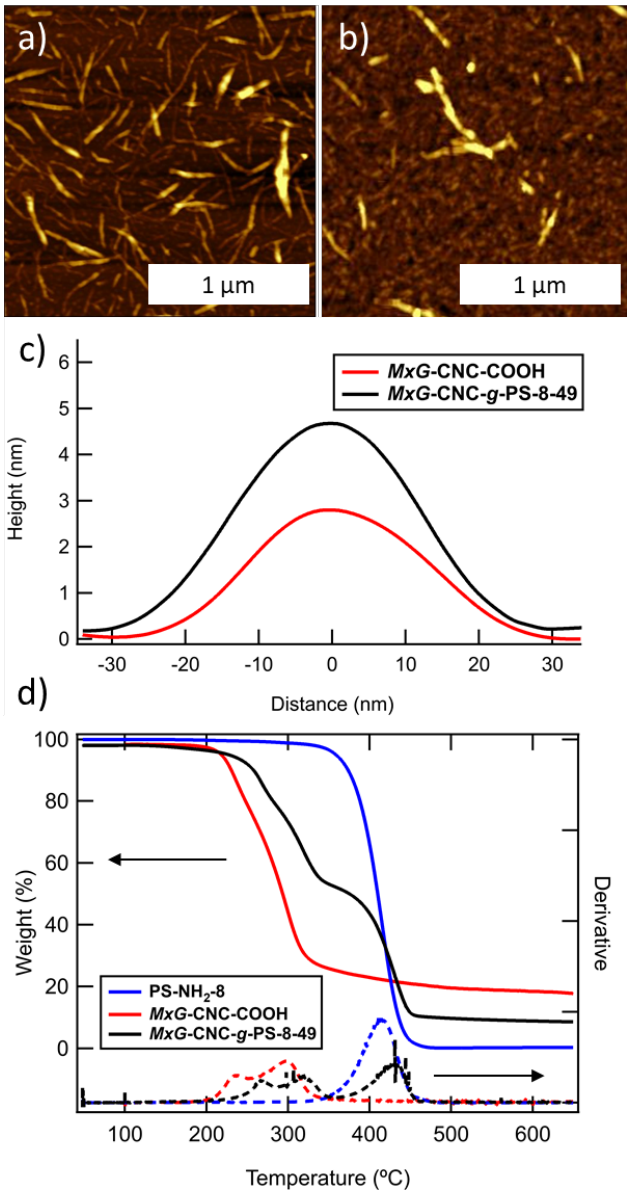

Figure 2.2. AFM height images of a) ***MxG*-CNC-COOH** and b) ***MxG*-CNC-*g*-PS-8-49** and c) the AFM height profiles obtained from these images. d) TGA of **PS-NH$_2$-8**, ***MxG*-CNC-COOH**, and ***MxG*-CNC-*g*-PS-8-49**.

Table 2.1. Sample information of polystyrene (PS)-grafted cellulose nanocrystals with associated symbols used in subsequent figures.

Samples	Molecular Weight (kg/mol) [a]	Weight % Polymer [b]	Graft Density (Chains/nm^2)[c]
***MxG*-CNC-*g*-PS-5-45** ⧗	5	45%	0.15
***MxG*-CNC-*g*-PS-8-49** ⋈	8	49%	0.11
***MxG*-CNC-*g*-PS-8-57** ▼	8	57%	0.15
***MxG*-CNC-*g*-PS-12-61** ◆	12	61%	0.11
***MxG*-CNC-*g*-PS-12-69** ◀▶	12	69%	0.17
***MxG*-CNC-*g*-PS-27-88** ●	27	88%	0.25
***MxG*-CNC-*g*-PS-34-55** ◤	34	55%	0.03
***MxG*-CNC-*g*-PS-34-80** ■	34	80%	0.11
***MxG*-CNC-*g*-PS-60-90** ▲	60	90%	0.13

[a] from GPC-MALS

[b] from TGA

[c] see SI and ref [39] for details of the calculation

Using the molecular weight determined by GPC-MALS and the calculated grafting density of the polymer on the CNC, the graft polymer conformation can be determined by comparing with the simulation data of poly(styrene)-grafted CNCs by Keten and coworkers.[42,43] As a note, the cross-sections of CNCs are dependent on cellulose source and processing but generally are more parallelogram-like.[27,30] However, as the polymer radius of gyration is similar to or greater than the *MxG*-CNC dimensions, the surface will be considered to be effectively curved for the following calculations. For curved surfaces the polymer conformation can be predicted to be in either a mushroom regime, with no interaction between surface polymer grafts, or in a polymer brush regime. This transition can be estimated to occur at

$$\sigma = \left(\pi R_g^2\right)^{-1} \tag{2.1}$$

where σ is the grafting density of the material in chains/nm^2 and the radius of gyration of the grafted polymer is $R_g \approx N^{0.5}$, with N being the degree of polymerization. When the grafting density is above this critical value, the polymer brush can be further subdivided into semidilute polymer brush (SDPB) and concentrated polymer brush (CPB). For brushes on particles (as opposed to flat surfaces) the curved nature of the particles can result in polymer grafts which have an inner core of CPB and an outer corona of SDPB, termed CPB/SDPB. From Keten and coworkers,[42,43] the critical degree of polymerization (N_{cr}) as a function of grafting density for the polymer to transition between CPB and CPB/SDPB can be estimated by the following equation,

$$N_{cr} = \frac{2r_0}{3a\sigma_0^{*1/2} l_m}\left(r_0^{-3/4}\sigma_0^{*3/4} b^{3/2} - 1\right) \tag{2.2}$$

where r_0 is the radius of the CNC, a and b are fitting parameters from the computational modeling, l_m is the contour monomer length, and σ_0^* is a dimensionless grafting density given by

$$\sigma_0^* = \frac{f l_m}{2\pi r_0} = \sigma L l_m \tag{2.3}$$

where f is the number of polymer grafts, σ is the grafting density calculated in chains/nm^2, and L is the average length of the nanorod, 300 nm.[30] *MxG*-CNCs are known to have a ribbon-like cross-section with height ca. 2.8 nm and width 8.5 nm, so a radius of 2.75 nm was used for r_0 to approximate the cross-sectional area (**Figure S2.16**). The fitting parameters ($a = 2$ and $b = 35.34$ A$^{0.5}$) and contour length ($l_m = 2.57$) are from Keten and coworkers.[43] The intersection of the mushroom transition line (eqn 2.1) and the CPB to SDPB transition line (eqn 2.2) provides a

critical grafting density below which the brush conformation is either mushroom at low molecular weight (or degree of polymerization) or SDPB at high molecular weights. Using this, the data from **Table 2.1** can be converted to a phase diagram (**Figure 2.3a**) which defines the various grafted polymer conformation regimes.

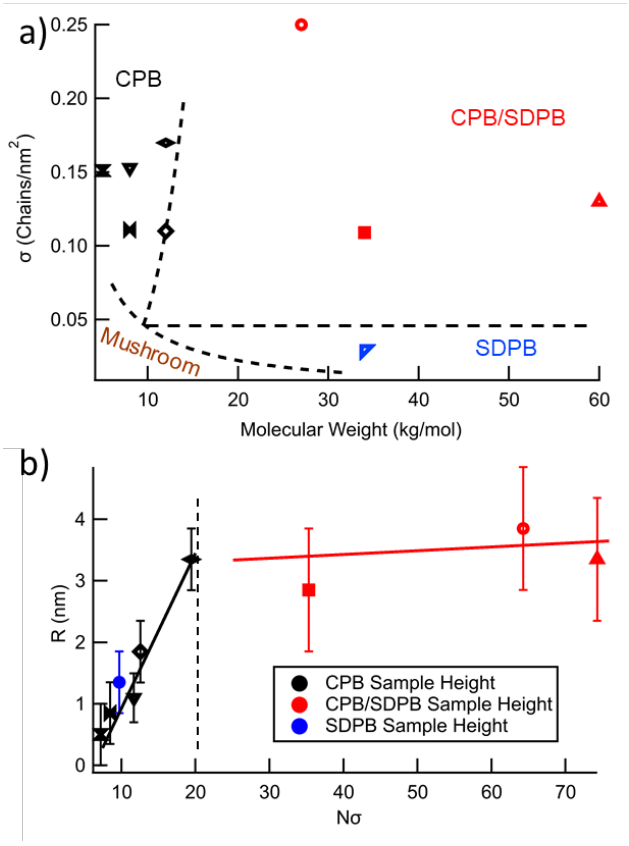

Figure 2.3: a) Phase space mapping the ***MxG*-CNC-*g*-PS** samples molecular weight, grafting density, and polymer brush conformation consisting of concentrated polymer brush (CPB), concentrated polymer brush with semidilute polymer brush corona (CPB/SDPB) and semidilute polymer brush (SDPB) and b) brush height, *R*, of ***MxG*-CNC-*g*-PS** samples plotted against the product of degree of polymerization and grafting density, with error from standard deviation of N=10 and lines provided to guide the eye. See **Table 2.1** for symbol designation.

The grafted polymer confirmations shown in the phase diagram in **Figure 2.3a** are based on the simulations and not experiments. However, Keten and coworkers[42,43] do provide relationships between degree of polymerization, grafting density, and predicted brush height that changes with conformation regime and can be experimentally examined. Specifically, they define the brush height, R, as

$$R = \frac{0.1abLl_m^2\sigma}{r_0^{1/2}}\left(\frac{N}{N_{cr}}\right)^x \tag{2.4}$$

where N is the degree of polymerization for the given polymer graft, $x = 1$ in the CPB regime or 0.5 in the CPB/SDPB regime, and N_{cr} being defined by eqn 2.2. The measured height of the PGNs on mica (H_{PGN}) by AFM (**Figures S2.14-2.15**) consists of two layers of grafted polymer (top and bottom) plus the CNC height (H_{CNC}) allowing the experimental determination of the brush height, R (= (H_{PGN}-H_{CNC})/2). Plotting this experimentally determined brush height versus $N\sigma$ it is possible to determine the transition between brush conformations. Plotting R as shown in **Figure 2.3b** a straight line can be drawn through the samples with a $N\sigma$ of less than 20. If these PGNs are in the CPB regime then $x = 1$ and the slope will equal $0.1abLl_m^2/r_0^{1/2}N_{cr}$, where N_{cr} is fixed at 120, the average value of N_{cr} for the ***MxG*-CNC-*g*-PS** samples in the CPB regime (calculated from eqn 2.2). The slope of the line obtained from the experimental data is 0.172 ± 0.035 (**Figure S2.17**), which compares to 0.256 ± 0.091 based on the simulation work.[43] It is worthwhile noting that the simulation data involves polymer-polymer and polymer-CNC interactions, while the measured height from AFM involves polymer-air interactions, which presumably results in a more condensed polystyrene brush (something that has been shown in literature for the AFM of other PGNs).[46] **Figure 2.3b** also clearly shows that above $N\sigma$ of 20 there is a significant change in the

slope consistent with a change in the polymer conformation (from CPB to SDPB/CPB) above this value.

Scanning electron microscopy of the as cast and melt-pressed (at 140°C for 30 minutes under 70 MPa) films offers some insight into the morphology of these ***MxG*-CNC-*g*-PS** materials. Specifically, **Figure 2.4** shows individualized nanoparticles in as cast samples up to graft molecular weights of ca. 34 kg/mol. Melt-pressing of these samples results in more continuous films unless the molecular weight of the graft is low, ca 5 kg/mol. After melt-pressing, both ***MxG*-CNC-*g*-PS-5-45** and ***MxG*-CNC-*g*-PS-60-90** show similarly low levels of porosity (**Table S2.3**). The difference in morphology can been seen in the optical images of the films, with the films consisting of individualized nanoparticles being opaque and the continuous films being more optically transparent. Interestingly, all the PGNs, even those that that have very high weight percentage (55 wt%) of CNCs, form mechanically robust, processable materials.

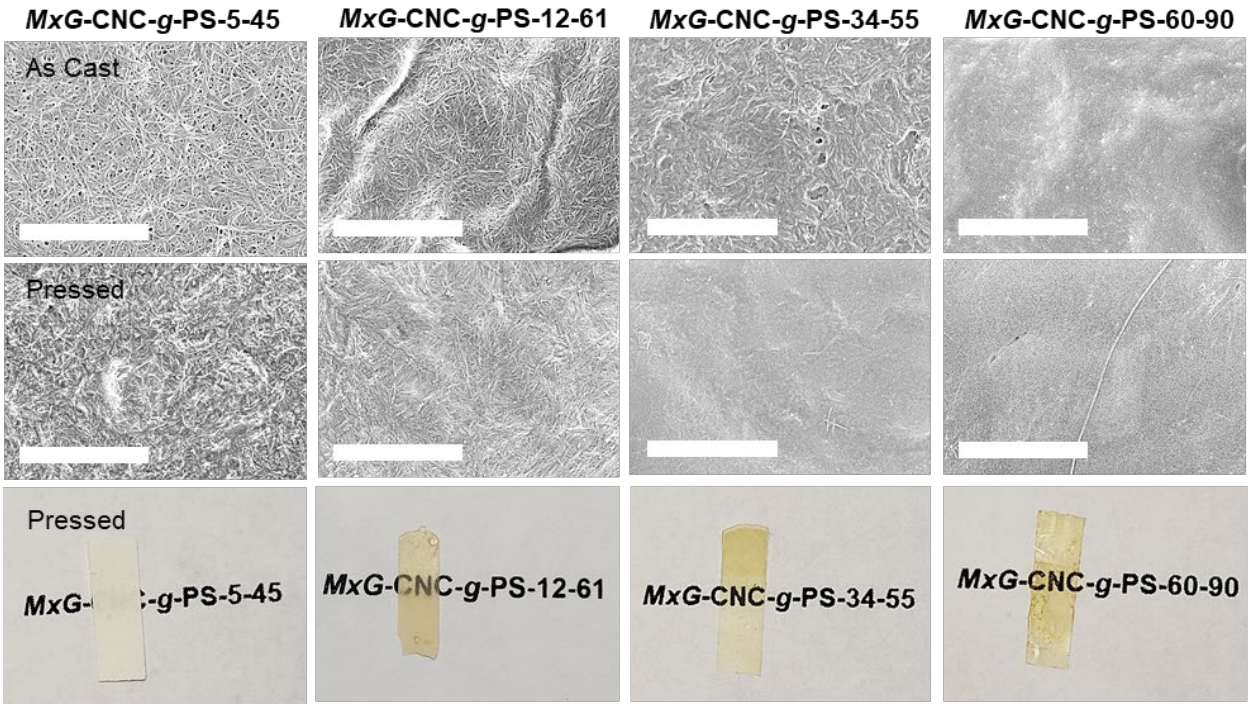

Figure 2.4: Scanning electron microscopy images (scale bar 2 μm) and optical images of ***MxG*-CNC-*g*-PS-5-45, *MxG*-CNC-*g*-PS-12-61, *MxG*-CNC-*g*-PS-34-55,** and ***MxG*-CNC-*g*-PS-60-90** showing both as cast and after melt pressing at 140°C for 30 minutes under 70 MPa.

Having confirmed the grafted polymer conformation and accessed robust PGN films, the mechanical properties of PGN materials were then investigated. To this end it was decided to explore the modulus and toughness of the melt-pressed ***MxG*-CNC-*g*-PS** films which gave more reproducible results compared to the as cast samples. Keten and coworkers predicted that low grafting density (σ) and low degree of polymerization (N) maximizes modulus while low grafting density and high degree of polymerization maximizes toughness.[42] **Figure 2.5a** shows the storage modulus versus temperature from tensile dynamic mechanical analysis (DMA) of the various ***MxG*-CNC-*g*-PS** films with similar grafting density (0.11 chains/nm^2) but different graft degree of polymerization. As expected, the data shows that with increasing molecular weight (8-60

kg/mol) and therefore lower weight fraction of the CNC (51-10%) in the PGNs there is a reduction in modulus above glass transition temperature (T_g). For context, the melt-pressed **PS-NH$_2$-60** film and a mixed, 2-component nanocomposite consisting of **MxG-CNC-COOH** with 90 wt% **PS-NH$_2$-12** are shown as controls. Relative to **PS-NH$_2$-60** the PGNs show a significant enhancement in modulus above T_g while the mixed, 2-component nanocomposite shows a similar modulus to that of ***MxG*-CNC-*g*-PS-60-90** film. The main advantage of the PGN architecture when it comes to modulus is the ability to access homogenous films with significantly higher nanofiller loading and therefore reinforcement. It is worthwhile noting that it was not possible to access homogenous two-component films using solution based (DMF) processing conditions with higher CNCs loadings (beyond 10wt%) similar to that accessed by the PGNs films, consistent with the literature.[47]

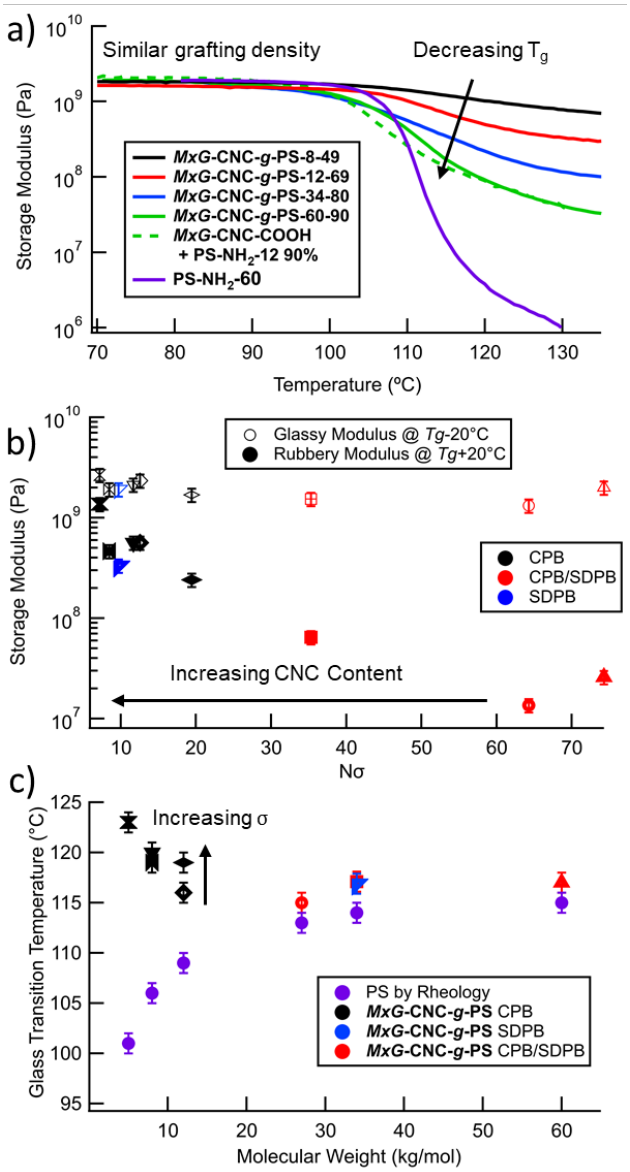

Figure 2.5: a) Tensile Dynamic Mechanical Analysis of select ***MxG*-CNC-*g*-PS** samples of similar grafting density (0.11 chains/nm^2), b) storage moduli in the glassy regime (20°C below T_g) and in the rubbery plateau (20°C above T_g) plotted versus product of degree of polymerization and grafting density, with error from standard deviation of N=3, and c) T_g plotted vs molecular weight of both the PGN system and PS homopolymer, as determined by shear rheology for the

Figure 2.5 Continued: homopolymer and from tensile DMA for the PGN system, with error from standard deviation of N=3. See **Table 2.1** for symbol designation.

Figure 2.5b shows the rubbery and glassy moduli (at T_g +/- 20 ℃) plotted (from the tensile DMA data) versus $N\sigma$ for all the films. The data shows that in the glassy state ($T<T_g$) the samples have only a slight dependence on $N\sigma$ with average modulus values of 2.0 GPa, while above T_g higher moduli tracks with a higher weight percent loading of CNC (or lower $N\sigma$) from 13 MPa to 1.37 GPa (**Figure S2.18**). This behavior is consistent with what is observed in other CNC-based nanocomposites,[47,48] where little reinforcement is seen in the glassy regime as the reinforcing CNC is of similar modulus to the glassy polymer while showing significant reinforcement in the rubbery regime with increasing nanofiller content.[47,49]

The glass transition temperature (T_g) of the PGN system do show a remarkable increase compared to PS homopolymer, particularly with the lower molecular weight grafts. **Figure 2.5c** shows the T_g of the ***MxG*-CNC-*g*-PS** films and corresponding **PS-NH$_2$** as a function of the PS (homopolymer or graft) molecular weight. While T_g was obtained from the peak of tan(delta) for all the materials, tensile DMA was used for the PGNs and oscillatory shear rheological measurements were used for the homopolymers (**Figures S2.19-2.20**). The T_g of the **PS-NH$_2$-60** film obtained by both shear rheology and tensile DMA was the same (**Figure S2.21**). The lowest molecular weight grafted PGN films (5 kg/mol) have a T_g value 20 ℃ above the corresponding homopolymer. This difference decreases as the molecular weight increases such that at higher molecular weights, the PGN films have a T_g ~1℃ above the corresponding polymer. The impact of grafted polymer and nanocomposite interfaces on the T_g has been widely studied and largely shows higher T_g in nanocomposites and PGN grafted systems, on account of 1) loss of chain end

mobility and free volume, 2) confinement of the polymer system, and 3) polymer–substrate interactions.[50–55] Even so, while a 20°C increase in T_g is not without precedent in model confined polymer interface systems,[51] it is among the higher in literature reported values observed in PGNs. It is also worthwhile noting that in the polymer-grafted CNCs that have similar molecular weight grafts at different densities, there does appear to be a slight increase (1-3°C) in T_g in the higher grafting density materials, as can be seen in **Figure 2.5c** with the 8 and 12 kg/mol grafted samples.

Nanoindentation of the ***MxG*-CNC-*g*-PS** films was used to analyze the material properties and fracture toughness of the films. **Figure 2.6a** shows characteristic load–displacement curves of PGN films with similar grafting density. By analyzing and fitting the unloading curves, the modulus (E) and hardness (H) can be obtained (**Figure S2.22**). Modulus follow similar trends as the glassy modulus of the PGN films shown in **Figure 2.5b** while the hardness varies between 0.1 and 0.4 MPa. Upon indentation, the residual impression (and any cracks formed) can be used to determine the fracture toughness. ***MxG*-CNC-*g*-PS** films with 5 kg/mol, 8 kg/mol and higher grafting density 12 kg/mol (***MxG*-CNC-*g*-PS-12-69**) polymer did not leave a distinct trigonal indentation and instead displayed major crack formation in the material, characteristic of a low fracture toughness material. All these easily fractured films are comprised of PGNs with CPB grafts. By contrast a majority of the SDPB or CPB/SDPB ***MxG*-CNC-*g*-PS** films show a trigonal indentation (expected due to the Berkovich tip) with cracks extending from the corners of the indentation that are on the order of or less than the size of the Berkovich tip center to corner length (**Figure S2.23**). Analyzing the indentation and crack formation via AFM (**Figure 2.6b, Figure S2.23**), the fracture toughness, K_c, can be quantified by

$$K_c = \frac{1.076 X_v \left(\frac{t}{l}\right)^{\frac{1}{2}} \left(\frac{E}{H}\right)^{\frac{2}{3}} P_{max}}{c^{\frac{3}{2}}} \quad (5)$$

where X_v is an empirically fit constant, t is the distance from center to Berkovich corner, l is the length of the emanating crack, c is the total crack length, and P_{max} is the maximum load.[56] In order to examine how both graft density (σ) and degree of polymerization (N) impacts the fracture toughness of these films **Figure 2.6c** plots the measured K_c of the ***MxG*-CNC-*g*-PS** films against N/σ.

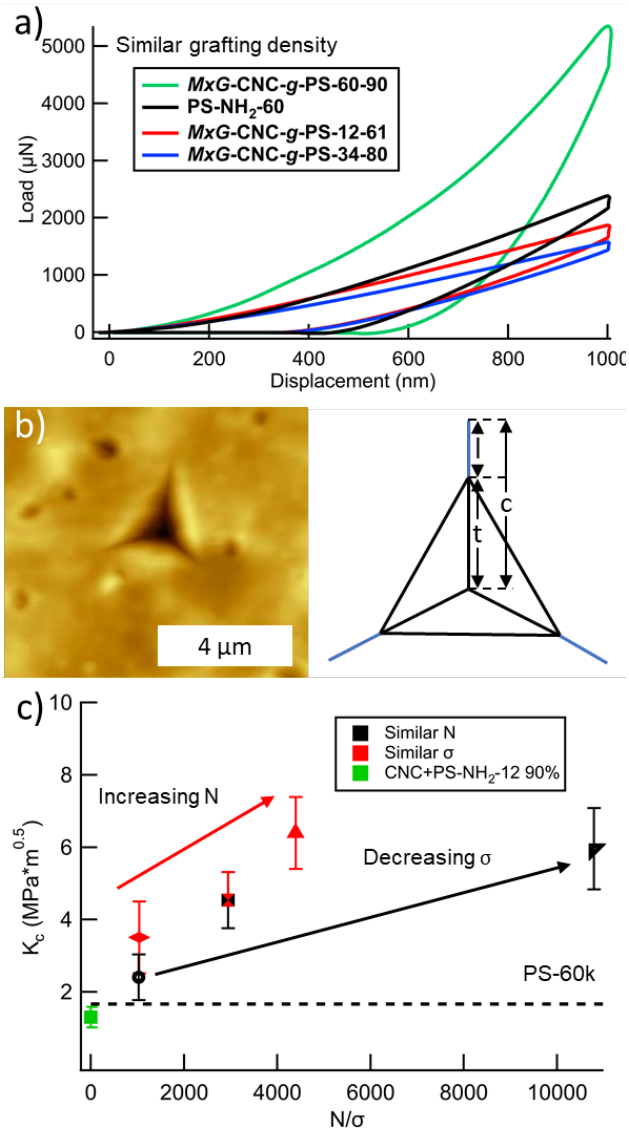

Figure 2.6: a) Load–displacement curves obtained by nanoindentation for ***MxG*-CNC-*g*-PS** films with a constant polymer grafting density (σ) but different degree of polymerization (N) of the graft, b) AFM of ***MxG*-CNC-*g*-PS-34-80** post-indentation with schematic of an indentation created using a Berkovich tip where c is the total crack length measured from the center of contact to the end of crack at the sample surface, t is the distance from the center of contact to the corner, and l is the length of the cracks emanating from the corners. c) Fracture toughness of ***MxG*-CNC-*g*-PS**

Figure 2.6 Continued: film versus divisor of degree of polymerization and grafting density with measured toughness of 60k reference polystyrene sample and **MxG-CNC-COOH** with 90 wt% **PS-NH$_2$-12** from N=10.

Interestingly, all measured samples show higher fracture toughness (K_c) than a 60 kg/mol PS film (60 kg/mol being the highest molecular weight graft used in this study), irrespective of grafting density and degree of polymerization. The mixed nanocomposite sample (**MxG-CNC-COOH** with 90 wt% **PS-NH$_2$-12**) shows a lower fracture toughness (1.3±0.3 MPa*m$^{0.5}$) relative to the PGN films, and akin to that of the homopolymer **PS-NH$_2$-60** (1.7±0.7 MPa*m$^{0.5}$). The PGNs with similar grafting density (0.11 chains/nm^2), ***MxG*-CNC-*g*-PS-12-61**, ***MxG*-CNC-*g*-PS-34-80**, and ***MxG*-CNC-*g*-PS-60-90** all show increasing fracture toughness (from 3.5±1.0 MPa*m$^{0.5}$ to 6.4±1.0 MPa*m$^{0.5}$) with increasing degree of polymerization. The PGNs with similar molecular weight (ca. 30 kg/mol) and thus degree of polymerization, ***MxG*-CNC-*g*-PS-27-88**, ***MxG*-CNC-*g*-PS-34-80**, and ***MxG*-CNC-*g*-PS-34-55**, all show increasing fracture toughness with decreasing grafting density, from 2.4±0.6 MPa*m$^{0.5}$ to 6.0±1.1 MPa*m$^{0.5}$. These data broadly support the predictions of Keten and coworkers[42] confirming that increasing fracture toughness is obtained with a relatively lower grafting density of higher degree of polymerization polymers.

In seeking to demonstrate the overall mechanical effects of the ***MxG*-CNC-*g*-PS** PGN films, along with homopolymer and a two-component composite, the rubbery modulus was plotted against the fracture toughness (**Figure 2.7**) and color being used to highlight the polymer conformation of the PGNs. While PGNs in the CPB regime form films of high modulus on account of their large nanofiller loading, as high as 55 wt% CNC, their fracture toughness is low. PGNs in the CPB/SDPB regime generally show an enhancement in fracture toughness, the significant

quantity of polymer needed to access that regime limits the nanofiller loading and thus the modulus. By accessing material with both high polymer degree of polymerization and relatively low grafting density, which permits both SDPB conformation and entanglement alongside a high nanofiller loading, it is possible to optimize both the modulus and fracture toughness.

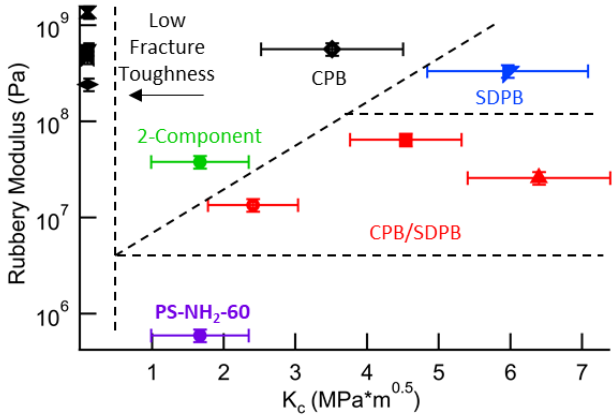

Figure 2.7: Rubbery modulus as determined by tensile DMA plotted against the fracture toughness as determined by nanoindentation for a variety of PGN, 2-component nanocomposite, and homopolymer samples. PGN samples are labeled according to their grafted polymer brush regime. Samples whose fracture toughness could not be calculated are to the far left.

2.5 CONCLUSION

***MxG*-CNC-*g*-PS** samples were synthesized with controlled grafted polymer degree of polymerization and density. AFM studies was used to determine the grafted polymer conformation as a function of both degree of polymerization and grafting density and it was shown that the mechanical properties of these one-component nanocomposites strongly depend upon the grafted polymer conformation and the total amount of polymer. Specifically, modulus measured by tensile DMA showed that trends of the materials below T_g (glassy) was relatively invariant with composition while above T_g (rubbery) there is a dramatic improvement in modulus with decreasing molecular weight and decreasing grafting density ranging from 13 MPa to 1.37 GPa, which is related to the amount of the CNC in the PGN. The PGN architecture allows access to homogenous films with as much as 55 wt% CNC resulting in films with GPa modulus above T_g. In measuring the T_g, PGNs in the CPB regime displayed T_g values 20°C higher than comparable ungrafted homopolymer, with the difference in T_g decreasing with increasing molecular weight. Fracture toughness measured by nanoindentation of the PGN films showed a significant improvement in their fracture toughness relative PS homopolymer of similar degree of polymerization (1.7±0.7 MPa*$m^{0.5}$), with the greatest improvement in fracture toughness with increasing degree of polymerization and decreasing grafting density (up to 6.4±1.0 MPa*$m^{0.5}$). Ultimately, the polymer grafted nanoparticle films enabled large loadings of nanorod filler (up to 55 wt%) with excellent mechanical properties and provides stronger understanding of the structure property relations of this new class of materials.

2.6 SUPPLEMENTAL INFORMATION

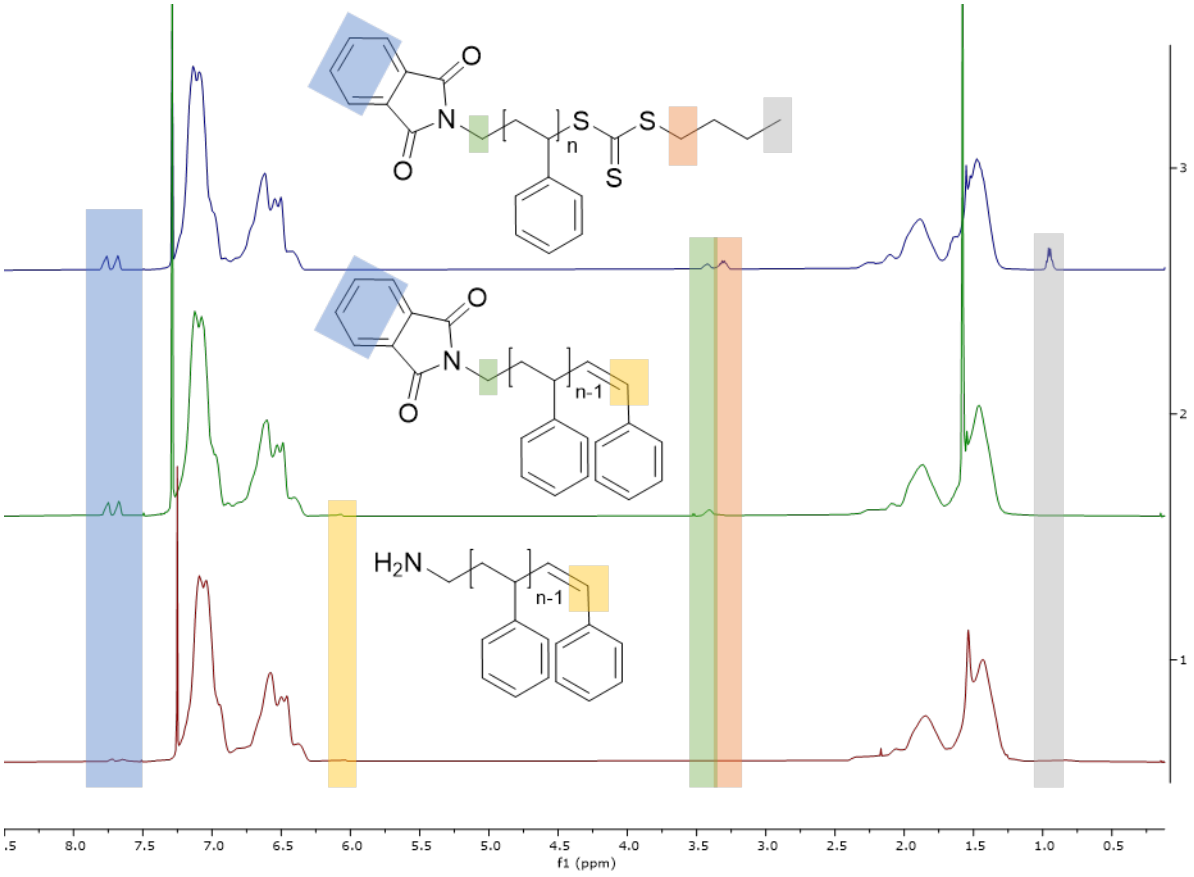

Figure S2.1: ^{1}H NMR (500 MHz, $CDCl_3$) spectra of **PS-8** (top, blue), **PS-Δ-8 (**after the thermolytic removal of butyl trithiocarbonate**)** (middle, green), and **PS-NH$_2$-8** (bottom, red).

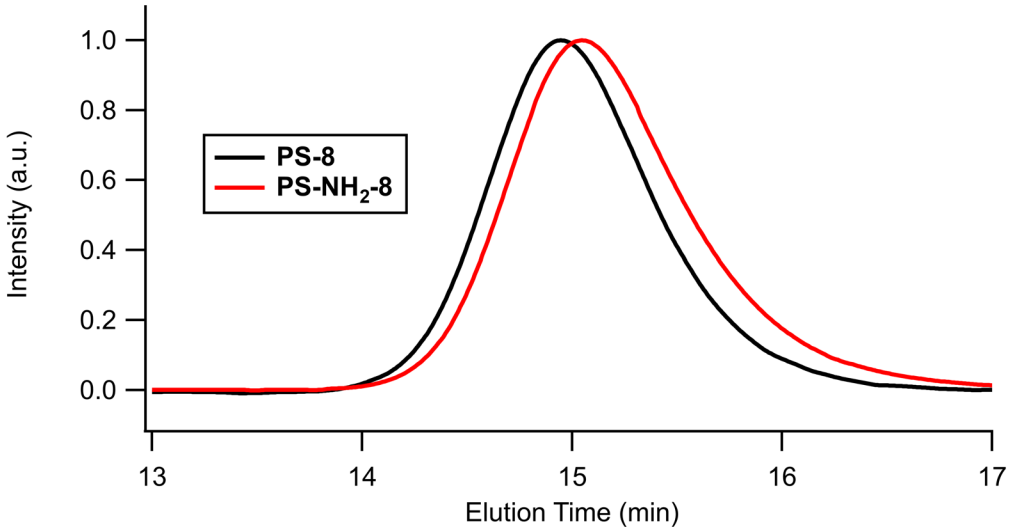

Figure S2.2: GPC-MALS of **PS-8** (black) and **PS-NH$_2$-8** (red).

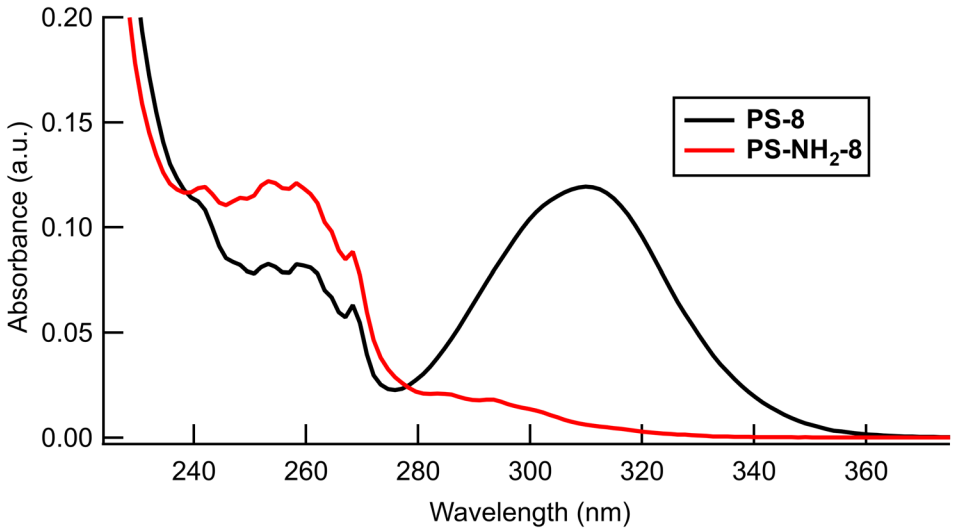

Figure S2.3: UV-Vis of **PS-8** (black) and **PS-NH$_2$-8** (red) with diminution of the 310 nm peak

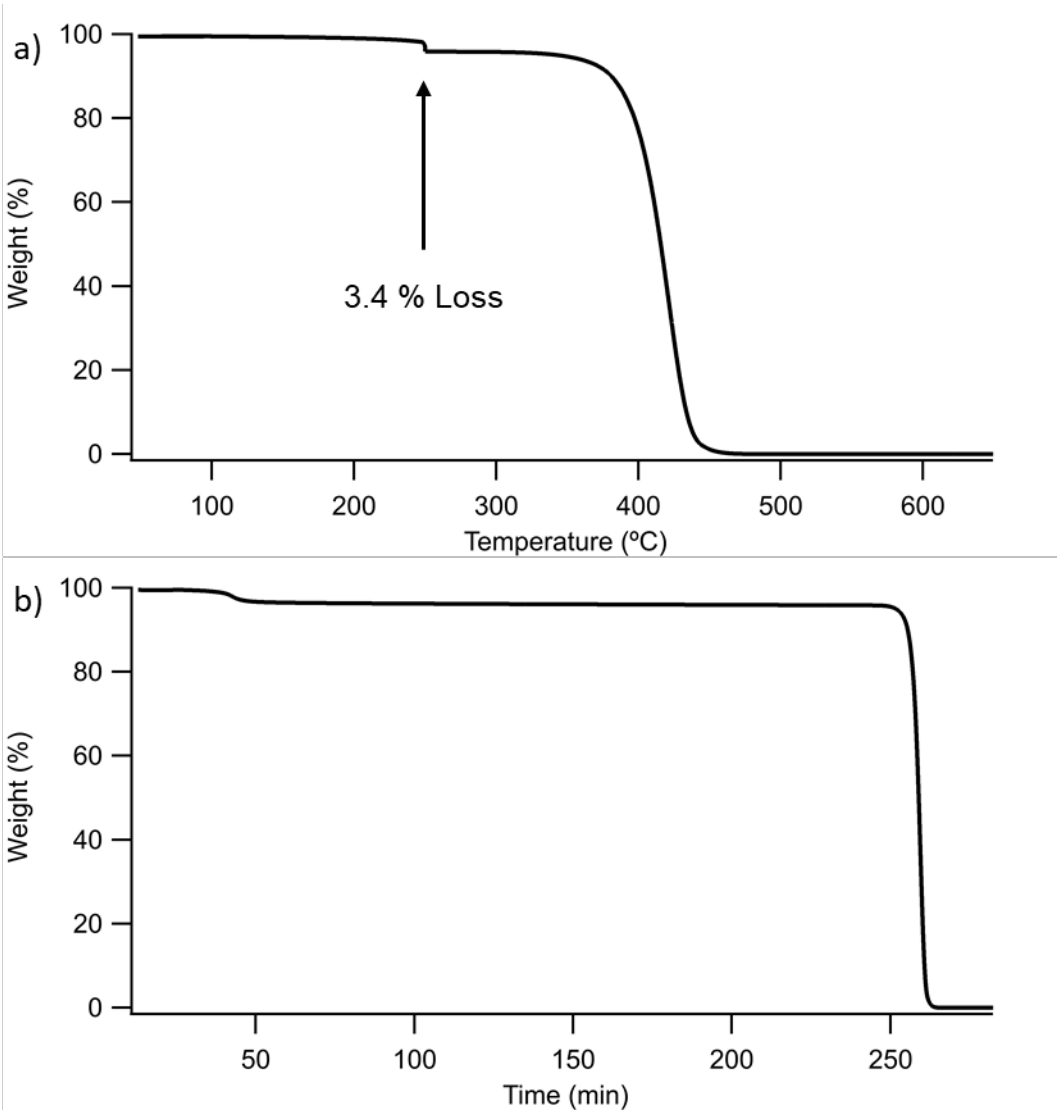

Figure S2.4: TGA (10°C per minute ramp rate) of **PS-5** with weight percent as a function of a) temperature and b) time showing 3.4% loss at 250°C over the span of 10 minutes, which aligns well with predicted weight percent loss of 3.3% after loss of the butyl trithiocarbonate.

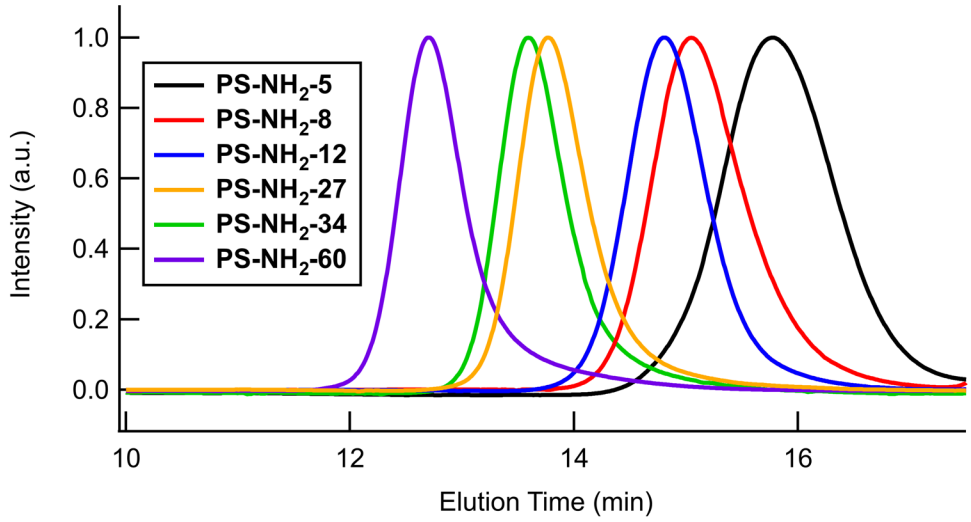

Figure S2.5: GPC-MALS of PS samples from **Table S2.1**

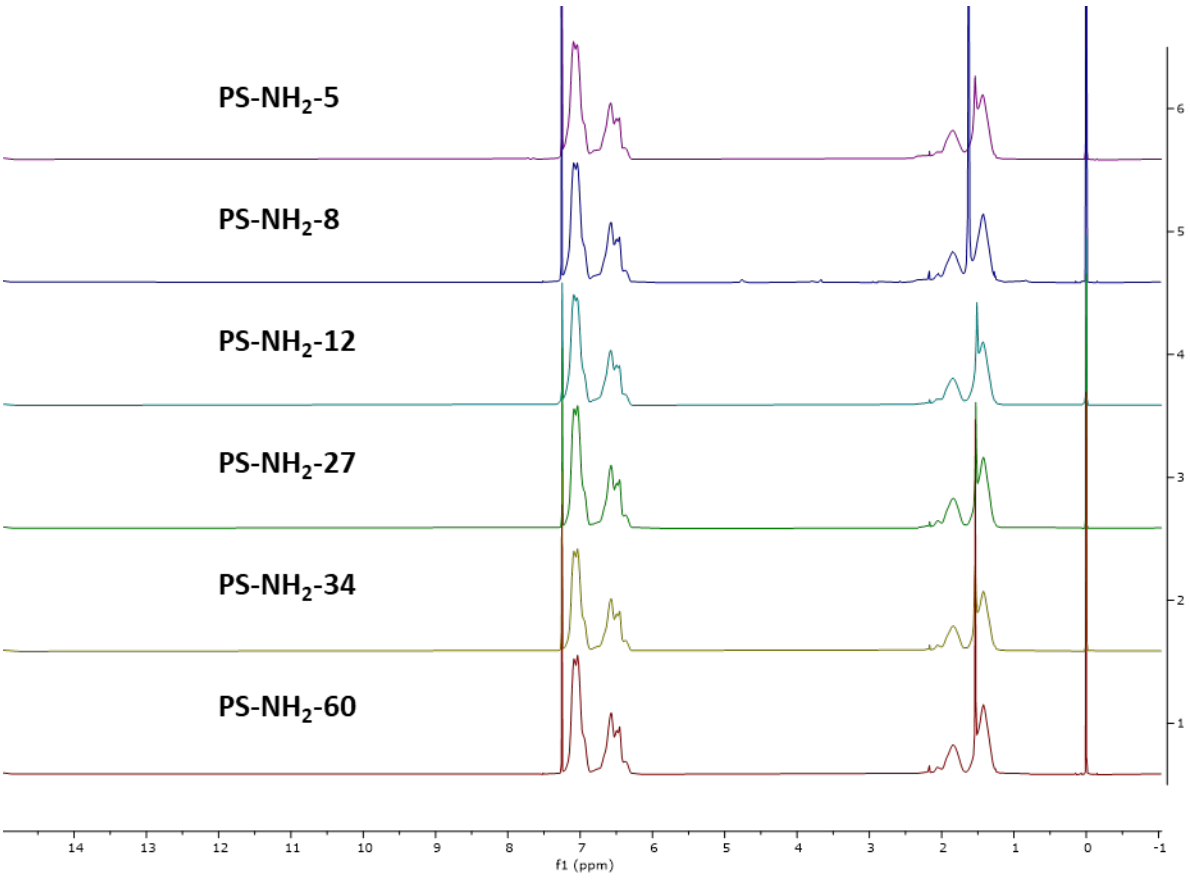

Figure S2.6: ^{1}H NMR (500 MHz, $CDCl_3$) spectra of PS samples from **Table S2.1**

Table S2.1: Homopolymer Synthesis Summary

	M_n, GPC-MALS (g/mol)	Dispersity, $Đ$
PS-NH$_2$-5	5200	1.08
PS-NH$_2$-8	8300	1.04
PS-NH$_2$-12	11500	1.05
PS-NH$_2$-27	27300	1.03
PS-NH$_2$-34	34400	1.03
PS-NH$_2$-60	60200	1.06

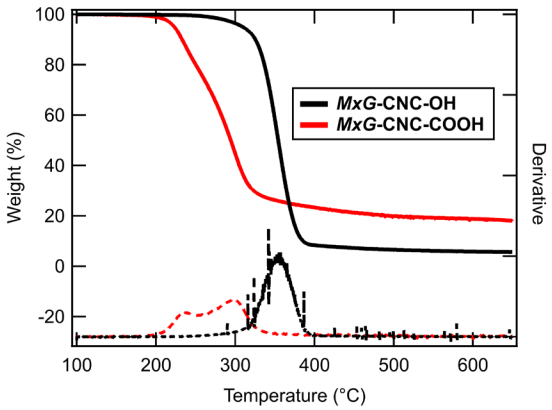

Figure S2.7: Thermal Gravimetric Analysis (TGA) of ***MxG*-CNC** before and after TEMPO oxidation (under nitrogen atmosphere with a heating rate of 10 °C/min).

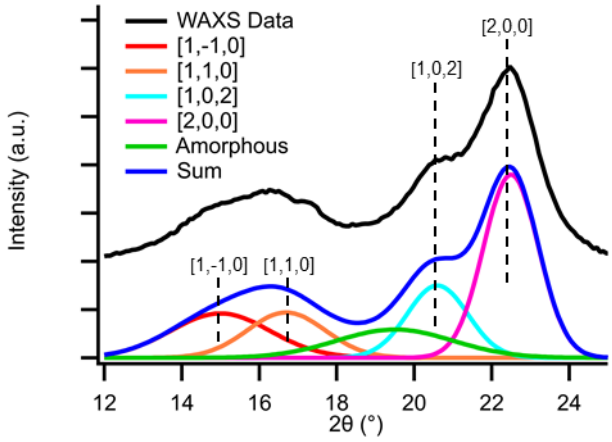

Figure S2.8: WAXS of ***MxG*-CNC-COOH** with labeled crystalline peaks and Gaussian fit to calculate crystallinity index. The Gaussian peaks corresponding to the various CNC crystal planes are notated by color. Note that original WAXS data is offset for clarity.

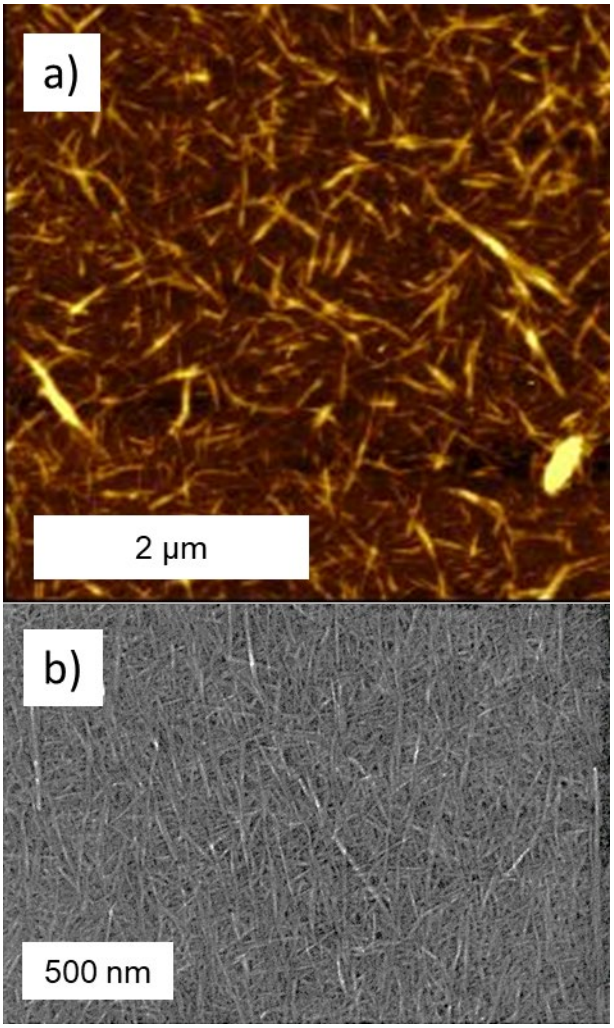

Figure S2.9: ***MxG*-CNC-COOH** a) AFM height image after casting on poly-L-lysine coated mica and b) SEM as cast from solvent exchanged solution and coated in 2 nm Pt/Pd

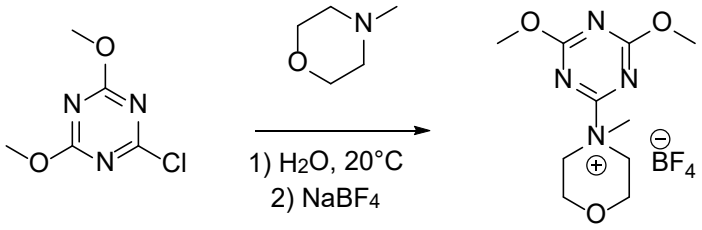

Scheme S2.1: Synthesis of the peptide coupling agent 4-(4,6-dimethoxy-1,3,5-triazin-2-yl)-4-methylmorpholinium tetrafluoroborate (**DMTMMBF4**)

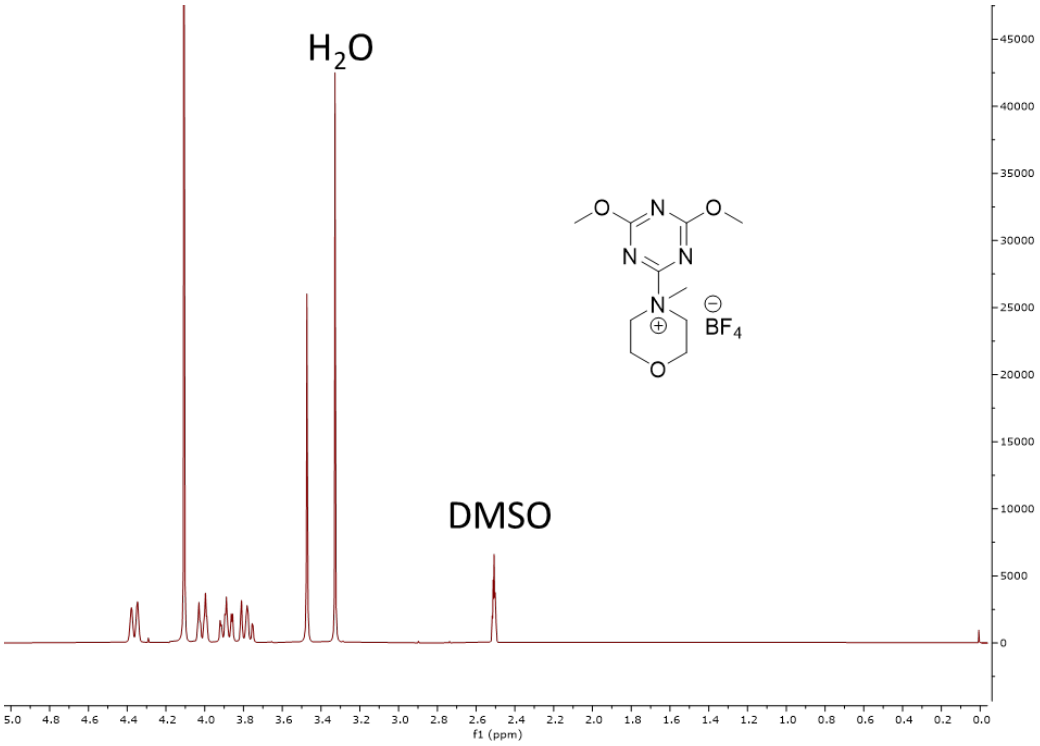

Figure S2.10: ^{1}H NMR (500 MHz, $CDCl_3$) spectra of **DMTMMBF4**

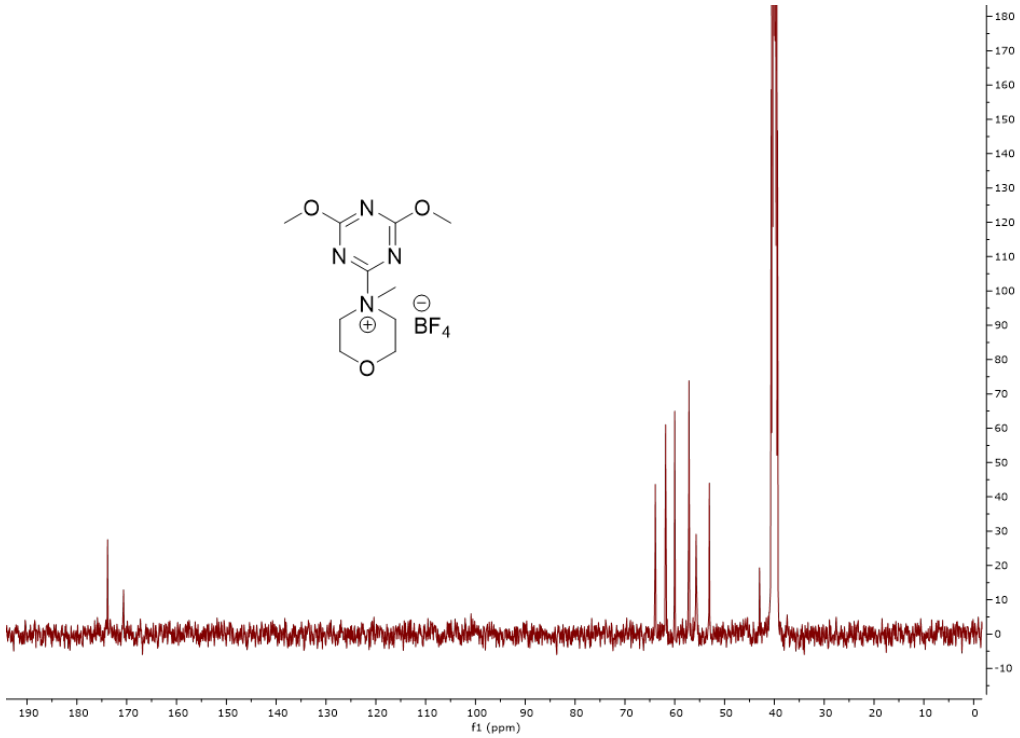

Figure S2.11: ^{13}C NMR (500 MHz, $CDCl_3$) spectra of **DMTMMBF$_4$**

To compare the coupling efficiency of various coupling reagents, more reactions were performed in the same conditions with CNCs suspension from solvent exchange and **PS-NH$_2$-8**. The obtained ***MxG*-CNC-*g*-PS-8** were examined by TGA. EDC/NHS (N-ethyl-N'-(3-(dimethylamino) propyl) carbodiimide)/(N-hydroxysuccinimide), DIC/HOBt (N,N'-diisopropylcarbodiimide)/(1-hydroxybenzotriazole) and DIC/NHS these three coupling reagents are common combination widely used in conjugation reaction between amino and carboxyl groups. DMTMMBF$_4$ has not yet been used in modification of cellulose nanoparticles. As shown in **Figure S2.13**, ***MxG*-CNC-*g*-PS** from reactions with DIC/HOBt as coupling reagent results in 52% PS in the PS-graft-CNCs by weight. PS-graft-CNCs from reactions with EDC/NHS as coupling reagent results in 32% PS

in the PS-graft-CNCs by weight. PS-graft-CNCs from reactions with $DMTMMBF_4$ result in 57% PS in the PS-graft-CNCs by weight. Among these four types of coupling reagents, $DMTMMBF_4$ shows the highest efficiency for coupling reaction between carboxylic acid groups on CNCs and the amine groups on PS, about one third of the -COOH groups on CNCs can be reacted with PS.

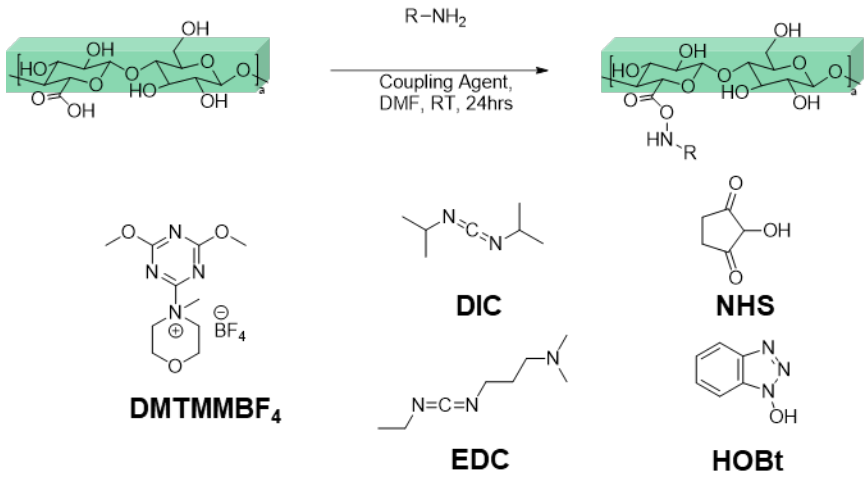

Scheme S2.2: Peptide coupling reaction using a variety of coupling reagents, **DIC/NHS**, **EDC/NHS**, **DIC/ HOBt**, and **$DMTMMBF_4$**.

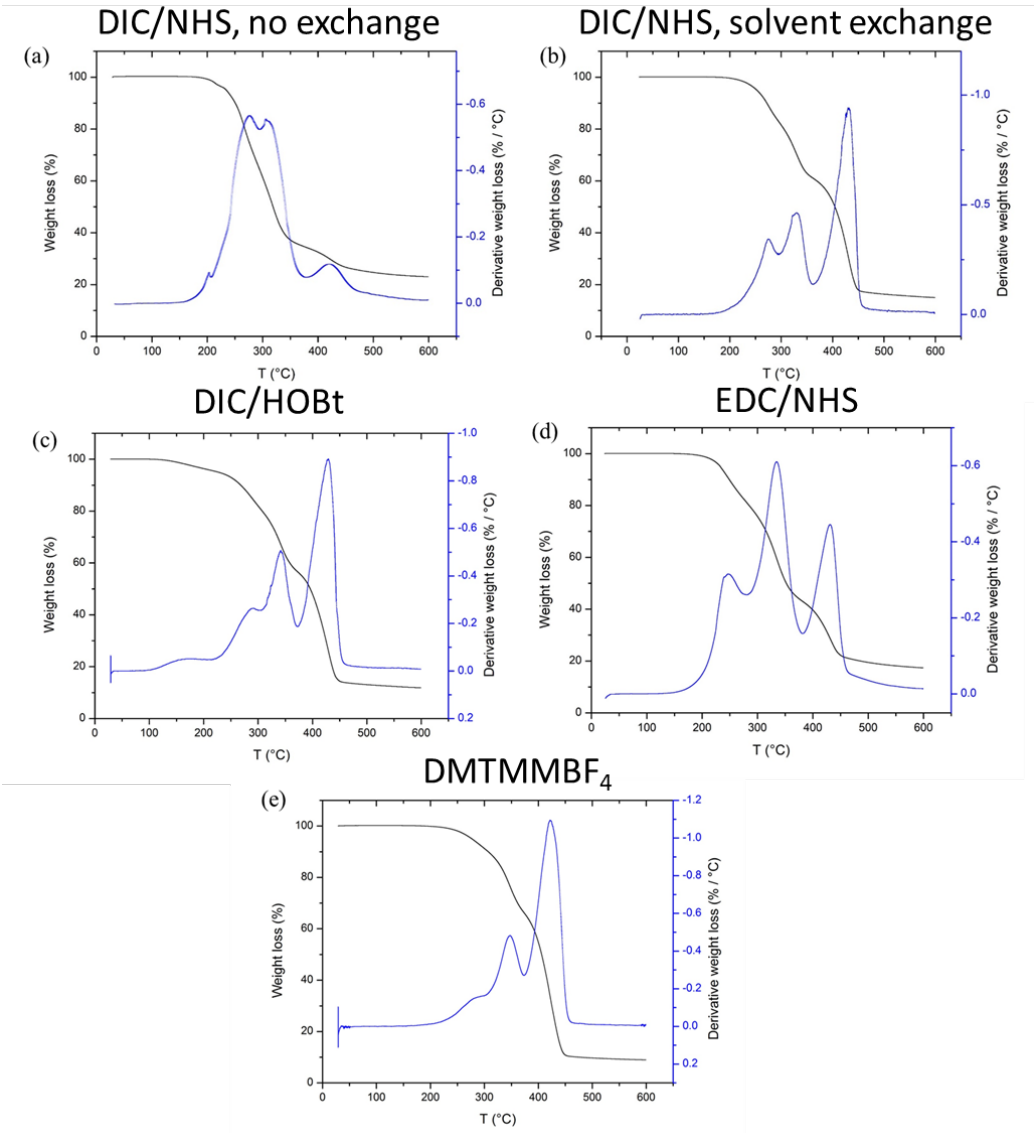

Figure S2.12: TGA of different peptide attachment chemistries and methods using **PS-NH$_2$-8** and ***MxG*-CNC-COOH**, specifically, a) from DIC/NHS as coupling reagents and CNCs dispersion from direct mixing, (b) from DIC/NHS as coupling reagents and CNCs dispersion from solvent-exchange, (c) from DIC/HOBt as coupling reagents and CNCs dispersion from solvent-exchange, (d) from EDC/NHS as coupling reagents and CNCs dispersion from solvent-exchange, and (e) from DMTMMBF$_4$ as coupling reagents and CNCs dispersion from solvent-exchange.

Table S2.2: Summary of the grafting efficiency of various coupling agents and conditions from **Figure S2.12**

Method	Coupling Agent	Wt% Polymer [a]
Direct mixing	DIC/NHS	12%
Solvent Exchange	DIC/NHS	40%
Solvent Exchange	DIC/HOBT	52%
Solvent Exchange	EDC/NHS	32%
Solvent Exchange	DMTMMBF4	57%

[a] from TGA

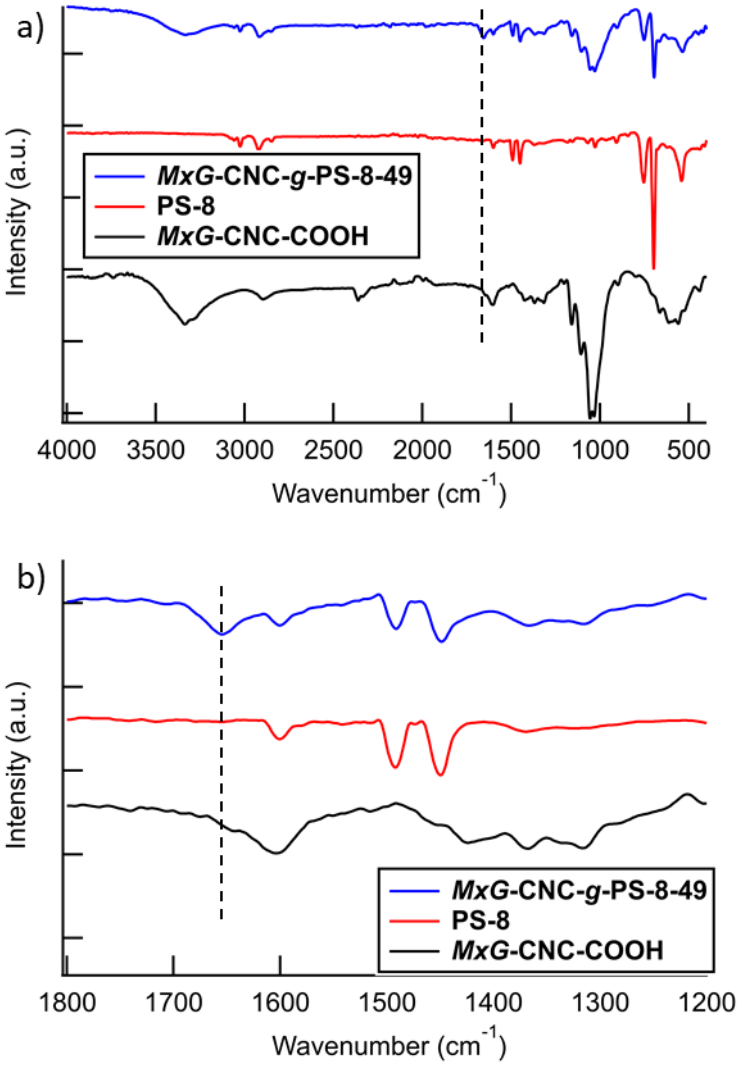

Figure S2.13: ATR-FTIR of ***MxG*-CNC-COOH, PS-8,** and ***MxG*-CNC-*g*-PS-8-49**, with line highlighting the -CONH- bond at 1650 cm^{-1} indicative of peptide coupling attachment, with a) showing the full spectrum while b) shows a zoomed in area of 1200-1800.

To calculate the polymer grafting density, $\sigma_{polymer}$, the following equation from literature[1] was used

$$\sigma_{polymer} = \frac{\Phi_{polymer}\rho_{CNC}V_{CNC}N_A}{\Phi_{CNC}MW_{polymer}SA_{CNC}} \quad \text{S2.1}$$

where Φ_{poly} and Φ_{CNC} are the weight fractions of polymer and CNC, respectively, ρ_{CNC} is the density of the CNC, V_{CNC} is the volume of an individual CNC, and SA_{CNC} is the surface area of an individual CNC, $MW_{polymer}$ is the molecular weight of the polymer as determined by GPC-MALS, and N_A is Avogadro's number. V_{CNC} and SA_{CNC} are both calculated using literature values for *MxG*-CNC, a rectangular prism with dimensions 8.5nm by 2.8nm by 300nm as determined by SANS.[2]

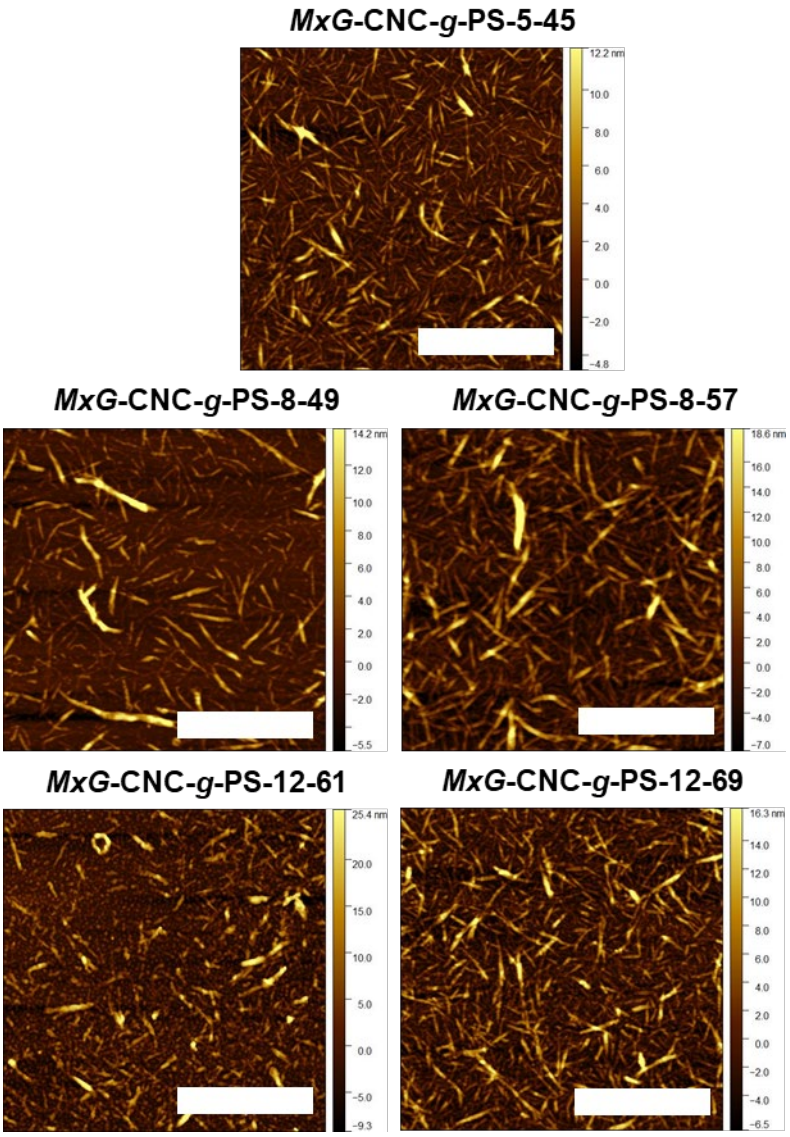

Figure S2.14: AFM of ***MxG*-CNC-*g*-PS** samples after casting on poly-L-lysine coated mica showing concentrated polymer brush (CPB) regime structure. Scale bar corresponds to 1 μm.

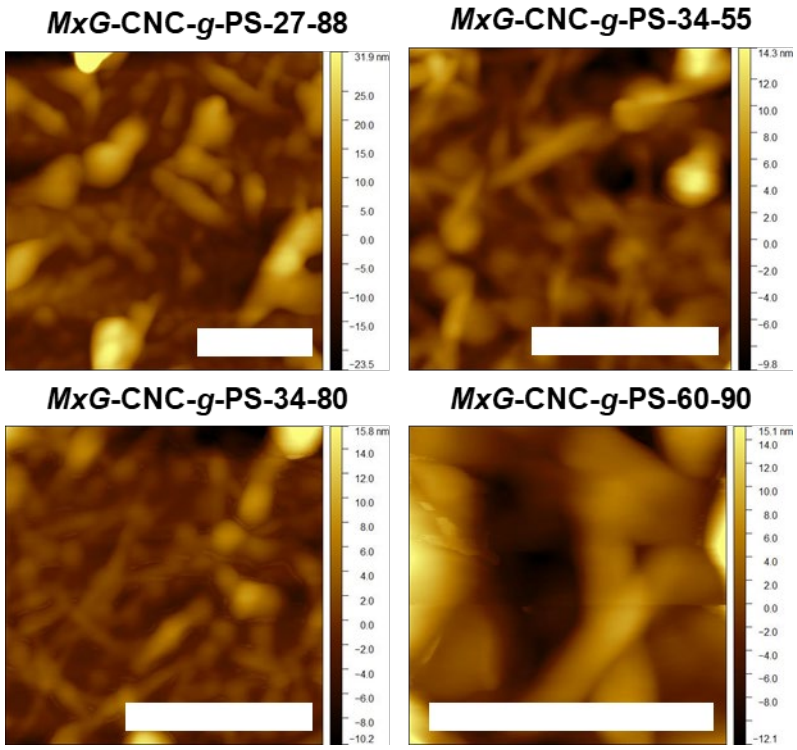

Figure S2.15: AFM of ***MxG*-CNC-*g*-PS** samples after casting on poly-L-lysine coated mica showing semidilute polymer brush (SDPB or CPB/SDPB) regime structure. Scale bar corresponds to 200 nm.

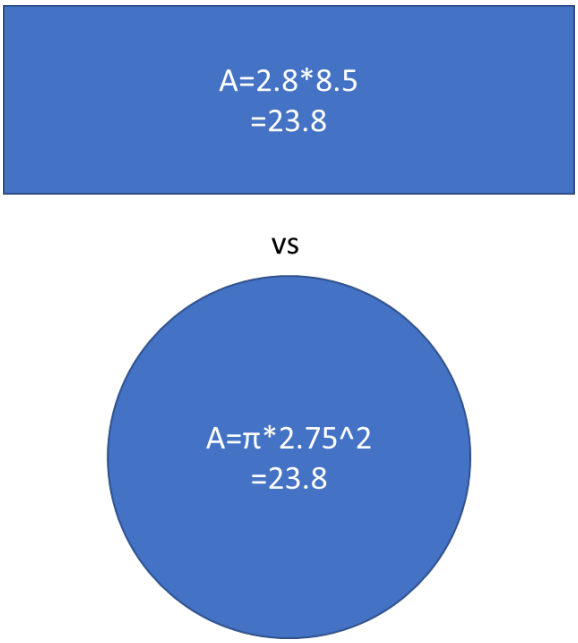

Figure S2.16: Size comparison rationalizing radius usage showing similar surface area for *MxG*-CNC with dimensions 2.8 nm by 8.5 nm and a circle of radius 2.75 nm

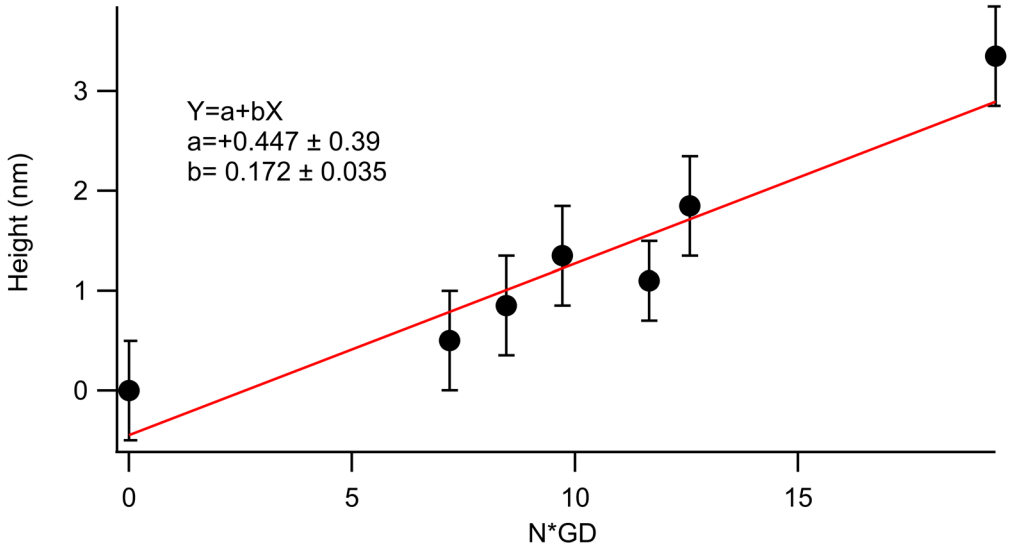

Figure S2.17: Linear Regression of the CPB data from **Figure 2.2c**.

To calculate the porosity of the ***MxG*-CNC-*g*-PS** samples, the sample density was measured and compared to a theoretical of samples with no void fraction. The density of measured samples (ρ_{sample}) was calculated by

$$\rho_{sample} = m/(l * w * t) \tag{S2.2}$$

where m is the sample mass and l, w, and t are the sample lengths, widths, and thicknesses respectively. The theoretical nanoparticle density (ρ_{theo}) was calculated as

$$\rho_{theo} = \frac{1}{\frac{\varphi_{CNC}}{\rho_{CNC}} + \frac{\varphi_{PS}}{\rho_{PS}}} \tag{S2.3}$$

where φ_{CNC} and φ_{PS} are the densities of the CNC (1.5 g/ml) and polystyrene (1.05), respectively, and φ_{CNC} and φ_{PS} are the weight fractions of CNC and PS as determined by TGA of the measured sample. Thus the porosity (P) can be calculated to be by combining eqn S2 and S3 to result in

$$P = 1 - \left(\frac{\rho_{sample}}{\rho_{theo}}\right) \tag{S2.4}$$

which allows for a comparison of porosity between samples by simple measurements of the mass and dimensions. **Table S2.3** then shows the calculated porosities of both as cast and pressed samples at the extremes of molecular weight and polymer volume fraction. Interestingly, although the as cast samples differ greatly in porosity, the pressed samples display similar values within error between the vastly different molecular weights and polymer weight fractions.

Table S2.3: Porosity calculation of as cast and pressed ***MxG*-CNC-*g*-PS** samples. N=3

Sample	Porosity [a]
***MxG*-CNC-*g*-PS-5-45** as cast	0.43±0.03
***MxG*-CNC-*g*-PS-5-45** pressed	0.09±0.06
***MxG*-CNC-*g*-PS-60-90** as cast	0.07±0.02
***MxG*-CNC-*g*-PS-60-90** pressed	0.06±0.03

[a] from eqn S2.4

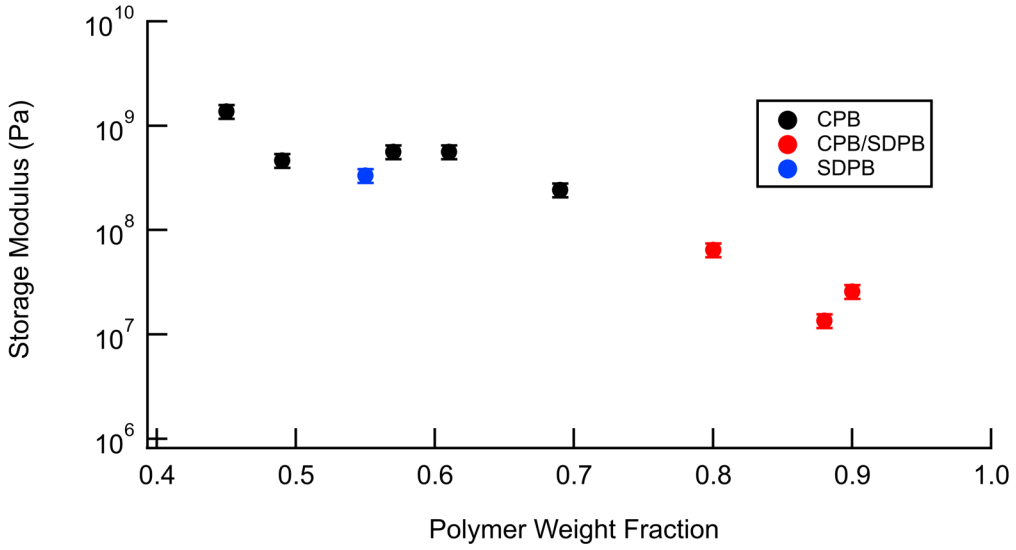

Figure S2.18: Analysis of the dynamic mechanical spectroscopy rubbery (Tg+20°C) modulus of ***MxG*-CNC-*g*-PS** samples versus weight fraction of polymer.

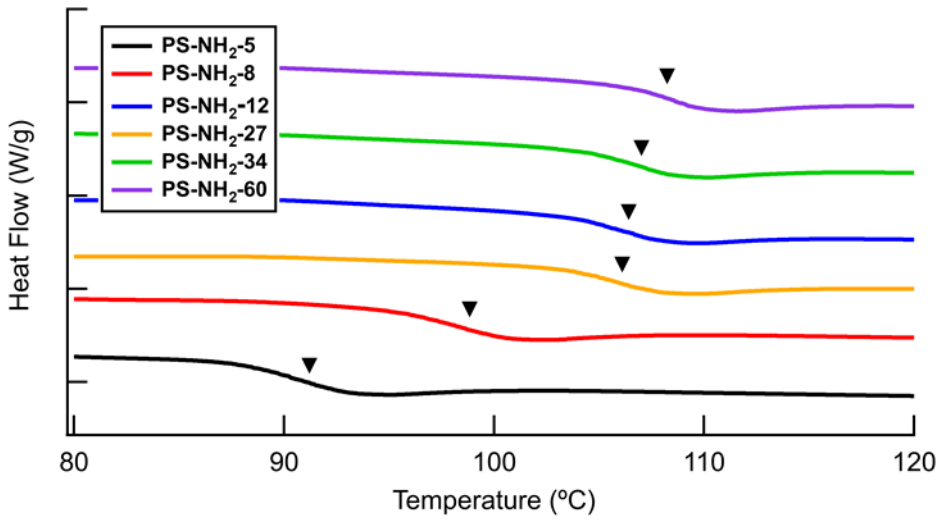

Figure S2.19: Differential Scanning Calorimetry (DSC) at a ramp rate of 10 °C per minute showing the second heating curve of the **PS-NH₂** samples, with arrows indicating the midpoint glass transition temperature.

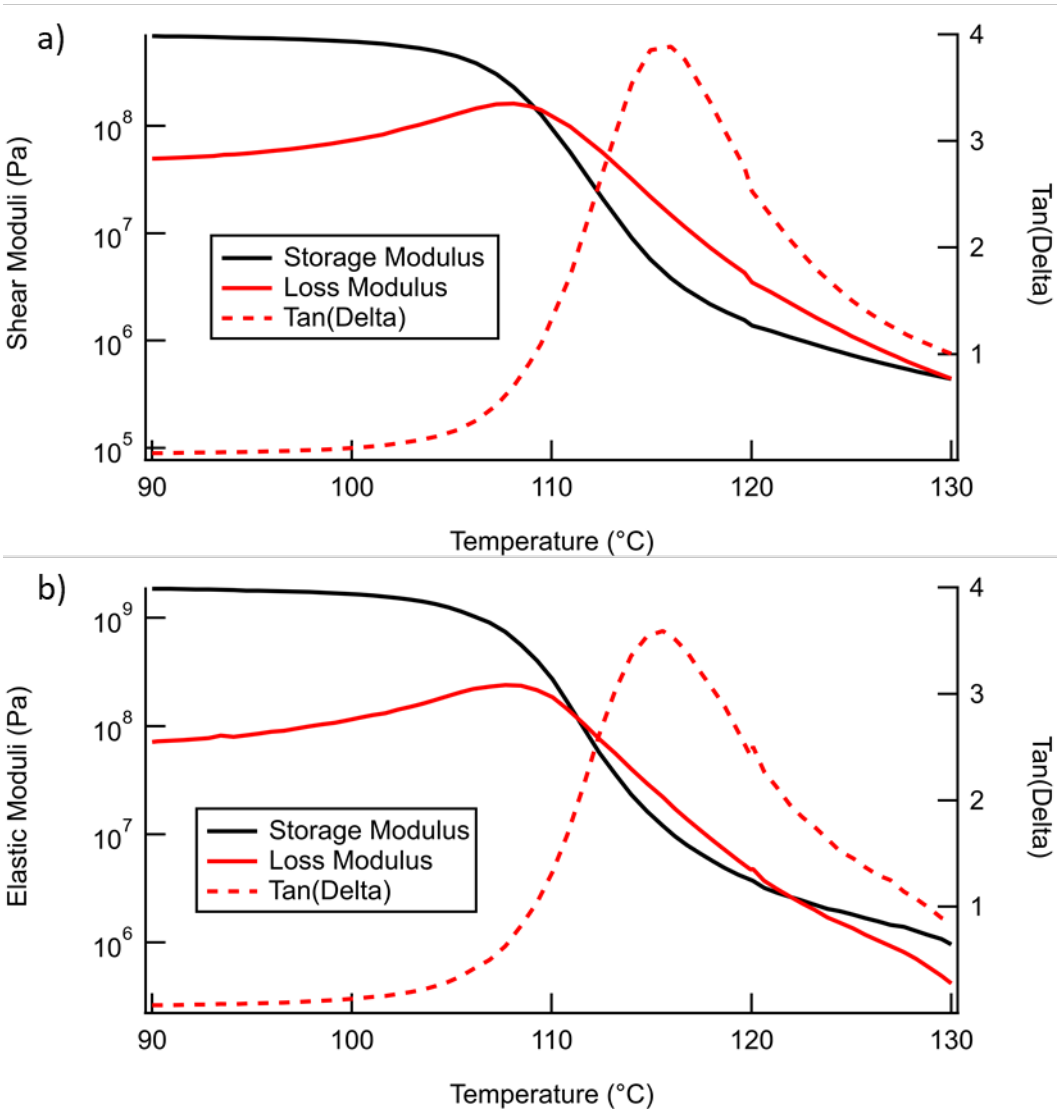

Figure S2.20: **PS-NH_2-60** in both tensile DMA and shear rheology displaying identical tan(delta) peaks, indicative of measuring the same T_g value.

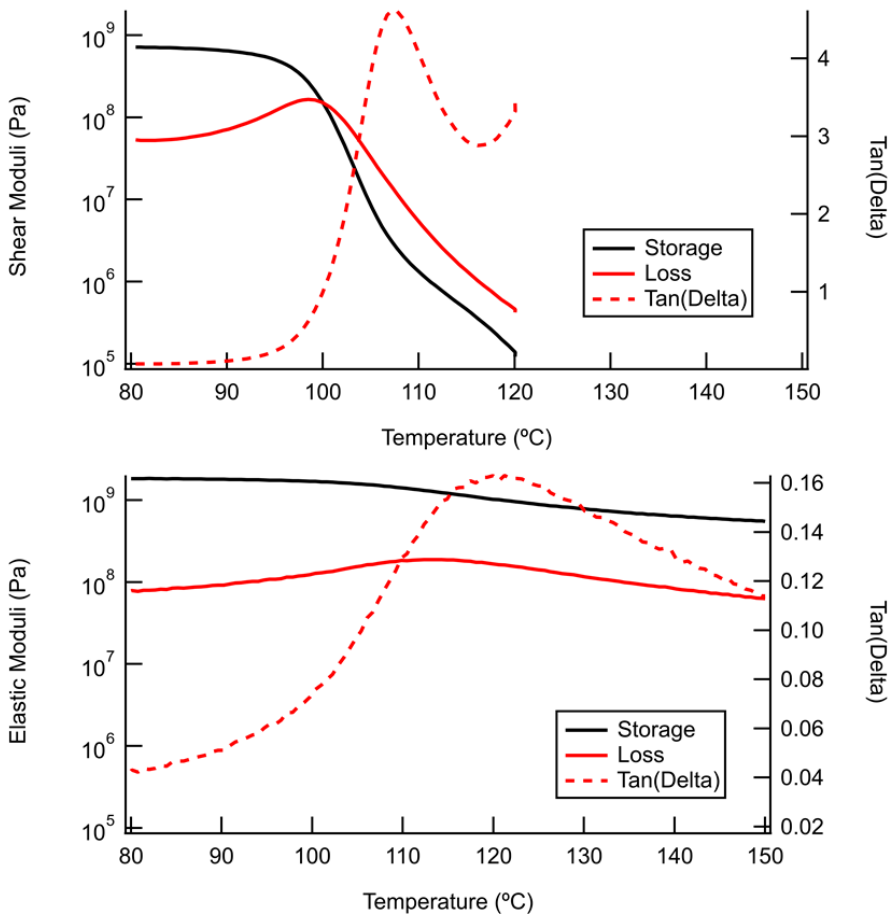

Figure S2.21: a) Example shear rheology of **PS-NH$_2$-8** homopolymer sample and DMA of ***MxG*-CNC-*g*-PS-8** sample which shows the clear shift in the Tan(Delta) peak.

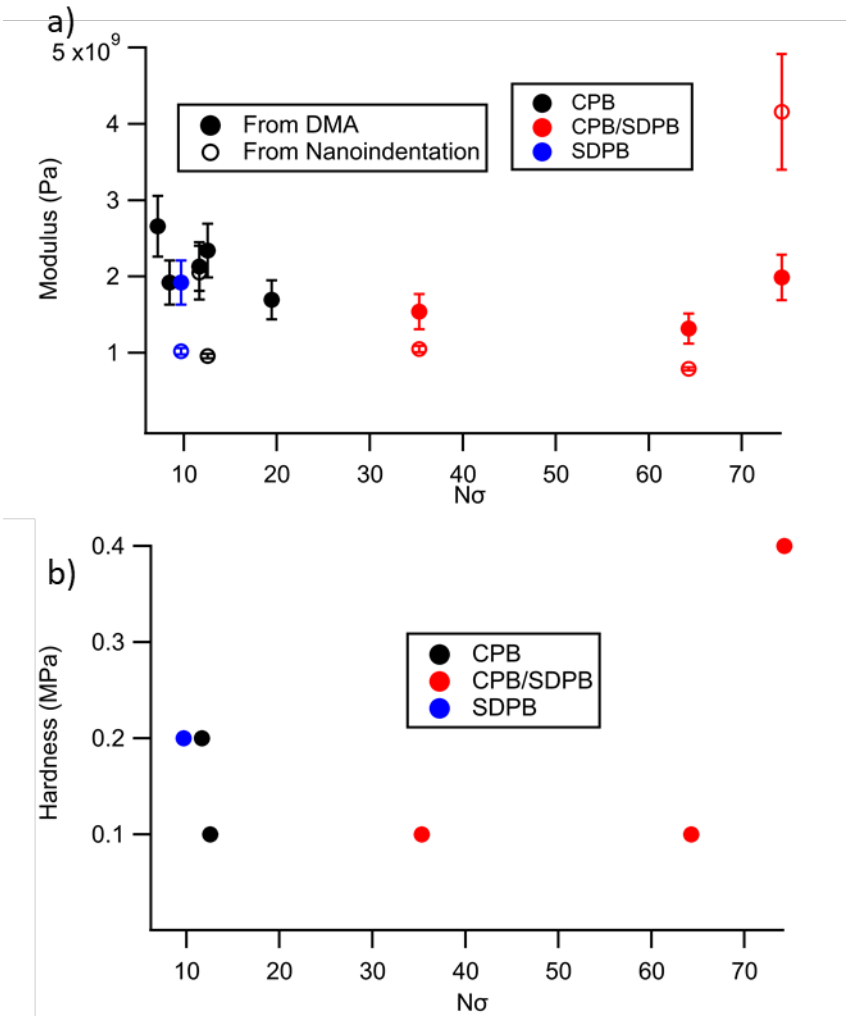

Figure S2.22 a) Glassy modulus data of ***MxG*-CNC-*g*-PS** samples from nanoindentation and DMA (N=3 for error) and b) Hardness data from nanoindentation fitting.

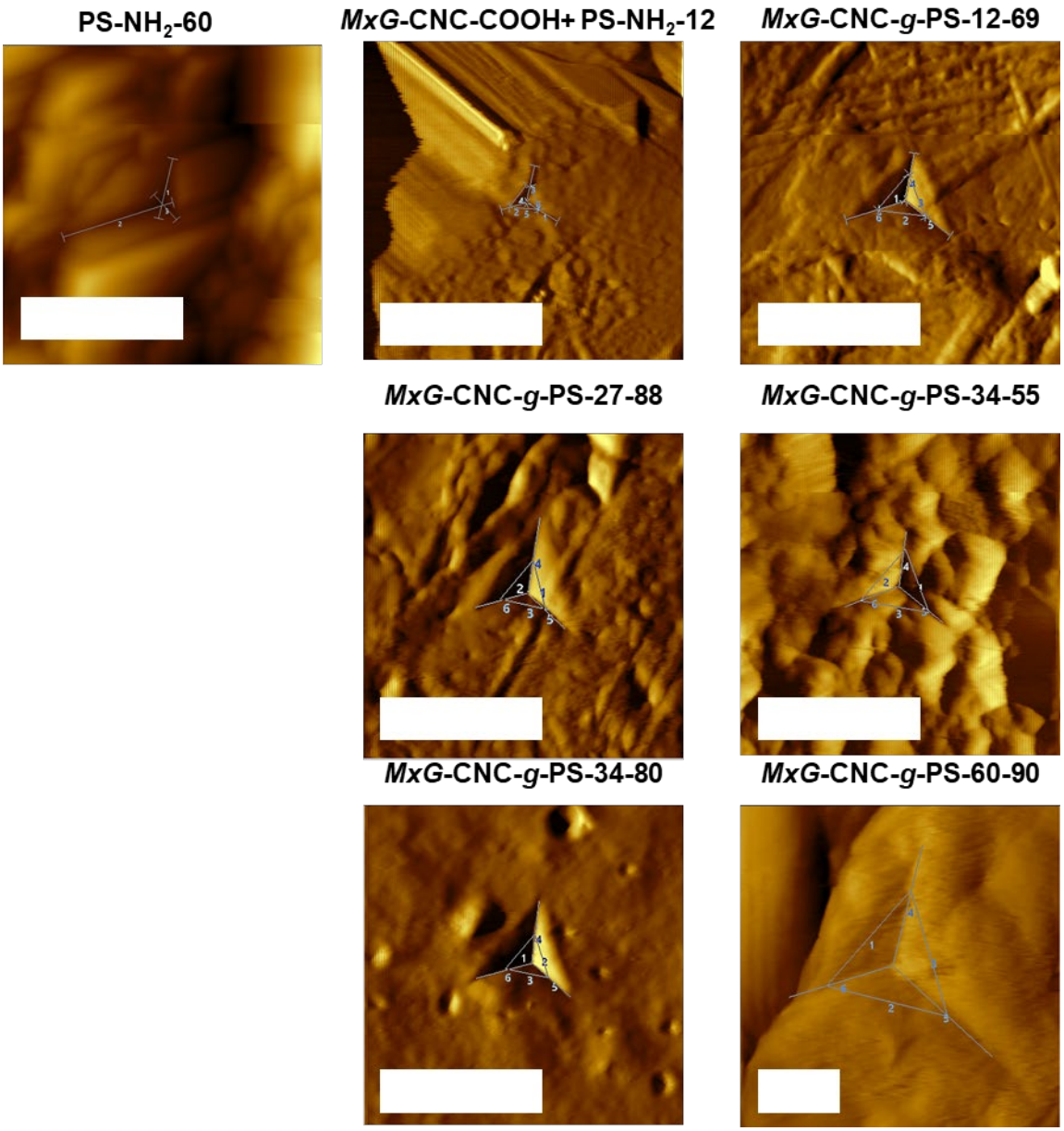

Figure S2.23: AFM of various ***MxG*-CNC-*g*-PS** samples post nanoindentation with labeled crack features. Scale bar is 2.5 μm.

2.7 REFERENCES

(1) Kumar, S. K.; Benicewicz, B. C.; Vaia, R. A.; Winey, K. I. 50th Anniversary Perspective: Are Polymer Nanocomposites Practical for Applications? *Macromolecules* **2017**, *50* (3), 714–731. https://doi.org/10.1021/acs.macromol.6b02330.

(2) Bet-Moushoul, E.; Mansourpanah, Y.; Farhadi, K.; Tabatabaei, M. TiO2 Nanocomposite Based Polymeric Membranes: A Review on Performance Improvement for Various Applications in Chemical Engineering Processes. *Chem. Eng. J.* **2016**, *283*, 29–46. https://doi.org/10.1016/j.cej.2015.06.124.

(3) Crosby, A. J.; Lee, J. Y. Polymer Nanocomposites: The "Nano" Effect on Mechanical Properties. *Polym. Rev.* **2007**, *47* (2), 217–229. https://doi.org/10.1080/15583720701271278.

(4) Cammarata, R. C. Mechanical Properties of Nanocomposite Thin Films. *Thin Solid Films* **1994**, *240*, 82–87. https://doi.org/10.1016/j.surfcoat.2008.06.131.

(5) Kumar, A.; Sharma, K.; Dixit, A. R. A Review of the Mechanical and Thermal Properties of Graphene and Its Hybrid Polymer Nanocomposites for Structural Applications. *J. Mater. Sci.* **2019**, *54* (8), 5992–6026. https://doi.org/10.1007/s10853-018-03244-3.

(6) Kim, D. J.; Jo, M. J.; Nam, S. Y. A Review of Polymer-Nanocomposite Electrolyte Membranes for Fuel Cell Application. *J. Ind. Eng. Chem.* **2015**, *21*, 36–52. https://doi.org/10.1016/j.jiec.2014.04.030.

(7) Gadim, T. D. O.; Vilela, C.; Loureiro, F. J. A.; Silvestre, A. J. D.; Freire, C. S. R.; Figueiredo, F. M. L. Nafion® and Nanocellulose: A Partnership for Greener Polymer Electrolyte Membranes. *Ind. Crops Prod.* **2016**, *93*, 212–218. https://doi.org/10.1016/j.indcrop.2016.01.028.

(8) Demirocak, D. E.; Srinivasan, S. S.; Stefanakos, E. K. A Review on Nanocomposite Materials for Rechargeable Li-Ion Batteries. *Appl. Sci.* **2017**, *7* (7), 1–26. https://doi.org/10.3390/app7070731.

(9) Ashraf, S.; Siddiqa, A.; Shahida, S.; Qaisar, S. Titanium-Based Nanocomposite Materials for Arsenic Removal from Water: A Review. *Heliyon* **2019**, *5* (5), e01577. https://doi.org/10.1016/j.heliyon.2019.e01577.

(10) Bassyouni, M.; Abdel-Aziz, M. H.; Zoromba, M. S.; Abdel-Hamid, S. M. S.; Drioli, E. A Review of Polymeric Nanocomposite Membranes for Water Purification. *J. Ind. Eng. Chem.* **2019**, *73*, 19–46. https://doi.org/10.1016/j.jiec.2019.01.045.

(11) Hore, M. J. A.; Korley, L. S. T. J.; Kumar, S. K. Polymer-Grafted Nanoparticles. *J. Appl. Phys.* **2020**, *128* (3). https://doi.org/10.1063/5.0019326.

(12) Fernandes, N. J.; Koerner, H.; Giannelis, E. P.; Vaia, R. A. Hairy Nanoparticle Assemblies

as One-Component Functional Polymer Nanocomposites: Opportunities and Challenges. *MRS Commun.* **2013**, *3* (1), 13–29. https://doi.org/10.1557/mrc.2013.9.

(13) Choi, J.; Hui, C. M.; Pietrasik, J.; Dong, H.; Matyjaszewski, K.; Bockstaller, M. R. Toughening Fragile Matter: Mechanical Properties of Particle Solids Assembled from Polymer-Grafted Hybrid Particles Synthesized by ATRP. *Soft Matter* **2012**, *8* (15), 4072. https://doi.org/10.1039/c2sm06915f.

(14) Schmitt, M.; Choi, J.; Min Hui, C.; Chen, B.; Korkmaz, E.; Yan, J.; Margel, S.; Burak Ozdoganlar, O.; Matyjaszewski, K.; Bockstaller, M. R. Processing Fragile Matter: Effect of Polymer Graft Modification on the Mechanical Properties and Processibility of (Nano-) Particulate Solids. *Soft Matter* **2016**, *12* (15), 3527–3537. https://doi.org/10.1039/C6SM00095A.

(15) Jiao, Y.; Tibbits, A.; Gillman, A.; Hsiao, M. S.; Buskohl, P.; Drummy, L. F.; Vaia, R. A. Deformation Behavior of Polystyrene-Grafted Nanoparticle Assemblies with Low Grafting Density. *Macromolecules* **2018**, *51* (18), 7257–7265. https://doi.org/10.1021/acs.macromol.8b01524.

(16) Midya, J.; Cang, Y.; Egorov, S. A.; Matyjaszewski, K.; Bockstaller, M. R.; Nikoubashman, A.; Fytas, G. Disentangling the Role of Chain Conformation on the Mechanics of Polymer Tethered Particle Materials. *Nano Lett.* **2019**, *19* (4), 2715–2722. https://doi.org/10.1021/acs.nanolett.9b00817.

(17) Dan, N.; Tirrell, M. Polymers Tethered to Curved Interfaces. A Self-Consistent-Field Analysis. *Macromolecules* **1992**, *25* (11), 2890–2895. https://doi.org/10.1021/ma00037a016.

(18) Halperin, A.; Tirrell, M.; Lodge, T. P. Tethered Chains in Polymer Microstructures. In *Macromolecules: Synthesis, Order and Advanced Properties*; pp 31–71. https://doi.org/10.1007/BFb0051635.

(19) Ohno, K.; Morinaga, T.; Koh, K.; Tsujii, Y.; Fukuda, T. Synthesis of Monodisperse Silica Particles Coated with Well-Defined, High-Density Polymer Brushes by Surface-Initiated Atom Transfer Radical Polymerization. *Macromolecules* **2005**, *38* (6), 2137–2142. https://doi.org/10.1021/ma048011q.

(20) Tai, Y.; Morinaga, T.; Ohno, K.; Tsujii, Y.; Fukuda, T. Fixation of Colloidal Crystals Formed by Monodisperse Silica Particles Grafted with Concentrated Polymer Brush. *Polym. Prepr. Japan* **2006**, *55* (2), 3420.

(21) Ohno, K.; Morinaga, T.; Takeno, S.; Tsujii, Y.; Fukuda, T. Suspensions of Silica Particles Grafted with Concentrated Polymer Brush: Effects of Graft Chain Length on Brush Layer Thickness and Colloidal Crystallization. *Macromolecules* **2007**, *40* (25), 9143–9150. https://doi.org/10.1021/ma071770z.

(22) Muhd Julkapli, N.; Bagheri, S. Nanocellulose as a Green and Sustainable Emerging

Material in Energy Applications: A Review. *Polym. Adv. Technol.* **2017**, *28* (12), 1583–1594. https://doi.org/10.1002/pat.4074.

(23) Eichhorn, S. J.; Dufresne, A.; Aranguren, M.; Marcovich, N. E.; Capadona, J. R.; Rowan, S. J.; Weder, C.; Thielemans, W.; Roman, M.; Renneckar, S.; Gindl, W.; Veigel, S.; Keckes, J.; Yano, H.; Abe, K.; Nogi, M.; Nakagaito, A. N.; Mangalam, A.; Simonsen, J.; Benight, A. S.; Bismarck, A.; Berglund, L. A.; Peijs, T. Review: Current International Research into Cellulose Nanofibres and Nanocomposites. *J. Mater. Sci.* **2010**, *45* (1), 1–33. https://doi.org/10.1007/s10853-009-3874-0.

(24) Mariano, M.; El Kissi, N.; Dufresne, A. Cellulose Nanocrystals and Related Nanocomposites: Review of Some Properties and Challenges. *J. Polym. Sci. Part B Polym. Phys.* **2014**, *52* (12), 791–806. https://doi.org/10.1002/polb.23490.

(25) Shojaeiarani, J.; Bajwa, D. S.; Chanda, S. Cellulose Nanocrystal Based Composites: A Review. *Compos. Part C Open Access* **2021**, *5* (May), 100164. https://doi.org/10.1016/j.jcomc.2021.100164.

(26) Calvino, C.; Macke, N.; Kato, R.; Rowan, S. J. Development, Processing and Applications of Bio-Sourced Cellulose Nanocrystal Composites. *Prog. Polym. Sci.* **2020**, *103*. https://doi.org/10.1016/j.progpolymsci.2020.101221.

(27) Habibi, Y.; Lucia, L. A.; Rojas, O. J. Cellulose Nanocrystals: Chemistry, Self-Assembly, and Applications. *Chem. Rev.* **2010**, *110* (6), 3479–3500. https://doi.org/10.1021/cr900339w.

(28) Dong, X. M.; Revol, J. F.; Gray, D. G. Effect of Microcrystallite Preparation Conditions on the Formation of Colloid Crystals of Cellulose. *Cellulose* **1998**, *5* (1), 19–32. https://doi.org/10.1023/A:1009260511939.

(29) Zhang, Y.; Edelbrock, A. N.; Rowan, S. J. Effect of Processing Conditions on the Mechanical Properties of Bio-Inspired Mechanical Gradient Nanocomposites. *Eur. Polym. J.* **2019**, *115* (March), 107–114. https://doi.org/10.1016/j.eurpolymj.2019.03.022.

(30) Cudjoe, E.; Hunsen, M.; Xue, Z.; Way, A. E.; Barrios, E.; Olson, R. A.; Hore, M. J. A.; Rowan, S. J. Miscanthus Giganteus: A Commercially Viable Sustainable Source of Cellulose Nanocrystals. *Carbohydr. Polym.* **2017**, *155*, 230–241. https://doi.org/10.1016/j.carbpol.2016.08.049.

(31) Weiss, A. M.; MacKe, N.; Zhang, Y.; Calvino, C.; Esser-Kahn, A. P.; Rowan, S. J. In Vitro and in Vivo Analyses of the Effects of Source, Length, and Charge on the Cytotoxicity and Immunocompatibility of Cellulose Nanocrystals. *ACS Biomater. Sci. Eng.* **2021**, *7* (4), 1450–1461. https://doi.org/10.1021/acsbiomaterials.0c01618.

(32) Cao, X.; Habibi, Y.; Lucia, L. A. One-Pot Polymerization, Surface Grafting, and Processing of Waterborne Polyurethane-Cellulose Nanocrystal Nanocomposites. *J. Mater. Chem.* **2009**, *19* (38), 7137. https://doi.org/10.1039/b910517d.

(33) Lin, N.; Dufresne, A. Physical and/or Chemical Compatibilization of Extruded Cellulose Nanocrystal Reinforced Polystyrene Nanocomposites. *Macromolecules* **2013**, *46* (14), 5570–5583. https://doi.org/10.1021/ma4010154.

(34) Habibi, Y.; Goffin, A.-L.; Schiltz, N.; Duquesne, E.; Dubois, P.; Dufresne, A. Bionanocomposites Based on Poly(ε-Caprolactone)-Grafted Cellulose Nanocrystals by Ring-Opening Polymerization. *J. Mater. Chem.* **2008**, *18* (41), 5002. https://doi.org/10.1039/b809212e.

(35) Wohlhauser, S.; Delepierre, G.; Labet, M.; Morandi, G.; Thielemans, W.; Weder, C.; Zoppe, J. O. Grafting Polymers from Cellulose Nanocrystals: Synthesis, Properties, and Applications. *Macromolecules* **2018**, *51* (16), 6157–6189. https://doi.org/10.1021/acs.macromol.8b00733.

(36) Morandi, G.; Heath, L.; Thielemans, W. Cellulose Nanocrystals Grafted with Polystyrene Chains through Surface-Initiated Atom Transfer Radical Polymerization (SI-ATRP). *Langmuir* **2009**, *25* (14), 8280–8286. https://doi.org/10.1021/la900452a.

(37) Wohlhauser, S.; Kuhnt, T.; Meesorn, W.; Montero De Espinosa, L.; Zoppe, J. O.; Weder, C. One-Component Nanocomposites Based on Polymer-Grafted Cellulose Nanocrystals. *Macromolecules* **2020**, *53*, 821–834. https://doi.org/10.1021/acs.macromol.9b01612.

(38) Kato, R.; Lettow, J. H.; Patel, S. N.; Rowan, S. J. Ion-Conducting Thermoresponsive Films Based on Polymer-Grafted Cellulose Nanocrystals. *ACS Appl. Mater. Interfaces* **2020**, *12*, 54083–54093. https://doi.org/10.1021/acsami.0c16059.

(39) Lettow, J. H.; Kaplan, R. Y.; Nealey, P. F.; Rowan, S. J. Enhanced Ion Conductivity through Hydrated, Polyelectrolyte-Grafted Cellulose Nanocrystal Films. *Macromolecules* **2021**, *54* (14), 6925–6936. https://doi.org/10.1021/acs.macromol.1c01155.

(40) Hansoge, N. K.; Huang, T.; Sinko, R.; Xia, W.; Chen, W.; Keten, S. Materials by Design for Stiff and Tough Hairy Nanoparticle Assemblies. *ACS Nano* **2018**, *12* (8), 7946–7958. https://doi.org/10.1021/acsnano.8b02454.

(41) Hansoge, N. K.; Keten, S. Effect of Polymer Chemistry on Chain Conformations in Hairy Nanoparticle Assemblies. *ACS Macro Lett.* **2019**, 1209–1215. https://doi.org/10.1021/acsmacrolett.9b00526.

(42) Postma, A.; Davis, T. P.; Evans, R. A.; Li, G.; Moad, G.; O'Shea, M. S. Synthesis of Well-Defined Polystyrene with Primary Amine End Groups through the Use of Phthalimido-Functional RAFT Agents. *Macromolecules* **2006**, *39* (16), 5293–5306. https://doi.org/10.1021/ma060245h.

(43) Raw, S. A. An Improved Process for the Synthesis of DMTMM-Based Coupling Reagents. *Tetrahedron Lett.* **2009**, *50* (8), 946–948. https://doi.org/10.1016/j.tetlet.2008.12.047.

(44) Pyun, J.; Kowalewski, T.; Matyjaszewski, K. Synthesis of Polymer Brushes Using Atom

Transfer Radical Polymerization. *Macromol. Rapid Commun.* **2003**, *24* (18), 1043–1059. https://doi.org/10.1002/marc.200300078.

(45) Fujisawa, S.; Ikeuchi, T.; Takeuchi, M.; Saito, T.; Isogai, A. Superior Reinforcement Effect of TEMPO-Oxidized Cellulose Nanofibrils in Polystyrene Matrix: Optical, Thermal, and Mechanical Studies. *Biomacromolecules* **2012**, *13* (7), 2188–2194. https://doi.org/10.1021/bm300609c.

(46) Mendez, J.; Annamalai, P. K.; Eichhorn, S. J.; Rusli, R.; Rowan, S. J.; Foster, E. J.; Weder, C. Bioinspired Mechanically Adaptive Polymer Nanocomposites with Water-Activated Shape-Memory Effect. *Macromolecules* **2011**, *44* (17), 6827–6835. https://doi.org/10.1021/ma201502k.

(47) Askar, S.; Li, L.; Torkelson, J. M. Polystyrene-Grafted Silica Nanoparticles: Investigating the Molecular Weight Dependence of Glass Transition and Fragility Behavior. *Macromolecules* **2017**, *50* (4), 1589–1598. https://doi.org/10.1021/acs.macromol.7b00079.

(48) Rittigstein, P.; Priestley, R. D.; Broadbelt, L. J.; Torkelson, J. M. Model Polymer Nanocomposites Provide an Understanding of Confinement Effects in Real Nanocomposites. *Nat. Mater.* **2007**, *6* (4), 278–282. https://doi.org/10.1038/nmat1870.

(49) Koerner, H.; Opsitnick, E.; Grabowski, C. A.; Drummy, L. F.; Hsiao, M. S.; Che, J.; Pike, M.; Person, V.; Bockstaller, M. R.; Meth, J. S.; Vaia, R. A. Physical Aging and Glass Transition of Hairy Nanoparticle Assemblies. *J. Polym. Sci. Part B Polym. Phys.* **2016**, *54* (2), 319–330. https://doi.org/10.1002/polb.23931.

(50) Dang, A.; Hui, C. M.; Ferebee, R.; Kubiak, J.; Li, T.; Matyjaszewski, K.; Bockstaller, M. R. Thermal Properties of Particle Brush Materials: Effect of Polymer Graft Architecture on the Glass Transition Temperature in Polymer-Grafted Colloidal Systems. *Macromol. Symp.* **2013**, *331–332* (1), 9–16. https://doi.org/10.1002/masy.201300062.

(51) Sunday, D. F.; Green, D. L. Thermal and Rheological Behavior of Polymer Grafted Nanoparticles. *Macromolecules* **2015**, *48* (23), 8651–8659. https://doi.org/10.1021/acs.macromol.5b00987.

(52) Sakib, N.; Koh, Y. P.; Huang, Y.; Mongcopa, K. I. S.; Le, A. N.; Benicewicz, B. C.; Krishnamoorti, R.; Simon, S. L. Thermal and Rheological Analysis of Polystyrene-Grafted Silica Nanocomposites. *ACS Appl. Mater. Interfaces* **2020**. https://doi.org/10.1021/acs.macromol.9b02127.

(53) Fischer-Cripps, A. C. *Nanoindentation*, 3rd ed.; Springer, 2011. https://doi.org/10.1007/978-1-4757-5943-3_4.

Chapter 3

Enhanced Ion Conductivity through Hydrated, Polyelectrolyte-grafted Cellulose Nanocrystal Films

3.1 ABSTRACT

Ionically conductive, hydrated polyelectrolyte nanocomposites are prepared from iodomethane treated poly(2-vinylpyridine) (**mPV**)-grafted cellulose nanocrystals (***MxG*-CNC-*g*-mPV**). These polyelectrolyte-grafted nanoparticle (PEGN) films exhibit an order of magnitude higher iodide ion conductivity relative to **mPV** films and a high in-plane/through-plane anisotropy. The PEGN architecture prevents CNC aggregation maximizing the CNC/polyelectrolyte interface. PEGN films were prepared with varying polymer graft density (0.03-0.12 chains/nm^2) and molecular weight (7k-30k g/mol). The greatest ion conductivity enhancement is observed with lower molecular weight, higher density grafts: ca. 89±6 mS/cm (140±10 mS/cm accounting for the volume of the CNC) versus 3.3±0.4 mS/cm for ungrafted **mPV**. Poly(styrene-*block*-2-vinylpyridine)-grafted CNCs were prepared in which the insulating polystyrene-block or the conducting **mPV**-block was directly attached to the CNCs; only the films with the **mPV**-block closest to the CNCs exhibited an enhancement in conductivity relative to **mPV**. Together, these data point to beneficial CNC/polyelectrolyte interfacial effects resulting in significant ionic conductivity enhancement along the length of the CNCs in these films.

3.2 INTRODUCTION

Ion-conducting polyelectrolyte materials are being investigated and utilized in a wide range of technologies, from lithium ion[1] and redox-flow batteries[2] to fuel cells.[3] While high ion conductivity is integral to the performance of these materials, challenges remain in accessing high ion conductivity while maintaining mechanical integrity. One possible route to overcome these challenges are ionically conductive nanocomposites, which have the potential of simultaneously maximizing both membrane mechanical integrity and ionic conductivity.[4–8] Some inorganic nanofillers (e.g. SiO_2,[9] Al_2O_3,[10] Li_3N,[11] $Li_{1.3}Al_{0.3}Ti_{1.7}(PO_4)_3$,[12] $Li_{0.33}La_{0.557}TiO_3$[13]) have been shown to impart an increase in ionic conductivity when there are beneficial effects, such as Lewis acid-base interactions and/or disruption of matrix crystallization, at the matrix/filler interface. Even so, high loadings of nanofiller are intrinsically capped by phase separation and aggregation of the nanofiller which results in both a reduction in ionic conductivity and mechanical reinforcement.

One route to reduce aggregation of nanoparticles and aid processing is to graft polymers from/to the nanoparticle surface. Judicious choice of the grafted polymer results in compatibilization of the polymer-grafted nanoparticles (PGNs)[14] with the matrix yielding more homogenous composites. As such, the literature is replete with examples of PGNs that when embedded in the appropriate matrix, exhibit enhanced mechanical properties.[15–23] Films that consist solely of the PGNs result in what has been termed one-component nanocomposites (OCNs).[24] OCNs eliminate phase segregation of the matrix and nanofiller allowing access to homogenously dispersed composite films with nanoparticle loading levels that are hard to attain with more conventional mixed (two component) systems. As a result OCN films can exhibit a

higher modulus and toughness relative to their two-component nanocomposite derivatives.[25–27] Studies into this class of material, mainly focused on the mechanical properties of PGNs based on spherical nanoparticles, have shown that the density and molecular weight of the grafted polymer are key parameters in their structure/property relationship. As a general guide, to optimize toughness in these systems the grafted polymer should ideally be beyond its entanglement molecular weight and the polymer grafting density should be such to induce a semidilute polymer brush regime, although in order to maximize both modulus and toughness high loadings of nanofiller must be balanced.[27–29] As the ionic conductivity of polyelectrolytes are also impacted by polymer conformation and interchain interactions,[30–32] the grafting density and radius of gyration ought to impact the ionic conductivity properties of the OCNs.

Polyelectrolyte grafted nanoparticles (PEGNs) have been used as fillers/additives in a variety of applications, such as conductive membranes,[33] water harvesting,[34] emulsion stabilization,[35] and catalytic activity enhancement.[36] There are much fewer examples of PEGN only films that have been reported in the literature (note: technically most of these reported films are not just the PEGN as they are usually imbibed with water or an ionic liquid to enable ion conduction). Most reports in the literature on nanosphere-based PEGNs show reduced conductivities relative to the corresponding polyelectrolytes.[37,38] However, there are examples where an enhancement in ion conductivity is observed. For example, it has been reported that hydrated poly((*p*-vinyl-benzyl) trimethylammonium tetrafluoroborate) grafted to 16 nm silica nanoparticles showed enhanced conductivity relative to the hydrated polymer alone.[39] In those studies it was shown that the molecular weight of the grafted polymer appears to have an effect on conductivity with an increase in ionic conductivity up to around 12 kg/mol (based on molecular

weight determination using a sacrificial initiator in the grafting-from process) before decreasing again at higher molecular weight grafts. The increased ion conductivity was ascribed to the formation of a highly conductive layer at the polymer/silica interface.

Cellulose nanocrystals (CNCs)[18,19,40–45] are organic, biobased, and highly crystalline nanorods with easily accessible surface chemistries, which have been incorporated into polyelectrolyte membranes in order to enhance their mechanical properties.[46–48] While most studies reported materials with reduced ionic conductivity,[46,49,50] a few CNC-based nanocomposites have shown increased ionic conductivity in which beneficial interfacial effects have been suggested.[48,51] For example, Cheng *et al*. synthesized CNCs with quaternary ammonium groups functionalized on the surface and incorporated them into a poly(phenylene oxide) matrix functionalized with similar quaternary ammonium groups.[48] When immersed in water the resulting materials showed a 60% higher ionic conductivity than the homopolymer (60 vs 38 mS/cm) at 80 °C peaking at a 2 wt.% CNC loading. In addition, the fuel cell performance confirmed a higher peak power density using this anion exchange membrane. Similarly, Rincón-Iglesias *et al*. prepared nanocomposites of CNCs in ι-carrageenan, a marine sulfated polysaccharide isolated from red algae (*Rhodophyta*), and measured the mechanical properties and dielectric response of the bio-sourced nanocomposite membrane at ambient conditions.[51] The ionic conductivity of the composite material peaked at 10 wt.% CNCs with roughly a 3-fold improvement in conductivity. However, in both of the two-component (CNC filler and polymer matrix) composites discussed above the conductivity enhancement was limited at higher CNC content, which was explained by aggregation and phase separation of the CNCs leading to a drop in both ion conduction and mechanical properties.

Recent experimental and computational work on CNC-based PGN films has begun probing the mechanical property enhancement of these systems. Weder and coworkers reported the first examples of CNC-based OCNs and have shown that this class of materials also exhibit mechanical property enhancement (toughness and modulus) consistent with previous OCN films based on spherical nanofillers.[52] OCNs consisting of poly(methyl methacrylate) grafted from CNCs show remarkable toughening with OCNs that contain as much as 20 wt% CNC while maintaining similar levels of elastic modulus as compared to the corresponding two-component nanocomposites.[52] In the same work, poly(hexyl methacrylate) grafted CNC-based OCNs show higher modulus but similar toughness relative to their two-component nanocomposites counterparts. Computational work by Keten and coworkers on CNC-containing OCNs indicate that to optimize both modulus and toughness the grafted polymers should ideally be in the semidilute polymer brush regime (which can be achieved by tuning grafting density and degree of polymerization) and have a CNC wt% of ca. 60 %.[28,29] More recently, the mechanical properties and ion conductivity of films of PGNs composed of uncharged poly(2-phenylethyl methacrylate) grafted to CNCs imbibed with ionic liquid (IL) have been reported.[53] These IL-imbibed OCN films (30 wt% IL) exhibited a 70-fold increase in tensile strength and higher ionic conductivity relative to the ionic liquid imbibed homopolymer or the ionic liquid containing multi-component composite prepared from the unfunctionalized CNC embedded in a poly(2-phenylethyl methacrylate) matrix. This later study also showed that the IL-imbibed CNC-based PGNs exhibit a slight enhancement in conductivity relative to the IL-imbibed polymer, suggesting that the CNCs maybe playing a beneficial role on the ion conductivity in these films. However, to the best of our knowledge there are no studies on the ion conductivity of films formed from polyelectrolyte-grafted CNCs and the impact that the polymer graft molecular weight and density has on their ionic conductivity. Furthermore, given

the anisotropic nature of CNC nanorods it is possible that films of these PEGNs could exhibit anisotropic electronic properties.

Reported herein are studies aimed at synthesizing and studying polyelectrolyte CNC-based PGNs with the specific goal of understanding how the nature of the polyelectrolyte graft (molecular weight and grafting density) as well as volume fraction of CNC has on the iodide ion conductivity of this class of material. The targeted PEGNs are comprised of CNCs grafted with methylated poly(2-vinylpyridine) (**mPV**), formed by reaction of the poly(2-vinylpyridine)-grafted CNC with iodomethane. **mPV** was selected as the polyelectrolyte graft as it has previously been studied in confined block copolymer systems and as a polymer brush on flat surfaces, making it a useful model material on account of its relatively facile synthesis and well investigated (iodide) ion conductivity behavior.[30,54–56]

3.3 EXPERIMENTAL METHODS

3.3.1 Instrumentation

Nuclear Magnetic Resonance Spectroscopy. The ^{1}H NMR spectra were recorded on a Bruker Ascend Advance II+ 500 MHz spectrometer at 25 °C using $CDCl_3$ as solvent. All NMR spectra were processed by MestReNova software.

Electrospray Mass Spectroscopy. Electrospray mass spectroscopy (ESI-MS) experiments were conducted using an Agilent 6135 quadrupole LC/MS system equipped with a 50 x 4.6 mm Poroshell 120 EC-C18 column (Agilent). A gradient elution of 10-100% acetonitrile in H_2O (+0.1% TFA) was conducted over 10 min and then held at 100% acetonitrile for 2.5 min, and absorbance was measured at 220 nm.

Gel Permeation Chromatography- Multi-angle Light Scattering and UV-VIS Spectrometry. Polymer molecular weights and dispersities as well as UV-VIS spectra were determined by gel permeation chromatography-multi-angle light scattering (GPC-MALS) with in-line UV-VIS spectrometry, measured on a Shimadzu Prominence LC system with PL gel Mixed-D columns with Wyatt Dawn Heleos MALS (658 nm laser), Wyatt Optilab T-rEX refractive index (RI) detectors, and Shimadzu SPD-M30A Photodiode Array detector (200-800 nm). HPLC grade tetrahydrofuran (THF) as the eluent (1mL/min) at 25 °C. The data were processed by Wyatt Astra software.

Conductometric titration. The content of carboxylic acid groups on CNCs was determined by conductometric titrations using a Accumet XL benchtop pH/conductivity meter (Fisher Scientific). Typically, 25 mg of CNC was dispersed in 80 mL DI water by sonication, and pH was adjusted

around 3 by adding 15 μL of HCl (33 wt%). Then 0.01 M NaOH was added slowly till pH around about 11. The conductivity was plotted against the volume of consumed NaOH.

Wide Angle X-ray Scattering (WAXS). The degree of crystallinity was determined by Synchrotron WAXS experiments were performed at the DND-CAT 5-ID-D beamline of the Advanced Photon S3 Source (Argonne National Laboratory, Argonne, IL) using a triple detector system for simultaneous data collection SAXS and WAXS regimes. Two-dimensional (2D) data were collected on Rayonix CCD area detectors using an exposure time of ca. 0.1 s. Gaussian deconvolution and crystallinity index analysis followed literature precedent.[57]

Atomic force microscopy (AFM). The dimensions of CNCs and ***MxG*-CNC-*g*-PV** samples were investigated by Asylum Research Oxford Instruments Cypher ES AFM. A drop of CNCs suspension (0.01 wt%) was placed on a freshly cleaved mica surface which was pretreated with poly-l-lysine solution, and then rinsed off after five minutes. The images were acquired using AC Tapping mode. The sizes of nanoparticles were analyzed by Gwyddion software.

Scanning electron microscope (SEM). SEM images of the cast films were taken with the Carl Zeiss−Merlin field emission scanning electron microscope. The acceleration voltage was 1.0 kV with a working distance of 2 to 3 mm using an in-lens detector. Two nanometers of Pt/Pd was sputtered onto the surface of the device using the Cressington 108 Auto Sputter Coater to reduce electron beam charging and improve the image quality.

Fourier transform infrared spectroscopy (FTIR). FTIR spectra were collected on a Shimadzu FTIR instrument. Solid samples were placed directly on the ATR crystal, and then the spectra were averaged from 46 scans from 550 to 4000 cm^{-1} with a resolution of 4 cm^{-1}.

Thermal gravimetric analysis (TGA). TGA experiments were carried out on a thermogravimetric analyzer (TA Instrument Discovery). Samples were heated from 30 to 650 °C under nitrogen atmosphere with a heating rate of 10 °C/min.

X-ray Photoelectron Spectroscopy (XPS). XPS spectra were acquired on a Kratos Axis 165 with an aluminum filament operated at 12 kV and 10 mA.

Electrochemical Impedance Spectroscopy. The electrochemical properties of the samples were probed using the Gamry reference 600 potentiostat/galvanostat. AC electrical impedance spectroscopy (EIS) measurements were made from 1 MHz to 1 Hz by connecting the samples via either larger Pt/ Pd 20 nm deposited pads with the Cressington 108 Auto Sputter Coater or between sheets of Pt foil to the potentiostat/ galvanostat. An amplitude voltage of 10 mV was used. For in-plane samples, electrode distance was 1 cm while surface area probed was 0.5 cm width by the measured PEGN film thickness between 20-70 μm. For through-plane samples electrode distance was the PEGN film thickness while the surface area probed was 0.13 cm^2. The measurements were made in a chamber with controlled temperature (25 °C) and relative humidity (65-95% RH) after an equilibration period of 2 hrs. Interdigitated electrodes were fabricated and utilized for EIS following literature procedures.[55,58]

Water Uptake. Water uptake experiments were conducted by placing the sample in a chamber with controlled temperature (25 °C) and relative humidity (65-95% RH) for 2 hours followed by rapidly ramping to 100 °C at 20 °C/min and held for 15 minutes on the TGA instrument.

3.3.2 Material Synthesis

Materials. *Miscanthus x. Giganteus* (*MxG*) in the form of ground stalks were donated by Aloterra Energy LLC, Conneaut, Ohio. 2-Vinylpyridine and styrene were purchased from Sigma-Aldrich and passed through a basic alumina column immediately prior to usage. Hydrochloric acid (HCl), and sodium hydroxide (NaOH) were purchased from Fisher Scientific. All other reagents were purchased from Sigma-Aldrich and used as received.

Synthesis of α-phthalimidomethyl-ω-thiolpoly(2-vinylpyridine) by RAFT. Phthalimidomethyl hexyl trithiocarbonate was synthesized for use as a chain transfer agent (CTA) following literature procedures (**Scheme S3.1** and **Figures S3.1-3.2**).[59] ^{1}H NMR (500 MHz in $CDCl_3$; δ ppm: 0.88 (tr, 3H, C**H**$_3$-), 1.29 (m, 4H, $CH_3C\mathbf{H}_2C\mathbf{H}_2CH_2CH_2CH_2$-), 1.39 (m, 2H, $CH_3CH_2CH_2C\mathbf{H}_2CH_2CH_2$-), 1.69 (m, 2H, $CH_3CH_2CH_2CH_2C\mathbf{H}_2CH_2$-), 3.36 (tr, 2H, -C**H**$_2$- S), 5.66 (s, 2H, N-C**H**$_2$-S), 7.74 (m, 2H, Ar**H**), 7.87(m, 2H, Ar**H**), ^{13}C NMR (101 MHz in $CDCl_3$; δ ppm: 14.0 (**C**H_3-), 22.5 ($CH_3\mathbf{C}H_2CH_2CH_2CH_2CH_2$-), 27.8 ($CH_3CH_2\mathbf{C}H_2CH_2CH_2CH_2CH_2$-), 28.6 ($CH_3CH_2CH_2\mathbf{C}H_2CH_2CH_2CH_2$-), 31.2 ($CH_3CH_2CH_2CH_2\mathbf{C}H_2CH_2CH_2$-) , 37.3 (-**C**$H_2$- S), 42.0 (N-**C**$H_2$-S), 123.7 (2 × o-Ph, **C**H), 131.8 (2 × Ph, **C**), 134.8 (2 × p-Ph, **C**H), 166.7 (**C**=O), 220.8 (**C**S_3)) and ESI-MS (353, measured 376, $[M]+Na^+$). Yield by mass = 50%.

Phthalimidomethyl hexyl trithiocarbonate (0.12 g), Azobisisobutyronitrile (AIBN) (0.006 g), and 2-vinylpyridine (16.6 g). were transferred to a 150 mL flask, underwent three freeze-pump-thaw cycles, and then heated at 60 °C for 24 h, followed by rapid quenching to room temperature. The mixture was diluted with THF (∼5 mL) and the polymer was precipitated into hexanes (100 mL), collected by filtration and dried in a vacuum oven at 40 °C for 24 h forming α-phthalimidomethyl-ω-hexyltrithiocarbonatepoly(2-vinylpyridine) (**PV$_x$**, where x denotes the degree of polymerization

as determined by GPC-MALS). Aminolysis of trithiocarbonate end groups followed previous literature precedent.[60] For example, **PV$_{286}$** (3 g, 0.0001 mol) was dissolved in 2 mls of THF. 2-Ethyl-1-hexyl amine (0.155 g, 0.0012 mol) and tributylphospine (0.061 g, 0.0003 mol) were added to the polymer solution. The mixture was sparged and reacted at RT for 72 hrs. Four different molecular weights of α-phthalimidomethyl-ω-thiolpoly(2-vinylpyridine) (**PV-SH$_x$**, where x denotes the degree of polymerization as determined by GPC-MALS) were prepared with molecular weights determined by ^{1}H NMR (**Figures S3.3-3.4**) and GPC-MALS (**Figures S3.5-3.6**), and dispersity (*Đ*) by GPC-MALS as shown in **Table S3.1**. UV-Vis was used to confirm the aminolysis of the trithiocarbonate end groups (**Figure S3.7**).

Diblock Copolymer (PS-PV) Synthesis. To synthesize α-phthalimidomethyl-ω-hexyltrithiocarbonatepoly(styrene)-*block*-poly(2-vinylpyridine), α-phthalimidomethyl-ω-hexyltrithiocarbonatepoly(styrene) macro-CTA was synthesized following similar protocol to **PV** except for using methanol as the precipitating solvent. Then α-phthalimidomethyl-ω-hexyltrithiocarbonatepoly(styrene) (3 g), AIBN (0.003 g), and 2-vinylpyridine (1.51 g). were transferred to a 100 mL flask and 3ml of THF was added. The mixture underwent three freeze-pump-thaw cycles, and then heated at 60 °C for 24 h, followed by rapid quenching to room temperature. The mixture was diluted with THF (~5 mL) and the polymer was precipitated into hexanes (100 mL), collected by filtration and dried in a vacuum oven at 40 °C for 24 h. The reduction to α-phthalimidomethyl-ω-thiolpoly(styrene)-*block*-poly(2-vinylpyridine) (**PS-PV-SH$_{x,y}$**, where x and y denote the degree of polymerization as determined by GPC-MALS of the respective blocks) followed identical protocol to PV. For the reverse diblock composition, α-phthalimidomethyl-ω-thiolpoly(2-vinylpyridine)-*block*-poly(styrene) (**PV-PS-SH$_{x,y}$**), similar processes were used beginning with a PV macro-CTA. For **PS-PV-SH$_{329,86}$**, $M_{n,GPC\text{-}MALS}$ = 43.2

kg/mol, $Đ$ = 1.13, and $M_{n,NMR}$ = 42.6 kg/mol, and f_{PV} = 0.21 (weight fraction PV) and for **PV-PS-SH$_{286,150}$,** $M_{n,GPC\text{-}MALS}$ = 45.6 kg/mol, $Đ$ = 1.17, and $M_{n,NMR}$ = 44.1 kg/mol, and f_{PV} = 0.65, as shown in **Table S3.2.**

Preparation of *MxG*-CNCs. *MxG*-CNCs were isolated from *Miscanthus x. Giganteus* stalks by hydrochloric acid hydrolysis, and then were further oxidized to obtain ***MxG*-CNC-COOH** by TEMPO oxidation according to previously published methods.[45] Allyl functionalized CNCs (***MxG*-CNC-Allyl)** were produced according to previously published methods.[61] Conductivity titration was performed before and after allyl functionalization to determine surface charge density and functionalization quantity, with ***MxG*-CNC-COOH** having surface charge density of 1000 mmol/kg while ***MxG*-CNC-Allyl** had surface charge density of 400 mmol/kg, resulting in allyl density of 600 mmol/kg.

Preparation of CNCs/THF suspension by solvent exchange. ***MxG*-CNC-Allyl** were first dispersed in 40 mL water with a concentration of 2.5 wt% by ultrasonication and 1 ml of saturated NaCl was added. The gel was collected by centrifugation (5 min, 8000 rpm), and the supernatant was poured off and collected. The remaining gel was resoaked in 40 mL of methanol for 2 h with constantly shaking, then separated by centrifugation. The same procedure was repeated two times with methanol and then two times with THF. The concentration of ***MxG*-CNC-Allyl** suspension was determined by thermal gravimetric analysis.

Grafting PV-SH onto MxG-CNC-Allyl. All reactions were done at a 1:1:0.1 equivalency of thiol to allyl functional group to AIBN. Most reactions were run in methanol, while diblock reactions were run in THF. To the solvent-exchanged and ultrasonicated ***MxG*-CNC-Allyl** samples were added the thiol functionalized polymer and AIBN in a 100ml RBF, retaining a concentration of 2.5 wt% CNC. The reaction was capped, sparged, and reacted for 24hrs at 60 ºC.

Fabrication and methylation of *MxG*-CNC-*g*-PV and standard nanocomposite films. ***MxG*-CNC-*g*-PV** were dissolved in THF and sonicated in a Branson CPX sonication bath before being cast into Teflon dishes. Solvent was allowed to evaporate at RT for 2 days. Comparative two component nanocomposites were prepared in an identical way using solvent exchanged ***MxG*-CNC-Allyl** with **PV_{68}** in THF and allowed to evaporate at RT for 2 days. ***MxG*-CNC-*g*-PV** PGN films were sealed in 150 ml jars with 2 ml iodomethane for 7 days. All films were approximately 2 cm in length, 0.5 cm in width, and 20-70 μm in thickness.

3.4 RESULTS AND DISCUSSION

In order to access the targeted PEGNs the first step was to synthesize poly(2-vinylpyridine) grafted CNCs. This was achieved using thiol-ene chemistry to graft a thiol-end capped poly(2-vinylpyridine) (**PV-SH**) to allyl-functionalized CNCs. **PV-SH** was prepared using RAFT polymerization of 2-vinylpyridine with phthalimidomethyl hexyl trithiocarbonate[59] as the chain transfer agent (CTA), followed by aminolysis of the trithiocarbonate endgroup with 2-ethylhexyl amine (**Scheme 3.1**).[62] A series of different molecular weight **PV-SH** (7100, 11900, 15800, and 30000 g/mol, dispersity, $Đ$ ca. 1.2)) was prepared in order to span the entanglement molecular weight of PV (ca. 10000 g/mol).[63] The polymers were characterized by nuclear magnetic resonance spectroscopy (^{1}H NMR), gel permeation chromatography multi-angle light scattering (GPC-MALS) and UV-Vis spectroscopy (**Figures S3.3-3.7, Table S3.1)**.

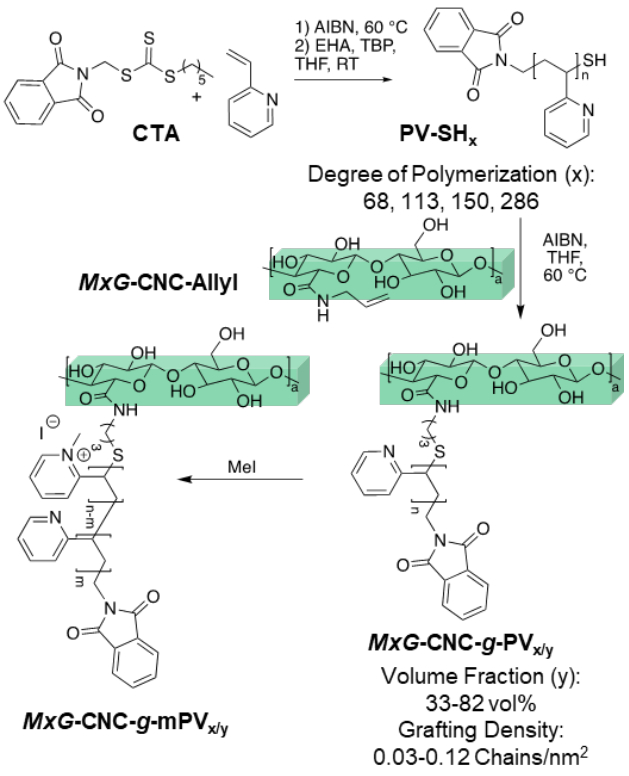

Scheme 3.1. Synthesis of polyelectrolyte-grafted CNCs (***MxG*-CNC-*g*-mPV$_{x/y}$**), where x refers to the degree of polymerization and y refers to the volume fraction of the grafted polymer. The thiol-end capped poly(2-vinylpyridine) (**PV-SH$_x$**), prepared via RAFT polymerization, was grafted to allyl-functionalized CNCs (***MxG*-CNC-Allyl**) via thiol-ene chemistry before being methylated with iodomethane to yield the ***MxG*-CNC-*g*-mPV$_{x/y}$** films.

Coupling of the **PV-SH$_x$** to the CNCs via thiol-ene chemistry requires the functionalization of the CNCs with alkene moieties. Carboxylic acid CNCs (***MxG*-CNC-COOH**) were obtained from *Miscanthus x. Giganteus* (via hydrochloric acid hydrolysis followed by TEMPO-mediated oxidation) using literature procedures.[45] TGA of the CNCs before and after TEMPO-mediated oxidation shows a slight reduction in thermal stability, with an onset of degradation at 350 °C and 210 °C, respectively (**Figure S3.8**). The resulting ***MxG*-CNC-COOHs** have a carboxylic acid density of ca. 1000 mmol/kg, as determined via conductometric titration, and a crystallinity index

of 85%, determined by wide angle x-ray scattering (WAXS) (**Figure S3.9**). The alkene moiety (allylamine) was reacted with ***MxG*-CNC-COOH** using peptide coupling conditions.[45,61] After functionalization, the ***MxG*-CNC-Allyl**'s have a residual surface charge of 400 mmol/kg, indicating ca. 60% functionalization of the carboxylic acids. It is worthwhile noting that these reaction conditions did not significantly alter the size and dimensions of the isolated CNCs during functionalization (from AFM, height = 2.2±0.5 and 2.1±0.7 nm, length = 290±60 nm and 280±50 nm for ***MxG*-CNC-COOH** and ***MxG*-CNC-Allyl**, respectively (n=20), **Figures S3.10, S3.11**). The ***MxG*-CNC-Allyl** were dispersed in water using ultrasonication, and the aqueous dispersion was then solvent exchanged into methanol. A radical initiated thiol-ene reaction was used to attach the thiol-endcapped **PV-SH$_x$** onto the surface allyl groups of ***MxG*-CNC-Allyl**. FTIR confirms the attachment via reduction of the C=C-H bend shoulder ca. 960-1010 cm^{-1}(**Figure S3.12**).

In order to purify the samples, three centrifugation, decanting, and redispersion cycles using acetone were used to remove ungrafted polymer, with the supernatant being collected. UV-Vis analysis of the supernatant quantified the amount of ungrafted polymer removed at each step (**Figure S3.13, Table S3.3**). For example, **PV-SH$_{286}$** (1.85 g) was reacted with 100 mg of ***MxG*-CNC-Allyl** corresponding to 1 eq. of thiol to surface allyl group. Three successive centrifugation steps removed 1.65g, 64.6 mg, and 15.9 mg, respectively, of the unreacted polymer. A fourth centrifugation cycle was used to estimate the amount of free polymer in the materials, with ca. 4.0 mg being removed suggesting that the grafted CNC contained less than 2 wt% free polymer. AFM images of the ***MxG*-CNC-Allyl** and resulting material after grafting with 7,100 g/mol **PV-SH$_{68}$** (***MxG*-CNC-*g*-PV$_{68/y}$**) are shown in **Figure 3.1a-b**, the height profile (**Figure 3.1c**) shows an

increase from 2.1±0.7 nm for ***MxG*-CNC-Allyl** to 3.7±0.4 nm for the grafted sample consistent with the attachment of the polymer to the CNCs.

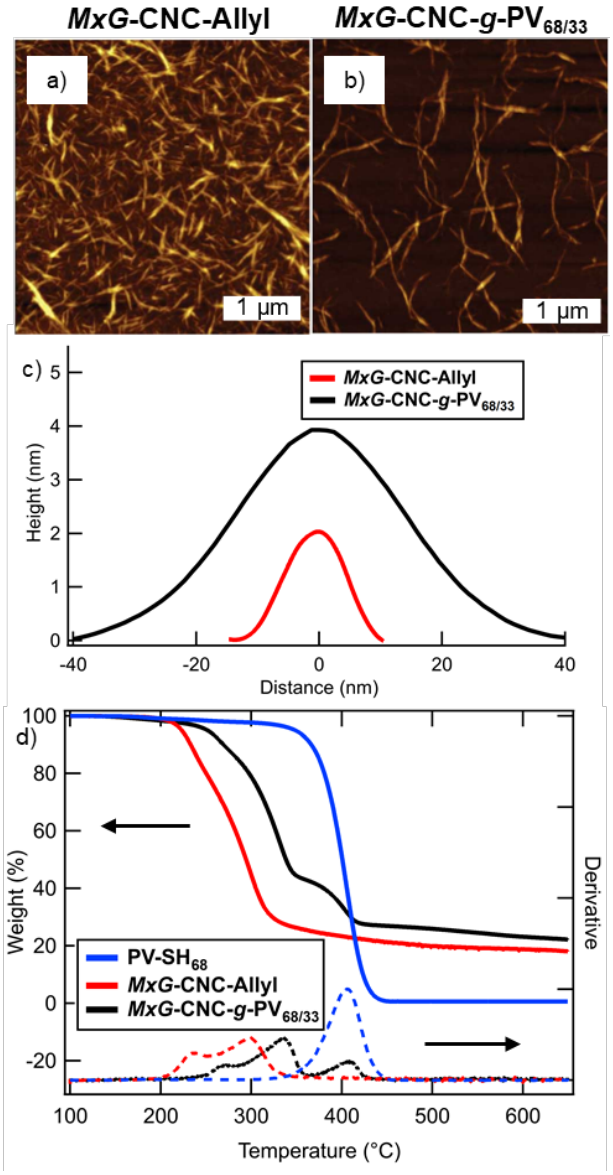

Figure 3.1. AFM height images of a) ***MxG*-CNC-Allyl** and b) ***MxG*-CNC-*g*-PV$_{68/26}$**. c) Example height profiles. d) TGA of **PV-SH$_{68}$**, ***MxG*-CNC-Allyl**, and ***MxG*-CNC-*g*-PV$_{68/26}$** along with the corresponding trace derivatives.

The polymer-grafted CNCs were cast into films as THF dispersions and the solvent allowed to evaporate at room temperature over 2 days to access film thicknesses of ca. 50 microns. Thermogravimetric analysis (TGA) of ***MxG*-CNC-*g*-PV$_{68/y}$** (**Figure 3.1d**) shows two clear regimes that align well with degradation of the CNC and PV. The weight percent of grafted polymer was calculated by comparing mass loss from 220 to 360 ℃, which predominantly corresponds to CNC degradation, to mass loss from 360 to 450 ℃ that predominantly corresponds to PV degradation. No residual THF is observed in these TGA measurements indicating the lack of trapped THF in the system. These PGN films were then exposed to a saturated atmosphere of iodomethane to methylate the grafted poly(2-vinylpyridine) and yield ***MxG*-CNC-*g*-mPV** films.[55] TGA of ***MxG*-CNC-*g*-mPV** shows an additional mass loss from 150 to 220 ℃ which corresponds to loss of the iodomethane and allows for the calculation of degree of methylation (**Figure S3.14**). In addition, x-ray photoemission spectroscopy (XPS) permits the direct measurement of the iodide to nitrogen ratio which can also be used to estimate the percentage of methylation of the pyridine rings (**Figure S3.15)**. Both TGA and XPS confirm similar methylpyridinium conversion percentage (65%) of all PEGN samples, indicating a similar iodide ion charge carrier concentration of the grafted polymers (**Figure S3.16**). The methylation percentage agrees well with literature precedent of mPV using a similar vapor based process for functionalization.[55] It should be noted that after methylation via iodomethane the grafted polyelectrolyte is a poly(2-vinylpyridine-co-2-vinyl-1-methylpyridinium iodide) copolymer but will be referred to herein as mPV.

The TGA data allows the volume percent of grafted polymer and grafting density of the polymer on the CNCs to be calculated (see SI and equations S3.1-3.4 for more details). From the weight percent of grafted polymer and the methylation percentage, it was calculated (using

equation S3.1) that ca. 26 vol.% of ***MxG*-CNC-*g*-PV$_{68/y}$** from **Figure 3.1** is PV, which is termed ***MxG*-CNC-*g*-PV$_{68/26}$** (where the 68 is the degree of polymerization of the grafted polymer and the 26 is the volume percentage of polymer). After treatment with iodomethane, the now methylated sample, ***MxG*- *MxG*-CNC-*g*-mPV$_{68/33}$**, contains 33 vol% mPV. Using the molecular weight of the polymer, the weight percent of grafted polymer, and dimensions of the CNC, the polymer grafting density can be calculated using equation S3.4 for ***MxG*-CNC-*g*-PV$_{68/26}$** to be 0.03 chains/nm^2. In order to access PGNs with increased volume of grafted polymer, the grafted samples could be re-submitted to the same reaction conditions. ***MxG*-CNC-*g*-PV$_{68/26}$** was re-reacted a total of 3 additional times to yield PGNs that contain ca. 48, 50 and 55 vol% of PV, or 57, 59, and 64 vol% mPV after methylation (**Table 3.1, full data in Table S3.4**). The PGNs with higher molecular weight grafted PV, ***MxG*-CNC-*g*-*m*PV$_{113/62}$**, ***MxG*-CNC-*g*-mPV$_{150/66}$**, and ***MxG*-CNC-*g*-mPV$_{286/82}$**, were obtained by reacting ***MxG*-CNC-Allyl** with the appropriate **PV-SH$_x$** (x = degree of polymerization 113, 150, or 286) twice followed by methylation. Comparing the density of the polymer grafts with simulation data of poly(styrene)-grafted CNCs by Keten,[28] a good approximation for PV on account of its similar polymer conformation,[64] it can be estimated that all the ***MxG*-CNC-*g*-PV$_{68/y}$** samples are in the concentrated polymer brush (CPB) regime while the remaining samples are in the concentrated polymer brush with semidilute polymer brush corona (CPB/SDPB) regime.

Table 3.1. Sample information of poly (2-vinylpyridine-co-2-vinyl-1-methylpyridinium iodide) (mPV)-grafted cellulose nanocrystals.

Sample	Molecular Weight (g/mol)[a]	Degree of polymerization	Volume % Polymer when methylated (%)[b]	Graft density (chains/nm^2)
***MxG*-CNC-*g*-mPV$_{68/33}$**	7100	68	33%	0.03
***MxG*-CNC-*g*-mPV$_{68/57}$**	7100	68	57%	0.09
***MxG*-CNC-*g*-mPV$_{68/59}$**	7100	68	59%	0.10
***MxG*-CNC-*g*-mPV$_{68/64}$**	7100	68	64%	0.12
***MxG*-CNC-*g*-mPV$_{113/57}$**	11900	113	57%	0.05
***MxG*-CNC-*g*-mPV$_{113/62}$**	11900	113	62%	0.06
***MxG*-CNC-*g*-mPV$_{150/57}$**	15800	150	57%	0.04
***MxG*-CNC-*g*-mPV$_{150/66}$**	15800	150	66%	0.06
***MxG*-CNC-*g*-mPV$_{286/62}$**	30000	286	62%	0.03
***MxG*-CNC-*g*-mPV$_{286/82}$**	30000	286	82%	0.07

[a] from GPC-MALS

[b] from TGA, methylation percentage, and eq S3.1

Scanning electron microscopy (SEM) images (**Figure 3.2**) show the top down and cross-sectional images of the PEGNs, ***MxG*-CNC-*g*-mPV$_{68/33}$** and ***MxG*-CNC-*g*-mPV$_{286/82}$**. The images of ***MxG*-CNC-*g*-mPV$_{68/33}$** (**Figure 3.2a**) show well-defined, individualized nanorods with voids in the film in contrast to the higher polymer content ***MxG*-CNC-*g*-mPV$_{286/82}$** films (**Figure 3.2b**) in which the voids are filled. Similar morphologies are seen prior to methylation and suggest a relatively homogenous coating of polymer on the individual CNCs (**Figure S3.17**). Interestingly, both samples, irrespective of polymer molecular weight or volume fraction, show layered morphologies in the cross-sectional micrographs (**Figure 3.2c-d**). The layered morphologies (shown running horizontally in the cross-sectional images) run parallel to the casting surface and

their formation is consistent with evaporation-induced self-assembly (EISA) which has been observed before in nanorod films.[65–68]

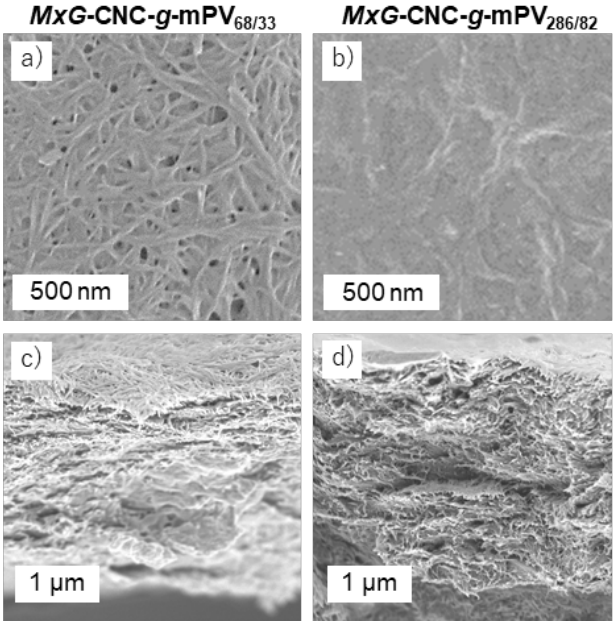

Figure 3.2. Scanning electron microscopy images of ***MxG*-CNC-*g*-mPV$_{68/33}$** and ***MxG*-CNC-*g*-mPV$_{286/82}$** in top down (a-b) and cross-section (c-d), the layers are formed parallel to the casting surface.

The iodide ion conductivity of mPV is impacted by the humidity of the environment as the water not only disassociates the iodide-pyridinium ion pair but also increases segmental mobility of the polymer.[54,55,69] As such it is important to understand how humidity impacts the water uptake of these PEGN films. To determine how much water is present within the different PEGNs, TGA was undertaken on films of ***MxG*-CNC-*g*-mPV$_{68/64}$** and ***MxG*-CNC-*g*-mPV$_{286/82}$** exposed to varying levels of humiditities from 65-95% (See **Figure S3.18** for characteristic TGA). The ***MxG*-**

CNC-*g*-mPV$_{68/64}$ film took up 6-12 wt.% water and the ***MxG*-CNC-*g*-mPV$_{286/82}$** film took up 8-14 wt.% (**Figure S3.19**) across the relative humidity range. In comparison, using the same method, **mPV-SH$_{113}$** showed a water uptake from 5-10% (**Figure S3.19**) across the same humidity range. The slight increase in water uptake of the PEGNs is attributed, at least in part, to the hydrophilic CNC nanofiller. When accounting for the volume percent of polymer, the PEGN samples show similar water uptake, approaching 20% in the polymer phase at 95% relative humidity, allowing comparison between the different samples.

To determine the conductivity of the PEGN films, electrochemical impedance spectroscopy (EIS) was used within a humidity-controlled chamber. On account of the clear structural anisotropy in the SEM images, the conductivity was measured both in a through-plane (perpendicular to the layering) and an in-plane (parallel to the layering) setup (**Figure 3.3a**). The interdigitated electrode literature has shown that polymer conductivity measurements on IDEs corresponds well with the bulk material measurements.[31,55] The conductivity, σ, of the films was calculated using the measured value of the resistance of the film, R_{film}, and the following equation,

$$\sigma = d/(R_{film}A) \tag{3.1}$$

where d is the separation distance between electrodes and A is the cross-sectional area probed.[58] The cross-sectional areas probed in the through-plane studies are the width and length of the top small electrode while the cross-sectional area probed of the in-plane studies are the width and thickness of the film.

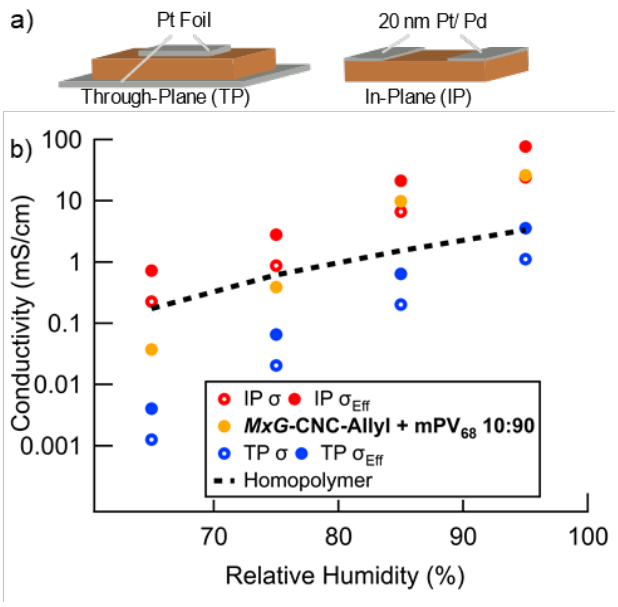

Figure 3.3. (a) Schematic of the in-plane or through-plane conductivity film measurements, (b) comparison of the room temperature conductivity (and effective polymer conductivity taking into account the CNC volume) of ***MxG*-CNC-*g*-mPV$_{68/33}$** both in-plane (IP) and through-plane (TP) as well as homopolymer conductivity versus relative humidity and the in-plane mixed samples ***MxG*-CNC-Allyl** with 90 vol% **mPV$_{68}$**. Experimental standard deviation of n=4 showed error of ~13% which is less than the marker size on graphs.

The through-plane and in-plane conductivity of the ***MxG*-CNC-*g*-mPV$_{68/33}$** films were measured as a function of relative humidity (**Figure 3.3b,** open circles). A sample Nyquist plot and model are provided in **Figure S3.20**. The in-plane measurement of ***MxG*-CNC-*g*-mPV$_{68/33}$** showed higher conductivity than homopolymer (**mPV-SH$_{150}$**) data (prepared by methylation of a film of **PV-SH$_{150}$** measured on interdigitated electrodes (IDEs)) across all measured relative humidities even though the PEGN film consists of 67 vol% (when dry) of the non-conducting crystalline CNC. Note, it was not possible to obtain reliable data from the homopolymer using the

set up in **Figure 3.3a** on account of brittle fracture at low RH and material flow at high RH during, which demonstrates the enhanced material robustness of the PEGN film system relative the homopolymer.[53] IDE based conductivity measurements were employed, which are known to accurately reflect material conductivity.[58]

The in-plane conductivity of ***MxG*-CNC-*g*-mPV$_{68/33}$** films is an order of magnitude higher than the through plane conductivity, 24±3 mS/cm as compared to 1.1±0.1 mS/cm at 95% relative humidity. Given that a significant percentage of the PEGN film consists of the non-ion-conducting, crystalline CNC and the degree of polymer methylation is similar (65%) between the different samples, an effective polymer conductivity, σ_{eff}, was calculated which considers that the ion conductivity is only occurring through the polyelectrolyte volume fraction, and is defined as

$$\sigma_{eff}=\sigma/\Phi_V \tag{3.2}$$

where Φ_V is the polymer volume fraction. Using the effective conductivity in **Figure 3.3b** (filled circles), the in-plane conductivity rises an order of magnitude higher than the homopolymer to an in-plane value of σ_{eff} of 77±10 mS/cm while the through-plane conductivity of 3.6±0.5 mS/cm now roughly corresponds with the homopolymer measurement of 3.3±0.4 mS/cm, all at 95% relative humidity.

A few important caveats are needed to best put this data into context. Although SEM shows the presence of voids in some of these dry PEGN films, samples are not corrected for porosity as there will be different degrees of swelling of the polymer chains at the different humidities. As such it is possible that the effective conductivity of the grafted ionic polymer may be even higher

than is calculated when only adjusting for the volume fraction of the CNCs. Additionally, two different control films, one consisting of ***MxG*-CNC-Allyl** after vapor treatment with iodomethane and a second consisting of non-methylated ***MxG*-CNC-*g*-PV$_{68/26}$**, both exhibit negligible conductivity at all tested humidities which indicates that CNC surface functionality alone without **mPV** cannot account for the conductivity increases observed. Furthermore, the two-component composite film of ***MxG*-CNC-Allyl** with 90 vol% **mPV$_{68}$** does show some conductivity enhancement in the in-plane direction (in **Figure 3.3b**) but not to the same degree, presumably on account (at least in part) of the lower CNC loading. Two-component composites with higher CNC loadings were attempted but showed significant phase segregation and demixing of the CNC nanofiller. It is worthwhile noting that the two-component composite film of ***MxG*-CNC-Allyl** with 90 vol% **mPV$_{68}$** appears as a continuous film in the SEM (**Figure S3.21**) and do not show the void structure observed in the PEGN films (**Figure 3.2**). Ultimately, these controls help to confirm that the iodide conductivity and its enhancement are being measured.

To more directly probe the effect of the CNC interface on ion conductivity, PEGNs were targeted in which the grafted polymer was a diblock of mPV and a non-ion conducting block (which for this study was polystyrene, PS). In particular, it was of interest to see if the nature of the block attached to the CNCs, either the insulating PS block or the ion-conducting mPV block (**Figure 3.4a**), was important in the ionic conductivity of the PNGs. To this end, two diblock copolymers were synthesized in which the thiol end group was attached to either the PS block or the PV block using similar RAFT chemistry to before (**Scheme S3.2**). **PS-PV-SH$_{329,86}$** has a PS block of $M_{n,GPC\text{-}MALS}$ = 34.2 kg/mol and PV block of $M_{n,GPC\text{-}MALS}$ = 9.0 kg/mol, dispersity = 1.13, and f_{PV} = 0.21 while **PV-PS-SH$_{286,150}$** has PV block of $M_{n,GPC\text{-}MALS}$ = 30.0 kg/mol and PS block of

$M_{n,GPC\text{-}MALS}$ = 15.6 kg/mol, dispersity = 1.17, and f_{PV} = 0.65. Grafting of these polymers to the ***MxG*-CNC-Allyl** allows access to PNGs that have similar overall molecular weights (45.6 kg/mol for ***MxG*-CNC-*g*-PS-mPV$_{150,286/60}$** vs. 43.2 kg/mol for ***MxG*-CNC-*g*-mPV-PS$_{86,329/64}$**), total polymer volume fractions (60 vs 64 vol%) and grafting densities (ca. 0.02 chains/nm^2). However, the inner block to outer block ratio is not identical, with f_{PS} = 0.35 for ***MxG*-CNC-*g*-PS-mPV$_{150,286/60}$** vs. f_{PV} = 0.21 for ***MxG*-CNC-*g*-mPV-PS$_{86,329/64}$**. As a result, the volume fractions of mPV polyelectrolyte differ, which is taken into account when calculating the effective conductivity of the materials. SEM shows that both films have similar structures to those observed in the ***MxG*-CNC-*g*-mPV$_{286/82}$** sample (**Figures S3.22-S3.26**).

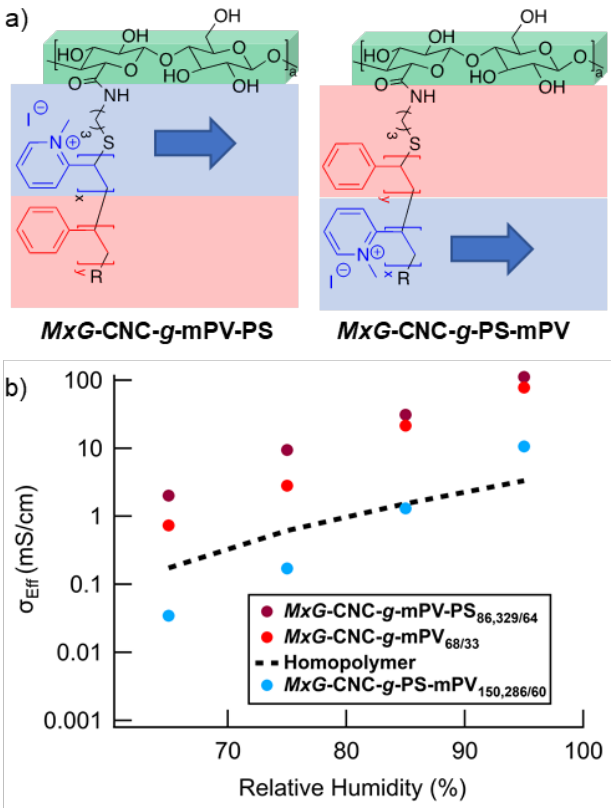

Figure 3.4: a) A cartoon of the two diblock grafted CNCs with either **mPV** (***MxG*-CNC-*g*-mPV-PS$_{86,329/64}$**) or PS (***MxG*-CNC-*g*-PS-mPV$_{150,286/60}$**) directly attached to the CNC surface. b) Effective conductivities (considering only the volume fraction of **mPV**) of the two diblock-grafted PEGN plotted against relative humidity along with homopolymer and ***MxG*-CNC-*g*-mPV$_{68/33}$**. Experimental standard deviation is less than the marker size on graphs. See **Figure S3.27** for measured data (not adjusted for vol% of CNC).

When the PS block is covalently attached to the CNC (***MxG*-CNC-*g*-PS-mPV$_{150,286/60}$**), a significant reduction in effective ionic conductivity (corrected for the volume fraction of mPV relative to the other components (PS and CNC)) of the mPV is observed (**Figure 3.4b**). Measured conductivity data of the samples are shown in **Figure S3.27**. It appears that the introduction of a hydrophobic/non-conducting boundary layer between the ion-conducting mPV and the CNC

results in the conductivity dropping to a value more akin to the homopolymer, consistent with the CNC/polyelectrolyte interface playing an important role in the iodide ion transport (**Figure 3.4a**). If this CNC/polyelectrolyte interface does play a role then it can be expected that attaching the ion-conducting mPV block directly to the CNCs (and having the PS as the outer block) should yield a very different effect. Intriguingly, the ***MxG*-CNC-*g*-mPV-PS$_{86,329/64}$** films needed longer equilibration times at a given relative humidity to reach a consistent conductivity value, presumably on account of the hydrophobic PS outer block layer slowing down water transport into these films. Nonetheless, the equilibrated effective conductivity of the mPV inner block in ***MxG*-CNC-*g*-mPV-PS$_{86,329/64}$** shows a similar enhancement in conductivity to that of ***MxG*-CNC-*g*-mPV$_{68/33}$** (**Figure 3.4b**) confirming that the conductivity enhancement is dependent on the CNC/polyelectrolyte interface

Having confirmed the effect of the CNC/polyelectrolyte interface on the ion conductivity of these PEGNs, it can be expected that their ion conductivity will be impacted by the overall CNC/polyelectrolyte interfacial area. The grafted polymer molecular weight and grafting density can be used to alter the overall interfacial area in the PEGNs. However, it is important to note that doing this will also vary the volume fraction of the polymer as well as impact the brush regime/conformation of the grafted polymer. Thus, to get a better understanding of the structure/property relationships in this class of ion-conducting materials the PEGNs with different polymer graft molecular weight, density and volume fraction (**Table 3.1**) were reacted with iodomethane as before and their ionic conductivity studied. For all these studies the PEGN films are measured in-plane and at 95% relative humidity.

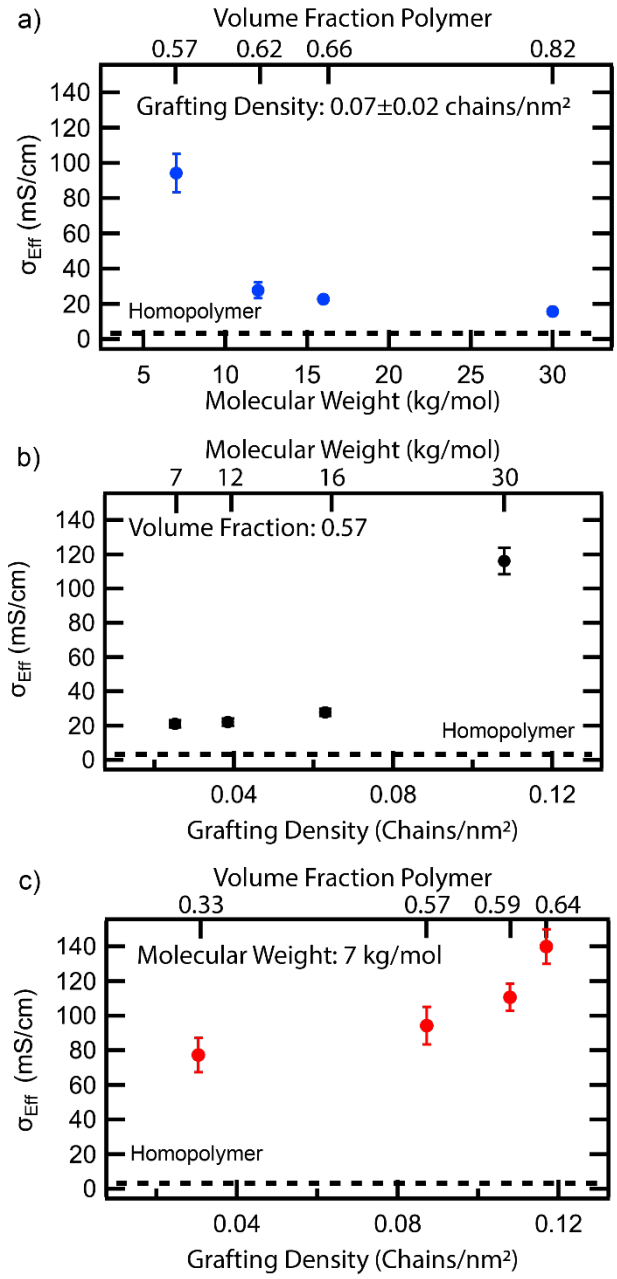

Figure 3.5. Effective conductivities of the **mPV** in the methylated PEGN films with a) similar grafting density but different molecular weight and grafting density, b) same volume fraction but differing molecular weights and grafting density, and c) same molecular weight grafted polyelectrolyte but different grafting density and volume fraction. Dotted lines correspond to conductivity of methylated homopolymer and all conductivity data is obtained from 95% relative

humidity and room temperature samples. Experimental standard deviation of n=2 showed error on graphs. See **Figure S3.28** for the measured conductivity of the films (not adjusted for vol% of CNC).

Figure 3.5a shows the effective conductivity (σ_{eff}) of ***MxG*-CNC-*g*-mPV** PEGN samples with similar grafting density (calculated grafting densities of ca. 0.07 ± 0.02 chains/nm^2) but with different molecular weight grafts. Of course, increasing the molecular weight of the graft also increases the polymer volume fraction. Comparing ***MxG*-CNC-*g*-mPV$_{68/57}$**, ***MxG*-CNC-*g*-mPV$_{113/62}$**, ***MxG*-CNC-*g*-mPV$_{150/66}$**, ***MxG*-CNC-*g*-mPV$_{286/82}$**, σ_{eff} decreases from 116±7 to 21±2 mS/cm, approaching the homopolymer conductivity value (3.3±0.4 mS/cm) with the highest molecular weight polymer grafts. Thus, as the molecular weight increases, and the CNC surface area to polymer volume decreases, the conductivity of the hydrated grafted polymer chains behaves more like the hydrated homopolymer, displaying a reduced conductivity enhancement. This is consistent with CNC/polyelectrolyte interface playing a significant role in the conductivity enhancement.

This raises the question of what happens if the polymer volume fraction is kept the same, but the grafting density is altered (which can be done by varying the molecular weight of the graft). If the CNC/polyelectrolyte interface was the only controlling factor to conductivity enhancement, samples with similar volume percent of polymer ought to show similar levels of enhancement. However, **Figure 3.5b** clearly shows that this is not the case as all the PEGNs have a polymer volume fraction of ca. 0.57 and resulting σ_{eff} ranges from 110 (for ***MxG*-CNC-*g*-mPV$_{68/57}$**) to 21 mS/cm (for ***MxG*-CNC-*g*-mPV$_{286/57}$**). Thus, the highest conductivity is observed for the PEGN with the lowest degree of polymerization (68) and highest grafting density (0.09 chains/nm^2).

Clearly, the degree of enhancement in conductivity differs depending on the molecular weight and grafting density even at similar volume percent polymer, suggesting that the nature of the CNC/polyelectrolyte interface plays a role in the conductivity enhancement in addition to simply the amount of nanofiller surface area.

To further probe the nature of the CNC/polyelectrolyte interface, the molecular weight was held constant at degree of polymerization while the grafting density was increased, which also results in an increasing overall volume of polymer and a decreasing CNC/polyelectrolyte interfacial surface area. **Figure 3.5c** shows that there is an increase in σ_{eff} (77±10 to 140±10 mS/cm) for ***MxG*-CNC-*g*-mPV$_{68/y}$** polymer graft series films as the grafting density increases (0.03 to 0.12 chains/nm^2). Thus, while the data in **Figure 3.5a** shows a strong relationship between the conductivity and the CNC/polyelectrolyte interfacial surface area, the data in **Figure 3.5b,c** show that the density of polymer grafts also play a significant role in the materials' ionic conductivity. One possible explanation for this could be the changing conformation of the grafted polymer at higher densities aiding ion transport.

The ability to enhance the effective conductivity of ionic polymers grafted to CNCs relative to homopolymer represents an interesting benefit for the use of CNCs in ion conducting materials. Polymers grafted to other surfaces have shown mixed effects on conductivity. For example, previous work on mPV brushes grafted to flat silica surfaces have not shown conductivity enhancement relative to ungrafted mPV,[30,55] albeit in those studies lower molecular weights of PV (1.3 kg/mol grafted vs 6.2 kg/mol ungrafted) and higher grafting densities (5 chains/nm^2) were investigated. A drop in conductivity with dense polymer grafts (1.2 chains/ nm^2) has been measured in PEO brushes with LiTFSI which was attributed to reduced segmental mobility of the

polymer.[31] Thus, measuring the increase in effective conductivity of the ***MxG*-CNC-*g*-mPV** system compared to **mPV**, highlights the impact of the CNC interface. The enhancement in conductivity effect by the CNC interface is further supported by the high anisotropy of in-plane vs through-plane conductivity. Literature examples of ionically conductive nanocomposites based on randomly aligned nanorods with beneficial surface-polymer interactions show greater enhancement than nanospheres.[4] This enhancement is attributed to the long, continuous surfaces that the nanorods provide which permits a more efficacious usage of the beneficial surface-polymer interactions. As further evidence for the interfacial conductivity enhancement, when considering the layered structural anisotropy in the PEGN films (**Figure 3.2c-d**), one would expect a high conductivity anisotropy if the CNC interface is the driving factor in the conductivity enhancement. Thus, the conjunction of the extended network of in-plane layers shown in the SEM images in **Figure 3.2c-d** with conductivity enhancement via in-plane measurements in **Figure 3.3b** supports that the CNCs are providing a beneficial CNC/polyelectrolyte interaction with the iodide containing mPV polymer.

3.5 CONCLUSION

The iodide ion conductivity of mPV in these PEGN films, which have as much as 67 vol% CNC, show a remarkable deviation from homopolymer conductivity. Taken together, the anisotropic conductivity, the grafted diblock copolymer studies, and the impact of polymer molecular weight and graft density all point towards a positive interfacial effect between the mPV and the CNC surface which causes the enhancement in conductivity along the length of the CNC. The exact reason for this enhanced conductivity is not fully understood, however possible hypotheses for this effect include the concentration of water at the CNC surface, surface-aided ion dissociation, and the presence of surface charges (carboxylate ions) on the CNCs. Recently the conductivity of mPV has been shown to be impacted by the relative humidity of the environment because the water not only enhances the polymer dynamics but also facilitates ion hopping.[69] In particular, water helps to shorten ion-pyridinium association time and assists ions to hop by temporarily providing additional coordination. Cellulose nanocrystals are hydrophilic and well-known to increase water uptake in matrix materials.[44,70,71] This was confirmed in the ***MxG*-CNC-*g*-mPV** PEGNs as the nanocomposites had higher water uptake than the **mPV** homopolymer (20 wt% vs 10 wt%). Thus, not only may there be more available carriers due to the additional dissociated ions, but a concentration of water at the CNC surface may act as potential pathways for venturing from hopping site to hopping site, increasing both carrier number and carrier mobility. The surface functionality of the CNCs, which consists of alcohols, amides, and carboxylic acids, may interact with the quaternary pyridinium iodide, aiding in the ion dissociation and thus increasing conductivity yet also impact the hydrophilicity of the CNC surface.[72,73] Specifically, hydrogen bonding from the alcohol and amide functionalities may aid ion disassociation while residual surface charge from the carboxylate may help to shorten ion-

pyridinium association time. Future studies are needed to tease apart these inter-related hypotheses, as well as to determine the specific mechanism for the nature of the polymer/CNC interface impacting the conductivity enhancement which will be investigated in later chapters. Nonetheless, the ability of the CNC/polyelectrolyte interface to enhance ion conductivity, along with the known ability of PEGNs to exhibit enhance mechanical properties, offers a route to designing new robust, ion conductive membranes for a range of electrochemical energy production or storage applications.[74]

3.6 SUPPLEMENTAL INFORMATION

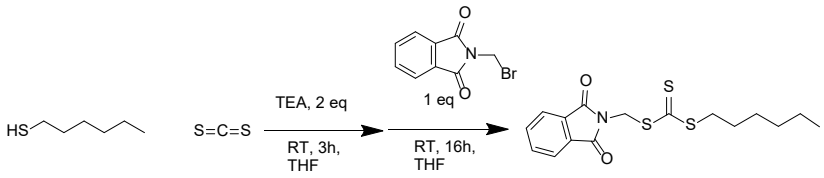

Scheme S3.1: Synthesis of the chain transfer agent phthalimidomethyl hexyl trithiocarbonate

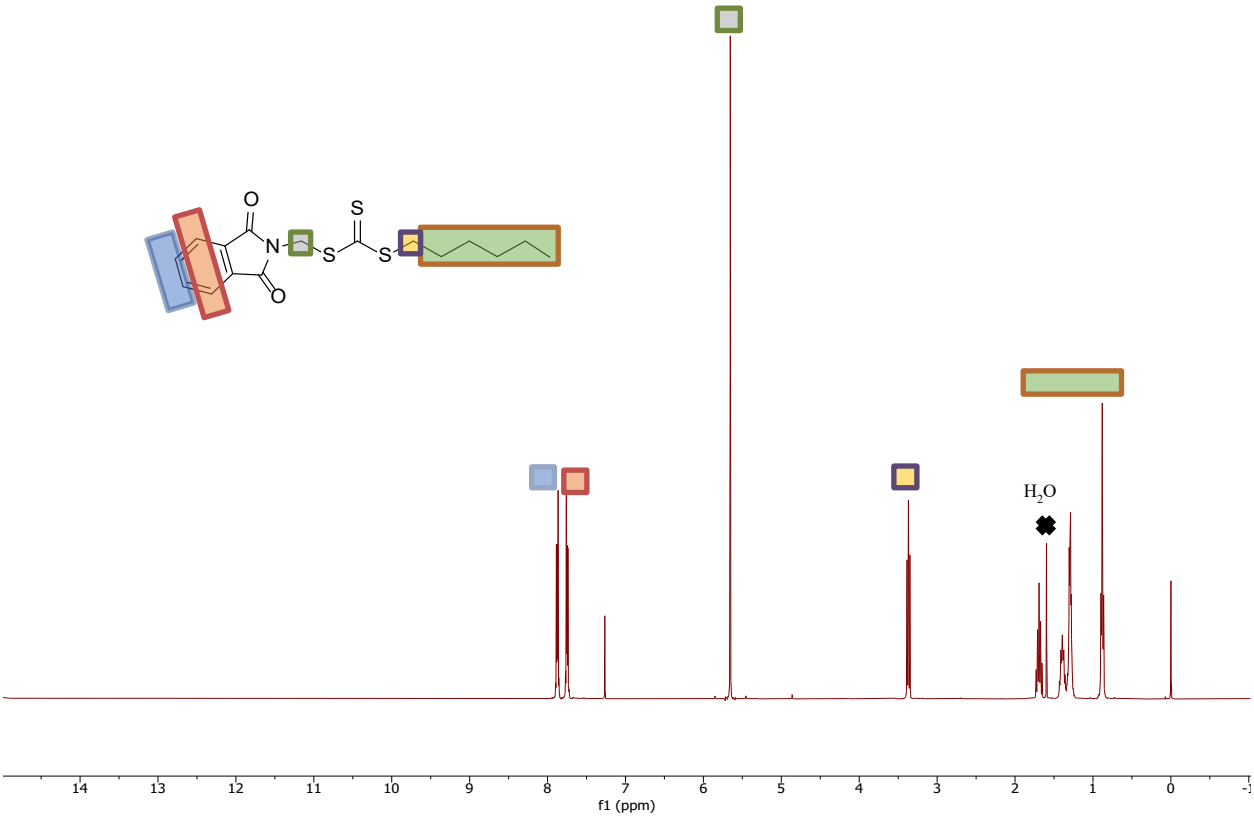

Figure S3.1: ^{1}H NMR (500 MHz, $CDCl_3$) spectra of phthalimidomethyl hexyl trithiocarbonate

Figure S3.2: ^{13}C NMR (101 MHz, $CDCl_3$) spectra of phthalimidomethyl hexyl trithiocarbonate

Table S3.1: Homopolymer Synthesis Summary

	M_n, ^{1}H NMR (g/mol)	M_n, GPC-MALS (g/mol)	Degree of Polymerization (DP)	Dispersity, $Đ$
PV-SH$_{68}$	6900	7100	68	1.14
PV-SH$_{113}$	11100	11900	113	1.20
PV-SH$_{150}$	15700	15800	150	1.24
PV-SH$_{286}$	29400	30000	286	1.17
PS$_{324}$	34100	34200	329	1.02

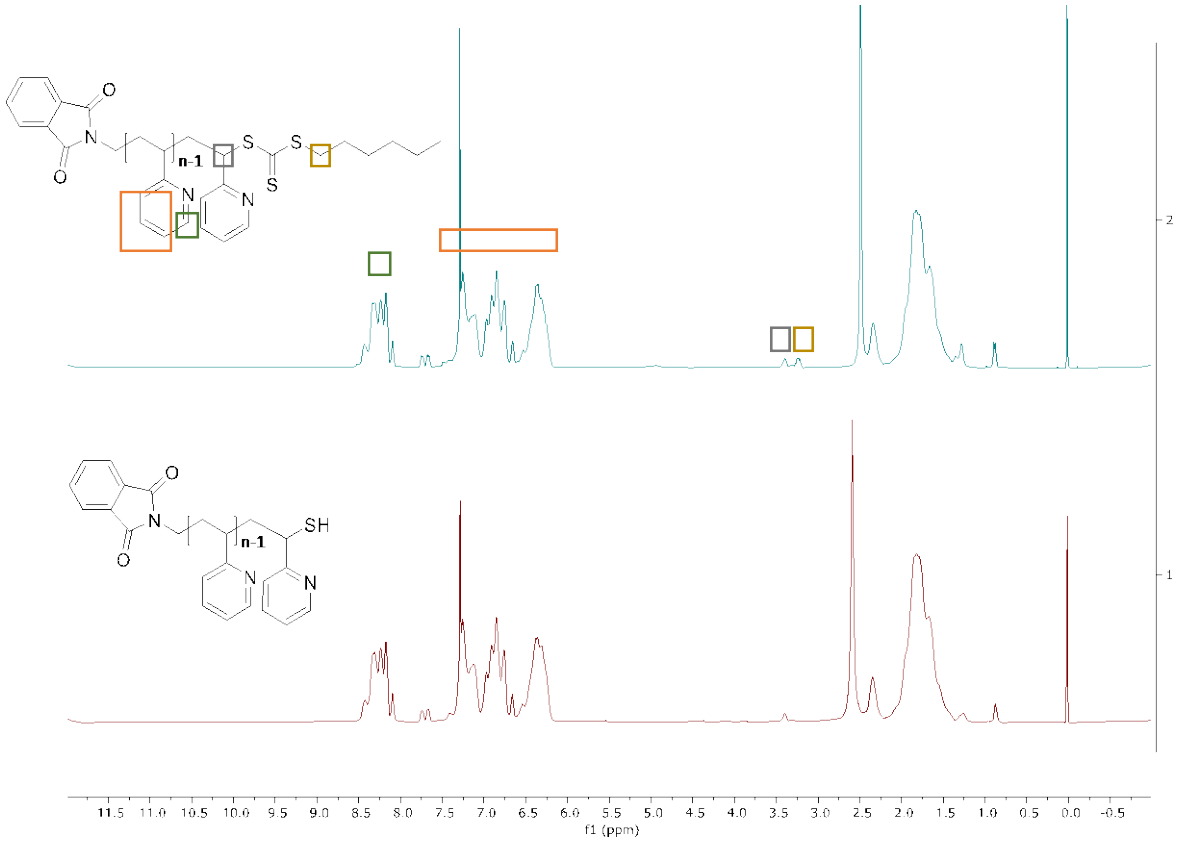

Figure S3.3: ^{1}H NMR (500 MHz, $CDCl_3$) spectra of **PV$_{68}$** (top, teal) and **PV-SH$_{68}$** (bottom, red) which shows the diminishment of the 3.3 ppm peak indicative of trithiocarbonate to thiol conversion

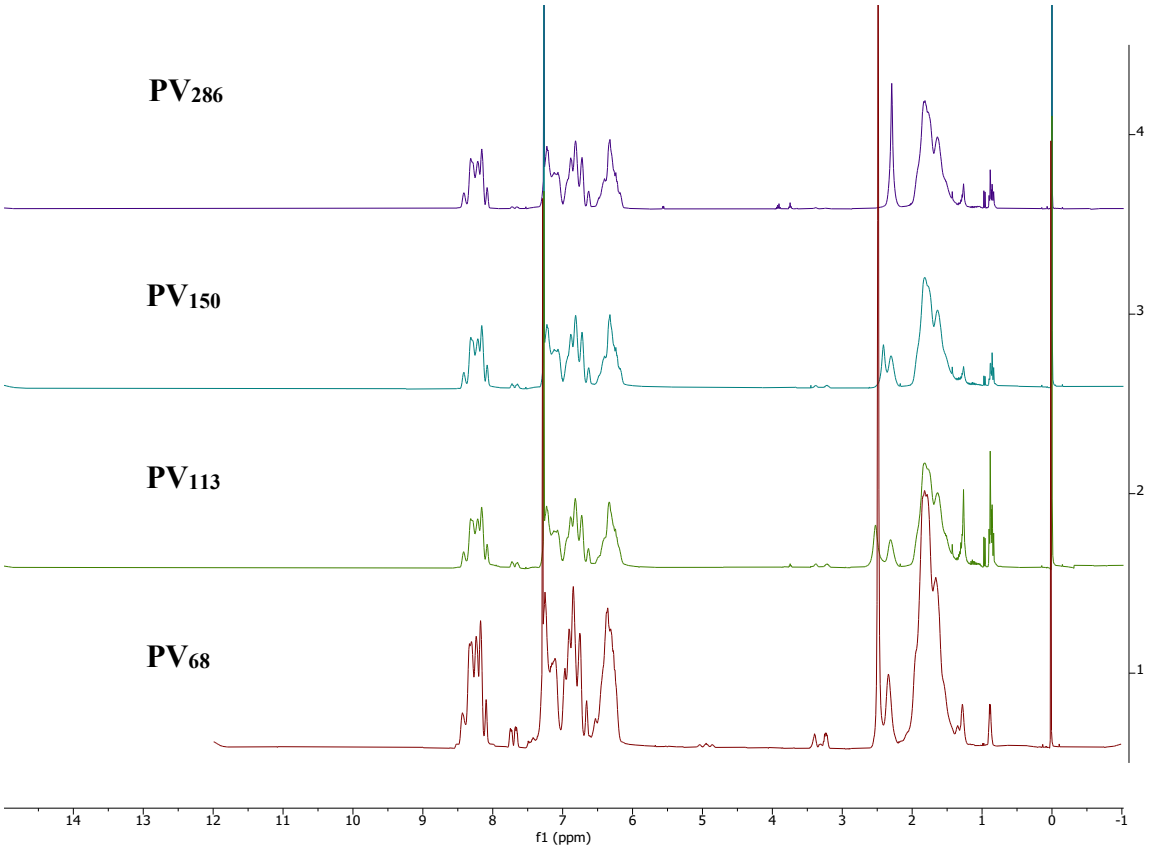

Figure S3.4: ^{1}H NMR (500 MHz, $CDCl_3$) spectra of **PV_{68}, PV_{113}, PV_{150}**, and **PV_{286}** which permit analysis of molecular weight by end group analysis

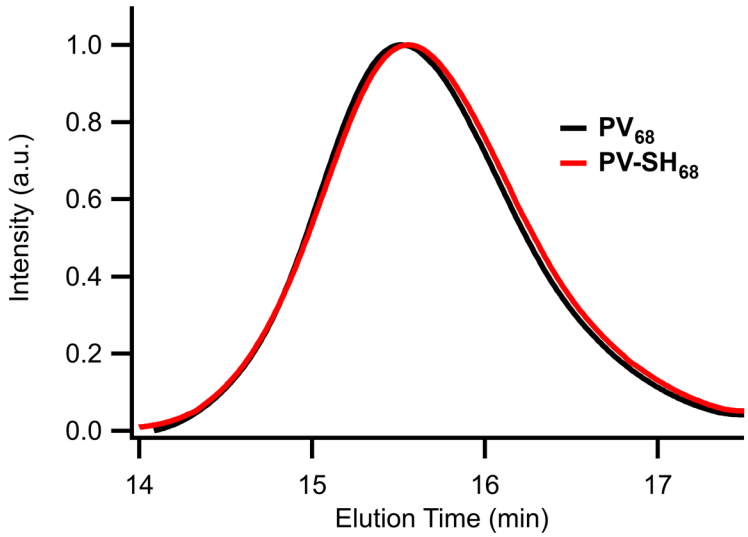

Figure S3.5: GPC-MALS of **PV$_{68}$** (black) and **PV-SH$_{68}$** (red).

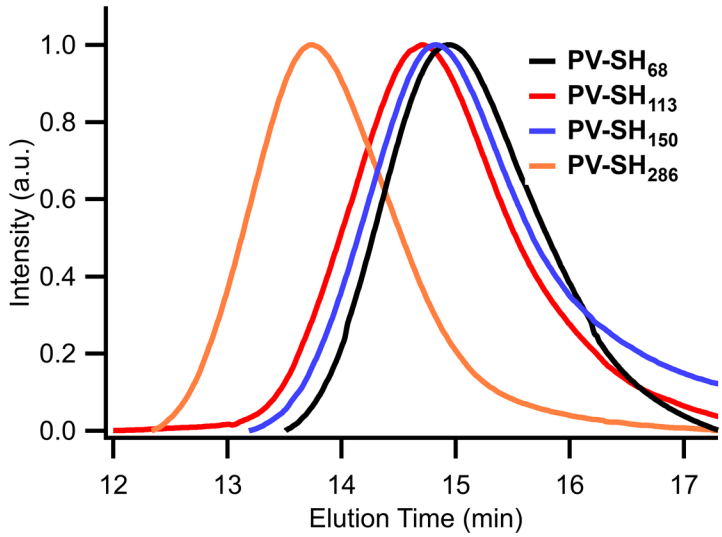

Figure S3.6: GPC-MALS **PV-SH$_{68}$, PV-SH$_{113}$, PV-SH$_{150}$**, and **PV-SH$_{286}$**.

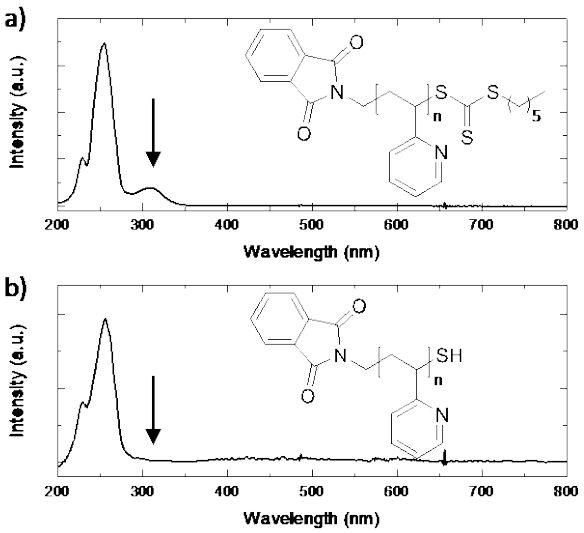

Figure S3.7: UV-Vis of a) **PV$_{68}$** and b) **PV-SH$_{68}$** with demarcation of the diminution of the 310 nm peak

Table S3.2: Diblock copolymer synthesis summary with regard to each block

	M_n, 1, ^{1}H NMR (g/mol)	M_n, 1, GPC-MALS (g/mol)	M_n, 2, GPC-MALS (g/mol)	f_{PV}	M_n Total (g/mol)	M_n Total (g/mol)	Dispersity, $Đ$
PV-PS-SH$_{286,150}$	29400	30000	15600	0.65	44100	45600	1.17
PS-PV-SH$_{329,86}$	34100	34200	9000	0.21	42600	43200	1.13

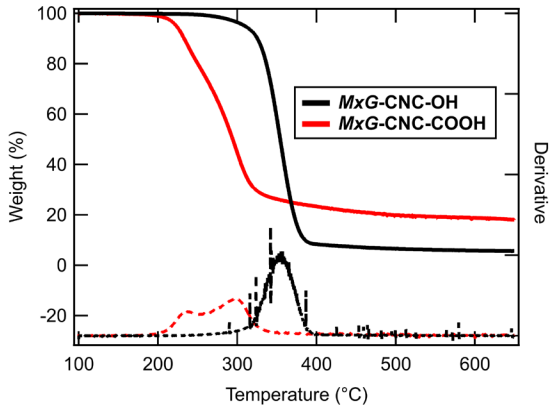

Figure S3.8: Thermal Gravimetric Analysis (TGA) of ***MxG*-CNC** before and after TEMPO oxidation (under nitrogen atmosphere with a heating rate of 10 °C/min).

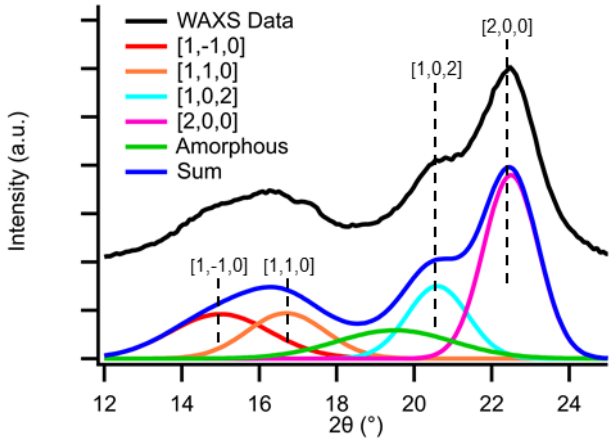

Figure S3.9: WAXS of ***MxG*-CNC-COOH** with labeled crystalline peaks and Gaussian fit to calculate crystallinity index. The Gaussian peaks corresponding to the various CNC crystal planes are notated by color. Note that original WAXS data is offset for clarity.

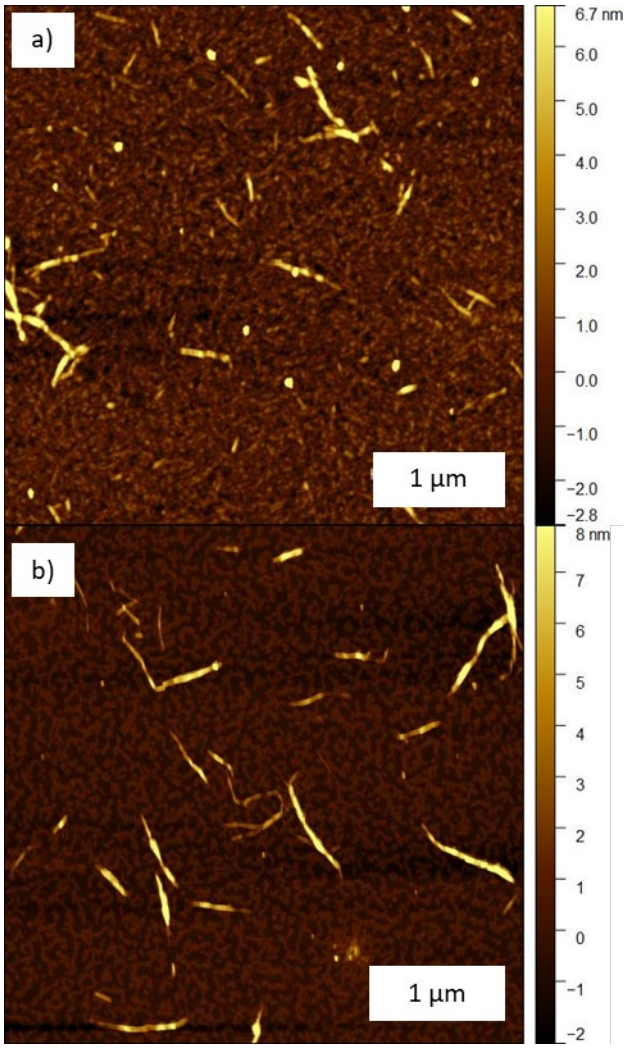

Figure S3.10: AFM height images of a) ***MxG*-CNC-COOH** and b) ***MxG*-CNC-Allyl** cast on poly-L-lysine coated mica

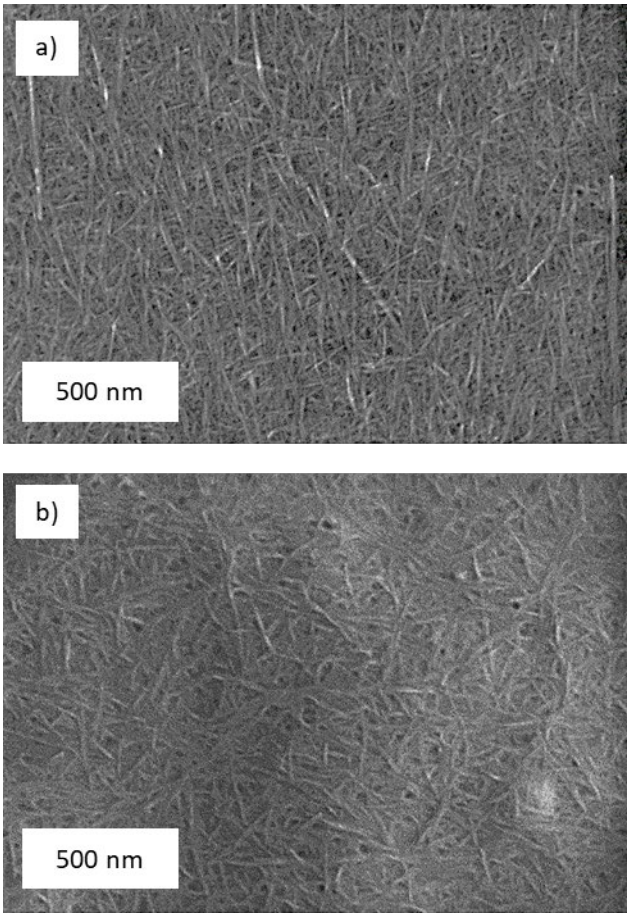

Figure S3.11: SEM of a) ***MxG*-CNC-COOH** and b) ***MxG*-CNC-Allyl** as cast from solvent exchanged solution and coated in 2 nm Pt/Pd

To calculate the volume fraction of polyelectrolyte ($VolFrac_{PE}$) in the ***MxG*-CNC-*g*-mPV** system, the following equation is used in accordance with literature precedent,[75]

$$VolFrac_{PE} = \frac{\frac{\Phi_{polymer}}{\rho_{polymer}} f_{P2VP} + \frac{\Phi_{polymer}}{MW_{2VP}} \frac{x_M MW_I}{\rho_I} f_{PV}}{\frac{\Phi_{polymer}}{\rho_{polymer}} + \frac{\Phi_{polymer}}{MW_{2VP}} \frac{x_M MW_I}{\rho_I} f_{PV} + \frac{\Phi_{CNC}}{\rho_{CNC}}} \quad \text{S3.1}$$

where Φ_{poly} and Φ_{CNC} are the weight fractions of polymer and CNC, respectively, $\rho_{polymer}$, ρ_I, and ρ_{CNC} are the densities of the polymer, iodomethane, and CNC, respectively, MW_{2VP} and MW_I are the molecular weights of 2-vinylpyridine and iodomethane, f_{PV} is the weight fraction of PV in a grafted PS-PV diblock copolymer and $x_M$is the methylation percentage of the polymer (65% in all cases). In this work, $\Phi_{polymer}$and Φ_{CNC} are determined by thermogravimetric analysis while $MW_{polymer}$ is determined by gel permeation chromatography, multiangle light scattering. Literature values of 1.5 g/cm^3 and 1.08 g/cm^3 was used for ρ_{CNC} and $\rho_{polymer}$ for PV and diblock copolymers, respectively.[41,63] For the case of grafted diblock copolymers, the individual block wt% must also be taken into account.

The surface density of allyl groups (σ_{allyl}), as number of allyl groups per nm^2, is given by,

$$\sigma_{allyl} = \frac{n_{allyl}}{SA_{CNC}} = \frac{\varphi_{allyl} \rho_{CNC} V_{CNC} N_A}{SA_{CNC}} \quad \text{S3.2}$$

where n_{allyl} is the number of allyl sites per CNC, φ_{allyl} is the density of allyl groups given as mmol/kg, ρ_{CNC} is the CNC density, V_{CNC} is the volume of an individual CNC, and SA_{CNC} is the

surface area of an individual CNC. For determining φ_{allyl}, the difference was taken of sample conductometric titration before adding allylamine (1000 mmol/kg) and after (400 mmol/kg) resulting in a value of 600 mmol of allyl groups per kg of CNC. Literature values of 1.5 g/cm^3 was used for ρ_{CNC}.[41] V_{CNC} and SA_{CNC} are both calculated using literature values for *MxG*-CNC, a rectangular prism with dimensions 8.5nm by 2.8nm by 300nm as determined by SANS.[45] The value of σ_{allyl} is calculated to be 0.55 allyl groups per nm^2.

To calculate the polymer grafting density on CNC, $\sigma_{polymer}$, the density of polymer chains ($\varphi_{polymer}$) as given as mmol/kg can be defined as

$$\varphi_{polymer} = \frac{\Phi_{polymer}}{\Phi_{CNC} MW_{polymer}} \quad \text{S3.3}$$

where $\Phi_{polymer}$ is the weight fraction polymer, Φ_{CNC} is the weight fraction CNC, and $MW_{polymer}$ is the polymer molecular weight. By performing a similar analysis to equation S3.2 and inserting equation S3.3, the polymer grafting density on CNC can be defined as

$$\sigma_{polymer} = \frac{\Phi_{polymer} \rho_{CNC} V_{CNC} N_A}{\Phi_{CNC} MW_{polymer} SA_{CNC}} \quad \text{S3.4}$$

where all of the input quantities are either literature values or measured quantities. The conversion of allyl sites to polymer grafted sites, x, can be defined as,

$$x = \frac{\sigma_{polymer}}{\sigma_{allyl}} = \frac{\Phi_{Poly}}{\Phi_{CNC}\varphi_{Allyl}MW_{polymer}} \quad \text{S3.5}$$

and has calculated values ranging from 4% to 21% depending on molecular weight of grafting polymer and number of times of re-reaction.

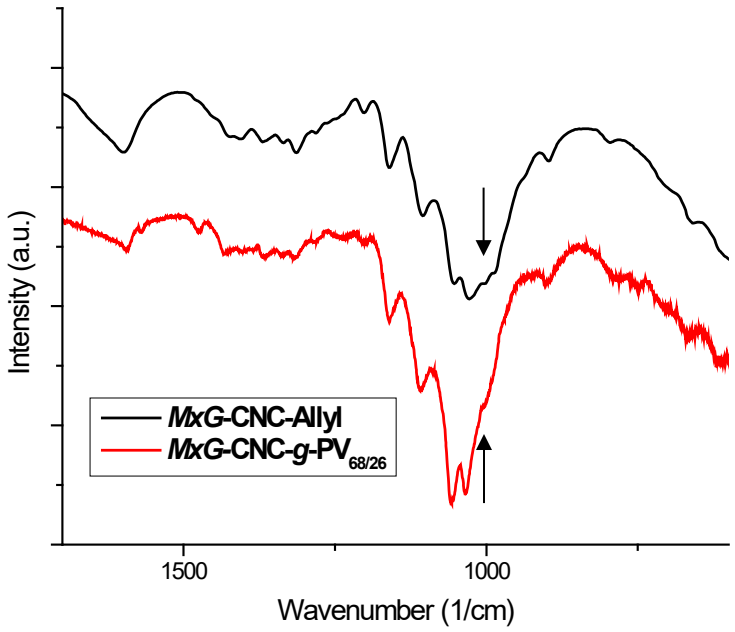

Figure S3.12: ATR-FTIR of ***MxG*-CNC-Allyl** and **MxG-CNC-*g*-PV$_{68/26}$**, with arrows highlighting the reduction of the C=C-H bend shoulder ca. 960-1010 cm^{-1}.

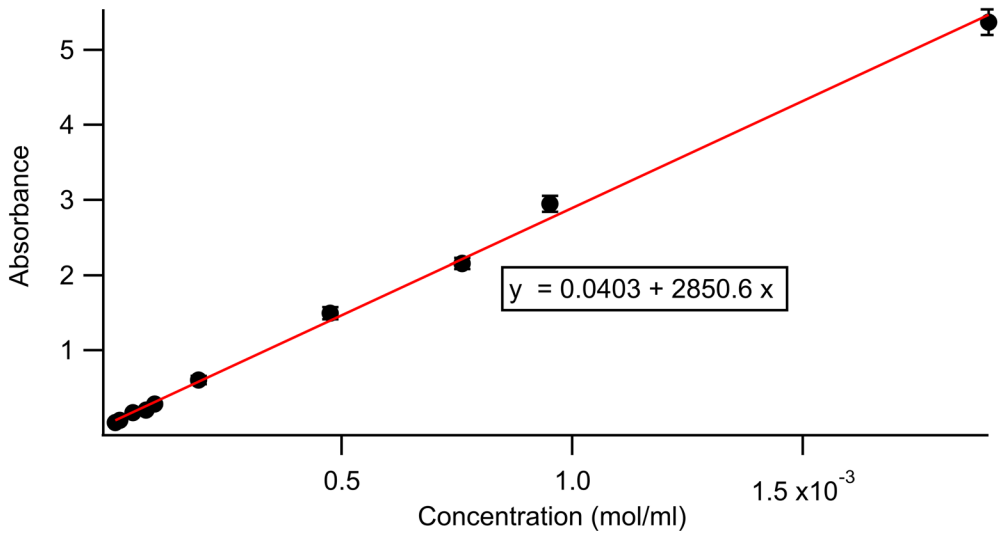

Figure S3.13: UV-Vis derived concentration data of **PV-SH$_{286}$** in methanol

Table S3.3: Concentration data and percentages of free polymer for given numbers of centrifugations of ***MxG*-CNC-*g*-mPV$_{286/62}$**

# of centrifuges	Concentration (mol/ml)	Polymer Removed (mg)	Free Polymer %
1	44.7	1650	827%
2	1.79	64.6	32%
3	0.441	15.9	8%
4	0.373	4.47	2%

Table S3.4: Summary of all PGN samples

Sample	Molecular Weight, M_n (g/mol) of polymer graft	Wt% Polymer	Vol% Polymer	Vol% Polymer when methylated	Grafting Density (chains/nm^2)
***MxG*-CNC-*g*-mPV$_{68/33}$**	7100	20%	26%	33%	0.03
***MxG*-CNC-*g*-mPV$_{68/57}$**	7100	40%	48%	57%	0.09
***MxG*-CNC-*g*-mPV$_{68/59}$**	7100	42%	50%	59%	0.10
***MxG*-CNC-*g*-mPV$_{68/64}$**	7100	47%	55%	64%	0.12
***MxG*-CNC-*g*-mPV$_{113/57}$**	11900	40%	48%	57%	0.05
***MxG*-CNC-*g*-mPV$_{113/62}$**	11900	45%	53%	62%	0.06
***MxG*-CNC-*g*-mPV$_{150/57}$**	15800	40%	48%	57%	0.04
***MxG*-CNC-*g*-mPV$_{150/66}$**	15800	50%	58%	66%	0.06
***MxG*-CNC-*g*-mPV$_{286/62}$**	30000	45%	53%	62%	0.03
***MxG*-CNC-*g*-mPV$_{286/82}$**	30000	70%	76%	82%	0.07
***MxG*-CNC-*g*-PS-mPV$_{150,286/60}$**	45600	50%	58%	60%	0.02
***MxG*-CNC-*g*-mPV-PS$_{86,329/64}$**	43200	50%	58%	64%	0.02

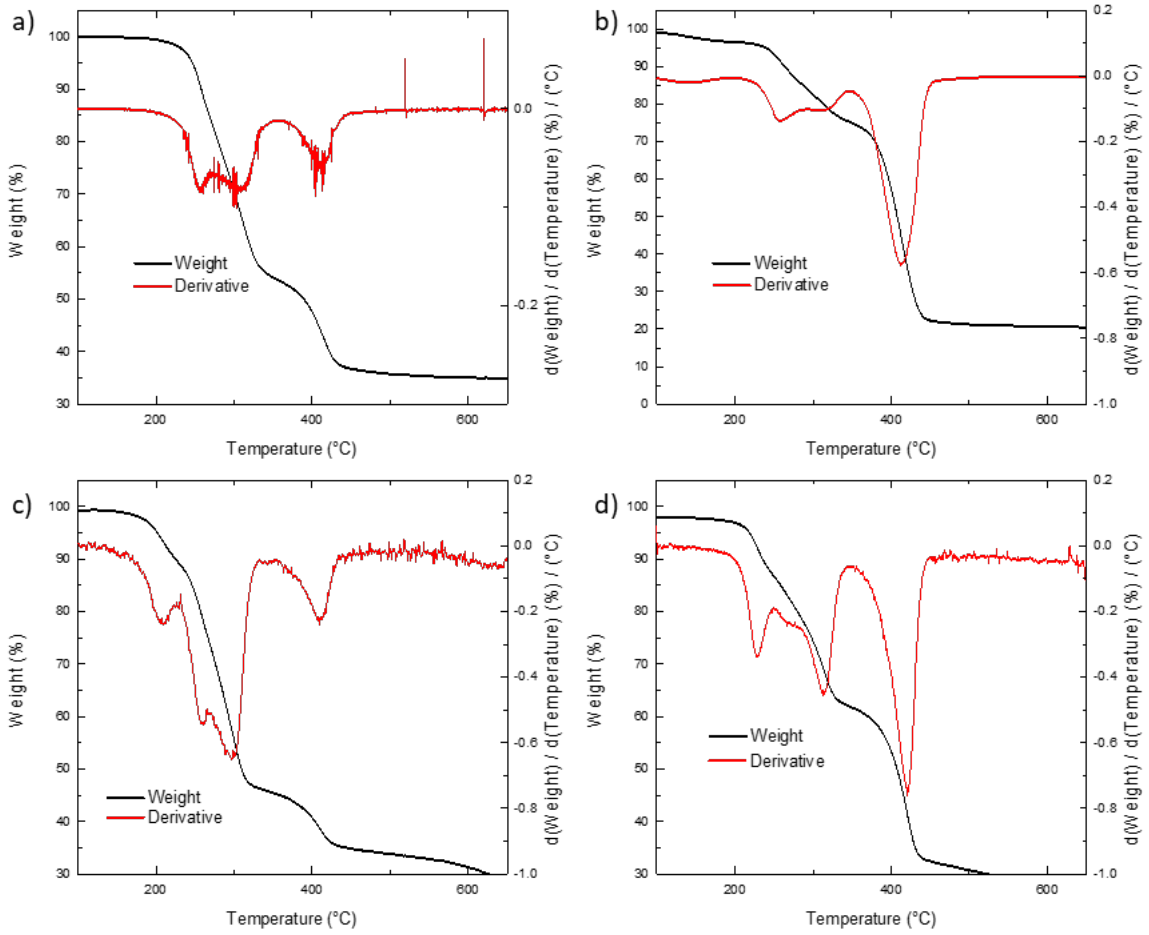

Figure S3.14: Thermogravimetric analysis (TGA) of ***MxG*-CNC-*g*-mPV$_{68/33}$** and ***MxG*-CNC-*g*-mPV$_{286/82}$** before (a, b) and after (c, d) methylation under nitrogen atmosphere with a heating rate of 10 °C/min.

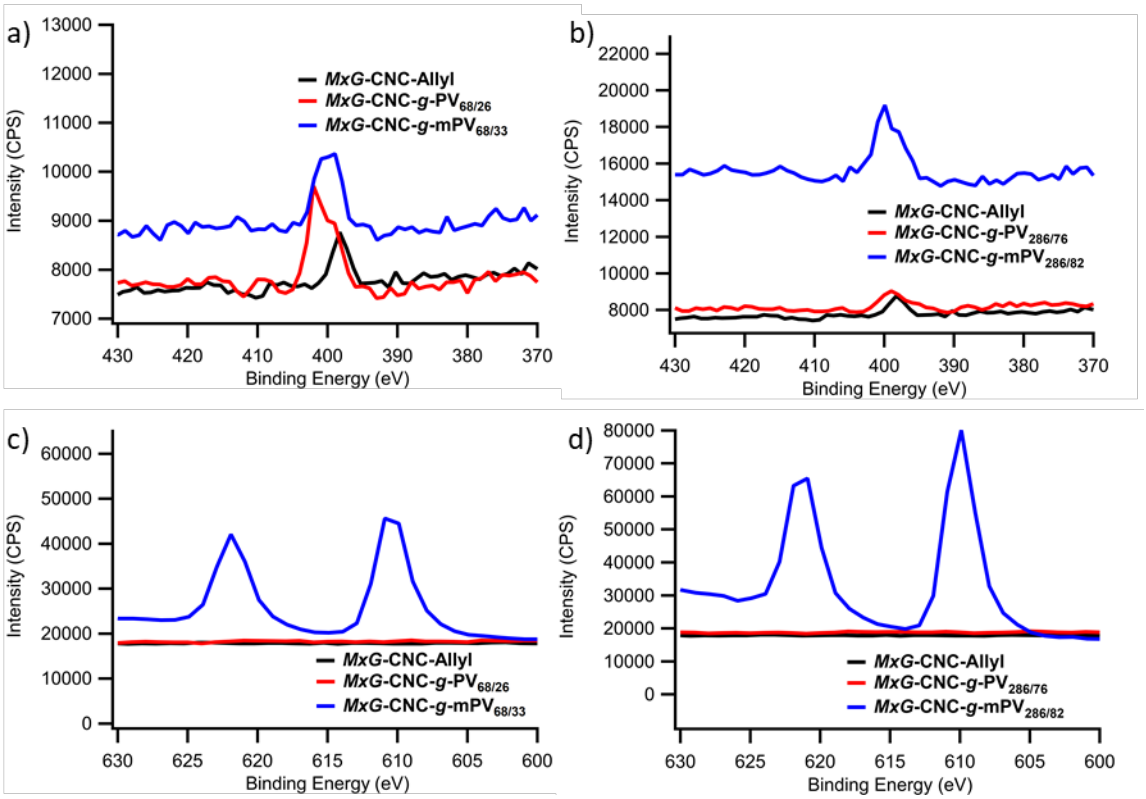

Figure S3.15: X-ray photoelectron spectroscopy (XPS) of nitrogen 1S peak comparing ***MxG*-CNC-Allyl** and both methylated and unmethylated a) ***MxG*-CNC-*g*-mPV$_{68/33}$** and b) ***MxG*-CNC-*g*-mPV$_{286/82}$** and the iodide 3D peaks comparing ***MxG*-CNC-Allyl** and both methylated and unmethylated c) ***MxG*-CNC-*g*-mPV$_{68/33}$** and d) ***MxG*-CNC-*g*-mPV$_{286/82}$.**

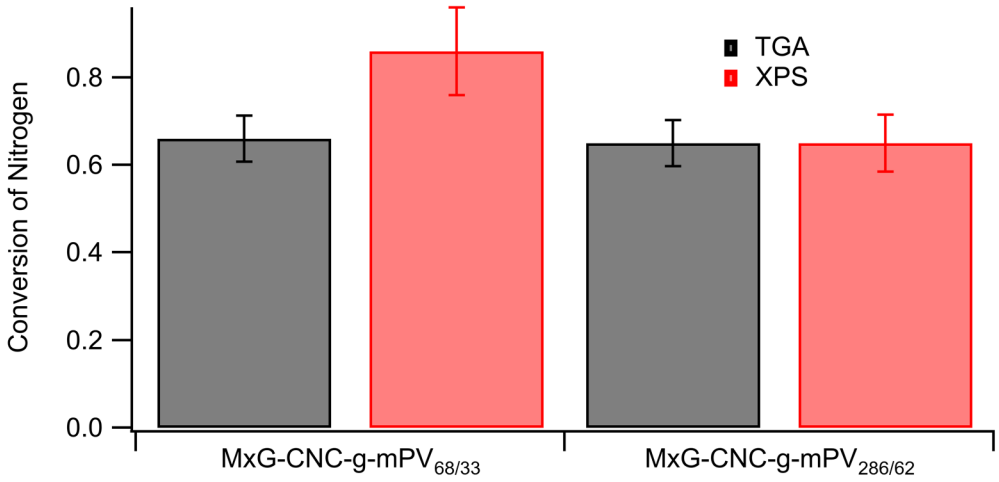

Figure S3.16: Measured degree of methylation of ***MxG*-CNC-*g*-mPV$_{68/33}$** and ***MxG*-CNC-*g*-mPV$_{286/82}$** obtained from TGA and XPS data.

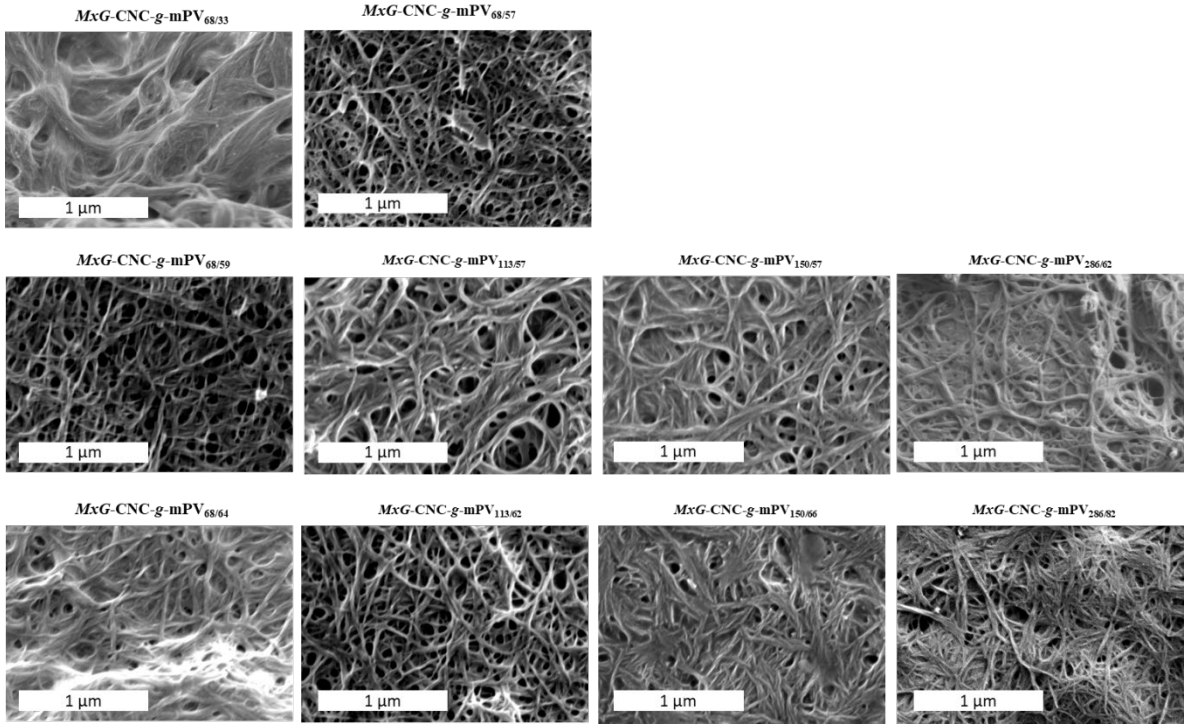

Figure S3.17: SEM of various ***MxG*-CNC-*g*-mPV**, as labeled coated in 2 nm Pt/Pd

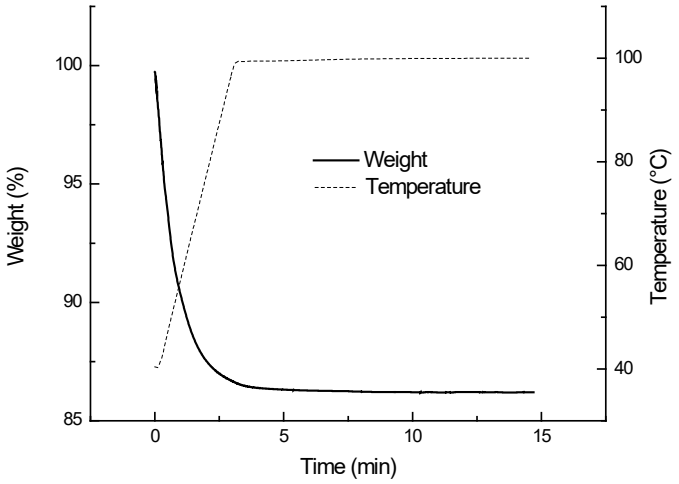

Figure S3.18: Characteristic TGA for measuring the water uptake of ***MxG*-CNC-*g*-mPV$_{286/82}$** at 95% RH

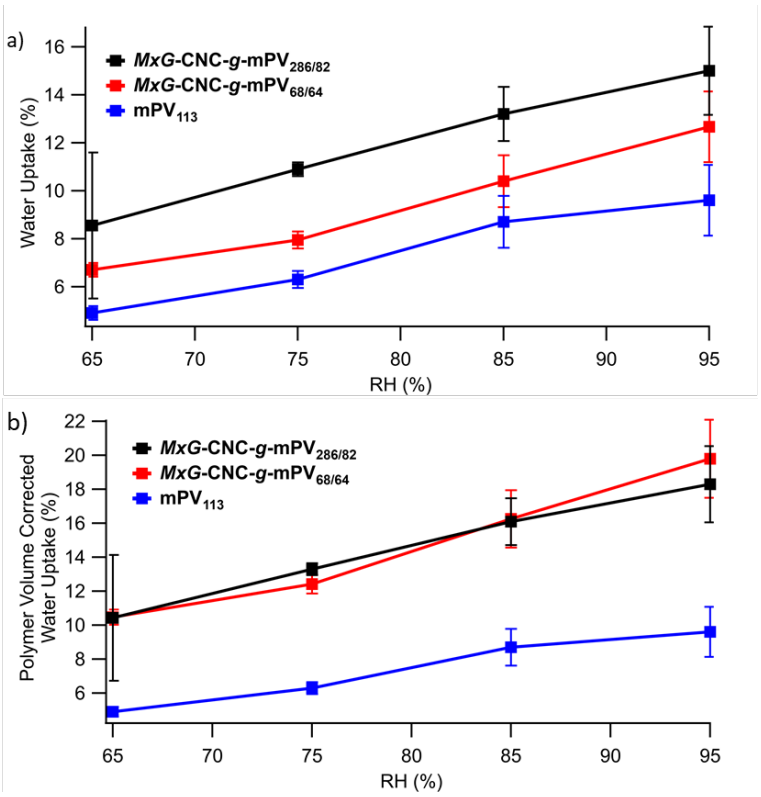

Figure S3.19: a) Measured water uptake and b) calculated water uptake of mPV component (adjusted for volume fraction of CNC) for ***MxG*-CNC-*g*-mPV$_{68/64}$** and ***MxG*-CNC-*g*-mPV$_{286/82}$**

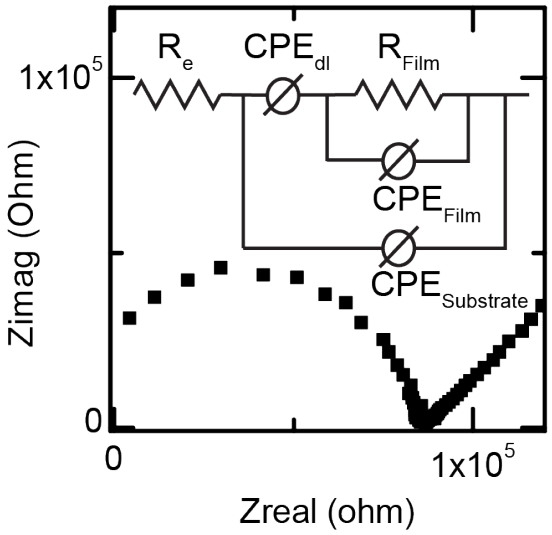

Figure S3.20: Nyquist plot and model fit for in-plane ***MxG*-CNC-*g*-mPV$_{68/33}$**

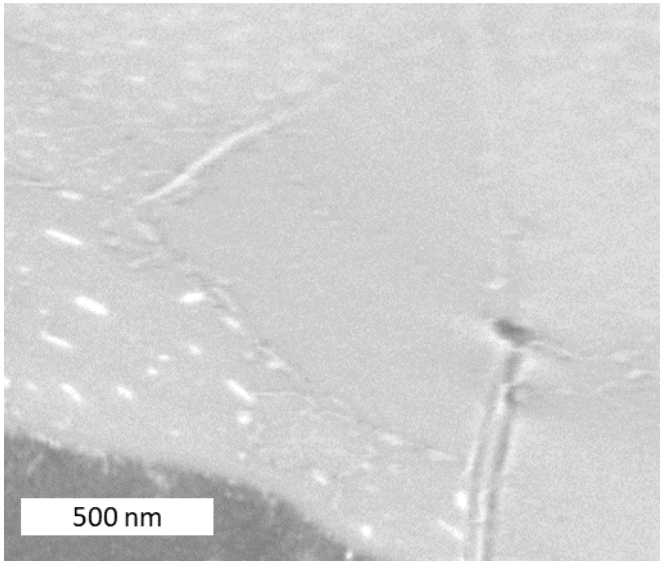

Figure S3.21: SEM of **mPV$_{68}$** with 10 vol% ***MxG*-CNC-Allyl** noting a flat surface in comparison to the individualized nanofibers of **Figure S3.16**.

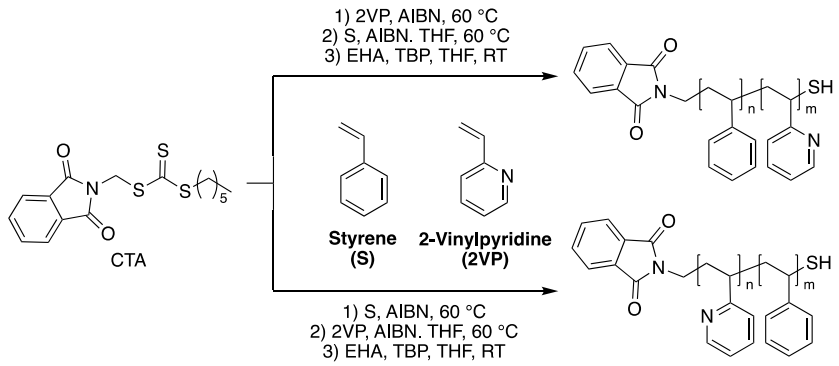

Scheme S3.2: Synthesis of the thiol-endcapped PS-PV block copolymers

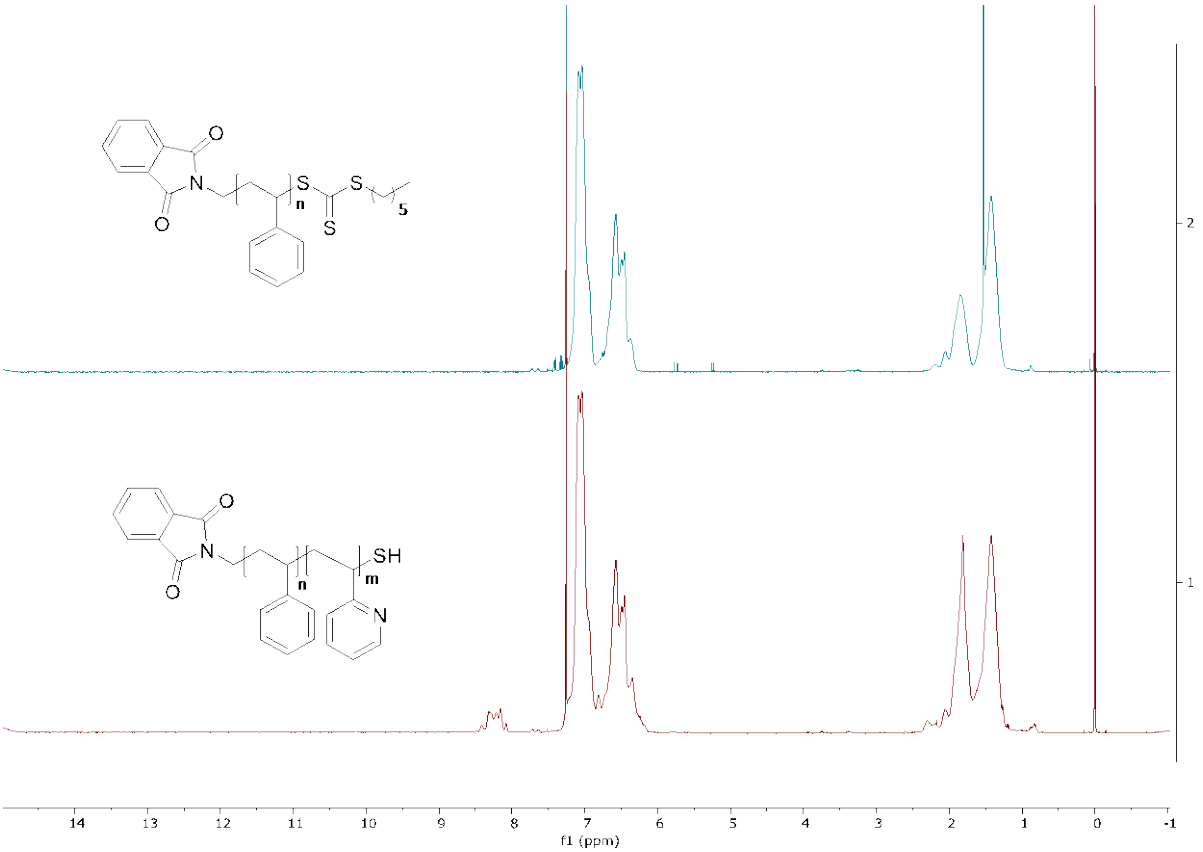

Figure S3.22: ^{1}H NMR (500 MHz, $CDCl_3$) spectra of **PS$_{329}$** and **PS-PV-SH$_{329,86}$**. Integration yields a f_{PV} = 0.21.

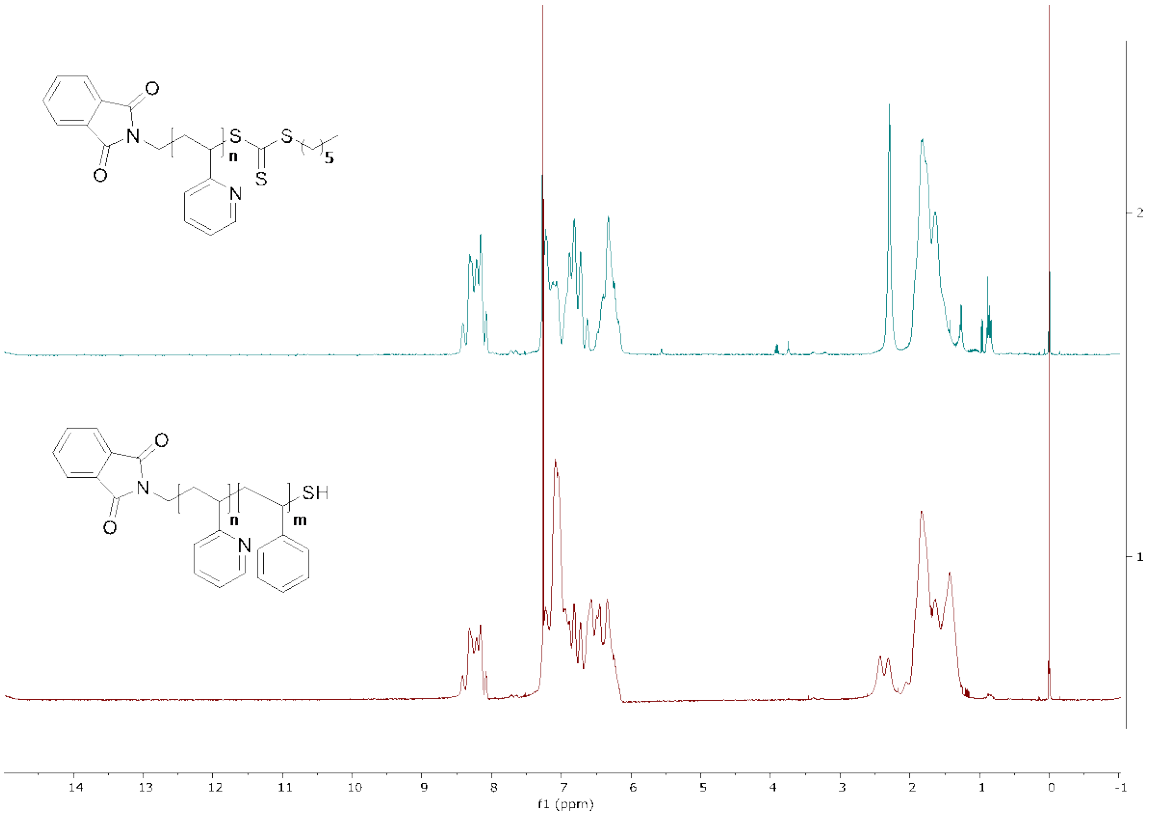

Figure S3.23: ^{1}H NMR (500 MHz, $CDCl_3$) spectra of **PV$_{286}$** and **PV-PS-SH$_{286,150}$**. Integration yields a $f_{PV} = 0.65$.

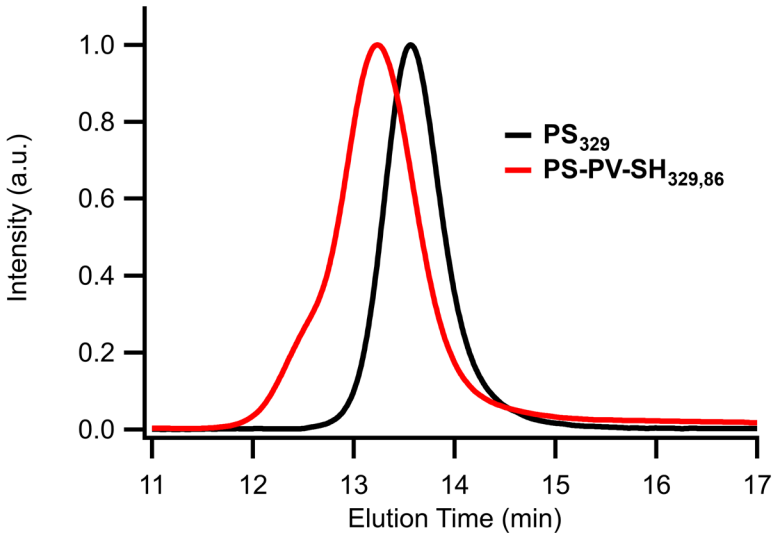

Figure S3.24: **PS-PV-SH$_{329,86}$** (red) and **PS$_{329}$** (black) GPC-MALS traces. Some chain end coupling is noted.

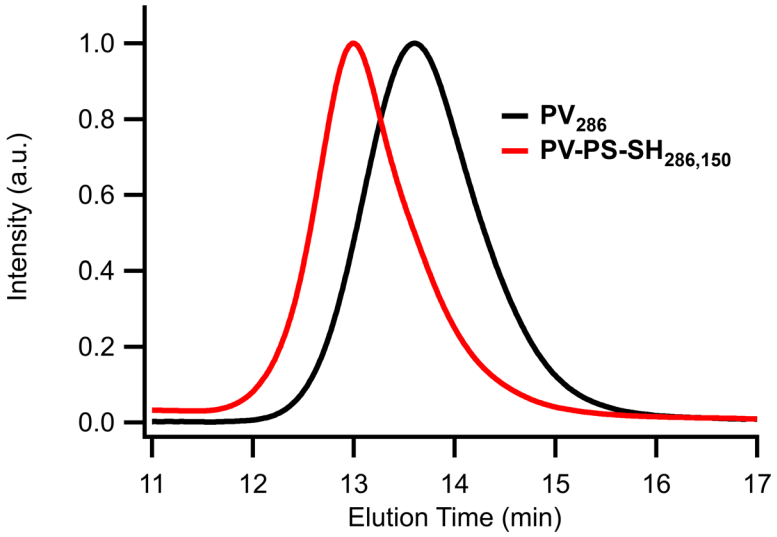

Figure S3.25: PV-PS-SH$_{286,150}$ (red) and **PV$_{286}$** (black) GPC-MALS Traces

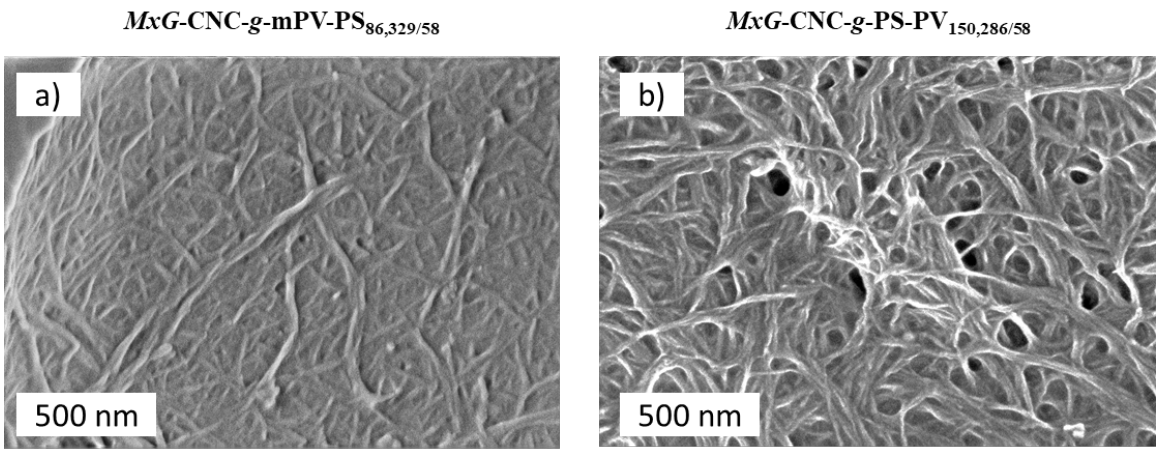

Figure S3.26: SEM of a) ***MxG*-CNC-*g*-PV-PS$_{86,329/58}$** and b) ***MxG*-CNC-*g*-PS-PV$_{150,286/58}$** coated in 2 nm Pt/Pd.

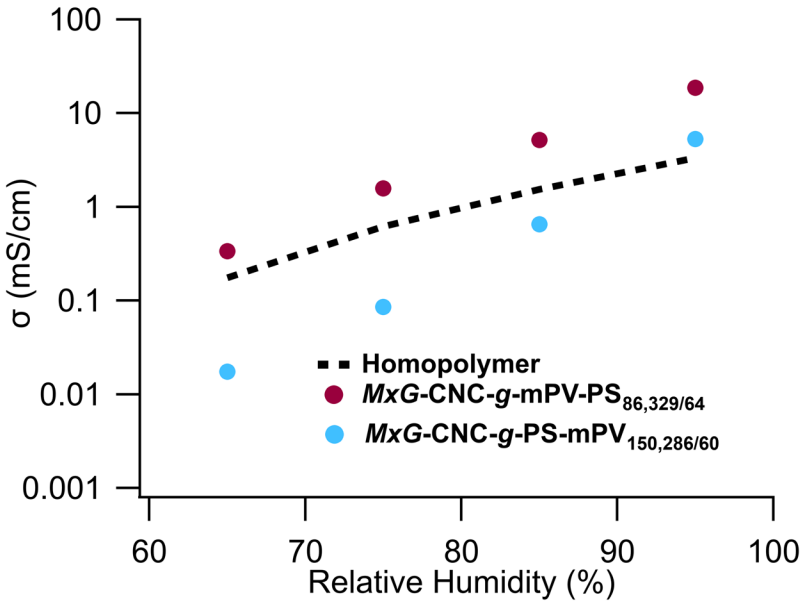

Figure S3.27: Measured conductivity data of the two diblock-grafted samples plotted against relative humidity along with **mPV** homopolymer (measured by IDE) for comparison (data adjusted for mPV volume fraction is shown in **Figure 3.4b**).

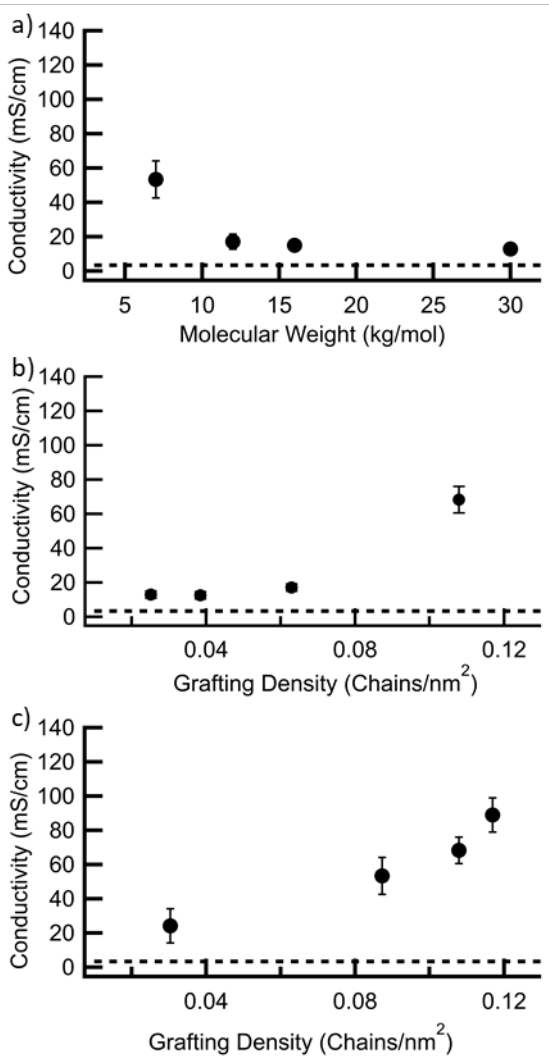

Figure S3.28: Measured conductivities of the **mPV** in the methylated PEGN films with a) similar grafting density but different molecular weight and grafting density, b) same volume fraction but differing molecular weights and grafting density, and c) same molecular weight grafted polyelectrolyte but different grafting density and volume fraction. Dotted lines correspond to conductivity of methylated homopolymer and all conductivity data is obtained from 95% relative humidity and room temperature samples. (data adjusted for **mPV** volume fraction is shown in **Figure 3.5**).

3.7 REFERENCES

(1) Placke, T.; Kloepsch, R.; Dühnen, S.; Winter, M. Lithium Ion, Lithium Metal, and Alternative Rechargeable Battery Technologies: The Odyssey for High Energy Density. *J. Solid State Electrochem.* **2017**, *21* (7), 1939–1964. https://doi.org/10.1007/s10008-017-3610-7.

(2) Shi, Y.; Eze, C.; Xiong, B.; He, W.; Zhang, H.; Lim, T. M.; Ukil, A.; Zhao, J. Recent Development of Membrane for Vanadium Redox Flow Battery Applications: A Review. *Appl. Energy* **2019**, *238* (December 2018), 202–224. https://doi.org/10.1016/j.apenergy.2018.12.087.

(3) Beyene, H. D.; Werkneh, A. A.; Ambaye, T. G. Current Updates on Waste to Energy (WtE) Technologies: A Review. *Renew. Energy Focus* **2018**, *24* (March), 1–11. https://doi.org/10.1016/j.ref.2017.11.001.

(4) Liu, W.; Lin, D.; Sun, J.; Zhou, G.; Cui, Y. Improved Lithium Ionic Conductivity in Composite Polymer Electrolytes with Oxide-Ion Conducting Nanowires. *ACS Nano* **2016**, *10* (12), 11407–11413. https://doi.org/10.1021/acsnano.6b06797.

(5) Liu, W.; Lee, S. W.; Lin, D.; Shi, F.; Wang, S.; Sendek, A. D.; Cui, Y. Enhancing Ionic Conductivity in Composite Polymer Electrolytes with Well-Aligned Ceramic Nanowires. *Nat. Energy* **2017**, *2* (5), 1–7. https://doi.org/10.1038/nenergy.2017.35.

(6) Bet-Moushoul, E.; Mansourpanah, Y.; Farhadi, K.; Tabatabaei, M. TiO2 Nanocomposite Based Polymeric Membranes: A Review on Performance Improvement for Various Applications in Chemical Engineering Processes. *Chem. Eng. J.* **2016**, *283*, 29–46. https://doi.org/10.1016/j.cej.2015.06.124.

(7) Tang, C.; Hackenberg, K.; Fu, Q.; Ajayan, P. M.; Ardebili, H. High Ion Conducting Polymer Nanocomposite Electrolytes Using Hybrid Nanofillers. *Nano Lett.* **2012**, *12* (3), 1152–1156. https://doi.org/10.1021/nl202692y.

(8) Gurevitch, I.; Buonsanti, R.; Teran, A. A.; Gludovatz, B.; Ritchie, R. O.; Cabana, J.; Balsara, N. P. Nanocomposites of Titanium Dioxide and Polystyrene-Poly(Ethylene Oxide) Block Copolymer as Solid-State Electrolytes for Lithium Metal Batteries. *J. Electrochem. Soc.* **2013**, *160* (9), A1611–A1617. https://doi.org/10.1149/2.117309jes.

(9) Kim, J. W.; Ji, K. S.; Lee, J. P.; Park, J. W. Electrochemical Characteristics of Two Types of PEO-Based Composite Electrolyte with Functional SiO2. *J. Power Sources* **2003**, *119–121*, 415–421. https://doi.org/10.1016/S0378-7753(03)00263-5.

(10) Qian, X.; Gu, N.; Cheng, Z.; Yang, X.; Wang, E.; Dong, S. Impedance Study of (PEO)10LiClO4-Al2O3 Composite Polymer Electrolyte with Blocking Electrodes. *Electrochim. Acta* **2001**, *46* (12), 1829–1836. https://doi.org/10.1016/S0013-4686(00)00723-4.

(11) Manuel Stephan, A.; Nahm, K. S. Review on Composite Polymer Electrolytes for Lithium Batteries. *Polymer (Guildf).* **2006**, *47* (16), 5952–5964. https://doi.org/10.1016/j.polymer.2006.05.069.

(12) Wang, Y. J.; Pan, Y.; Kim, D. Conductivity Studies on Ceramic Li1.3Al0.3Ti1.7(PO4) 3-Filled PEO-Based Solid Composite Polymer Electrolytes. *J. Power Sources* **2006**, *159* (1 SPEC. ISS.), 690–701. https://doi.org/10.1016/j.jpowsour.2005.10.104.

(13) Liu, W.; Liu, N.; Sun, J.; Hsu, P. C.; Li, Y.; Lee, H. W.; Cui, Y. Ionic Conductivity Enhancement of Polymer Electrolytes with Ceramic Nanowire Fillers. *Nano Lett.* **2015**, *15* (4), 2740–2745. https://doi.org/10.1021/acs.nanolett.5b00600.

(14) Kumar, S. K.; Ganesan, V.; Riggleman, R. A. Perspective: Outstanding Theoretical Questions in Polymer-Nanoparticle Hybrids. *J. Chem. Phys.* **2017**, *147* (2). https://doi.org/10.1063/1.4990501.

(15) Cao, X.; Habibi, Y.; Lucia, L. A. One-Pot Polymerization, Surface Grafting, and Processing of Waterborne Polyurethane-Cellulose Nanocrystal Nanocomposites. *J. Mater. Chem.* **2009**, *19* (38), 7137. https://doi.org/10.1039/b910517d.

(16) Lin, N.; Dufresne, A. Physical and/or Chemical Compatibilization of Extruded Cellulose Nanocrystal Reinforced Polystyrene Nanocomposites. *Macromolecules* **2013**, *46* (14), 5570–5583. https://doi.org/10.1021/ma4010154.

(17) Habibi, Y.; Goffin, A.-L.; Schiltz, N.; Duquesne, E.; Dubois, P.; Dufresne, A. Bionanocomposites Based on Poly(ε-Caprolactone)-Grafted Cellulose Nanocrystals by Ring-Opening Polymerization. *J. Mater. Chem.* **2008**, *18* (41), 5002. https://doi.org/10.1039/b809212e.

(18) Wohlhauser, S.; Delepierre, G.; Labet, M.; Morandi, G.; Thielemans, W.; Weder, C.; Zoppe, J. O. Grafting Polymers from Cellulose Nanocrystals: Synthesis, Properties, and Applications. *Macromolecules* **2018**, *51* (16), 6157–6189. https://doi.org/10.1021/acs.macromol.8b00733.

(19) Morandi, G.; Heath, L.; Thielemans, W. Cellulose Nanocrystals Grafted with Polystyrene Chains through Surface-Initiated Atom Transfer Radical Polymerization (SI-ATRP). *Langmuir* **2009**, *25* (14), 8280–8286. https://doi.org/10.1021/la900452a.

(20) Hore, M. J. A. Polymers on Nanoparticles: Structure & Dynamics. *Soft Matter* **2019**, *15* (6), 1120–1134. https://doi.org/10.1039/c8sm02110d.

(21) Hore, M. J. A.; Korley, L. S. T. J.; Kumar, S. K. Polymer-Grafted Nanoparticles. *J. Appl. Phys.* **2020**, *128* (3). https://doi.org/10.1063/5.0019326.

(22) Kumar, S. K.; Jouault, N.; Benicewicz, B.; Neely, T. Nanocomposites with Polymer Grafted Nanoparticles. *Macromolecules* **2013**, *46* (9), 3199–3214. https://doi.org/10.1021/ma4001385.

(23) Chancellor, A. J.; Seymour, B. T.; Zhao, B. Characterizing Polymer-Grafted Nanoparticles: From Basic Defining Parameters to Behavior in Solvents and Self-Assembled Structures. *Anal. Chem.* **2019**, *91* (10), 6391–6402. https://doi.org/10.1021/acs.analchem.9b00707.

(24) Fernandes, N. J.; Koerner, H.; Giannelis, E. P.; Vaia, R. A. Hairy Nanoparticle Assemblies as One-Component Functional Polymer Nanocomposites: Opportunities and Challenges. *MRS Commun.* **2013**, *3* (1), 13–29. https://doi.org/10.1557/mrc.2013.9.

(25) Schmitt, M.; Choi, J.; Min Hui, C.; Chen, B.; Korkmaz, E.; Yan, J.; Margel, S.; Burak Ozdoganlar, O.; Matyjaszewski, K.; Bockstaller, M. R. Processing Fragile Matter: Effect of Polymer Graft Modification on the Mechanical Properties and Processibility of (Nano-) Particulate Solids. *Soft Matter* **2016**, *12* (15), 3527–3537. https://doi.org/10.1039/C6SM00095A.

(26) Choi, J.; Hui, C. M.; Pietrasik, J.; Dong, H.; Matyjaszewski, K.; Bockstaller, M. R. Toughening Fragile Matter: Mechanical Properties of Particle Solids Assembled from Polymer-Grafted Hybrid Particles Synthesized by ATRP. *Soft Matter* **2012**, *8* (15), 4072. https://doi.org/10.1039/c2sm06915f.

(27) Jiao, Y.; Tibbits, A.; Gillman, A.; Hsiao, M. S.; Buskohl, P.; Drummy, L. F.; Vaia, R. A. Deformation Behavior of Polystyrene-Grafted Nanoparticle Assemblies with Low Grafting Density. *Macromolecules* **2018**, *51* (18), 7257–7265. https://doi.org/10.1021/acs.macromol.8b01524.

(28) Hansoge, N. K.; Keten, S. Effect of Polymer Chemistry on Chain Conformations in Hairy Nanoparticle Assemblies. *ACS Macro Lett.* **2019**, 1209–1215. https://doi.org/10.1021/acsmacrolett.9b00526.

(29) Hansoge, N. K.; Huang, T.; Sinko, R.; Xia, W.; Chen, W.; Keten, S. Materials by Design for Stiff and Tough Hairy Nanoparticle Assemblies. *ACS Nano* **2018**, *12* (8), 7946–7958. https://doi.org/10.1021/acsnano.8b02454.

(30) Arges, C. G.; Li, K.; Zhang, L.; Kambe, Y.; Wu, G.-P.; Lwoya, B.; Albert, J. N. L.; Nealey, P. F.; Kumar, R. Ionic Conductivity and Counterion Condensation in Nanoconfined Polycation and Polyanion Brushes Prepared from Block Copolymer Templates. *Mol. Syst. Des. Eng* **2019**, *4*, 365. https://doi.org/10.1039/c8me00081f.

(31) Dong, B. X.; Bennington, P.; Kambe, Y.; Sharon, D.; Dolejsi, M.; Strzalka, J.; Burnett, V. F.; Nealey, P. F.; Patel, S. N. Nanothin Film Conductivity Measurements Reveal Interfacial Influence on Ion Transport in Polymer Electrolytes. *Mol. Syst. Des. Eng.* **2019**, *4* (3), 597–608. https://doi.org/10.1039/c9me00011a.

(32) Teran, A. A.; Tang, M. H.; Mullin, S. A.; Balsara, N. P. Effect of Molecular Weight on Conductivity of Polymer Electrolytes. *Solid State Ionics* **2011**, *203* (1), 18–21. https://doi.org/10.1016/j.ssi.2011.09.021.

(33) Jia, Z.; Yuan, W.; Zhao, H.; Hu, H.; Baker, G. L. Composite Electrolytes Comprised of

Poly(Ethylene Oxide) and Silica Nanoparticles with Grafted Poly(Ethylene Oxide)-Containing Polymers. *RSC Adv.* **2014**, *4* (77), 41087–41098. https://doi.org/10.1039/c4ra07262f.

(34) Liu, G.; Cai, M.; Wang, X.; Zhou, F.; Liu, W. Core-Shell-Corona-Structured Polyelectrolyte Brushes-Grafting Magnetic Nanoparticles for Water Harvesting. *ACS Appl. Mater. Interfaces* **2014**, *6* (14), 11625–11632. https://doi.org/10.1021/am502351x.

(35) Saleh, N.; Sarbu, T.; Sirk, K.; Lowry, G. V.; Matyjaszewski, K.; Tilton, R. D. Oil-in-Water Emulsions Stabilized by Highly Charged Polyelectrolyte-Grafted Silica Nanoparticles. *Langmuir* **2005**, *21* (22), 9873–9878. https://doi.org/10.1021/la050654r.

(36) Mei, Y.; Sharma, G.; Lu, Y.; Ballauff, M.; Drechsler, M.; Irrgang, T.; Kempe, R. High Catalytic Activity of Platinum Nanoparticles Immobilized on Spherical Polyelectrolyte Brushes. *Langmuir* **2005**, *21* (26), 12229–12234. https://doi.org/10.1021/la052120w.

(37) Jiao, Y.; Chou, T.; Akcora, P. Design of Ion-Containing Polymer-Grafted Nanoparticles for Conductive Membranes. *Macromolecules* **2015**, *48* (14), 4910–4917. https://doi.org/10.1021/acs.macromol.5b00758.

(38) Agrawal, A.; Choudhury, S.; Archer, L. A. A Highly Conductive, Non-Flammable Polymer-Nanoparticle Hybrid Electrolyte. *RSC Adv.* **2015**, *5* (27), 20800–20809. https://doi.org/10.1039/c5ra01031d.

(39) Wang, P.; Zhou, Y. N.; Luo, J. S.; Luo, Z. H. Poly(Ionic Liquid)s-Based Nanocomposite Polyelectrolytes with Tunable Ionic Conductivity Prepared via SI-ATRP. *Polym. Chem.* **2014**, *5* (3), 882–891. https://doi.org/10.1039/c3py01025b.

(40) Mariano, M.; El Kissi, N.; Dufresne, A. Cellulose Nanocrystals and Related Nanocomposites: Review of Some Properties and Challenges. *J. Polym. Sci. Part B Polym. Phys.* **2014**, *52* (12), 791–806. https://doi.org/10.1002/polb.23490.

(41) Eichhorn, S. J.; Dufresne, A.; Aranguren, M.; Marcovich, N. E.; Capadona, J. R.; Rowan, S. J.; Weder, C.; Thielemans, W.; Roman, M.; Renneckar, S.; Gindl, W.; Veigel, S.; Keckes, J.; Yano, H.; Abe, K.; Nogi, M.; Nakagaito, A. N.; Mangalam, A.; Simonsen, J.; Benight, A. S.; Bismarck, A.; Berglund, L. A.; Peijs, T. Review: Current International Research into Cellulose Nanofibres and Nanocomposites. *J. Mater. Sci.* **2010**, *45* (1), 1–33. https://doi.org/10.1007/s10853-009-3874-0.

(42) Calvino, C.; Macke, N.; Kato, R.; Rowan, S. J. Development, Processing and Applications of Bio-Sourced Cellulose Nanocrystal Composites. *Progress in Polymer Science*. 2020, pp 1–21. https://doi.org/10.1016/j.progpolymsci.2020.101221.

(43) Capadona, J. R.; Van Den Berg, O.; Capadona, L. A.; Schroeter, M.; Rowan, S. J.; Tyler, D. J.; Weder, C.; Berg, O. V. a N. D. E. N. A Versatile Approach for the Processing of Polymer Nanocomposites with Self-Assembled Nanofibre Templates. *Nat. Nanotechnol.* **2007**, *2* (12), 765–769. https://doi.org/10.1038/nnano.2007.379.

(44) Dagnon, K. L.; Way, A. E.; Carson, S. O.; Silva, J.; Maia, J.; Rowan, S. J. Controlling the Rate of Water-Induced Switching in Mechanically Dynamic Cellulose Nanocrystal Composites. *Macromolecules* **2013**, *46* (20), 8203–8212. https://doi.org/10.1021/ma4008187.

(45) Cudjoe, E.; Hunsen, M.; Xue, Z.; Way, A. E.; Barrios, E.; Olson, R. A.; Hore, M. J. A.; Rowan, S. J. Miscanthus Giganteus: A Commercially Viable Sustainable Source of Cellulose Nanocrystals. *Carbohydr. Polym.* **2017**, *155*, 230–241. https://doi.org/10.1016/j.carbpol.2016.08.049.

(46) Gadim, T. D. O.; Vilela, C.; Loureiro, F. J. A.; Silvestre, A. J. D.; Freire, C. S. R.; Figueiredo, F. M. L. Nafion® and Nanocellulose: A Partnership for Greener Polymer Electrolyte Membranes. *Ind. Crops Prod.* **2016**, *93*, 212–218. https://doi.org/10.1016/j.indcrop.2016.01.028.

(47) Kim, D. J.; Jo, M. J.; Nam, S. Y. A Review of Polymer-Nanocomposite Electrolyte Membranes for Fuel Cell Application. *J. Ind. Eng. Chem.* **2015**, *21*, 36–52. https://doi.org/10.1016/j.jiec.2014.04.030.

(48) Cheng, X.; Wang, J.; Liao, Y.; Li, C.; Wei, Z. Enhanced Conductivity of Anion-Exchange Membrane by Incorporation of Quaternized Cellulose Nanocrystal. *ACS Appl. Mater. Interfaces* **2018**, *10* (28), 23774–23782. https://doi.org/10.1021/acsami.8b05298.

(49) Jabbour, L.; Bongiovanni, R.; Beneventi, D. Cellulose-Based Li-Ion Batteries : A Review. *Cellulose* **2013**, No. 20, 1523–1545. https://doi.org/10.1007/s10570-013-9973-8.

(50) Kreuer, K. D. Ion Conducting Membranes for Fuel Cells and Other Electrochemical Devices. *Chem. Mater.* **2014**, *26* (1), 361–380. https://doi.org/10.1021/cm402742u.

(51) Rincón-Iglesias, M.; Lizundia, E.; Costa, C. M.; Lanceros-Méndez, S. Tailoring Electrical and Mechanical Properties of All-Natural Polymer Composites for Environmentally Friendlier Electronics. *ACS Appl. Polym. Mater.* **2020**, *2* (4), 1448–1457. https://doi.org/10.1021/acsapm.9b01098.

(52) Wohlhauser, S.; Kuhnt, T.; Meesorn, W.; Montero De Espinosa, L.; Zoppe, J. O.; Weder, C. One-Component Nanocomposites Based on Polymer-Grafted Cellulose Nanocrystals. *Macromolecules* **2020**, *53*, 821–834. https://doi.org/10.1021/acs.macromol.9b01612.

(53) Kato, R.; Lettow, J. H.; Patel, S. N.; Rowan, S. J. Ion-Conducting Thermoresponsive Films Based on Polymer-Grafted Cellulose Nanocrystals. *ACS Appl. Mater. Interfaces* **2020**, *12*, 54083–54093. https://doi.org/10.1021/acsami.0c16059.

(54) Kambe, Y.; Arges, C. G.; Patel, S. N.; Stoykovich, M. P.; Nealey, P. F. Ion Conduction in Microphase-Separated Block Copolymer Electrolytes. *Electrochemical Society Interface*. 2017, pp 61–67. https://doi.org/10.1149/2.F07171if.

(55) Arges, C. G.; Kambe, Y.; Suh, H. S.; Ocola, L. E.; Nealey, P. F. Perpendicularly Aligned,

Anion Conducting Nanochannels in Block Copolymer Electrolyte Films. *Chem. Mater.* **2016**, *28* (5), 1377–1389. https://doi.org/10.1021/acs.chemmater.5b04452.

(56) Virgili, J. M.; Hexemer, A.; Pople, J. A.; Balsara, N. P.; Segalman, R. A. Phase Behavior of Polystyrene-Block-Poly(2-Vinylpyridine) Copolymers in a Selective Ionic Liquid Solvent. *Macromolecules* **2009**, *42* (13), 4604–4613. https://doi.org/10.1021/ma900483n.

(57) Weiss, A. M.; MacKe, N.; Zhang, Y.; Calvino, C.; Esser-Kahn, A. P.; Rowan, S. J. In Vitro and in Vivo Analyses of the Effects of Source, Length, and Charge on the Cytotoxicity and Immunocompatibility of Cellulose Nanocrystals. *ACS Biomater. Sci. Eng.* **2021**, *7* (4), 1450–1461. https://doi.org/10.1021/acsbiomaterials.0c01618.

(58) Sharon, D.; Bennington, P.; Liu, C.; Kambe, Y.; Dong, B. X.; Burnett, V. F.; Dolejsi, M.; Grocke, G.; Patel, S. N.; Nealey, P. F. Interrogation of Electrochemical Properties of Polymer Electrolyte Thin Films with Interdigitated Electrodes. *J. Electrochem. Soc.* **2018**, *165* (16), H1028–H1039. https://doi.org/10.1149/2.0291816jes.

(59) Postma, A.; Davis, T. P.; Evans, R. A.; Li, G.; Moad, G.; O'Shea, M. S. Synthesis of Well-Defined Polystyrene with Primary Amine End Groups through the Use of Phthalimido-Functional RAFT Agents. *Macromolecules* **2006**, *39* (16), 5293–5306. https://doi.org/10.1021/ma060245h.

(60) Discekici, E. H.; Shankel, S. L.; Anastasaki, A.; Oschmann, B.; Lee, I.-H.; Niu, J.; McGrath, A. J.; Clark, P. G.; Laitar, D. S.; de Alaniz, J. R.; Hawker, C. J.; Lunn, D. J. Dual-Pathway Chain-End Modification of RAFT Polymers Using Visible Light and Metal-Free Conditions. *Chem. Commun.* **2017**, *53* (11), 1888–1891. https://doi.org/10.1039/C6CC08370F.

(61) Zhang, Y.; Edelbrock, A. N.; Rowan, S. J. Effect of Processing Conditions on the Mechanical Properties of Bio-Inspired Mechanical Gradient Nanocomposites. *Eur. Polym. J.* **2019**, *115* (March), 107–114. https://doi.org/10.1016/j.eurpolymj.2019.03.022.

(62) Discekici, E. H.; Shankel, S. L.; Anastasaki, A.; Oschmann, B.; Lee, I.-H.; Niu, J.; McGrath, A. J.; Clark, P. G.; Laitar, D. S.; de Alaniz, J. R.; Hawker, C. J.; Lunn, D. J. Dual-Pathway Chain-End Modification of RAFT Polymers Using Visible Light and Metal-Free Conditions. *Chem. Commun.* **2017**, *53* (11), 1888–1891. https://doi.org/10.1039/C6CC08370F.

(63) Takahashi, Y.; Ochiai, N.; Matsushita, Y.; Noda, I. Viscoelastic Properties of Poly(2-Vinylpyridine) in Bulk and Solution. *Polym. J.* **1996**, *28* (12), 1065–1070. https://doi.org/10.1295/polymj.28.1065.

(64) Matsuchita, Y.; Shimizu, K.; Nakao, Y.; Choshi, H.; Noda, I.; Nagasawa, M. Preparation and Characterization of Poly(2-Vinylpyridine)s with Narrow Molecular Weight Distributions. *Polym. J.* **1986**, *18* (4), 361–366.

(65) Wargacki, S. P.; Pate, B.; Vaia, R. A. Fabrication of 2D Ordered Films of Tobacco Mosaic

Virus (TMV): Processing Morphology Correlations for Convective Assembly. *Langmuir* **2008**, *24* (10), 5439–5444. https://doi.org/10.1021/la7040778.

(66) Shopsowitz, K. E.; Qi, H.; Hamad, W. Y.; MacLachlan, M. J. Free-Standing Mesoporous Silica Films with Tunable Chiral Nematic Structures. *Nature* **2010**, *468* (7322), 422–426. https://doi.org/10.1038/nature09540.

(67) Meseck, G. R.; Terpstra, A. S.; MacLachlan, M. J. Liquid Crystal Templating of Nanomaterials with Nature's Toolbox. *Curr. Opin. Colloid Interface Sci.* **2017**, *29*, 9–20. https://doi.org/10.1016/j.cocis.2017.01.003.

(68) Natarajan, B.; Emiroglu, C.; Obrzut, J.; Fox, D. M.; Pazmino, B.; Douglas, J. F.; Gilman, J. W. Dielectric Characterization of Confined Water in Chiral Cellulose Nanocrystal Films. *ACS Appl. Mater. Interfaces* **2017**, *9* (16), 14222–14231. https://doi.org/10.1021/acsami.7b01674.

(69) Chu, W.; Webb, M. A.; Deng, C.; Colon, Y. J.; Kambe, Y.; Krishnan, S.; Nealey, P. F.; de Pablo, J. J. Understanding Ion Mobility in P2VP/NMP+I − Polymer Electrolytes: A Combined Simulation and Experimental Study. *Macromolecules* **2020**, *53* (8), 2783–2792. https://doi.org/10.1021/acs.macromol.9b02329.

(70) Mendez, J.; Annamalai, P. K.; Eichhorn, S. J.; Rusli, R.; Rowan, S. J.; Foster, E. J.; Weder, C. Bioinspired Mechanically Adaptive Polymer Nanocomposites with Water-Activated Shape-Memory Effect. *Macromolecules* **2011**, *44* (17), 6827–6835. https://doi.org/10.1021/ma201502k.

(71) Nanocomposites, S. P.; Capadona, J. R.; Shanmuganathan, K.; Tyler, D. J.; Rowan, S. J.; Weder, C.; J, S. Stimuli-Responsive Polymer Nanocomposites Inspired by the Sea Cucumber Dermis. *Science (80-.).* **2008**, No. March, 1370–1375. https://doi.org/10.1126/science.1153307.

(72) Jin, L.; Li, W.; Xu, Q.; Sun, Q. Amino-Functionalized Nanocrystalline Cellulose as an Adsorbent for Anionic Dyes. *Cellulose* **2015**, *22* (4), 2443–2456. https://doi.org/10.1007/s10570-015-0649-4.

(73) Zhang, T.; Cheng, Q.; Ye, D.; Chang, C. Tunicate Cellulose Nanocrystals Reinforced Nanocomposite Hydrogels Comprised by Hybrid Cross-Linked Networks. *Carbohydr. Polym.* **2017**, *169*, 139–148. https://doi.org/10.1016/j.carbpol.2017.04.007.

(74) Gallo, A. B.; Simões-Moreira, J. R.; Costa, H. K. M.; Santos, M. M.; Moutinho dos Santos, E. Energy Storage in the Energy Transition Context: A Technology Review. *Renew. Sustain. Energy Rev.* **2016**, *65*, 800–822. https://doi.org/10.1016/j.rser.2016.07.028.

(75) Sharon, D.; Bennington, P.; Dolejsi, M.; Webb, M. A.; Dong, B. X.; De Pablo, J. J.; Nealey, P. F.; Patel, S. N. Intrinsic Ion Transport Properties of Block Copolymer Electrolytes. *ACS Nano* **2020**, *14* (7), 8902–8914. https://doi.org/10.1021/acsnano.0c03713.

Chapter 4

Orientation Dependent Ionic Conductivity of Polyelectrolyte-grafted Cellulose Nanocrystal Films

4.1 INTRODUCTION

Previous literature investigation of aligned nanofiber-based nanocomposites, as compared to either nanorods or nanosphere inclusions, yielded the greatest degree of enhancement in conductivity within the same set of materials. For example, work by Liu et al. utilized $Li_{0.33}La_{0.557}TiO_3$ nanofiller with $LiClO_4$ in poly(acrylonitrile) due to beneficial surface-matrix interactions by participating in lithium-ion transport for enhanced conductivity. Initial work established that nanowires enhanced ionic transport better than spherical nanoparticles at similar loadings due to extended regimes of enhanced transport along the nanorods compared to the spheres.[1] Building upon this finding, well aligned nanorods established by electrospinning yielded even greater ionic conductivity, enhancing it by greater than an order of magnitude compared to random nanorod orientations. Additionally, the angle of nanorods compared to the applied current was experimentally and computationally studied resulting in good agreement, which showed that perfectly parallel (highest conductivity) compared to perpendicular (lowest conductivity) orientation had over 3 orders of magnitude difference in conductivity. Thus, if measurement setups either align nanofiller perpendicular or parallel to applied electric fields, particularly of conductivity enhancing interfaces, the impact on ionic conductivity can be massive.

The discovery of enhancement in ionic conductivity of polymer electrolyte grafted nanoparticles (PEGNs) based on methylated poly(2-vinylpyridine) (**mPV**) grafted to cellulose nanocrystals (CNCs) solvent cast to form ***MxG*-CNC-*g*-mPV** films shown in chapter 3 was a fortuitous outcome of attempting to confirm the volume fraction of grafted polymer via interpolation from ionic conductivity measurements. However, in doing so, the initial measurement setup yielded an intriguing double hemisphere in Nyquist plot (used to calculate the conductivity) of the electrical impedance spectroscopy (EIS) for the in-plane sample with only a

single hemisphere for the through-plane measurement. A single hemisphere can be correlated to physically intuitive Randall cell model, which can then be used to determine the material conductivity.[2,3] However, two-hemispheres would correlate to two conductivity values,[2] a surprise for this system. Nonetheless, looking at both calculated values, a strong anisotropy in conductivity, made the material system intriguing with in-plane conductivity showing an order of magnitude enhancement.

To probe this effect, the material structure and ionic conductivity were investigated using Scanning Electron Microscopy, Wide Angle X-Ray Scattering, and variations on the experimental setup for EIS. The results of those experiments constitute this chapter.

4.2 EXPERIMENTAL METHODS

4.2.1 Instrumentation

Scanning Electron Microscopy (SEM): SEM images of the cast films were taken with the Carl Zeiss−Merlin field emission scanning electron microscope. The acceleration voltage was 1.0 kV with a working distance of 2 to 3 mm using an in-lens detector. Two nanometers of Pt/Pd was sputtered onto the surface of the device using the Cressington 108 Auto Sputter Coater to reduce electron beam charging and improve the image quality.

Wide Angle X-Ray (WAXS): WAXS experiments were performed on a laboratory SAXSLAB GANESHA 300 XL system. On the GANESHA system, samples were irradiated using a Cu Kα source (λ = 0.154 nm) at a voltage of 40 kV for 30 min. Through-plane measurements were performed by irradiating perpendicularly to the cast film while in-plane measurements were performed by irradiating films attached to a silicon substrate in a parallel method.

Atomic force microscopy (AFM). The dimensions of ***MxG*-CNC-*g*-PV** were investigated by Asylum Research Oxford Instruments Cypher ES AFM. A drop of CNCs suspension (0.01 wt%) was placed on a freshly cleaved mica surface which was pretreated with poly-l-lysine solution, and then rinsed off after five minutes. The images were acquired using AC Tapping mode. The sizes of nanoparticles were analyzed by Gwyddion software.

Electrochemical Impedance Spectroscopy (EIS): The electrochemical properties of the samples were probed using the Gamry reference 600 potentiostat/galvanostat. AC electrical impedance spectroscopy (EIS) measurements were made from 1 MHz to 1 Hz by connecting the samples in either an in-plane or through-plane method. For through-plane measurements, the film sample was connected between sheets of Pt foil to the potentiostat/ galvanostat. For in-plane measurements, the film sample was connected via either platinum wire connections using a Teflon holding

mechanism or via larger Pt/ Pd 20 nm deposited pads with the Cressington 108 Auto Sputter Coater An amplitude voltage of 10 mV was used. The measurements were made in a chamber with controlled temperature (25 °C) and relative humidity (65-95% RH) after an equilibration period of 2 hrs. For in-plane measurements on interdigitated electrodes (IDEs), samples were prepared on IDEs using an identical method to the AFM samples and connected to the potentiostat.

4.2.2 Material Synthesis

The ***t*-CNC-*g*-mPV** films studied in this chapter were synthesized in a similar manner to materials described in Chapter 3. A detailed synthetic scheme is described elsewhere (see also Chapter 3). Specifically, *tunicate* (*t*) CNCs with allyl surface functionality were prepared as previously described. α-Phthalimidomethyl-ω-thiolpoly(2-vinylpyridine) (**PV-SH**) was synthesized via RAFT polymerization of 2-vinylpyridine followed by reduction of the trithiocarbonate via aminolysis. In distinction to the thermally driven radical generation of radicals for thiol-ene reactions in Chapter 3, ***t*-CNC-*g*-PV** nanoparticles were synthesized using Phenylbis(2,4,6-trimethylbenzoyl)phosphine oxide (BAPO) to generate radicals via UV light, following the same 1:1:0.1 ratio of allyl group to polymer thiol to BAPO. All molecular weights and dispersities were determined via GPC-MALS (THF) with corresponding ^{1}H NMR characterization. Weight percent of polymer was calculated via Thermal gravimetric analysis, with volume percent polymer and grafting density calculations following previously described analysis from Chapter 3.

4.3 RESULTS AND DISCUSSION

The material investigated in this work is ***t*-CNC-*g*-PV$_{68/26}$** which becomes ***t*-CNC-*g*-mPV$_{68/33}$** when methylated with iodomethane to introduce the conductive iodide. In this nomenclature, the grafted polymer has a degree of polymerization of 68, with a volume percent of grafted polymer either of 26% prior to methylation or 33% after methylation. The synthetic scheme of this materials is shown in **Scheme 4.1**, where the principal distinction from the work in Chapter 3 is the use of Tunicate CNCs and a BAPO radical initiator.

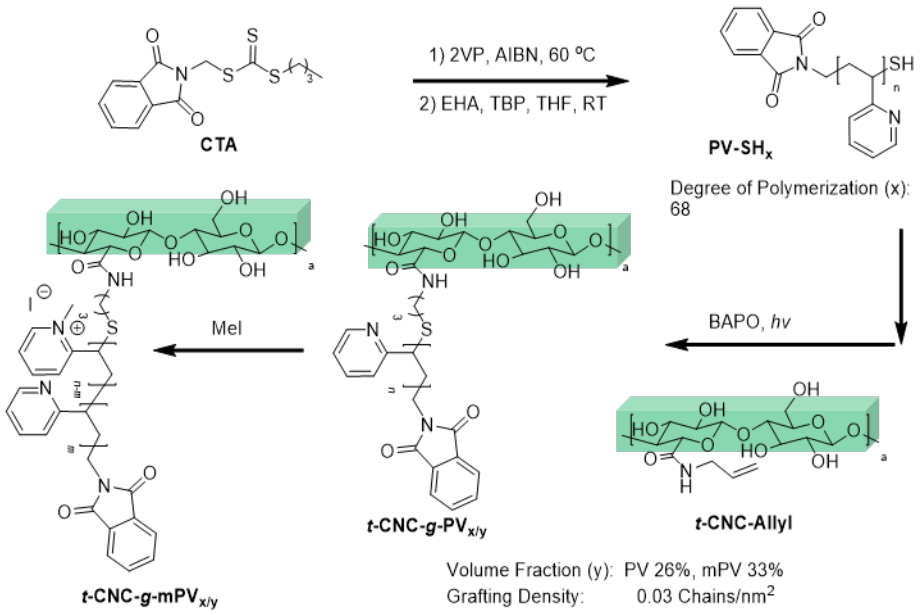

Scheme 4.1: Synthesis of ***t*-CNC-*g*-mPV$_{68/33}$** using thiol-ene reaction to attach thiol terminated poly(2-vinylpyridine) (**PV-SH**) to tunicate sourced CNCs with attached allyl functionality (***t*-CNC-Allyl**) to **make *t*-CNC-*g*-PV$_{68/26}$**, after which reaction with iodomethane produces the desired product.

EIS measurements of ***t*-CNC-*g*-mPV$_{68/33}$** shows standard Randell cell-based Nyquist plots for through-plane measurements however in-plane shows two hemispheres corresponding to two electrochemical processes, which in literature is correlated with two conductivities.[2] The resistance of a material film, R_{film}, can be modeled by fitting a Randell cell to the Nyquist plot hemisphere. **Figure 4.1** shows the Nyquist plots of ***t*-CNC-*g*-mPV$_{68/33}$** alongside the experimental set ups for through-plane and in-plane measurements. Specifically, **Figure 4.1d** shows a perfect example of a Randell cell setup with a single hemisphere, which is clear evidence for a single, principal electrochemical process namely ionic conductivity for the through-plane measurement.[4] However, **Figure 4.1e** shows two hemispheres corresponding to two electrochemical processes. Given that conductivity, σ, is defined by,

$$\sigma = d/(R_{film}A) \tag{4.1}$$

where d is the separation distance between electrodes and A is the cross-sectional area probed, understanding which hemisphere to fit, and thus which electrochemical process corresponding to in-plane conductivity, is of utmost importance to determine.

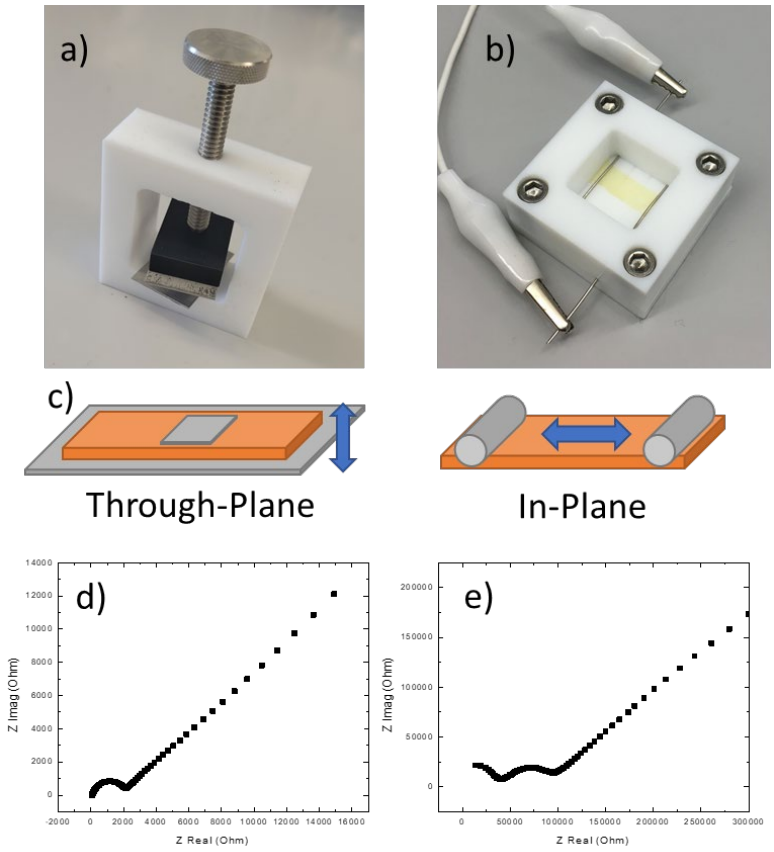

Figure 4.1: Optical image of the a) through-plane and b) in-plane instrument for measuring electrical impedance spectroscopy, c) cartoon depiction of the through-plane and in-plane, d) through plane and e) in-plane Nyquist plots of the *t*-CNC-*g*-mPV$_{68/33}$ film at 85% RH

Scanning electron microscopy (SEM) images (**Figure 4.2**) show the top down and cross-sectional images of the ***t*-CNC-*g*-mPV$_{68/33}$** film which helps to elucidate the structure of the PEGN film. The top-down image (**Figure 4.2a**) shows well-defined, individualized nanorods. Further results in Chapter 3 showed similar morphologies in both higher molecular weight and higher grafting density samples with higher polymer content filling in the void structure. The cross-sectional image (**Figure 4.2b**) shows clear layered morphologies where the layered are perpendicular to the film thickness and run parallel to the casting surface. The formation of these

layers is consistent with evaporation-induced self-assembly (EISA) which has been observed before in nanorod films, and throughout CNC based PGN films in this body of work.[5–8]

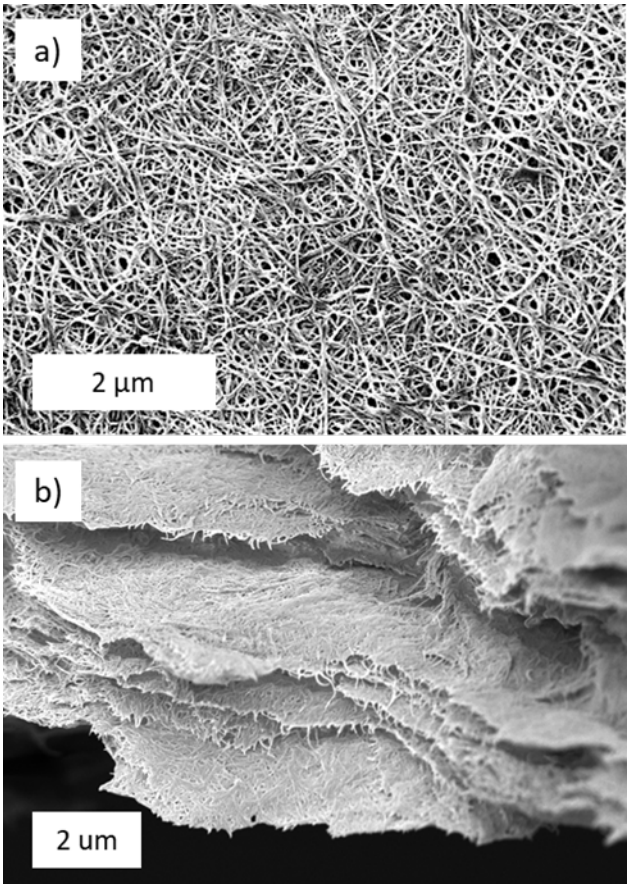

Figure 4.2: Scanning electron microscopy of ***t*-CNC-*g*-mPV$_{68/33}$** from a) top-down and b) cross-sectional directions.

Analysis of the wide-angle x-ray scattering (WAXS) data for the ***t*-CNC-*g*-mPV$_{68/33}$** film confirms the layered structure evident in the SEM images. **Figure 4.3a** shows the WAXS with the x-ray beam perpendicular to the sample. The images show clear isotropy regarding the azimuthal orientation of the signal. As a note, this corresponds to the cellulose interchain spacing in the CNC component of the nanoparticles, with the [1-10], [110], [102]/[012] and [200] peaks being most evident at q_y=1.05. 1.15, 1.5, and 1.6 A^{-1} at q_x=0 respectively, which aligns well with literature

precedent.[9–11] In contrast, **Figure 4.3b** shows the WAXS parallel to the film, as if one was looking down the cross-sectional SEM in **Figure 4.2b**. The image in **Figure 4.3b** shows a clear anisotropy, with the [102]/[012] signal being absent in the y direction but concentrated in the x direction while the [1-10] and [200] signals being strengthened in the y direction but absent in the x direction. This too aligns with literature precedent of aligned CNC samples further confirming the layered structure in the ***t*-CNC-*g*-mPV$_{68/33}$** film.[11]

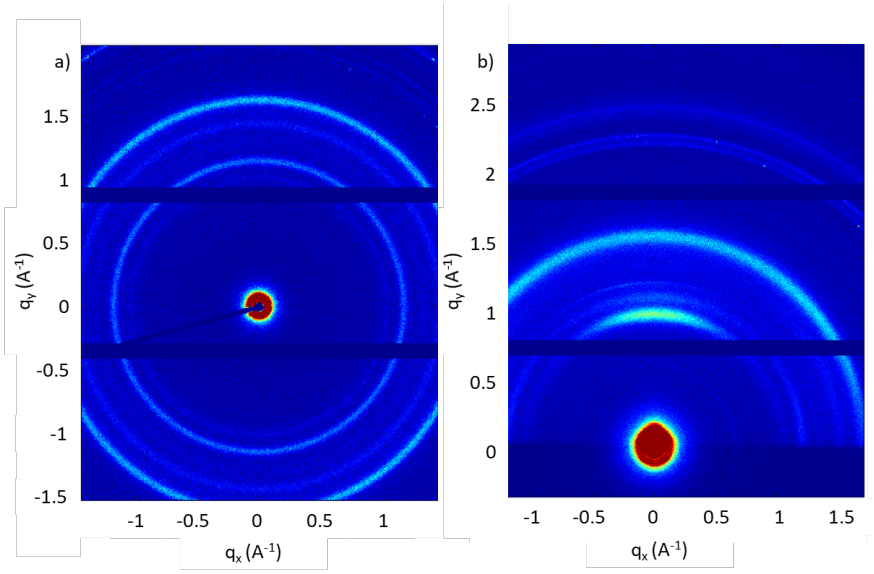

Figure 4.3: Wide angle x-ray scattering (WAXS) of ***t*-CNC-*g*-PV$_{68/26}$** film a) perpendicular to the film (through-planes) and b) parallel to the film (in-plane).

With the layered structure confirmed, electrical impedance spectroscopy can be used to further analyze the ***t*-CNC-*g*-mPV$_{68/33}$** films. By changing the measurement parameters (the length, width, and thickness) of the sample, the in-plane measurement can better determine which hemisphere aligns with the material conductivity. For the in-plane measurement, the film resistance (R_{film}) defined in eqn 4.1 can be rearranged to become

$$R_{film} = \frac{1}{\sigma} * \frac{l}{w * t} \tag{4.2}$$

where l is the length of film between the electrodes, w is the measured width of the films, and t it the measured thickness of the films. As a note, the resistance of a material will correspond with the diameter of the hemisphere in the impedance, which is normally accounted for in fitting the data. Thus, by halving the width, one would expect the resistance to be doubled, while halving the length, one would expect the resistance to be halved. **Figure 4.4** shows the Nyquist plots of ***t*-CNC-*g*-mPV$_{68/33}$** films with varied measurement parameters at 95% RH, with **Figure 4.4a** showing the control measurement. As the width, length, and both parameters are changed (**Figure 4.4b-d**), the first hemisphere (low impedance) changes exactly as would be expected, while the second hemisphere (higher impedance) remains constant throughout the different measurements. This offers clear evidence that the first hemisphere corresponds to the in-plane resistance of the film, but still leaves the second hemisphere as a mystery.

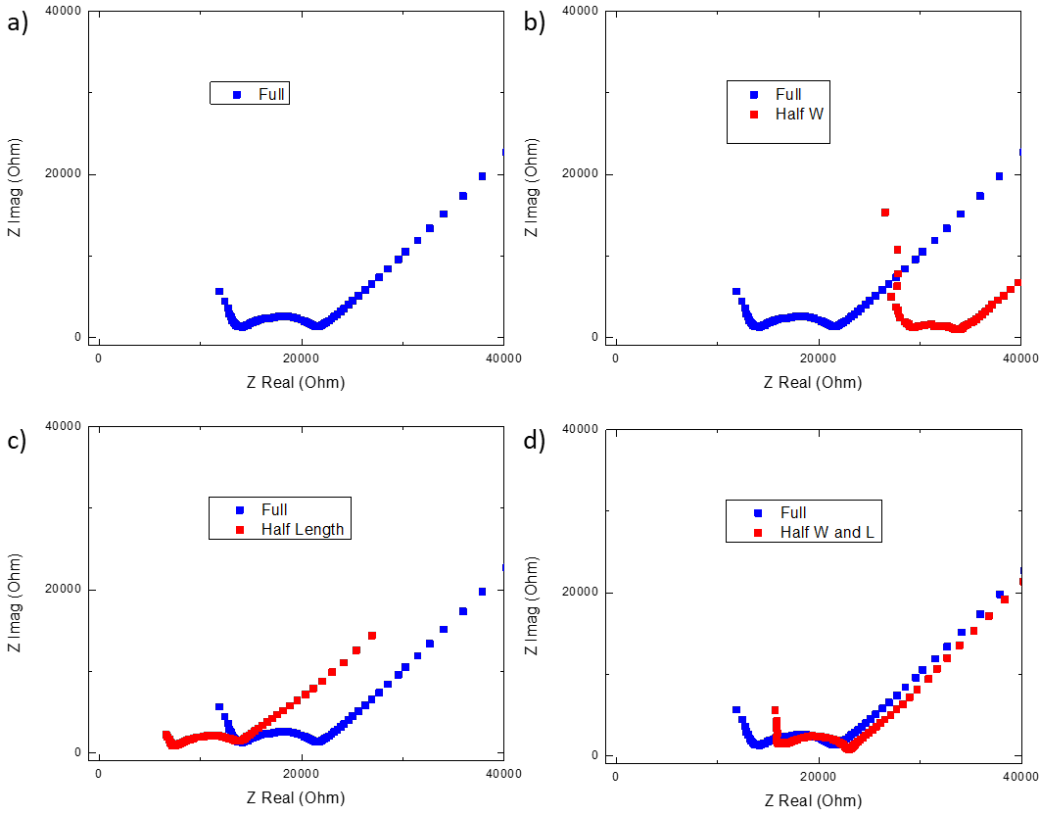

Figure 4.4: Nyquist plots of ***t*-CNC-*g*-mPV$_{68/33}$** films with varied measurement parameters at 95% RH. a) Control film, b) half width, c) half length, d) both half width and length.

The through-plane and in-plane conductivity of the ***t*-CNC-*g*-mPV$_{68/33}$** films were measured as a function of relative humidity (**Figure 4.5b,** open circles). The in-plane measurement of ***t*-CNC-*g*-mPV$_{68/33}$** showed higher conductivity than homopolymer (methylated 20 kg/mol purchased PV) data (prepared by methylation of a film of PV measured on interdigitated electrodes (IDEs))[12] across all measured relative humidities even though the PEGN film consists of 67 vol% (when dry) of the non-conducting crystalline CNC. Note, it was not possible to obtain reliable data from the homopolymer using the set up in **Figure 4.1a** on account of brittle fracture at low RH and material flow at high RH during, which demonstrates the enhanced material robustness of the

PEGN film system relative the homopolymer.[13] IDE based conductivity measurements were employed, which are known to accurately reflect material conductivity.[3]

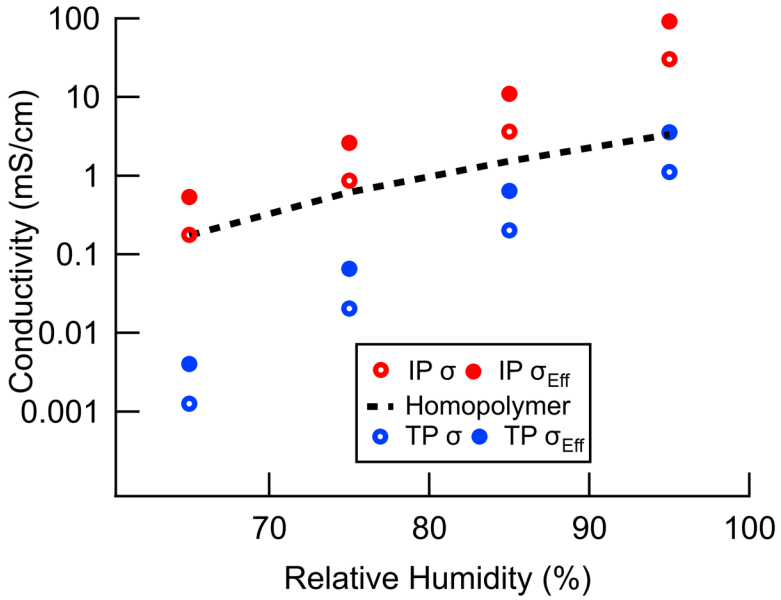

Figure 4.5: Comparison of the room temperature conductivity (and effective polymer conductivity taking into account the CNC volume) of ***MxG*-CNC-*g*-mPV$_{68/33}$** both in-plane (IP) and through-plane (TP) as well as homopolymer conductivity versus relative humidity. Experimental standard deviation of n=4 showed error of ~13% which is less than the marker size on graphs.

The in-plane conductivity of ***t*-CNC-*g*-mPV$_{68/33}$** films is an order of magnitude higher than the through plane conductivity, 30±4 mS/cm as compared to 1.1±0.1 mS/cm at 95% relative humidity. Given that a significant percentage of the PEGN film consists of the non-ion-conducting, crystalline CNC and the degree of polymer methylation is similar (65%) between the different samples, an effective polymer conductivity, σ_{eff}, was calculated which considers that the ion conductivity is only occurring through the polyelectrolyte volume fraction, and is defined as

$$\sigma_{eff}=\sigma/\Phi_V \quad (4.3)$$

where Φ_V is the polymer volume fraction. Using the effective conductivity in **Figure 4.5b** (filled circles), the in-plane conductivity rises an order of magnitude higher than the homopolymer to an in-plane value of σ_{eff} of 92±10 mS/cm while the through-plane conductivity of 3.6±0.5 mS/cm now roughly corresponds with the homopolymer measurement of 6.0±0.4 mS/cm, all at 95% relative humidity.

Interdigitated electrodes (IDEs) offer another method of determining material conductivity, specifically enabling the measurement of the in-plane conductivity of the ***MxG*-CNC-*g*-mPV$_{68/33}$** samples. **Figure 4.6a** shows the atomic force microscopy of the ***MxG*-CNC-*g*-PV$_{68/20}$** samples showing a monolayer of interconnected nanorods. Additionally, the film displays open, void like components lacking PGN material. **Figure 4.6b** shows the in-plane Nyquist plot of the ***MxG*-CNC-*g*-mPV$_{68/33}$** sample on the IDEs. Importantly, the signal displays only a single hemisphere as opposed to **Figure 4.1e** in which the in-plane measurement displayed two characteristic hemispheres. Showing a single hemisphere indicates that measuring a single electrochemical process is possible, clearing any interpretive difficulty of modeling conductivity from the EIS spectra. In plotting the conductivity data in **Figure 4.6c**, the IDE based measurement falls below by one third of the interpretive spectra from the two hemisphere results (**Figure 4.5**) while still displaying the conductivity enhancement above the ungrafted homopolymer samples. This difference can be attributed to the void spacing seen in the AFM results which although showing percolating pathways, still displays large non-conductive voids in the film.

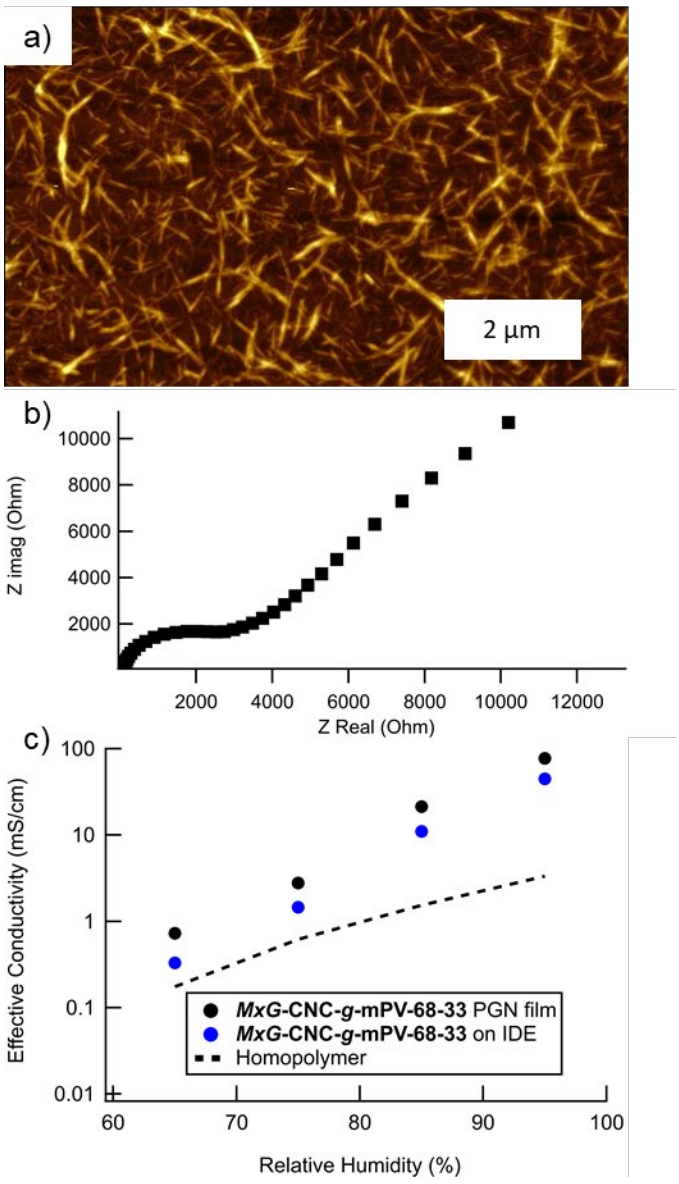

Figure 4.6: a) AFM images of ***MxG*-CNC-*g*-PV-68-20** on cleaved mica, b) Nyquist plot of in-plane measurements of ***MxG*-CNC-*g*-mPV-68-33** on IDEs, and c) Conductivity comparing ***MxG*-CNC-*g*-mPV-68-33** films vs ***MxG*-CNC-*g*-mPV-68-33** on IDEs as well as homopolymer as a function of relative humidity.

In order to probe the nature of the second hemisphere, the applied pressure to the in-plane electrodes was changed. As the electrodes are pressed into the films, changing the applied pressure

controls the electrode interface. Although the specific amount of applied stress is not measured, the relative stresses, either by lessening the amount of applied pressure or taking the applied pressure beyond finger tight, can be compared on the same measured sample, which is shown in **Figure 4.7**. **Figure 4.7a** shows when pressure is lessened, whereupon there is too little pressure for good contact and subsequently high resistance that has no relevance to the material measured. However, when analyzing the effect of medium pressure (what is done for all the measurements so far) and high pressure, the change in the Nyquist plot is distinct. Specifically, **Figure 4.7b** shows that there is no change in the first hemisphere, while the second changes as to be more resistive for high pressure. Although the specific details of the pressure-based dependence are difficult to ascertain, but altering the pressure the contact area is altered which may result in a more resistive interface.

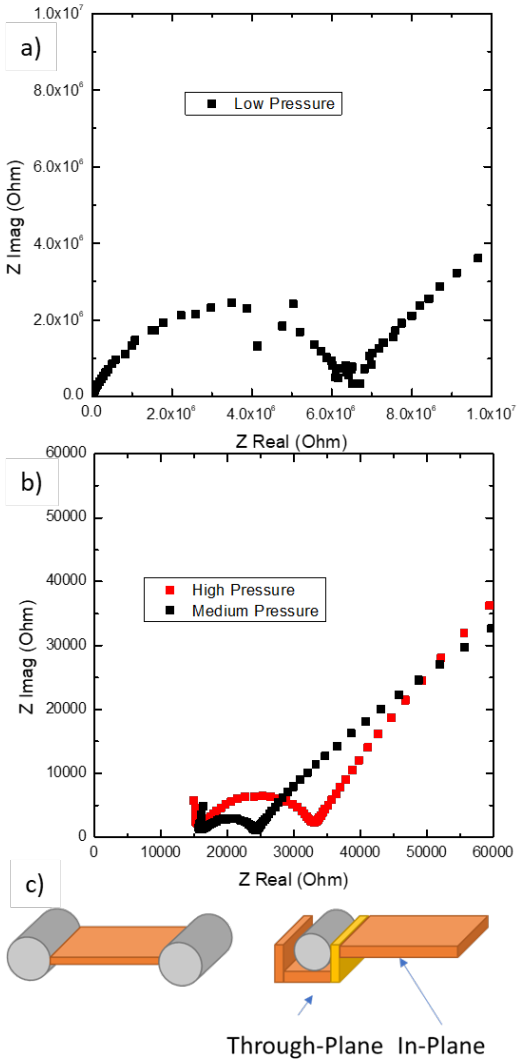

Figure 4.7: In-plane Nyquist plots of ***t*-CNC-*g*-mPV$_{68/33}$** films with variable pressure upon applied Pt wires, a) showing low pressure and b) showing medium (used for all other investigation) and high pressures and c) showing a cartoon explanation for a through-plane and in-plane measurement simultaneously in the sample due to the impinging wire electrode.

In fact, because **Figure 4.5** indicated that there is a clear anisotropy in conductivity between the in plane and through plane directions, **Figure 4.7c** shows a cartoon depiction where

the Pt electrode wire is causing a small through-plane interface to form at the electrode contact. As a first approximation to test this, the relative resistances can be estimated from eqn 4.2. In **Figure 4.7b**, the medium pressure samples show a first hemisphere resistance of 15000 ohms while the second hemisphere shows a resistance of 10000 ohms. Using the in-plane measurement values of a thickness of 70 microns, length of 1 cm, width of 0.67 cm, and conductivity of 30 mS/cm, a resistance of 7500 ohms can be predicted. Using the through plane measurement values of a thickness of 70 microns, length of 140 microns (two times the thickness), width of 0.67 cm, and conductivity of 1.1 mS/cm, a resistance of 2600 ohms can be predicted. Although this is far less than the measured value, it should be noted that the second hemisphere of at 95%RH has varied from 4000 ohms to the value from **Figure 4.7b** of 10000 ohms, thus as a first approximation the interface is slightly more resistive than predicted. Nonetheless, measuring the electrical impedance of the film without imposing the through plane interface would avail to remove this second hemisphere.

In order to only measure the in-plane component of conductivity, a thin (20 nm) layer of Pt/Pd was sputter coated onto the ***t*-CNC-*g*-mPV$_{68/33}$** film to be used as contacts as well as to define the length between electrodes. **Figure 4.8** shows both the cartoon representations of the measurement method alongside the associated Bode plots, where two peaks in the phase (red) are associated with two hemispheres in the Nyquist plot. In the case of the sputtered in-plane measurement, not only does the frequency location of the phase peak overlap with the similar location of the wire electrode-based measurement, but the measured conductivity matches within error (75±16 vs 92±23 mS/cm) for N=3.

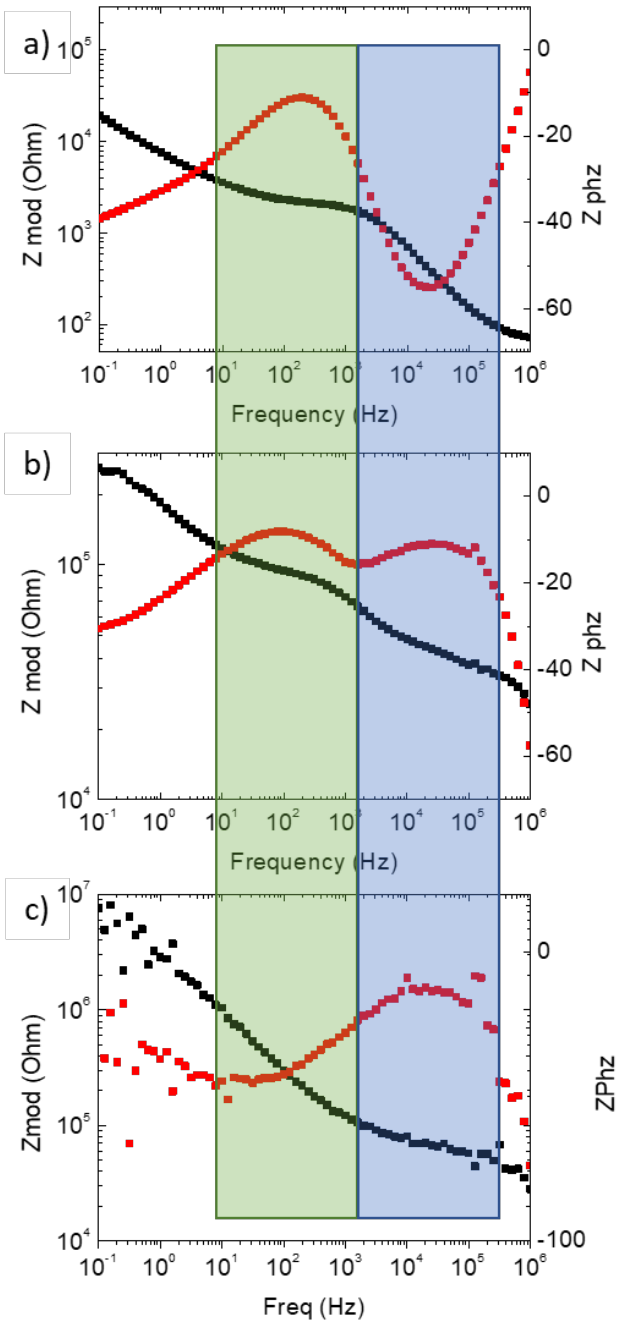

Figure 4.8: Bode plots of ***t*-CNC-*g*-mPV$_{68/33}$** films measured a) through-plane, b) in-plane with impinging wires, and c) in-plane with sputtered Pt/Pd

4.4 CONCLUSION

Polyelectrolyte grafted nanoparticle films composed of tunicate sourced CNCs and methylated poly(2-vinylpyridine) (***t*-CNC-*g*-mPV$_{68/33}$**) were investigated, displaying anisotropic ionic conductivities between the in-plane and through-plane directions. The electronic anisotropy followed the structural anisotropy seen in both scanning electron microscopy images and wide-angle x-ray scattering experiments. Interestingly, anomalous peaks in the Bode electrochemical plots and hemispheres in the Nyquist electrochemical plot were associated with the presence of an interfacial through-plane layer caused by impinging wire electrodes when measuring in-plane directions. Ultimately, by altering the measurement method by using sputter coated contact pads, the anomalous peaks/hemispheres were removed from measured spectra. This both supports the hypothesis of the interfacial through-plane layer as well as set up the necessary sample preparation for the experiments discussed in Chapter 3.

4.5 REFERENCES

(1) Liu, W.; Lin, D.; Sun, J.; Zhou, G.; Cui, Y. Improved Lithium Ionic Conductivity in Composite Polymer Electrolytes with Oxide-Ion Conducting Nanowires. *ACS Nano* **2016**, *10* (12), 11407–11413. https://doi.org/10.1021/acsnano.6b06797.

(2) Huggins, R. A. Simple Method to Determine Electronic Conductivity and Ionic Components of the Conductors in Mixed a Review. In *Ionics*; 2002; Vol. 8, pp 300–313. https://doi.org/10.1007/BF02376083.

(3) Sharon, D.; Bennington, P.; Liu, C.; Kambe, Y.; Dong, B. X.; Burnett, V. F.; Dolejsi, M.; Grocke, G.; Patel, S. N.; Nealey, P. F. Interrogation of Electrochemical Properties of Polymer Electrolyte Thin Films with Interdigitated Electrodes. *J. Electrochem. Soc.* **2018**, *165* (16), H1028–H1039. https://doi.org/10.1149/2.0291816jes.

(4) Sharon, D.; Bennington, P.; Dolejsi, M.; Webb, M. A.; Dong, B. X.; De Pablo, J. J.; Nealey, P. F.; Patel, S. N. Intrinsic Ion Transport Properties of Block Copolymer Electrolytes. *ACS Nano* **2020**, *14* (7), 8902–8914. https://doi.org/10.1021/acsnano.0c03713.

(5) Wargacki, S. P.; Pate, B.; Vaia, R. A. Fabrication of 2D Ordered Films of Tobacco Mosaic Virus (TMV): Processing Morphology Correlations for Convective Assembly. *Langmuir* **2008**, *24* (10), 5439–5444. https://doi.org/10.1021/la7040778.

(6) Shopsowitz, K. E.; Qi, H.; Hamad, W. Y.; MacLachlan, M. J. Free-Standing Mesoporous Silica Films with Tunable Chiral Nematic Structures. *Nature* **2010**, *468* (7322), 422–426. https://doi.org/10.1038/nature09540.

(7) Meseck, G. R.; Terpstra, A. S.; MacLachlan, M. J. Liquid Crystal Templating of Nanomaterials with Nature's Toolbox. *Curr. Opin. Colloid Interface Sci.* **2017**, *29*, 9–20. https://doi.org/10.1016/j.cocis.2017.01.003.

(8) Natarajan, B.; Emiroglu, C.; Obrzut, J.; Fox, D. M.; Pazmino, B.; Douglas, J. F.; Gilman, J. W. Dielectric Characterization of Confined Water in Chiral Cellulose Nanocrystal Films. *ACS Appl. Mater. Interfaces* **2017**, *9* (16), 14222–14231. https://doi.org/10.1021/acsami.7b01674.

(9) Zhang, Y.; Edelbrock, A. N.; Rowan, S. J. Effect of Processing Conditions on the Mechanical Properties of Bio-Inspired Mechanical Gradient Nanocomposites. *Eur. Polym. J.* **2019**, *115* (March), 107–114. https://doi.org/10.1016/j.eurpolymj.2019.03.022.

(10) Zhang, T.; Cheng, Q.; Ye, D.; Chang, C. Tunicate Cellulose Nanocrystals Reinforced Nanocomposite Hydrogels Comprised by Hybrid Cross-Linked Networks. *Carbohydr. Polym.* **2017**, *169*, 139–148. https://doi.org/10.1016/j.carbpol.2017.04.007.

(11) Elazzouzi-Hafraoui, S.; Nishiyama, Y.; Putaux, J. L.; Heux, L.; Dubreuil, F.; Rochas, C. The Shape and Size Distribution of Crystalline Nanoparticles Prepared by Acid Hydrolysis of Native Cellulose. *Biomacromolecules* **2008**, *9* (1), 57–65. https://doi.org/10.1021/bm700769p.

(12) Chu, W.; Webb, M. A.; Deng, C.; Colon, Y. J.; Kambe, Y.; Krishnan, S.; Nealey, P. F.; de Pablo, J. J. Understanding Ion Mobility in P2VP/NMP+I − Polymer Electrolytes: A Combined Simulation and Experimental Study. *Macromolecules* **2020**, *53* (8), 2783–2792. https://doi.org/10.1021/acs.macromol.9b02329.

(13) Kato, R.; Lettow, J. H.; Patel, S. N.; Rowan, S. J. Ion-Conducting Thermoresponsive Films Based on Polymer-Grafted Cellulose Nanocrystals. *ACS Appl. Mater. Interfaces* **2020**, *12*, 54083–54093. https://doi.org/10.1021/acsami.0c16059.

Chapter 5

Exploring Conductivity-Enhancing, Hydrated, Organic Interfaces with Interdigitated Electrodes

5.1 INTRODUCTION

Ionically conductive polyelectrolyte materials can be utilized across many energy technologies, from fuel cells[1] to lithium ion[2] and redox-flow batteries.[3] Nanofiller introduced into polyelectrolyte materials can result in nanocomposites with improved mechanical or electrical properties. Indeed, this field is broad and well-trodden, with much work in the literature that summarize the impact of different nanofillers in polyelectrolyte matrices.[2–10] Some inorganic nanofillers (e.g. SiO_2,[11] Al_2O_3,[12] Li_3N,[8] $Li_{1.3}Al_{0.3}Ti_{1.7}(PO_4)_3$,[13] $Li_{0.33}La_{0.557}TiO_3$[14]) have been shown to increase ionic conductivity with effects, such as Lewis acid-base interactions and/or disruption of matrix crystallization, at the matrix/filler interface being proposed as the reason. Importantly, nanofillers can attain high interfacial surface area. With additional surface area, beneficial interfacial interactions can be better magnified throughout a material, but only if the nanofiller is well integrated/dispersed. However, the wide variety of interactions (polymer, ion, surface, and plasticizing/solvating agents) and effects (filler aggregation, mechanical property changes), greatly complicates a more detail molecular understanding of the mechanism of enhanced ion conduction.

One method to study these interfaces is to use anisotropic nanofiller, where resulting material properties (which often display anisotropy) offer insight into the interfacial mechanisms. Anisotropic filler can form extended regions of polymer/filler interaction even at similar loadings, thus providing a better platform for study the polymer/filler interface. Although generally nanospheres have been studied in the ionically conductive nanocomposite literature, Cui and coworkers have produced a number of papers investigating different geometries of $Li_{0.33}La_{0.557}TiO_3$ nanoparticles in poly(acrylonitrile) (PAN) with $LiClO_4$.[14–16] All investigated nanospheres, nanorods, and nanowires showed significant increases in ion conductivity relative to

the polymer matrix alone. It was proposed that the LLTO material's positive-charged oxygen vacancies on the surfaces of the nanofiller are able to associate with the anions, which increases the quantity of free Li+ ions while also providing an increased mobility by allowing vacancy pathway diffusion in the LLTO surface, therefore enhancing conductivity. Nanowires displayed the greatest degree of material anisotropy. When the nanowires are aligned parallel to the applied electric field, the composites exhibited 3 orders of magnitude increase in conductivity (relative to the polymer matrix) however when the nanowires are aligned perpendicular to the electric field the composites approximated the conductivity of the filler-free matrix.[16] These investigations suggest that the extended surfaces of the nanorods and nanowires allow for better percolation ion conducting channels throughout the bulk of the material.

Anisotropic organic nanofillers have also being explored in polyelectrolyte composites. In particular, cellulose nanocrystals (CNCs)[17–24] have shown promise as organic, biobased, and highly crystalline nanorods with easily accessible surface chemistries.[9,25,26] Many studies reported materials with excellent mechanical properties but reduced ionic conductivity,[25,27,28] yet a few CNC-based nanocomposites have shown increased ionic conductivity that have been suggested to occur on account of beneficial interfacial effects.[26,29] For example, Cheng *et al*. synthesized functionalized CNCs with quaternary ammonium groups and introduced them into a poly(phenylene oxide) matrix functionalized with similar quaternary ammonium groups for use as anion exchange membranes.[26] When immersed in water, the resulting materials showed enhanced ionic conductivity (60% higher) peaking at a 2 wt.% CNC loading at 80 °C. The increase in conductivity was attributed to the hydrophilic CNC surface which was supported by transmission electron microscopy with the phosphotungstic acid stain reacting to water near the CNC surface, which showed interconnected pathways attributed to the water at the CNC surfaces. However other

works investigating CNC-based nanocomposites attribute enhancement to difference mechanisms.[29] Rincón-Iglesias et al. prepared nanocomposites of CNCs in ι-carrageenan, a marine sulfated polysaccharide isolated from red algae (Rhodophyta). The ionic conductivity of the composite material peaked at 10 wt.% CNCs with roughly a 3-fold improvement in conductivity. In fitting the frequency dependence of the dielectric response, attribute enhancement to additional surface site hopping.[29] Even so, further mechanistic investigation was limited due to aggregation and phase separation of the CNCs at higher loadings leading to a drop in both ion conduction and mechanical properties.

Our prior work investigated hydrated polymer grafted nanoparticle films consisting of CNCs with grafted methylated poly(2-vinypyridine) (mPV) at various polymer architectures, grafting densities, and molecular weights.[30] At all grafting densities and molecular weights the materials displayed enhanced ionic conductivities compared to the polymer matrix alone, maximizing at high nanofiller content and lower molecular weight of the graft. The impact of the interface on ionic conductivity enhancement was probed by attaching diblock copolymers consisting of the ionically conductive mPV and non-conductive polystyrene (PS), with either the PS or mPV block attached to the CNC surface. When the mPV block was attached, similar levels of ionic conductivity enhancement were measured while when the PS block was attached to the surface the measured conductivity dropped to being similar to the ungrafted polymer. As the CNC interface was shown critical in the enhancement, the mechanism was hypothesized to be related to either the surface functionality, as the surface alcohol groups could beneficially solvate the conductive iodide ion or the hydrophilic CNC surface increasing local water content which aids in polymer mobility and ion solvation.

The transport of ions through ionically conductive polymer membranes is generally understood to be governed by three transport mechanisms: surface site hopping, vehicular, and Grotthuss.[31] Surface site hopping permits anions to hop between solvation sites without the aid of water/solvent molecules and is correlated with the segmental mobility of polymer chain. Both anhydrous systems (like LiTFSI in PEO) and hydrated systems (like hydroxide ions in anion exchange membranes) tend to display this mechanism.[6,32] However, as water content increases in a hydrated system, vehicular and Grotthuss mechanisms can begin to dominate the overall anion transport. If water molecules solvate and co-diffuse with the anions it is termed the vehicular transport mechanism. However, if instead there is the diffusion of a proton defect through a static hydrogen bonded network of water molecules by the formation and cleavage of the oxygen-hydrogen covalent bonds then the process is termed the Grotthuss or proton jumping mechanism. For hydroxide ion transport in anion exchange membranes, both vehicular and Grotthuss mechanism substantially contribute to the overall conductivity while larger anions that cannot form the same hydrogen bonded networks with water are limited to either surface site hopping or vehicular vehicle transport.[33] Recent dual computational and experimental work by Chu *et al*. has highlighted the impact that water has upon ion conductivity in hydrated, **mPV** homopolymer.[34] Water plasticizes the polymer, increasing chain mobility and reducing the glass transition temperature of the polymer to below 25 °C at high water uptake, as well as solvates the conductive iodide ion, helping to transport it between cationic solvation sites. Although both effects impact the iodide ion conductivity, the water solvation was shown to play a particularly critical role as simulated mPV with artificially increased segmental mobility to match the hydrated system but without solvating water was shown have remarkably lower transport, in line with vehicular transport playing a more dominant role relative to surface site hopping. As a result, the alcohol

functionality, which can directly assist in iodide solvation via hydrogen bonding and can also hydrogen bond water which also aid in iodide/pyridinium dissociation, can impact the iodide transport through improved solvation of the ion. Even so, discerning between which element (hydrophilicity or alcohol functionality) more strongly impacts the conductivity at the interface remains difficult to determine without more experimental investigation.

Great strides have been made recently to probe the interface between ionically conductive polymer and inorganic materials through the use of interdigitated electrodes (IDEs).[35] IDEs enable the study of thin film materials by vastly increasing the surface area studied through use of the interdigitation. Although IDEs had been used previously to study material conductivity,[36] Sharon *et al*. thoroughly investigated how to optimize the measurement of the electrochemical impedance (which enables conductivity measurements) of polymer electrolyte thin films while studying the impact of different inorganic, dielectric materials layers.[35] Using IDEs, Dong *et al*. investigated poly(ethylene oxide) (PEO) with LiTFSI, where 10 kg/mol hydroxy terminated PEO was grafted to the IDE surface and subsequently 20 kg/mol PEO layers of varying thickness (ca. 10 to 250 nm) were added on top of the initial grafting.[37] Importantly, this system was studied in an anhydrous environment. The measured conductivity decreased as the added PEO film decreased in thickness, even as the ratio of PEO to LiTFSI remained constant. It was concluded that the grafted PEO layer forms an immobile interfacial zone that resulted in the deviation from the bulk PEO conductivity. This immobile interfacial layer was estimated to vary between 3nm to 10 nm as a function of the lithium to ethylene oxide ratio, r, ranging from 0.15 to 0.01 respectively. Although the work demurs as to the specific cause of the immobile interfacial layer, hypotheses are given such as reduced segmental mobility or uneven distribution of the LiTFSI salt due to the dense polymer grafts, yet ultimately IDEs provided the ideal platform for probing this nanothin interfacial effect.

Reported herein are studies aimed at studying hydrated, ionically conductive polymer at an organic interface with particular focus on the contributions of surface alcohol content and surface hydrophilicity on ionic conductivity. First the cellulose interfaces (specifically the alcohol functionalities) of methylate poly(2-vinylpyridine) (mPV) grafted cellulose nanocrystal (CNCs) PGNs will be altered via acetylation to remove any effect the surface CNC alcohol functionalities have on the ionic conductivity. As this changes both hydrophilicity and alcohol content, model surface brushes will be synthesized and grafted to IDEs to control and isolate hydrophilicity and alcohol content in order to determine their relative impacts on ionic conductivity enhancement for these interfacial types.

5.2 EXPERIMENTAL METHODS

5.2.1 Instrumentation

Fourier transform infrared spectroscopy (FTIR). FTIR spectra were collected on a Shimadzu FTIR instrument. Solid samples were placed directly on the ATR crystal, and then the spectra were averaged from 46 scans from 550 to 4000 cm^{-1} with a resolution of 4 cm^{-1}.

Nuclear Magnetic Resonance Spectroscopy. The ^{1}H NMR spectra were recorded on a Bruker Ascend Advance II+ 500 MHz spectrometer at 25 °C using D DMSO as solvent. All NMR spectra were processed by MestReNova software.

Gel Permeation Chromatography-Multiangle Light Scattering and UV-VIS Spectrometry (THF). Polymer molecular weight and dispersity was determined by gel permeation chromatography-multi-angle light scattering (GPC-MALS) measured on a Shimadzu Prominence LC system with PL gel Mixed-D columns with Wyatt Dawn Heleos MALS (658 nm laser), Wyatt Optilab T-rEX refractive index (RI) detectors, and an inline Shimadzu SPD-M30A Photodiode Array detector (200-800 nm) UV-Vis data on the samples. HPLC grade tetrahydrofuran (THF) as the eluent (1mL/min) at 25 °C. The data were processed by Wyatt Astra software.

Gel Permeation Chromatography (DMF). Polymer molecular weights and dispersities were determined by gel permeation chromatography on a Tosoh EcoSEC size exclusion chromatography System with Tosoh SuperAW3000 + Tosoh SuperAW4000 columns. DMF + 0.01 M LiBr was used as eluent. The data were processed using Tosoh software. Note that if possible the GPC-MALS (THF) unless materials were insoluble in THF, which resulted in the GPC (DMF) being used.

Water Contact Angle. Water contact angle measurements were made using a Krüss DSA100 Drop Shape Analyzer at ambient conditions using Elga Purelab Flex 3 purified water. Water droplets were produced with 2.0 µl volume. The data were processed using Krüss ADVANCE software.

Electrochemical Impedance Spectroscopy. The electrochemical properties of the samples were probed using the Gamry reference 600 potentiostat/galvanostat. AC electrical impedance spectroscopy (EIS) measurements were made from 1 MHz to 1 Hz by connecting the samples via either larger Pt/ Pd 20 nm deposited pads with the Cressington 108 Auto Sputter Coater or between sheets of Pt foil to the potentiostat/ galvanostat. An amplitude voltage of 10 mV was used. For acetylated **MxG-CNC-g-mPV** samples, electrode distance was 1 cm while surface area probed was 0.5 cm width by the measured PEGN film thickness between 50µm. For IDE samples, the contact pads were directly connected to the potentiostat. The measurements were made in a chamber with controlled temperature (25 °C) and relative humidity (65-95% RH) after an equilibration period of 15 min. Interdigitated electrodes were fabricated and utilized for EIS following literature procedures.[35,36]

Dynamic Vapor Sorption. The water uptake with relative humidity was measured using dynamic vapor sorption (DVS) of water at controlled temperature (25 °C) and relative humidity (0-95% RH). Measurements were don on a DVS Intrinsic from Surface Measurement Systems. 20 mg of polymer was placed in a preweighed aluminum pan inside the DVS chamber for each humidity condition. The powder was monitored until the weight of the film stabilizes within 0.01 mg/min over a 5 min interval. This film weights were recorded for RH from 0% to 95% and back to 0%; the second cycle (95% to 0%) is used to determine the water content for each sample.

5.2.2 Material Synthesis

Materials. Miscanthus x. Giganteus (ground stalks) were donated by Aloterra Energy LLC, Conneaut, Ohio. 2-Hydroxyethl acrylate, methyl acrylate, 4-hydroxybutyl acrylate, 2-[2-(2-methoxyethoxy)ethoxy]ethyl acrylate, 2-carboxyethyl acrylate, hydroxypropyl acrylate, 2-vinylpyridine, and glycidyl methacrylate were purchased from Sigma-Aldrich and passed through a basic alumina column immediately prior to usage. All other reagents were purchased from Sigma-Aldrich and used as received.

Acetylation of *MxG*-CNC-*g*-PV-7-20 Surface. ***MxG*-CNC-*g*-PV-7-20** (7 kg/mol and 20 vol% polymer) (100mg) identical to those studied previously[30] are dispersed in pyridine (0.5 wt%). 10 eq excess of acetic anhydride compared to alcohol content (130 mg) with a 0.1 eq of 4-Dimethylaminopyridine (DMAP) (10 mg). The reaction was conducted at 80 C for 8 hrs. To purify the sample, the sample was precipitated into hexanes, to yield a white precipitate. The precipitate was collected by centrifugation and redispersed in acetone by sonication, followed by further centrifugation to separate the precipitant and the supernatant. This was repeated 3 times. FTIR before and after reaction confirms acetylation of surface alcohols with particularly strong signal at 1750 cm^{-1} (**Figure S5.1**, **Scheme S5.1**)

Synthesis of poly(2-hydroxyethyl acrylate)-*co*-poly(methyl acrylate) by RAFT. Poly(2-hydroxyethyl acrylate)-co-poly(methyl acrylate) (**xHyM**) was synthesized as a model interfacial polymer to graft to silicon surfaces. 2-Hydroxyethyl acrylate (**H**) was copolymerized with methyl acrylate (**M**) at varying monomer compositions; relative weight fraction of **M** was varied at 0, 25%, 50%, 75% and 90%. For example, for **45H55M**, cyanomethyl dodecyl trithiocarbonate (0.016 g), azobisisobutyronitrile (AIBN) (0.0006 g), acrylate combination (0.5g **H** (4.4mmol) and 0.5 g **M** (5.7mmol)) and DMF (3 ml) were transferred to a 50 mL round bottom flask, sparged for

10 minutes, and then heated at 70 °C for 2 h, followed by rapid quenching to room temperature. The mixture was diluted with DMF (~5 mL) and the polymer was precipitated into diethyl ether (100 mL) three times and dried in a vacuum oven at 40 °C for 24 h forming **45H55M** with 45 mol% **H** and 55 mol% **M** (Note, the weight fraction of each component aligns well with feed quantity). ^{1}H NMR: (500 MHz, d_6-DMSO); δ ppm: 4.8 (**H**, 1H, HO-), 4.0 (**H**, 2H, C=O-O-C**H$_2$**-), 3.6 (**M**, 3H, C=O-O -CH_3 and **H**, 2H, HO-C**H$_2$**-), 2.1-2.4 (**M**+**H**, C=O-C**H**-), 1.3-1.7 (**M**+**H**, C=O-CH-C**H$_2$**-), 0.85 (dodecyl endgroup C**H$_3$**). From ^{1}H NMR, molecular weights (Mn) for **100H**, **70H30M**, **45H55M**, **21H79M**, **7H93M** were 25 kg/mol, 18 kg/mol, 18 kg/mol, 14kg/mol, and 13kg/mol, respectively (**Figures S5.2-5.4**). GPC (DMF): polymer series were measured against poly(methyl methacrylate) standards showing Đ<1.35 (**Figures S5.2-5.4**).

Synthesis of poly(2-hydroxyethyl acrylate)-*co*-poly(4-hydroxybutyl acrylate) by RAFT. Poly(2-hydroxyethyl acrylate)-co-poly(4-hydroxybutyl acrylate) (**xHyB**) was synthesized as a model interfacial polymer to graft to silicon surfaces. 2-Hydroxyethyl acrylate (**H**) was copolymerized with 4-hydroxybutyl acrylate (**B**) at varying monomer compositions; relative weight fraction of **B** was varied at 0, 25%, 50%, 75% and 100%. For example, for **57H43B**, cyanomethyl dodecyl trithiocarbonate (0.016 g), azobisisobutyronitrile (AIBN) (0.0006 g), acrylate combination (0.5g **H** (4.3 mmol) and 0.5 g **B** (3.4 mmol)) and DMF (3 ml) were transferred to a 50 mL round bottom flask, sparged for 10 minutes, and then heated at 70 °C for 2 h, followed by rapid quenching to room temperature. The mixture was diluted with DMF (~5 mL) and the polymer was precipitated into diethyl ether (100 mL) three times and dried in a vacuum oven at 40 °C for 24 h. ^{1}H NMR: (500 MHz, d_6-DMSO); δ ppm: 4.8 (**H**, 1H, HO-), 4.5 (**B**, 1H, HO-), 4.0 (**H+B**, C=O-O-C**H$_2$**-), 3.6 (**H**, 2H, HO-C**H$_2$**-), 3.4 (**B**, 2H, HO-C**H$_2$**-), 2.1-2.4 (**H+B**,

C=O-C**H**-), 1.3-1.7 (**H+B**, C=O-CH-C**H₂**- and **B**, broad, -C**H₂**-C**H₂**-CH_2-OH), 0.85 (dodecyl endgroup C**H₃**). From ^{1}H NMR, molecular weights (Mn) for **100H**, **80H20B**, **57H43B**, **30H70B**, **100B** were 25 kg/mol, 17 kg/mol, 14 kg/mol, 15 kg/mol, and 14 kg/mol, respectively (**Figures S5.2-5.4**). GPC (DMF): polymer series were measured against poly(methyl methacrylate) standards showing Đ<1.5 (**Figures S5.2-5.4**).

Synthesis of poly(2-hydroxyethyl acrylate)-*co*-poly(2-[2-(2-methoxyethoxy)ethoxy]ethyl acrylate) by RAFT. Poly(2-hydroxyethyl acrylate)-co-poly(2-[2-(2-methoxyethoxy)ethoxy]ethyl acrylate) (**xHyG**) was synthesized as a model interfacial polymer to graft to silicon surfaces. 2-Hydroxyethyl acrylate (**H**) was copolymerized with 2-[2-(2-methoxyethoxy)ethoxy]ethyl acrylate (**G**) at varying monomer compositions; relative weight fraction of **G** was varied at 0, 25%, 50%, 75% and 90%. For example, for **63H37G**, cyanomethyl dodecyl trithiocarbonate (0.016 g), azobisisobutyronitrile (AIBN) (0.0006 g), acrylate combination (0.5g **H** (4.3 mmol) and 0.5 g **G** (1.1 mmol)) and DMF (3 ml) were transferred to a 50 mL round bottom flask, sparged for 10 minutes, and then heated at 70 °C for 2 h, followed by rapid quenching to room temperature. The mixture was diluted with DMF (∼5 mL) and the polymer was precipitated into diethyl ether (100 mL) three times and dried in a vacuum oven at 40 °C for 24 h. ^{1}H NMR: (500 MHz, d_6-DMSO); δ ppm: 4.8 (**H**, 1H, HO-), 4.1 (**G**, 2H, C=O-O-C**H₂**-) 4.0 (**H**, 2H, C=O-O-C**H₂**-), 3.6 (**H**, 2H, HO--C**H₂**-), 3.5 (**G**, O-C**H₂**-C**H₂**-O), 3.4 (**G**, 3H, -O-C**H₃**) 2.1-2.4 (**H+G**, C=O-C**H**-), 1.3-1.7 (**H+G**, C=O-CH-C**H₂**- and), 0.85 (dodecyl endgroup C**H₃**). From ^{1}H NMR, molecular weights (Mn) for **100H**, **85H15G**, **63H37G**, **35H65G**, **17H83G** were 25 kg/mol, 16 kg/mol, 11 kg/mol, 10 kg/mol, and 9 kg/mol, respectively (**Figures S5.2-5.4**). GPC (DMF): polymer series were measured against poly(methyl methacrylate) standards showing Đ<1.37 (**Figures S5.2-5.4**).

Poly(2-vinylpyridine-co-glycidyl methacrylate) (XPV) Synthesis via RAFT. 2-cyano 2-propyl dodecyl trithiocarbonate (0.017 g), azobisisobutyronitrile (AIBN) (0.0008 g), 2-vinylpyridine (8.3 g), glycidyl methacrylate (0.166 g), and THF (80 ml) were transferred to a 150 mL flask, sparged for 10 minutes, and then heated at 60 °C for 24 h, followed by rapid quenching to room temperature. The mixture was diluted with THF (~5 mL) and the polymer was precipitated into hexanes (100 mL), collected by filtration and dried in a vacuum oven at 40 °C for 24 h forming Poly(2-vinylpyridine-co-glycidyl methacrylate) (**XPV-n**, where n refers to the wt% added glycidyl methacrylate). ^{1}H NMR: (500 MHz, $CDCl_3$); δ ppm: 8.7-6.1 (br PV), 3.5 (PGMA, 1H, O-CH_2-), 3.5 (PGMA, 1H, O-CH_2-), 2.2-1.2 (br PS), 1.0 (PGMA, 3H, -CH_3) (**Figure S5.6**). GPC-MALS (THF): M_n of 40 kg/mol, 50 kg/mol, and 30 kg/mol, for **XPV-2**, **XPV-4**, and **XPV-6**, respectively, and Đ~1.15 (**Figure S5.7** and **Table S5.2**).

Synthesis of poly(2-hydroxyethyl acrylate)-*co*-poly(*tert*-butyl acrylate) by RAFT. Poly(2-hydroxyethyl acrylate)-co-poly(*tert*-butyl acrylate) (**xHyT**) was synthesized as a model interfacial polymer to graft to silicon surfaces. 2-Hydroxyethyl acrylate (**H**) was copolymerized with *tert*-butyl acrylate (**T**) at varying monomer compositions; relative weight fraction of **M** was varied at 0, 25%, 50%, and 75%. For example, for **54H46T**, Cyanomethyl dodecyl trithiocarbonate (0.016 g), azobisisobutyronitrile (AIBN) (0.0006 g), acrylate combination (0.5 g **H** (4.3 mmol) and 0.5 g **C** (3.9 mmol)) and DMF (3 ml) were transferred to a 50 mL round bottom flask, sparged for 10 minutes, and then heated at 70 °C for 2 h, followed by rapid quenching to room temperature. The mixture was diluted with DMF (~5 mL) and the polymer was precipitated into diethyl ether (100 mL) three times and dried in a vacuum oven at 40 °C for 24 h. ^{1}H NMR: (500 MHz, d_6-DMSO); δ ppm: 4.8 (**H**, 1H, HO-), 4.0 (**H**, 2H, C=O-O-C**H₂**-), 3.6 (**H**, 2H, HO -C**H₂**-), 2.1-2.4 (**H+T**,

C=O-C**H**-), 1.3-1.7 (**H+T**, C=O-CH-C**H**$_2$-), 1.4 (**T**, 9H, C-(C**H**$_3$)$_3$), 0.85 (dodecyl endgroup C**H**$_3$). From ^{1}H NMR, molecular weights (Mn) for **100H**, **79H21T**, **46H54T**, and **25H75T**, were 25 kg/mol, 18 kg/mol, 6 kg/mol, and 9 kg/mol, respectively (**Figure S5.13**). GPC (DMF): polymer series were measured against poly(methyl methacrylate) standards showing Đ<1.37 (**Figure S5.14, Table S5.3**).

Synthesis of poly(2-hydroxyethyl acrylate)-*co*-poly(2-carboxyethyl acrylate) by RAFT. Poly(2-hydroxyethyl acrylate)-co-poly(2-carboxyethyl acrylate) (**xHyC**) was synthesized as a model interfacial polymer to graft to silicon surfaces. 2-Hydroxyethyl acrylate (**H**) was copolymerized with 2-carboxyethyl acrylate (**C**) at varying monomer compositions; relative weight fraction of **C** was varied at 0, 10%, and 20%. For example, for **90H10C**, cyanomethyl dodecyl trithiocarbonate (0.016 g), azobisisobutyronitrile (AIBN) (0.0006 g), acrylate combination (0.9 g **H** (7.7 mmol) and 0.1 g **C** (0.7 mmol)) and DMF (3 ml) were transferred to a 50 mL round bottom flask, sparged for 10 minutes, and then heated at 70 °C for 2 h, followed by rapid quenching to room temperature. The mixture was diluted with DMF (~5 mL) and the polymer was precipitated into diethyl ether (100 mL) three times and dried in a vacuum oven at 40 °C for 24 h. ^{1}H NMR: (500 MHz, d_6-DMSO); δ ppm: 4.8 (**H**, 1H, HO-), 4.3 (**C**, 2H, C=O-O-C**H**$_2$-) 4.0 (**H**, 2H, C=O-O-C**H**$_2$-), 3.6 (**H**, 2H, HO-C**H**$_2$-), 2.1-2.4 (**H+C**, C=O-C**H**-), 1.3-1.7 (**H+C**, C=O-CH-C**H**$_2$-), 0.85 (dodecyl endgroup C**H**$_3$). From ^{1}H NMR, molecular weight (Mn) for **90H10C** was 11 kg/mol (**Figure S5.15**). GPC (DMF): polymer series were measured against poly(methyl methacrylate) standards showing Đ>1.5, likely due to column interactions (**Figure S5.16, Table S5.3**).

Synthesis of poly(2-hydroxypropyl acrylate)-*co*-poly(3-hydroxypropyl acrylate) by RAFT. Poly(2-hydroxypropyl acrylate)-co-poly(3-hydroxypropyl acrylate) (**xP**) was synthesized as a model interfacial polymer to graft to silicon surfaces. Hydroxypropyl acrylate (**P**) was polymerized although initial monomer was confirmed to be 3:1 of 2-hydroxypropyl acrylate (**P_2**) :3-hydroxypropyl acrylate (**P_3**) via ^{1}H NMR. For example, for **100P**, Cyanomethyl dodecyl trithiocarbonate (0.016 g), Azobisisobutyronitrile (AIBN) (0.0006 g), hydroxypropyl acrylate (1 g **P** (7.7 mmol)) and DMF (3 ml) were transferred to a 50 mL round bottom flask, sparged for 10 minutes, and then heated at 70 °C for 2 h, followed by rapid quenching to room temperature. The mixture was diluted with DMF (~5 mL) and the polymer was precipitated into diethyl ether (100 mL) three times and dried in a vacuum oven at 40 °C for 24 h. ^{1}H NMR: (500 MHz, d_6-DMSO); δ ppm: 4.8 (**P**, 1H, HO-), 3.9 (**P_3**, 2H, C=O-O-C**H_2**-), 3.8 (**P_2**, 2H, C=O-O-C**H_2**-), 3.35 (**P**, 2H, HO-C**H_2**-), 2.1-2.4 (**P**, C=O-C**H**-), 1.3-1.7 (**P**, C=O-CH-C**H_2**-), 1.1 (**P_3**, 2H, -CH_2-C**H_2**- CH_2-), 1.0 (**P**, 3H, -C**H_3**), 0.85 (dodecyl endgroup C**H_3**). From ^{1}H NMR, molecular weight (Mn) for **100P** was 13 kg/mol (**Figure S5.17**). GPC (DMF): polymer series were measured against poly(methyl methacrylate) standards showing Đ<1.32 (**Figure S5.18, Table S5.3**).

Synthesis of poly(glycidyl methacrylate) by RAFT. Poly(glycidyl methacrylate) (**PGMA**) was synthesized as a functionalizable polymer to probe detailed alcohol effects. 2-Cyano,2-propyl dithiobenzoate (0.056 g), azobisisobutyronitrile (AIBN) (0.004 g), glycidyl methacrylate (5 g) and THF (10 ml) were transferred to a 50 mL round bottom flask, sparged for 10 minutes, and then heated at 70 °C for 2 h, followed by rapid quenching to room temperature. The mixture was diluted with THF (~10 mL) and the polymer was precipitated into hexanes (100 mL) three times and dried in a vacuum oven at 40 °C for 24 h. ^{1}H NMR: (500 MHz, d_6-DMSO); δ ppm: 4.3 (1H, C=O-O-

C**H₂**-), 3.7 (1H, C=O-O-C**H₂**-), 3.2 (1H, C=O-O-CH₂-C**H**-), 2.8 (1H, C=O-O-CH₂-[CH-O-C**H₂**-]), 2.6 (1H, C=O-O-CH₂-[CH-O-C**H₂**-]) From ^{1}H NMR, molecular weight (Mn) was 14 kg/mol (**Figures S5.19**). GPC (DMF) shows Đ~1.3 (**Figures S5.20**).

PGMA functionalization by epoxide ring opening

PGMA was functionalized using thiol epoxide ring opening to attach different thiols to the PGMA chain. Three different alcohols were attached: 3-mercapto-1-propanol, 1-mercapto-2-propanol, and 3-mercapto-1,2-propanediol form **PGMA-OH-1**, **PGMA-OH-2**, and **PGMA-Diol**. For example, to form **PGMA-OH-1**, **PGMA** (100 mg) and 3-mercapto-1-propanol (100mg, 1.5 eq) were dissolved in DMF. Using an ice bath, the solution was cooled and lithium hydroxide (1.1 mg, 0.07 eq) was added via a 20 mg/ml water solution. After 10 min, the reaction was brought to room temperature and allowed to stir for 18hrs. The solution was then precipitated into diethyl ether three times and dried in a vacuum oven at 40 °C for 24 h. **PGMA-OH-1:** ^{1}H NMR: (500 MHz, d_6-DMSO); δ ppm: 3.8 (2H, C=O-O-C**H₂**-), 3.5 (3H, -C**H**-OH, -C**H₂**-OH), 2.6 (4H, -C**H₂**-S-C**H₂**-), 1.7 (2H, -CH2-C**H2**-CH2-) From ^{1}H NMR, molecular weight (Mn) was 23 kg/mol (**Figures S5.19**). GPC (DMF) shows Đ~1.3 (**Figures S5.20**). **PGMA-OH-2:** ^{1}H NMR: (500 MHz, d_6-DMSO); δ ppm: 3.8 (4H, C=O-O-C**H₂**-, -2x C**H**-OH), 2.6 (4H, -C**H₂**-S-C**H₂**-), 1.1 (2H, -CH2-C**H₃**) From ^{1}H NMR, molecular weight (Mn) was 23 kg/mol (**Figures S5.19**). GPC (DMF) shows Đ~1.3 (**Figures S5.20**). **PGMA-Diol:** ^{1}H NMR: (500 MHz, d_6-DMSO); δ ppm: 3.8 (2H, C=O-O-C**H₂**-), 3.6 (2H, 2x -C**H**-OH), 3.4 (2H, -C**H₂**-OH),2.6 (4H, -C**H₂**-S-C**H₂**-), From ^{1}H NMR, molecular weight (Mn) was 25 kg/mol (**Figures S5.19**). GPC (DMF) shows Đ~1.3

Model Surface Fabrication. IDE were fabricated following previously detailed procedures and their surfaces were cleaned using oxygen-plasma treatment for 20 min.[35] Polymer brushes were side chain-grafted to the desired substrates by first spin-casting a 1 wt% brush in DMF solution to yield a ca. 15 nm thin film. The sample was then heated to 200 °C in the N_2-filled glovebox for 10 min in order to graft the alcohol moiety to the underlying substrate. Side chain-grafting occurs through a condensation reaction between the side chain –OH groups of the polymer and the SiO2 surface. Subsequently, the sample was sonicated in DMF for 10 min before being rinsed extensively with DMF to remove non-grafted polymer chains. The **XPV** polymer was spin-coated from anisole, with concentration (1-2 wt%) and spin RPM (2000-4000 RPM) controlling film thickness as determined by ellipsometry, iteratively altering concentration and spin RPM to attain the requisite thicknesses (15-200 nm). The sample was then heated to 250 °C in a N_2-filled glovebox for 5 min in order to crosslink the polymer samples to reduce polymer dewetting. Samples were then methylated by sealing in 150 ml jars with 2 ml iodomethane for 2 days. Film thickness was measured using spectroscopic ellipsometry. Optical characterization was performed in reflection mode with an Olympus BX60 microscope with a 20× objective.

5.3 RESULTS AND DISCUSSION

Using the previously well characterized ***MxG*-CNC-*g*-PV-68-20**, where 68 refers to the grafted polymer degree of polymerization and 20 refers to the volume percent polymer, acetylated ***MxG*-CNC-*g*-PV-68-20** was produced by reacting the surface CNC alcohol groups with acetic anhydride (**Scheme 5.1**). While characterizing the extent of reaction for surface alcohol groups is notoriously difficult,[38,39] FTIR confirms acetylation of the surface with appearance of strong signal at 1750 cm^{-1} (**Figure S5.1**). After casting into a film and methylating the sample is now referred to as acetylated ***MxG*-CNC-*g*-mPV-68-33**.

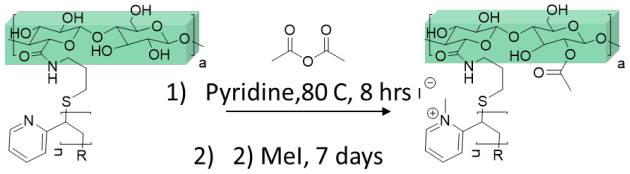

Scheme 5.1: Synthetic scheme for acetylated ***MxG*-CNC-*g*-mPV**

Analysis of the film structure by scanning electron microscopy shows similar microstructure as compared to the unacetylated version with individualized nanorods of similar dimensions (**Figure 5.1a-b**). **Figure 5.1c** shows the conductivity of ***MxG*-CNC-*g*-mPV-7-33** and acetylated ***MxG*-CNC-*g*-mPV-7-33** as a function of relative humidity. The conductivity, σ, of the film was calculated using the measured value of the resistance of the film, R_{film}, and the following equation,

$$\sigma = d/(R_{film}A) \quad (5.1)$$

where d is the separation distance between electrodes and A is the cross-sectional area probed.[35] As both materials contain nearly 70 vol% nonconductive CNC nanofiller, an effective polymer

conductivity, σ_{eff}, was calculated which considers that the ion conductivity is only occurring through the polyelectrolyte volume fraction, and is defined as

$$\sigma_{eff}=\sigma/\Phi_V \tag{5.2}$$

where Φ_V is the polymer volume fraction. Interestingly, the acetylated material shows a dramatic reduction in conductivity, falling nearly an order of magnitude below that of the homopolymer. As the polymer grafted nanoparticle structure is retained after reaction with the acetic anhydride, the presence of the acetyl functional groups rather than the alcohols seems to be dramatically impacting the material conductivity. However, the acetyl presence has two distinct effects: reduction of surface alcohol content and reduction of surface hydrophilicity. Additionally, the interface quality may be impacted even though FTIR and SEM (**Figure S5.1** and **Figure 5.1b**) seem to point to little change after reaction. Thus, a more controllable model surface is necessary to further distinguish between the impact of hydrophilicity and surface alcohol content in an easily tunable way.

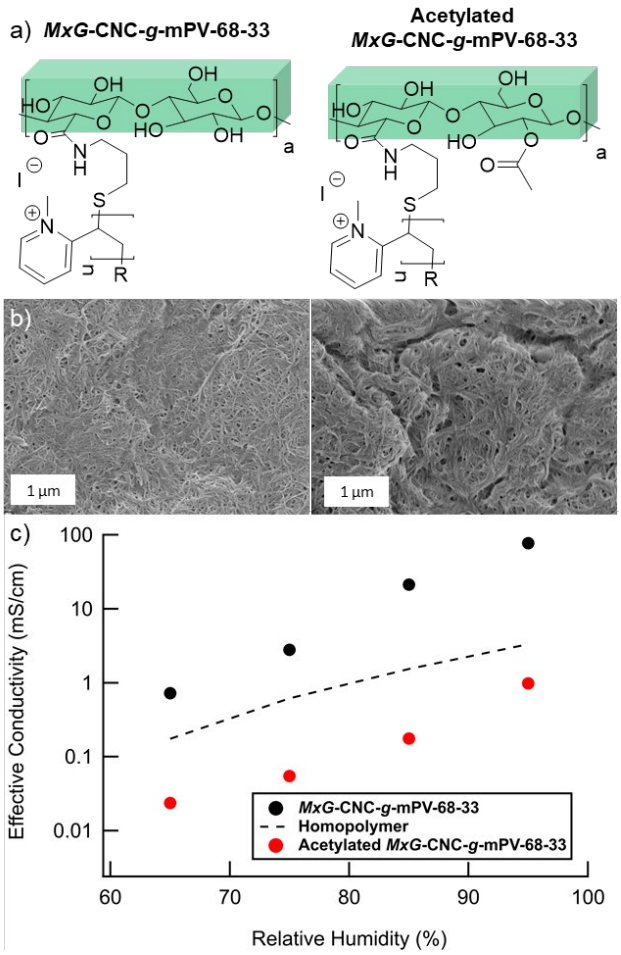

Figure 5.1: a) Chemical structure of ***MxG*-CNC-*g*-PV-7-20** and acetylated ***MxG*-CNC-*g*-PV-7-20** (full reaction scheme in **Scheme 5.1**). b) Scanning electron microscopy (SEM) of ***MxG*-CNC-*g*-mPV-7-33** and acetylated ***MxG*-CNC-*g*-mPV-7-33** and c) conductivity of ***MxG*-CNC-*g*-mPV-7-33** and acetylated ***MxG*-CNC-*g*-mPV-7-33** as a function of relative humidity.

In order to discern the relative impact of alcohol content and hydrophilicity, the model interfacial polymers should fulfill three conditions: 1) all must be graftable to the IDE surface, 2) contain a series of model polymers with controllable hydrophilicity with constant alcohol content, and 3) contain a series of model polymers with controllable alcohol content and constant hydrophilicity. To achieve this, polyacrylate copolymers were synthesized via RAFT from 2-

hydroxyethyl acrylate (**H**), methyl acrylate (**M**) 4-hydroxybutyl acrylate (**B**), or 2-[2-(2-methoxyethoxy)ethoxy]ethyl acrylate (**G**) (**Scheme 5.2**). Thus, a copolymer with 45 mol% 2-hydroxyethyl acrylate and 55 mol% methyl acrylate will be termed **45H55M**. The samples were characterized with ^{1}H NMR and GPC (DMF) to ascertain composition and molecular weight. By ^{1}H NMR, identifying peaks for each copolymer permitted the calculation of copolymer composition, specifically 4.8 ppm (**H**), 3.6 ppm (**M**), 4.4 ppm (**B**), and 3.4 (**G**) (**Figures S5.2-5.4**) showing the labeled compositions and M_n between 10 kg/mol and 20 kg/mol. Using GPC (DMF), the molecular weights and distributions of the polymers (M_n between 7 kg/mol and 24 kg/mol and Đ<1.35) were obtained relative to poly(methyl methacrylate) standards (**Figure S5.5**). Importantly, the M_n measured by ^{1}H NMR and GPC (DMF) are in close alignment (**Table S5.1**). By including some alcohol content in all copolymer compositions, they remain graftable to the IDE surface through side chain-grafting via a condensation reaction between the side chain alcohol groups and the SiO_2 surface.[40] These specific copolymers were chosen for a **xHyM** binary composition to broadly investigate the effect of reduced alcohol content (roughly modeling the acetylation reaction on the CNC surface from **Figure 5.1**) while the **B** content was chosen to maintain alcohol content while adjusting the hydrophilicity and **G** content was chosen to maintain hydrophilicity while adjusting alcohol content.

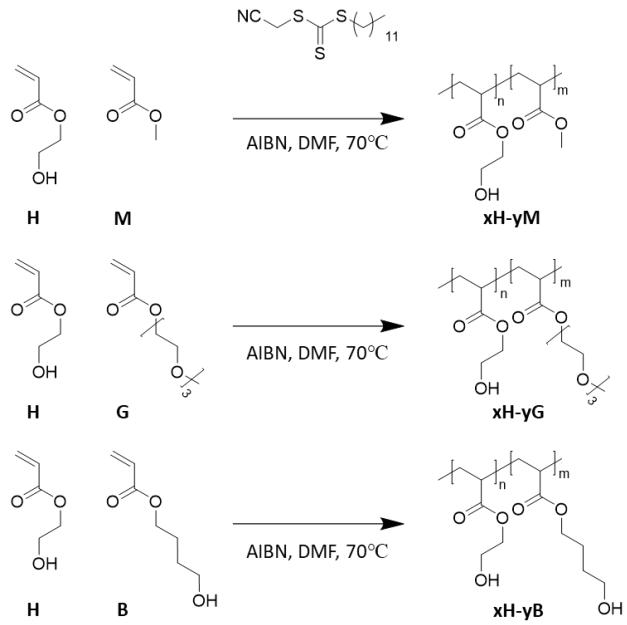

Scheme 5.2: Synthetic scheme for model copolymer samples

Figure 5.2 shows the fabrication procedures for the model IDE surface. In order to fabricate these devices, the silica passivated IDEs were cleaned with oxygen-plasma treatment for 20 min after which the polymer is spin coated from 1wt% DMF solution to form a ~10 nm thick film. The system was then heated to 200 ℃ for 10 minutes under N_2 atmosphere to side-chain graft the polymer to the IDE surface forming a brush, followed by sonication to remove the ungrafted polymer. Next, a poly(2-vinyl pyridine) (PV) was spin-coated onto the polymer brush surface from anisole, with solution concentration and spin rate used to control the film thickness (15nm-200nm). For a homopolymer system, the sample can be made ionically conductive by exposing the system to saturated iodomethane (MeI) vapor at RT for 2 days, introducing iodide ions, now referred to as **mPV**. For the case of the cross-linkable **XPV-n** system, the film was crosslinked at 250℃ for 5 minutes under N_2 atmosphere, before being exposure to MeI as before, now being referred to as **XmPV-n**.

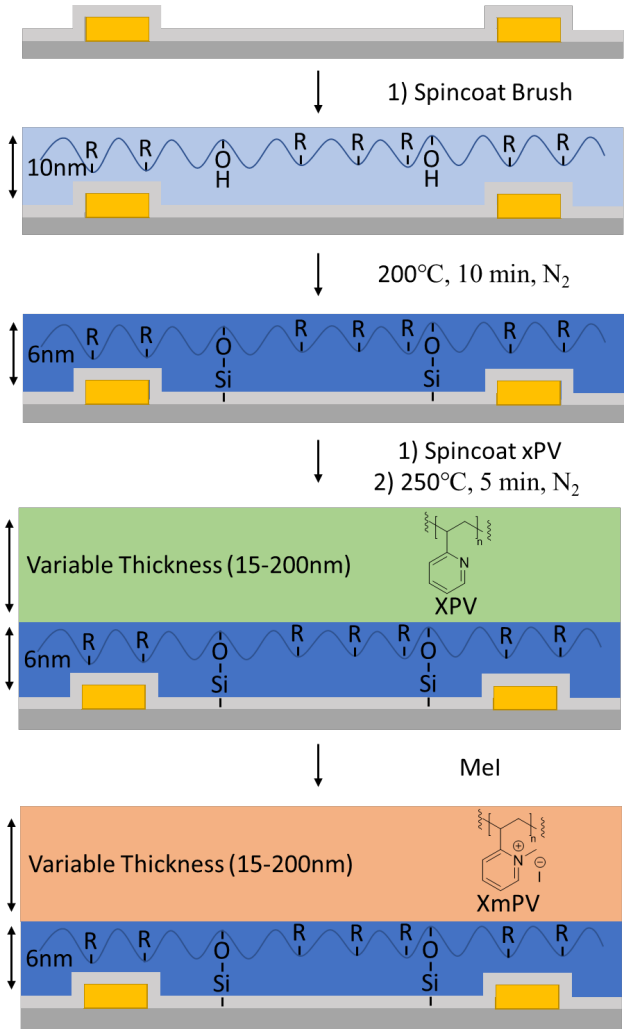

Figure 5.2: Fabrication procedures for the model IDE surface.

Figure 5.3a shows the chemical structures and nomenclatures for the synthesized copolymer series. After grafting to silicon wafers (to form brushes) and using water contact angle measurements, **Figure 5.3b** shows the dependence of the hydrophilicity (from water contact angle) on the composition of the copolymer brushes. Here a roughly linear relationship is seen between the **100H** and extremes of the other copolymer compositions. **xHyG** is roughly composition independent for water contact angle, although increasing slightly with higher **G** compositions.

Interestingly, an **xHyB** composition maintains similar loadings of alcohol content with the water contact angle following a nearly identically with the **xHyM** materials, permitting useful comparison as to the effect of alcohol content. Additionally, an **xHyG** composition alters the alcohol content while maintaining the water contact angle similar to the **100H** material. With these series of model interfacial brushes, the impact of alcohol content and hydrophilicity on ionic conductivity can be investigated.

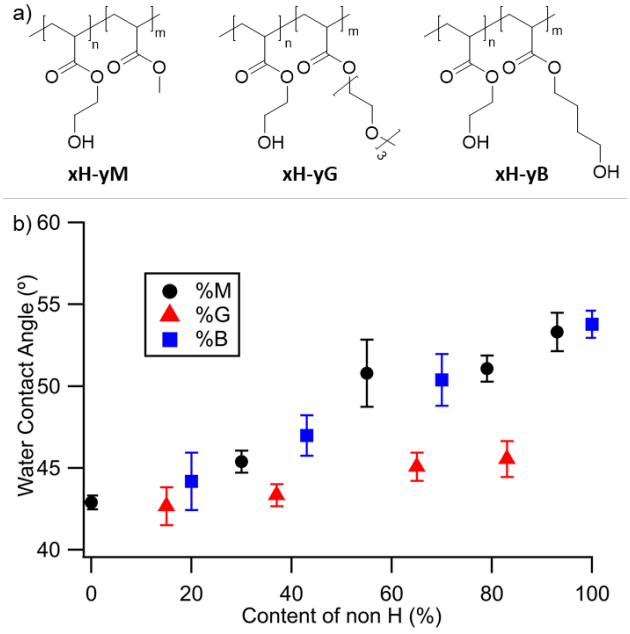

Figure 5.3: a) Chemical structures of **xHyM**, **xHyB**, and **xHyG**, b) water contact angle of brushes grafted to silica as a function of the non-H component of copolymer (y in these chemical structures)

The next step was to investigate the conductivities of the interfacial materials. **Figure 5.4a** shows the conductivity as a function of mPV film thickness on both the **100H** and **7H93M** brushes. Here a synthesized 16 kg/mol PV polymer (no glycidyl methacrylate) was used as the ion conducting layer. The conductivity of the mPV on the **100H** brush shows increasing conductivity as the film thickness is decreased, being 50x higher at 15nm thickness than the bulk homopolymer.

However, the conductivity of the mPV on the **7H93M** brush shows much less variation in conductivity with mPV film thickness and if anything, a lower conductivity with the thinnest mPV samples. This second set of data is consistent with the prior work by Dong *et al*,[37] where decreasing film thickness of PEO and LiTFSI on PEO brush displayed a reduction in conductivity assigned to the presence of an immobile interfacial layer. As such the increasing conductivity at reduced mPV film thickness with the brush surface coating containing more OH groups (**Figure 5.4a**) suggests that such chemistry at the interface has a significant beneficial effect for ion conductivity Interestingly, this behavior mirrors the acetylated CNC surface well, where the reduction of alcohol surface groups and decrease in hydrophilicity result in reduced ionic conductivity of the mPV.

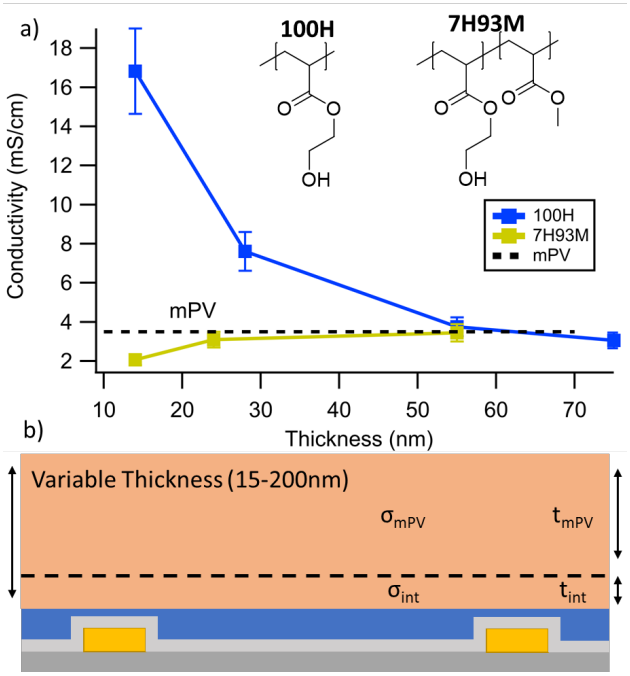

Figure 5.4: a) Conductivity vs thickness of top **mPV** layer on either **100H** or **7H93M** measured at 95% RH and b) cartoon schematic showing the bilayer nanothin film with bulk and interfacial layers.

Figure 5.4b shows how the conductive **mPV** film can be divided into a bulk region and an interfacial region, parallel to the applied electric field, in order to determine the interfacial layer conductivity and thickness in a similar manner to Dong *et al.*[37]. Thus a bilayer model can be employed with given conductivities (σ) and thicknesses (t) such that

$$\sigma_{total} t_{total} = \sigma_{mPV} t_{mPV} + \sigma_{int} t_{int} \tag{5.3}$$

where σ_{total} is the measured conductivity, t_{total} is the measured thickness, and $t_{total} = t_{mPV} + t_{int}$. Rearranging for linearization, the relationship becomes

$$\sigma_{total} = \frac{1}{t_{total}} t_{int}(\sigma_{int} - \sigma_{mPV}) + \sigma_{mPV} \tag{5.4}$$

which allows a relationship between the unknown interfacial conductivity (σ_{int}) and thickness (t_{int}) can be determined, specifically that $t_{int}(\sigma_{int} - \sigma_{mPV}) = 171.3$ upon fitting to the data in **Figure 5.4a**. Recall that in Chapter 3 the maximum conductivity sample (***MxG*-CNC-*g*-mPV$_{68/64}$**) had a value of 140±10 mS/cm. Using the AFM data therein, the polymer brush thickness can be determined to be 1.75 nm following similar procedure from Chapter 2. Given that this sample shows the greatest enhancement in conductivity, the polymer brush thickness should function as an estimate for the extent to which the interface can influence, thus being an estimate for the interfacial thickness. With this, the interfacial conductivity has a value of 101 mS/cm, remarkably showing that the interfacial conductivity agrees well with what is measured in the ***MxG*-CNC-*g*-mPV** system.[30]

While this initial set of data provided some interesting results, over time at the high relative humidities the electrochemical measurements begin to show degradation in signal quality. At high relative humidities (above 80%), mPV is known to have a depressed glass transition temperature (T_g) such that at room temperature the material is a rubber (T > T_g).[34] Thus it is necessary to

understand the stability of the mPV films on different brushes to ensure that the EIS measurements are reproducible and accurate, this is particularly important as it is known that thin films commonly dewet on materials of different surface energies.[35] **Figure 5.5** shows the Bode plots of 16 kg/mol **mPV** on **100H** and **7H93M** brushes at 95%RH at different time points. In order to correctly interpret EIS measurements, Bode plots should have a plateau in impedance and a peak in the phase (approaching 90°), and aberrations from this are correlated with poorer measurement quality. The mPV on the **100H** brushes show remarkable stability out to 50 minutes, with slight reduction in phase peak after 24 hours. In contrast, the **7H93M** brushes begin to show reduction in phase peak after 20 minutes with severe degradation after 30 minutes, alongside increases in measured resistance. To ensure reproducible data, particularly across the variety of brush materials synthesized, an alteration in the **mPV** material is needed to prevent dewetting.

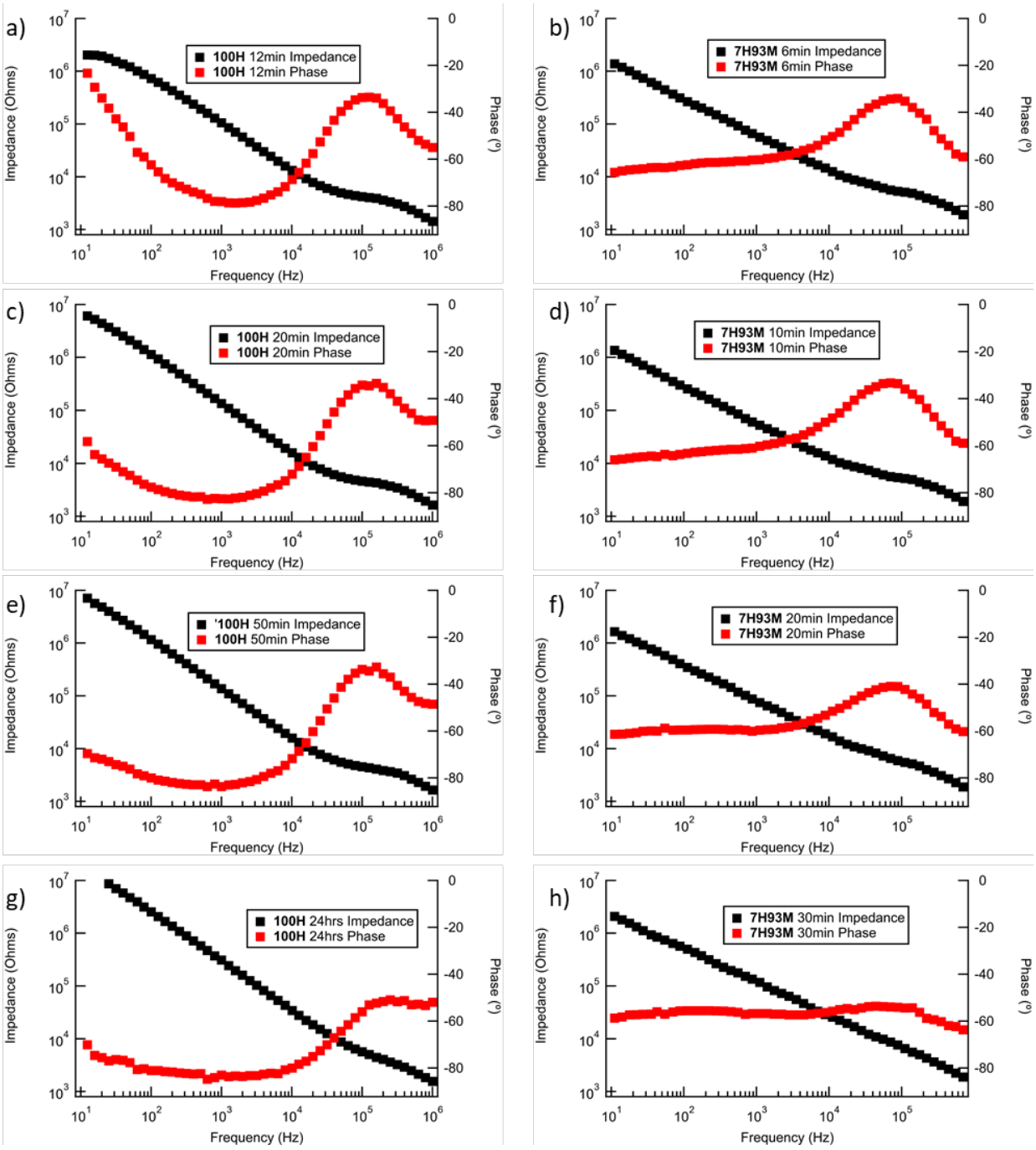

Figure 5.5: Bode plots of 60 nm 16 kg/mol **mPV** on **100H** and **7H93M** brushes at 95%RH over time.

To combat this effect, cross-linkable poly(2-vinylpyridine-co-glycidyl methacrylate) (**XPV-n**, where n refers to the mol% of glycidyl methacrylate) was synthesized via RAFT

polymerization of 2-vinylpyridine and glycidyl methacrylate using 2-cyano 2-propyl dodecyl trithiocarbonate as a chain transfer agent (**Scheme 5.3**). A cross-linkable poly(2-vinylpyridine) offers one route to reduce dewetting on the different polymer brushes, particularly at thin films which can have a higher likelihood of dewetting. ^{1}H NMR in $CDCl_3$ characterizes the quantity of included glycidyl methacrylate, resulting in **XPV-2**, **XPV-4**, and **XPV-6** (**Figure S5.6**). Using GPC-MALS (THF) the molecular weights of the samples were characterized resulting in Mn of 35 kg/mol, 52 kg/mol, and 25 kg/mol, respectively, and dispersity~1.15 (**Figure S5.7**). It is important to note that although these polymers have different molecular weights, it is the quantity of glycidyl methacrylate repeat unit that will define the molecular weight between crosslinks of the fully reacted materials.[41]

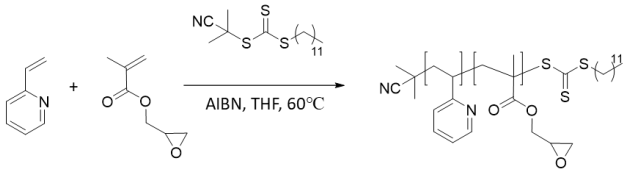

Scheme 5.3: Synthetic Scheme of **XPV-n** via RAFT

In order to ensure that the top, conductive layer maintains film quality, the films were exposed to high relative humidity to explore their potential stability with regard to dewetting. **Figure 5.6** shows optical images of a control 112 kg/mol **mPV** homopolymer and **XmPV-6** on the different extremes of brush compositions, looking at **100H**, **7H93M, 30H70B,** and **17H83G**. The mPV films were 15 nm thick and kept at 95% RH for 20 minutes. Although **7H93M** and **30H70B** show similar film quality between both samples, **XmPV-6** displayed superior film quality on the **100H** and **17H83G** brushes and also performed better than different glycidyl methacrylate

compositions (**Figure S5.8-S5.11**). Thus, having established the correct processing conditions for the conductive top layer, the conductivity of the interfaces can be studied.

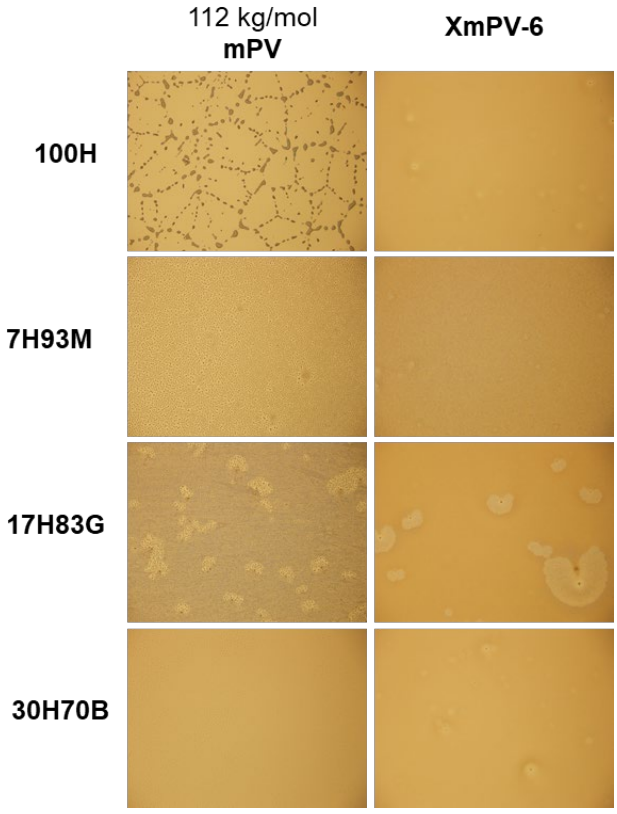

Figure 5.6: Optical images of 112 kg/mol **mPV** and **XmPV-6** on different brush compositions. Conductive top layers were 15 nm thick and held at 95% RH for 20 minutes. Image widths are 480 μm.

Using the crosslinkable PV, the impact of the various brush interfaces on the material conductivity can be fully explored. **Figure 5.7** shows the relative conductivity (measured conductivity using the dry **XPV** film thickness dimension divided by measured conductivity of bulk mPV) versus thickness of both the previously shown **mPV** on **100H** brush and new **XmPV-6** on **100H** and **100B** brushes. If the general water uptake is similar between **XmPV** of various thicknesses on the different brushes, then comparing the relative conductivity between bulk

conductivity and thin layer is valid due to both samples changing thickness by identical percentages. As the polymers used in brushes show less water uptake compared to **mPV** (between 35 and 40 wt% uptake for mPV compared to maximum of 25 wt% for **100H**),[42] the overall water uptake between **XmPV** thicknesses on brushes should remain relatively constant (**FIGURE S5.12**). Thus, in examining the relative conductivities of **XmPV-6** and **mPV** on **100H**, the samples remarkably fall on a relatively smooth curve showing increasing relative conductivity with decreasing thickness, indicative of conductivity enhancement. Additionally, by falling on a smooth curve, the data enable comparing between the lightly crosslinked **XmPV-6** and homopolymer **mPV**. However, as of this writing, the **100B** brush shows reduced conductivity compared to the **100H** brush, roughly by one third. Although **100B** shows very slight enhancement compared to homopolymer (1.5 times), the similar alcohol content brushes (**100H** and **100B**) seem to indicate that the brush hydrophilicity has an impact on the amount of conductivity enhancement. Further work will continue to investigate the entire breadth of brush compositions.

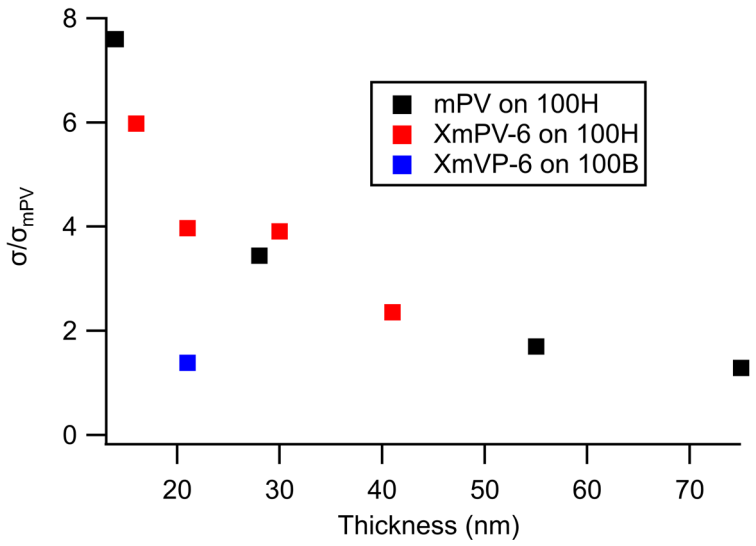

Figure 5.7: Relative conductivity, sample conductivity divided by the bulk **mPV** conductivity, of **mPV** and **XmPV-6** on **100H** and **100B** brushes, as labeled, at various thicknesses. Measurements were taken at 95% relative humidity.

In order to further probe the interface, additional polymer series were synthesized for future testing by collaborators. Following a similar RAFT method to the work in **Scheme 5.2**, **Scheme 5.4** shows the synthesized polymer series. Specifically, a poly(2-hydroxyethyl acrylate)-*co*-poly(*tert*-butyl acrylate) (**xHyT**) copolymer series with *tert*-butyl acrylate content at 25, 50, 75, and 90wt% addition enables probing particularly hydrophobic surfaces beyond that accessible with the **xHyM** series (**Figures S5.13-14**, **Table S5.3**). Next, a poly(2-hydroxyethyl acrylate)-*co*-poly(carboxyethyl acrylate) (**xHyC**) copolymer series with carboxyethyl acrylate content at 10 addition mirrors the residual carboxylic acid content of the CNCs in the ***MxG*-CNC-*g*-PV-7-20** materials (**Figures S5.15-16**, **Table S5.3**). Finally, a poly(hydroxypropyl acrylate) polymer (**100P**) where there is a 3:1 mixture of the 2-hydroxypropyl acrylate to 1-hydroxypropyl acrylate monomer addition resembles the combination of primary and secondary alcohol functional groups on the surface of the CNC (**Figures S5.17-18**, **Table S5.3**).

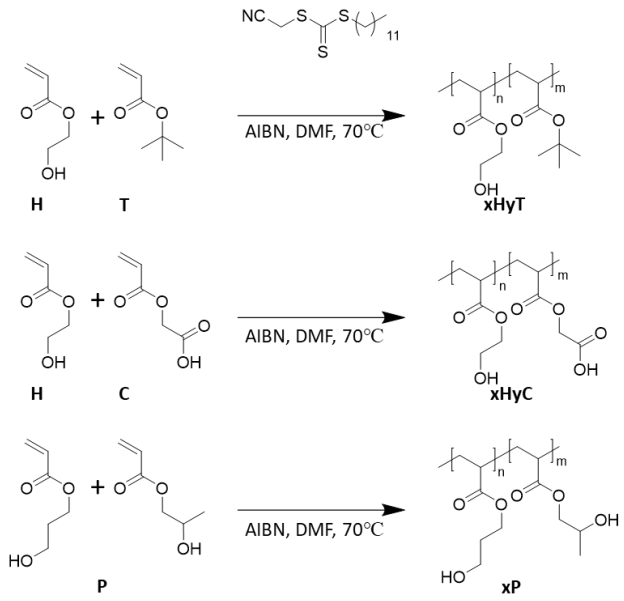

Scheme 5.4: Synthesis of **xHyT**, **xHyC**, and **xP** via RAFT.

To discern between the impact of surface alcohol functionality, particularly the impact of primary alcohol, secondary alcohol, and 1,2 diol, an additional series of polymer derived from poly(glycidyl methacrylate) were synthesized via RAFT and functionalized with thiol-epoxy chemistry (**Scheme 5.5**). First poly(glycidyl methacrylate) was synthesized with molecular weight by ^{1}H NMR being 14 kg/mol and GPC (DMF) Đ<1.3 (**Figure S5.19-20**). Complete functionalization with 3-mercapto-1-propanol, 1-mercapto-2-propanol, and 3-mercapto-1,2-propanediol form **PGMA-OH-1**, **PGMA-OH-2**, and **PGMA-Diol**, respectively, with conversion confirmed by ^{1}H NMR with total peak shifts (**Figure S5.19**). GPC (DMF) confirms a molecular weight shift and maintenance of dispersity (**Figure S5.20**). Although this system uses a slightly different polymer chemistry (methyl-methacrylate backbone, thioether sidechain linkage, and ubiquitous secondary alcohol resulting from the epoxide opening), by selectively varying the alcohol type (primary, secondary, and 1,2 diol) the impact on top-coat conductivity can be directly

compared to the **100H** and **100P** acrylate series to isolate impacts of the altered chemistry and, most importantly, impacts of the alcohol type.

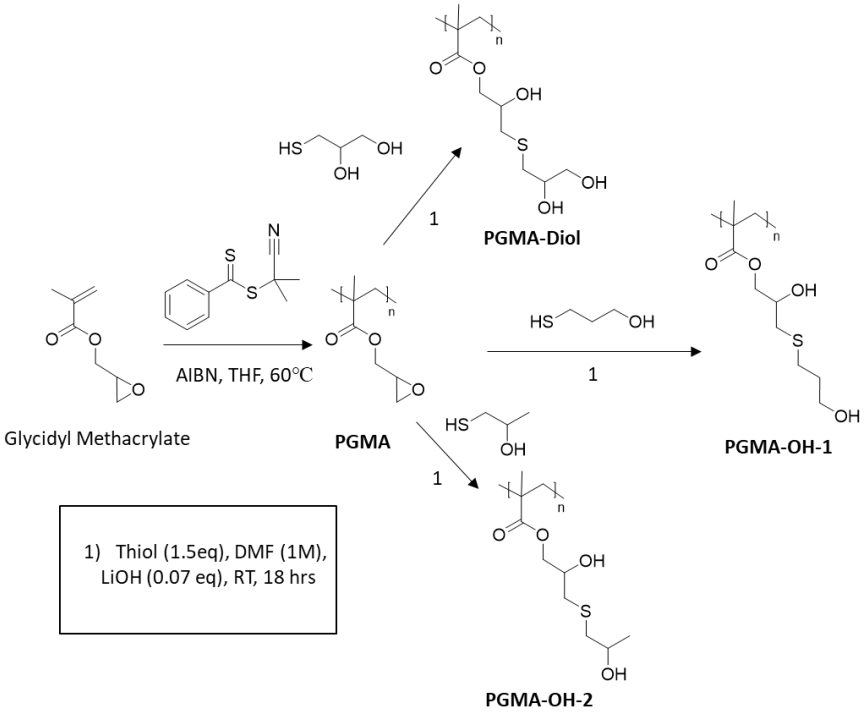

Scheme 5.5: Synthesis of **PGMA** via RAFT and functionalization via epoxide opening with thiols to form **PGMA-Diol**, **PGMA-OH-1**, and **PGMA-OH-2**

5.4 CONCLUSION AND FUTURE WORK

The interfacial impact on ionic conductivity of both methylate poly(2-vinylpyridine) grafted cellulose nanocrystals (***MxG*-CNC-*g*-mPV**) and model polymer brushes mimicking their surface were investigated. By acetylizing the surface alcohols of the ***MxG*-CNC-*g*-mPV**, the measured ionic conductivity dropped 2 orders of magnitude, from 30x conductivity enhancement beyond ungrafted, methylated homopolymer to a half order of magnitude below ungrafted, methylated homopolymer, which was hypothesized to either reduced alcohol content or reduced surface hydrophilicity. Three different model polymer brush series were synthesized to probe the effect of interfacial conductivity by grafting to interdigitated electrodes (IDEs) and subsequent spin-coating and functionalization of methylate poly(2-vinylpyridine) (**mPV**): 2-hydroxyethyl acrylate (**H**) with either methyl acrylate (**M**) 4-hydroxybutyl acrylate (**B**), or 2-[2-(2-methoxyethoxy)ethoxy]ethyl acrylate (**G**). The **100H** surface showed conductivity enhancement consistent with the CNC surface, with decreasing **mPV** polymer thickness showing increasing conductivity, while the **7H93M** surface showed conductivity reduction to below homopolymer showing the efficacy of a brush model system in displaying similar behavior to the bulk. However, the **xHyM** series does not perfectly distinguish between the impact of alcohol content or surface hydrophilicity, necessitating additional brush systems. The **xHyB** series controls for hydrophilicity while maintaining similar alcohol content to the **xHyM** series, and the **xHyG** series controls for alcohol content while maintaining similar hydrophilicity to the **100H** brush. Even so, samples showed dewetting at long times (30 min) at 95% RH via optical images, resulting in the synthesis and application of crosslinkable poly(2-vinylpyridine) (**XPV**).

Future work by collaborators will probe the thickness dependent ionic conductivity of the full synthesized brush series as well as the methylated **XPV**. Additionally, these collaborators will

measure the water uptake of the brush materials to further confirm the hydrophilicity dependencies of the resulting grafted surfaces. Finally, this will allow analysis of the interfacial impact on conductivity and its thickness into the **XmPV** material, which will permit conclusions regarding the relative impact of alcohol functionality and hydrophilicity on ionic conductivity of these interesting materials, while also providing insight into the possible conduction mechanisms causing the enhanced conductivity in the ***MxG*-CNC-*g*-mPV** System**.**

5.5 SUPPLEMENTAL INFORMATION

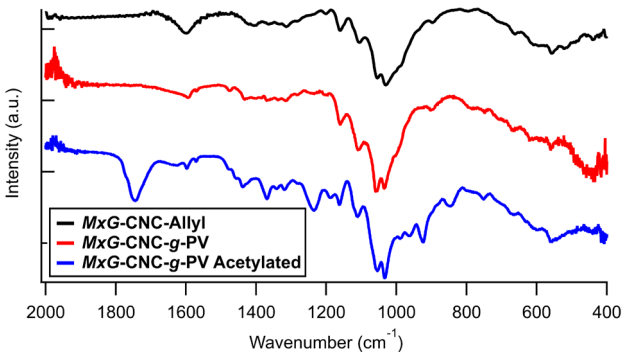

Figure S5.1: ATR-FTIR of ***MxG*-CNC-Allyl, *MxG*-CNC-*g*-PV**, and acetylated ***MxG*-CNC-*g*-PV**

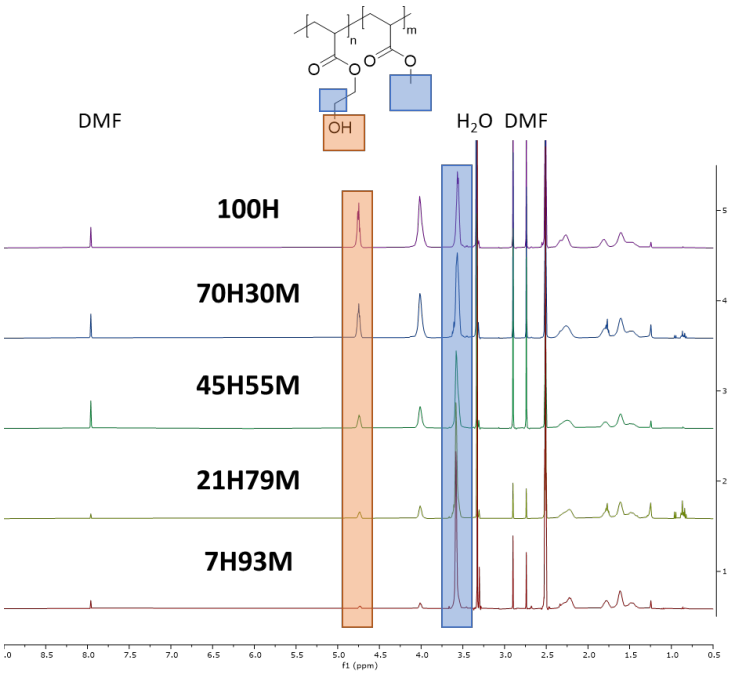

Figure S5.2: ^{1}H NMR (500 MHz, d_6-DMSO) spectra of **xHyM** samples from **Table S5.1**

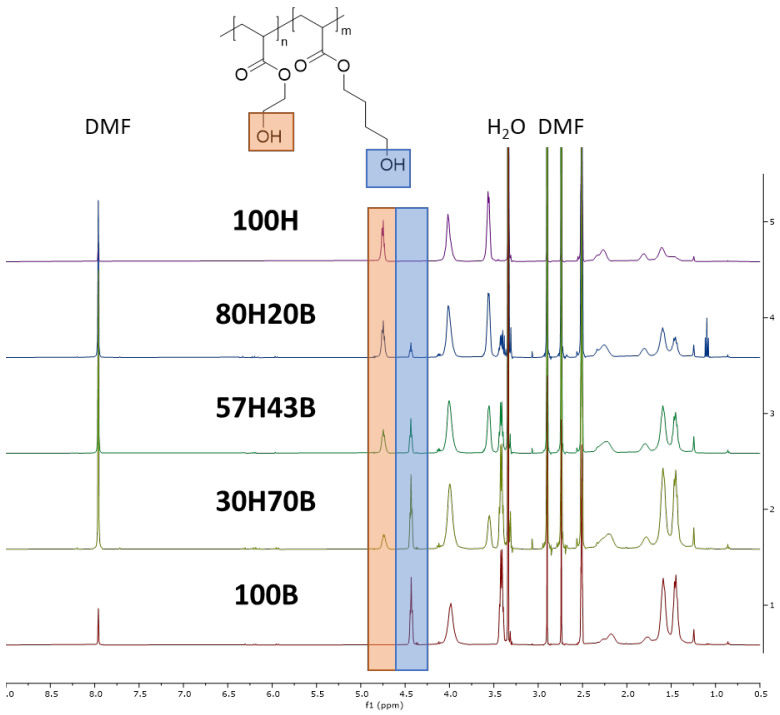

Figure S5.3: ^{1}H NMR (500 MHz, d_6-DMSO) spectra of **xHyB** samples from **Table S5.1**

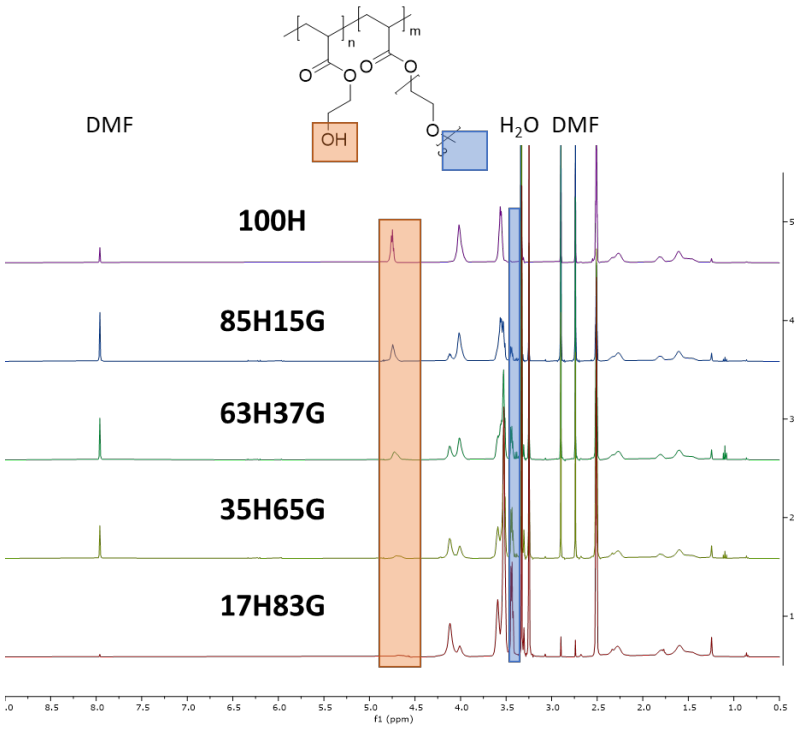

Figure S5.4: ^{1}H NMR (500 MHz, d_6-DMSO) spectra of **xHyG** samples from **Table S5.1**

As a note, Figure S5.5 seems to show some broad low elution time signal most evident in Figure S5.5b. This is attributed to some agglomeration in the DMF solvent for two reasons. First, the ^{1}H NMR based molecular weights via end group analysis match extremely well with the analysis of the high elution time peak of all suspect samples. Second, in-line UV-Vis elution at 310 nm follows perfectly with the RI based measurement indicative of RAFT CTA endgroup retention on all the polymer in the study.

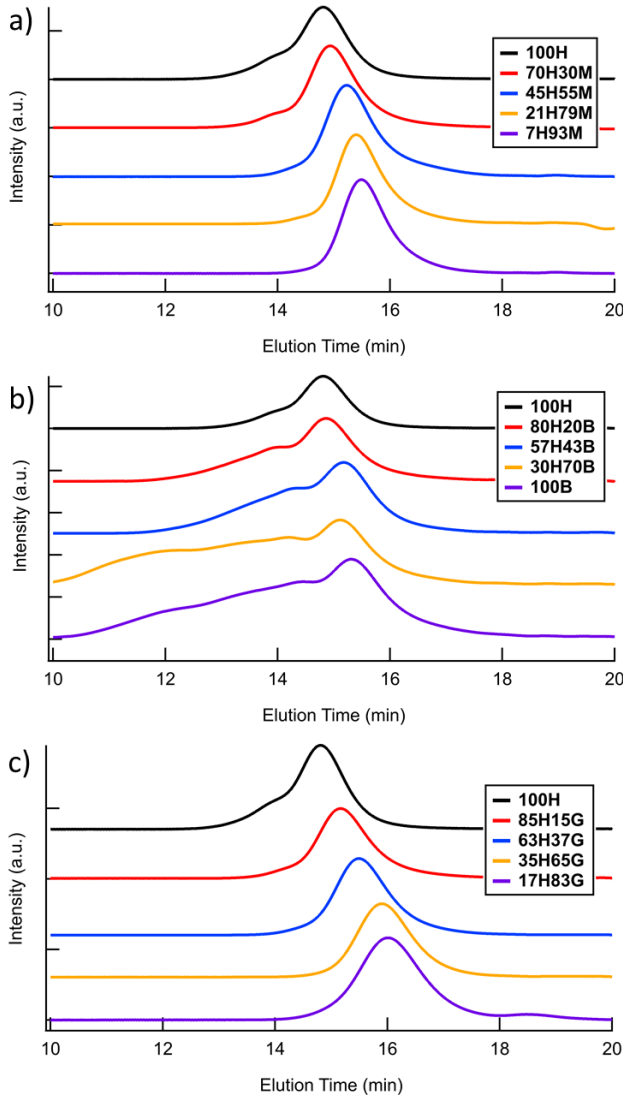

Figure S5.5: GPC (DMF) of model polymers for brushes, specifically a) **xHyM**, b) **xHyB**, and c) **xHyG** from **Table S5.1**

Table S5.1: Model polymer brush sample summary

Samples	Mn SEC [a] (kg/mol)	Dispersity [a]	Mn ^{1}H NMR [b] (kg/mol)	NonH Mol% [b]
100H	24	1.258	25	0%
85H15G	16	1.224	16	15%
63H37G	11	1.364	11	37%
35H65G	8	1.29	10	65%
17H83G	7	1.386	9	83%
70H30M	13	1.368	18	30%
45H55M	13	1.364	18	55%
21H79M	12	1.264	14	79%
7H93M	11	1.232	13	93%
80H20B	16	1.364	17	20%
57H43B	14	1.307	14	43%
30H70B	13	1.378	15	70%
100B	10	1.595	14	100%

[a] from GPC (DMF)

[b] from ^{1}H NMR

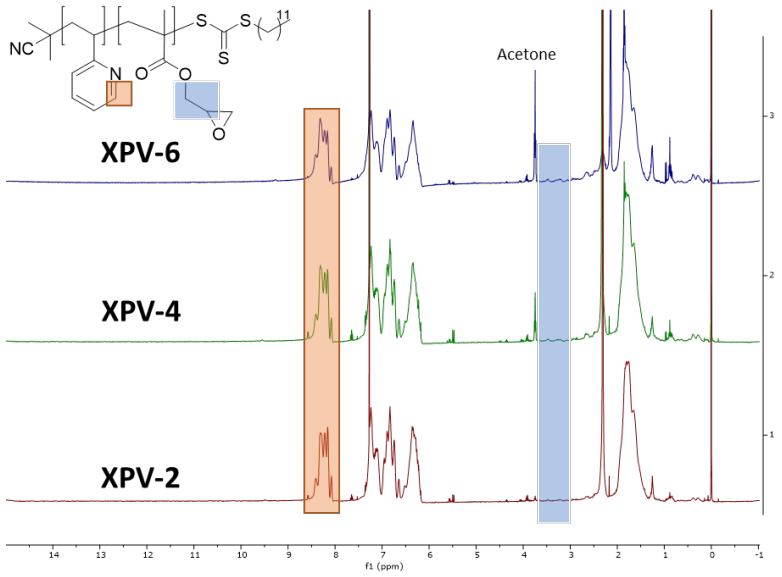

Figure S5.6: ^{1}H NMR (500 MHz, $CDCl_3$) spectra of **XPV-n** samples from **Table S5.2**

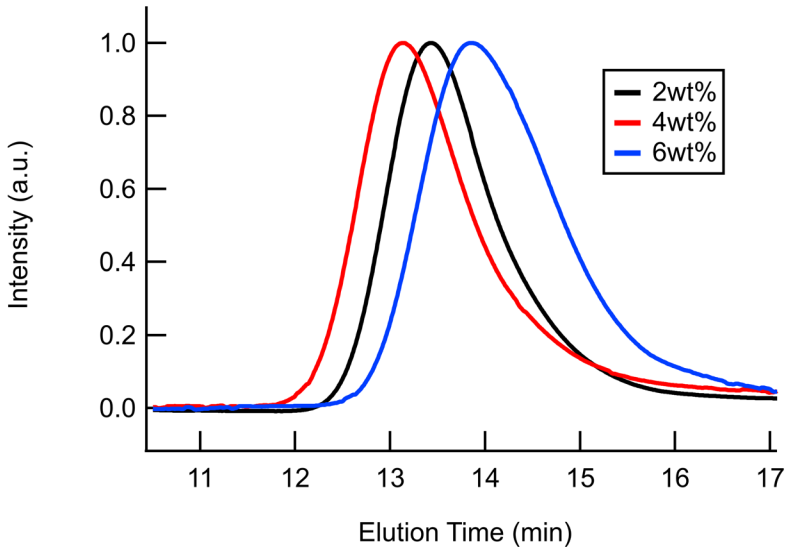

Figure S5.7: GPC-MALS (THF) of **XPV-n** samples from **Table S5.2**

Table S5.2: Crosslinking poly(2-vinylpyridine) sample summary

Sample	Mn (kg/mol) [a]	Dispersity [a]	wt% GMA [b]
XPV-2	35.5	1.11	2
XPV-4	52	1.13	4
XPV-6	25	1.15	6

[a] from GPC-MALS (THF)

[b] from ^{1}H NMR

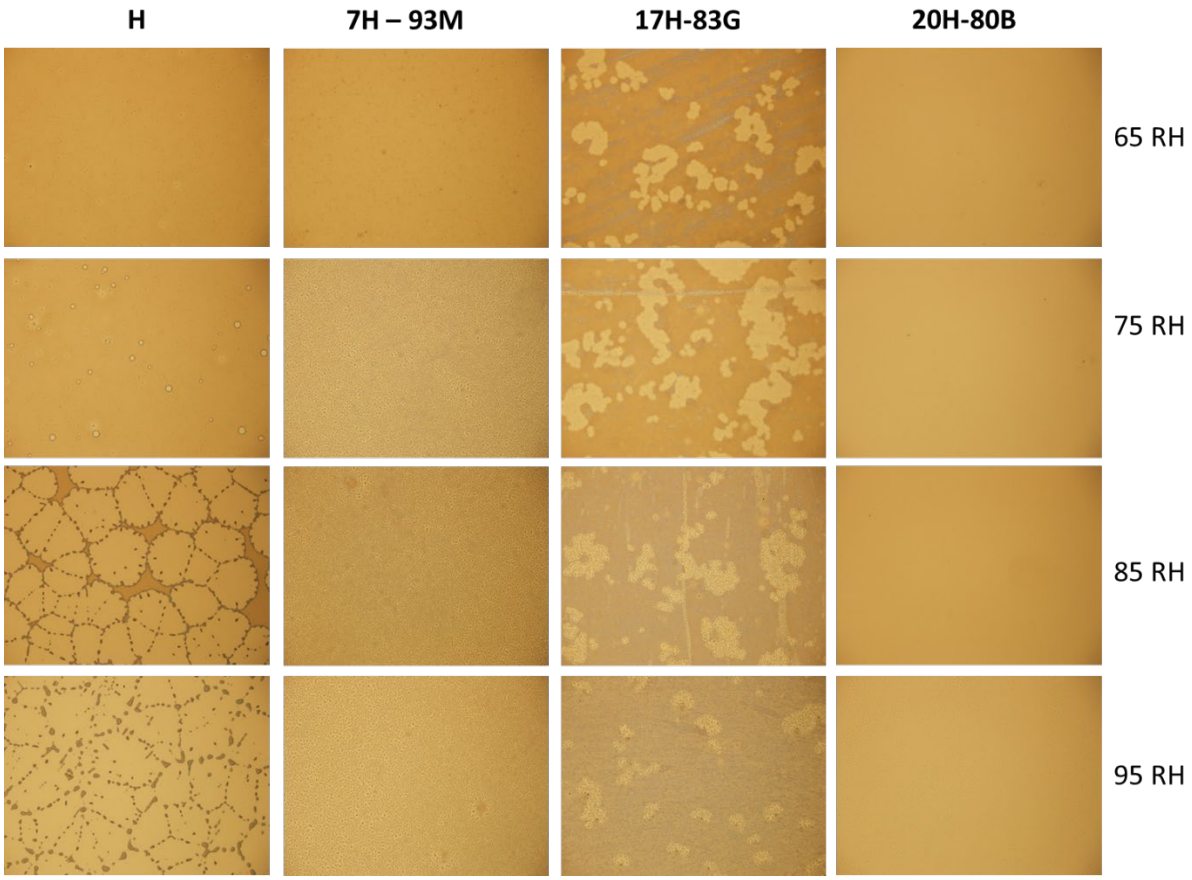

Figure S5.8 Optical images of 112 kg/mol **mPV** on different brush compositions and at different relative humidities. Conductive top layers were 15 nm thick and held for 30 minutes. Image widths are 480 μm.

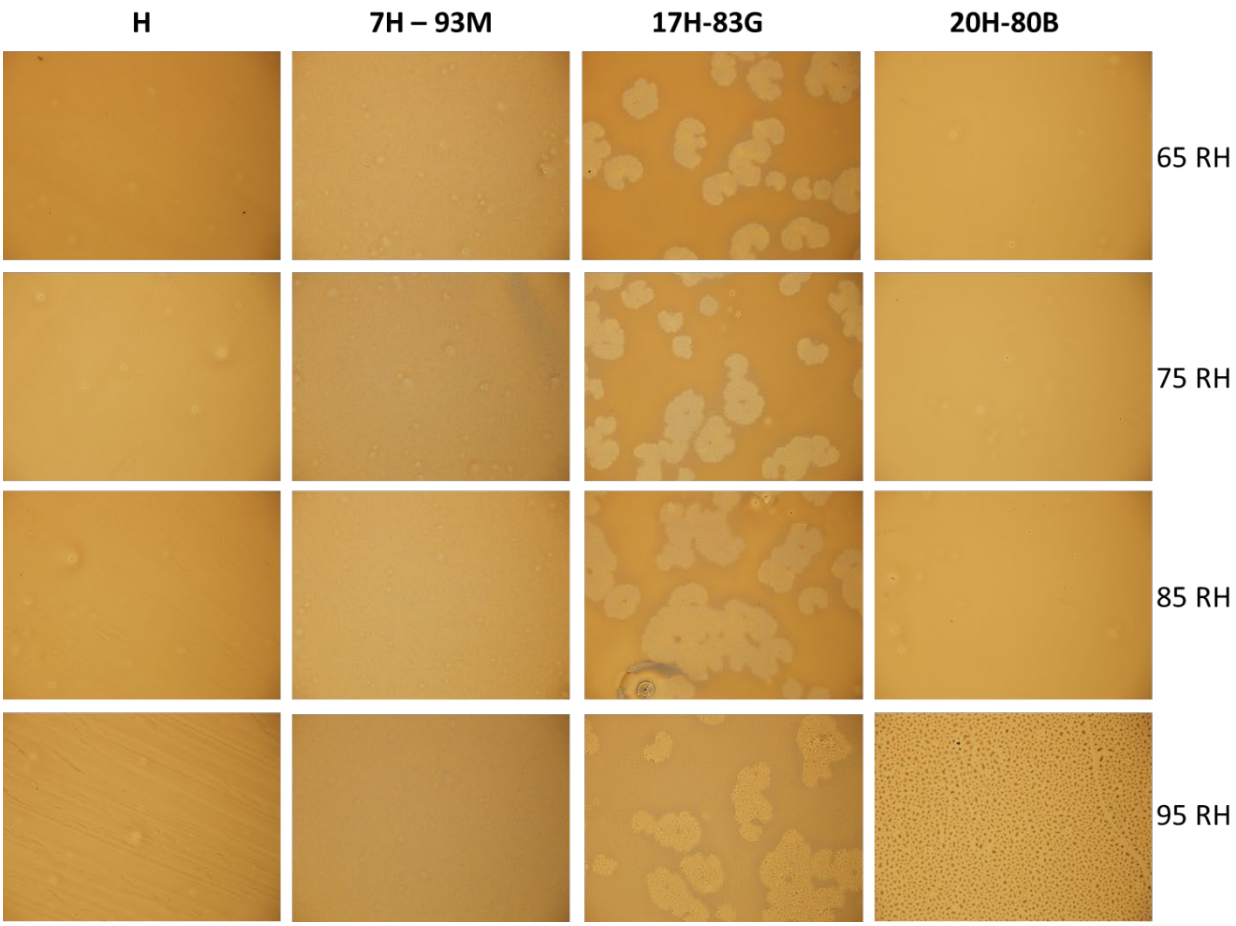

Figure S5.9 Optical images of **XmPV-2** on different brush compositions and at different relative humidities. Conductive top layers were 15 nm thick and held for 30 minutes. Image widths are 480 μm.

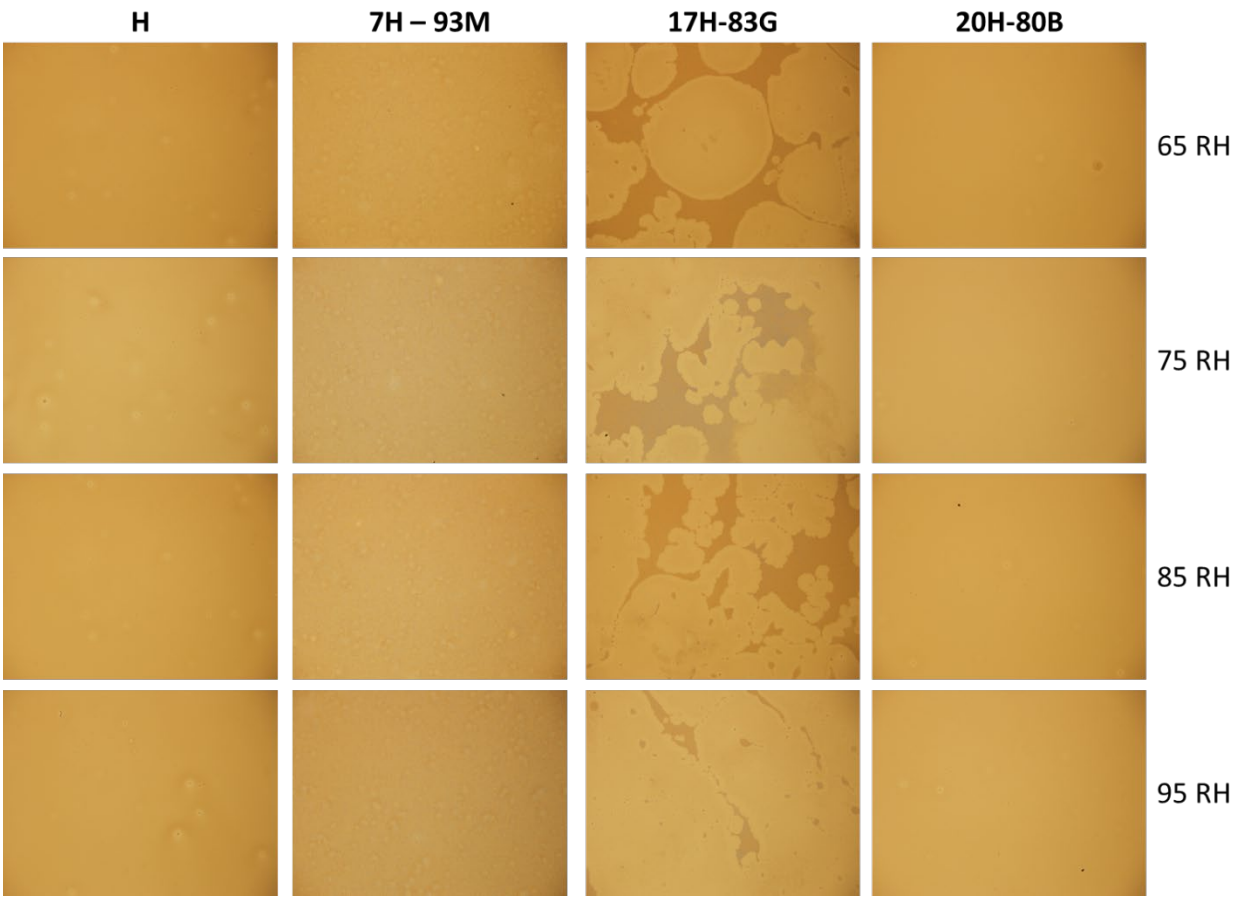

Figure S5.10 Optical images of **XmPV-4** on different brush compositions and at different relative humidities. Conductive top layers were 15 nm thick and held for 30 minutes. Image widths are 480 μm.

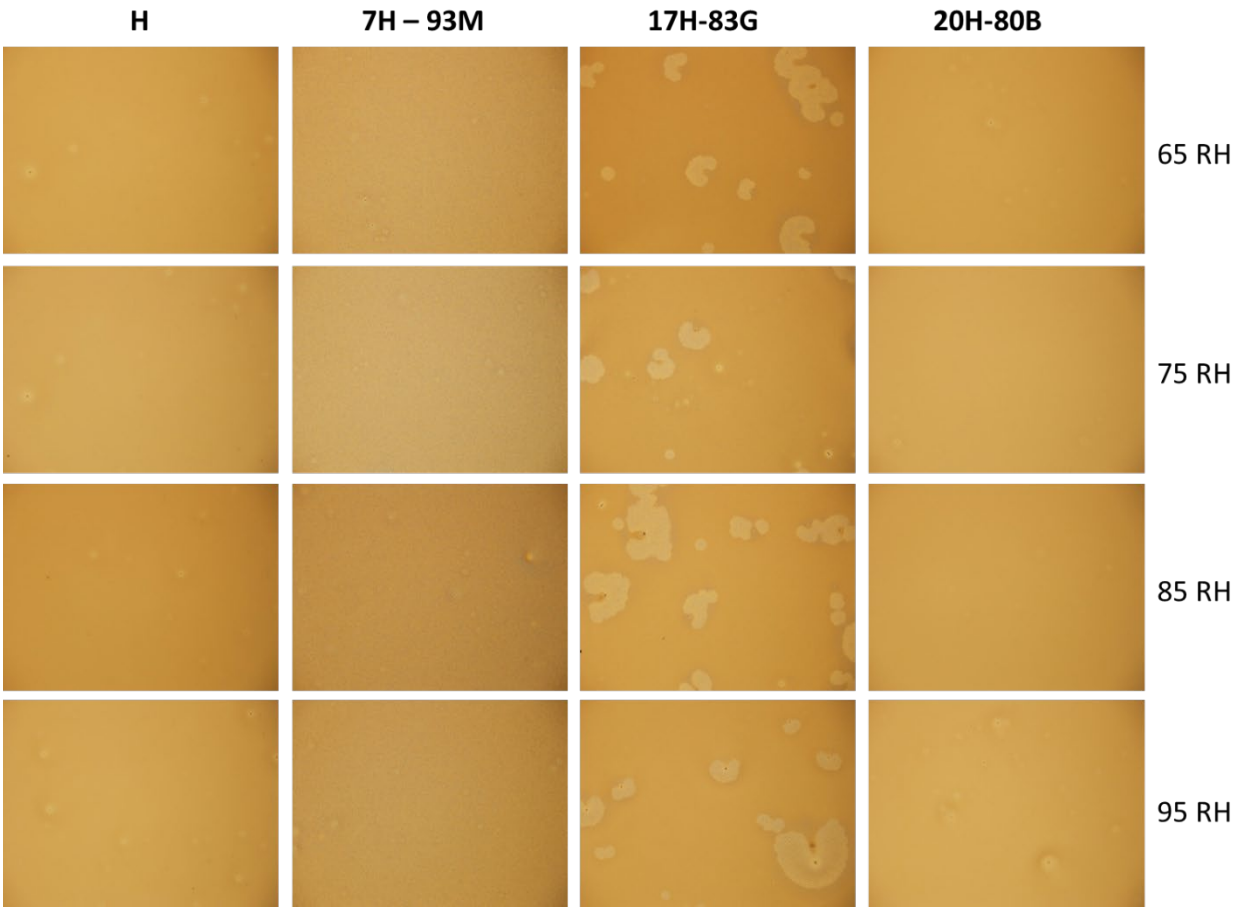

Figure S5.11: Optical images of **XmPV-6** on different brush compositions and at different relative humidities. Conductive top layers were 15 nm thick and held for 30 minutes. Image widths are 480 μm.

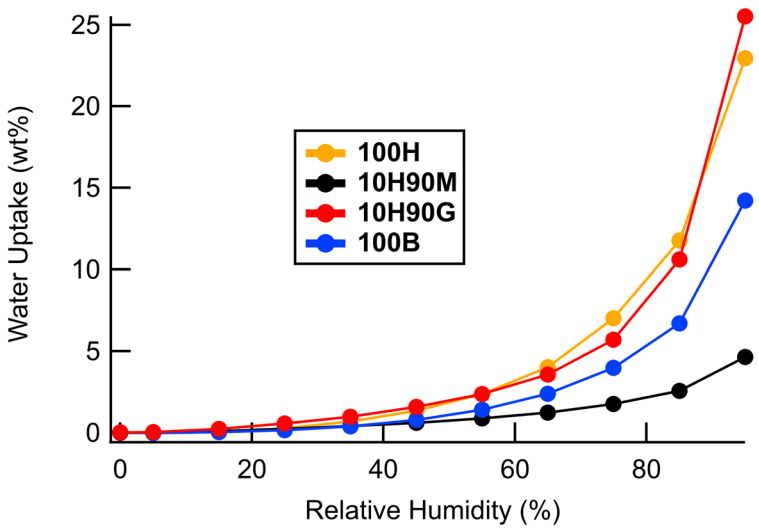

Figure S5.12: Dynamic vapor sorption of water at 25 °C into polymer materials for brushes.

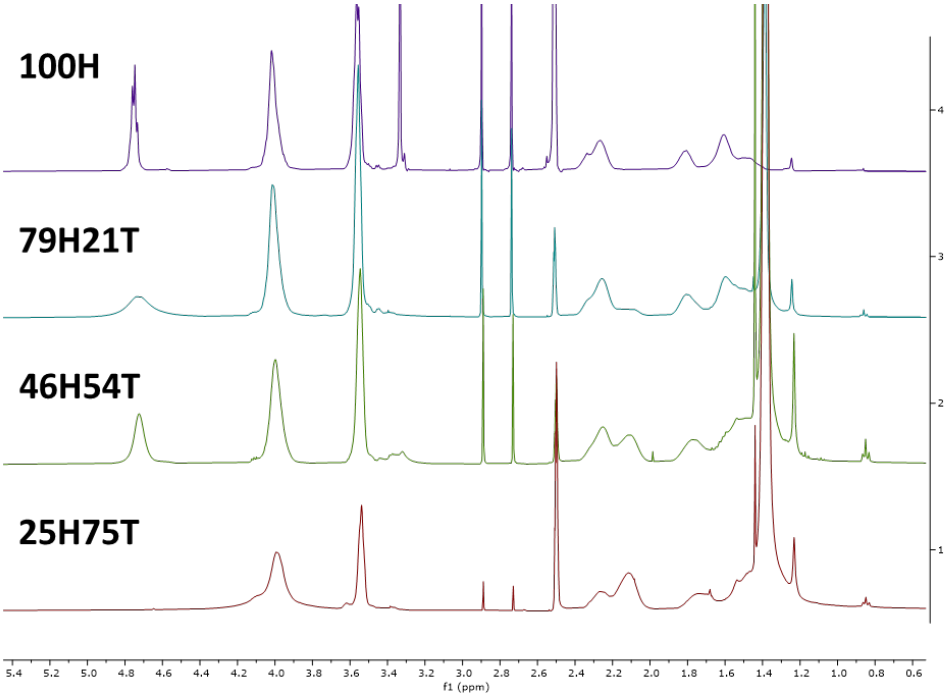

Figure S5.13: ^{1}H NMR (500 MHz, d_6-DMSO) spectra of **xHyT** series

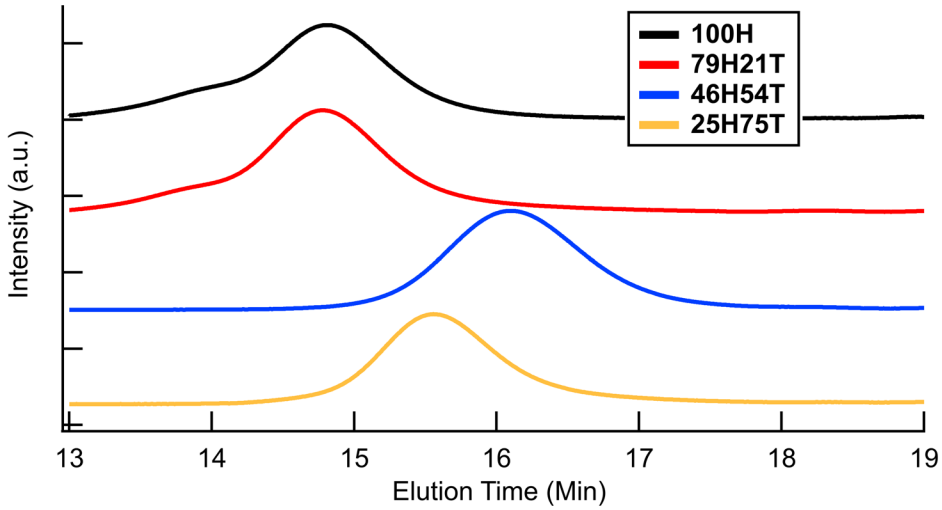

Figure S5.14: GPC (DMF) of **xHyT** series

Table S5.3: Model polymer brush sample summary **(**xHyT**,** xHyC, and xP**)**

Samples	Mn SEC [a] (kg/mol)	Dispersity [a]	Mn ^{1}H NMR [b] (kg/mol)	NonH Mol% [b]
79H21T	21	1.335	18	21%
46H54T	7	1.234	6	54%
25H75T	10	1.274	9	75%
90H10C	8	1.6	11	10%
100P	15	1.32	13	100%

[a] from GPC (DMF)

[b] from ^{1}H NMR

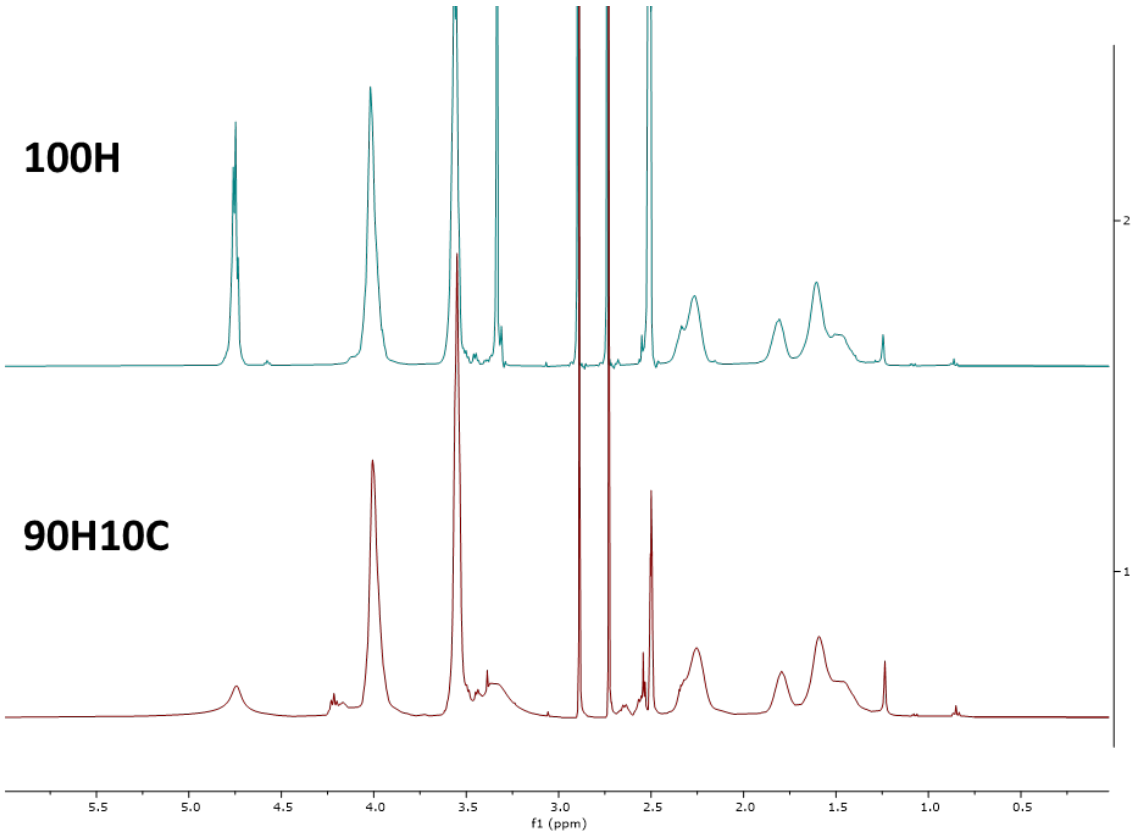

Figure S5.15: ^{1}H NMR (500 MHz, d_6-DMSO) spectra of **xHyC** series

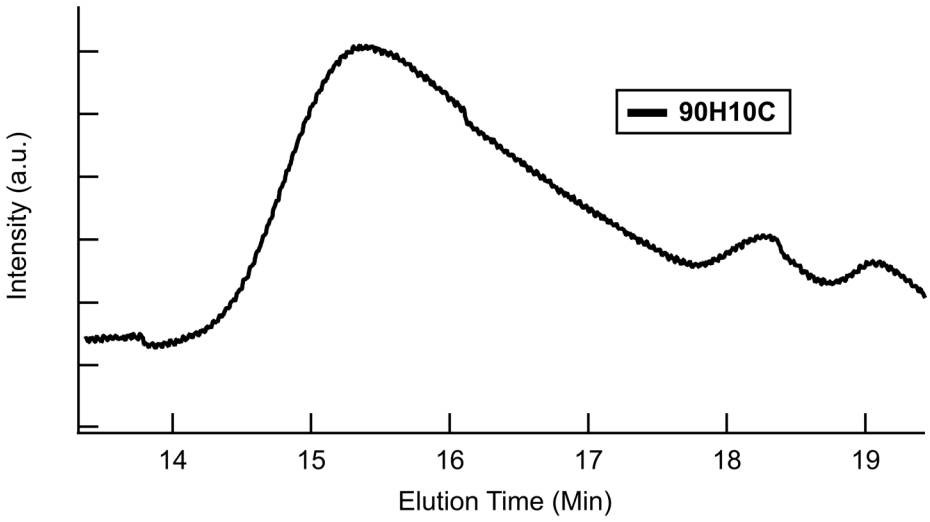

Figure S5.16: GPC (DMF) of **90H10C**

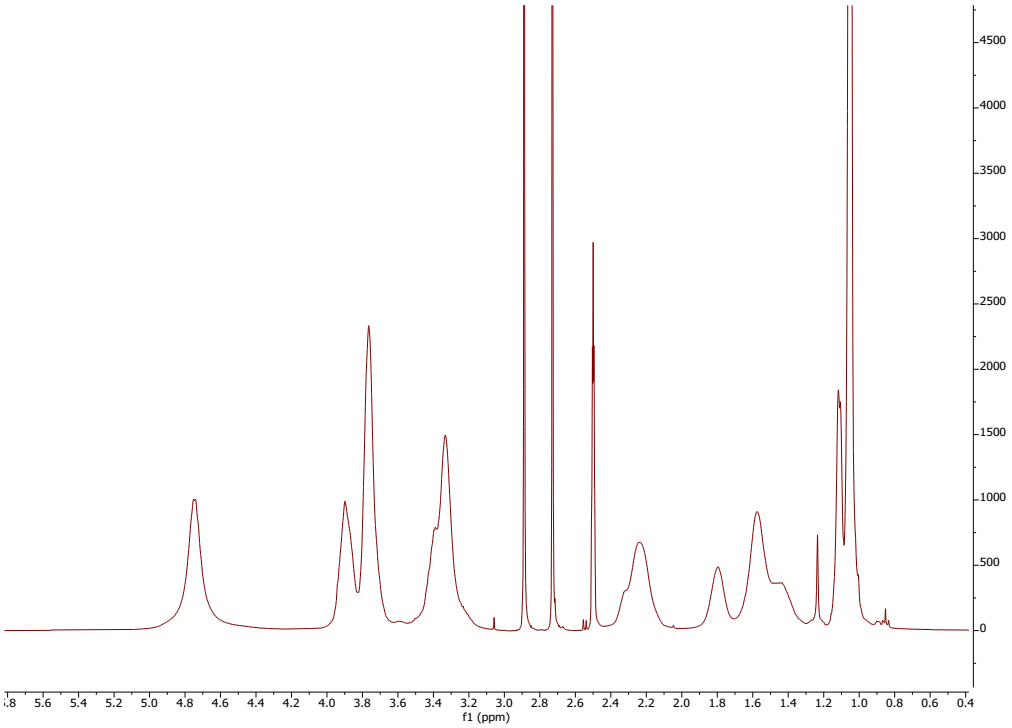

Figure S5.17: ^{1}H NMR (500 MHz, d_6-DMSO) spectra of **100P**

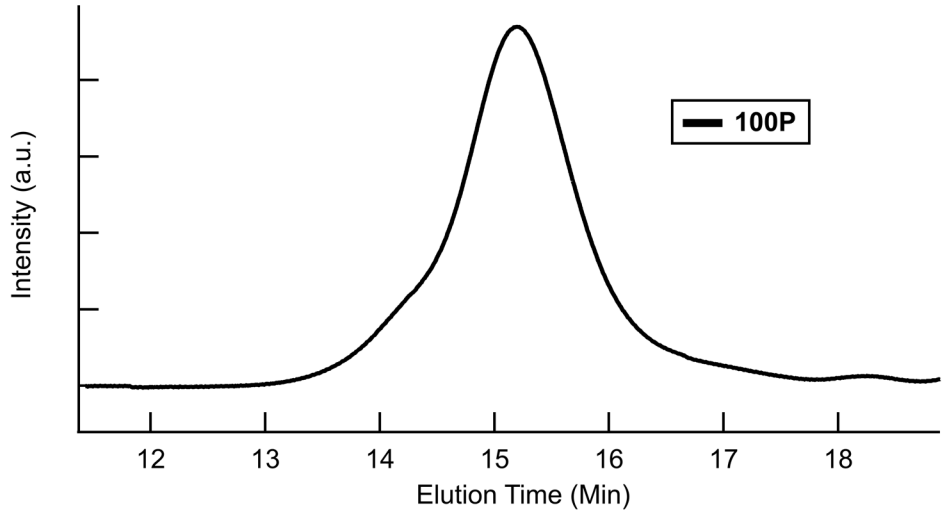

Figure S5.18: GPC (DMF) of **100P**

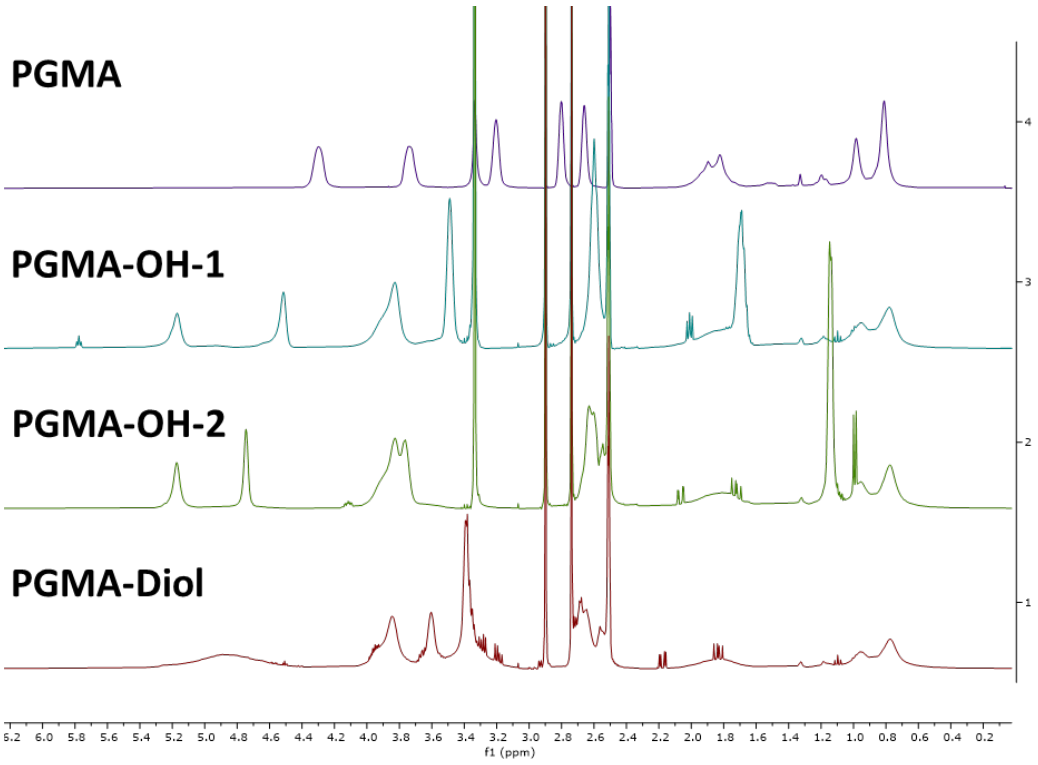

Figure S5.19: ^{1}H NMR (500 MHz, d_6-DMSO) spectra of **PGMA** series

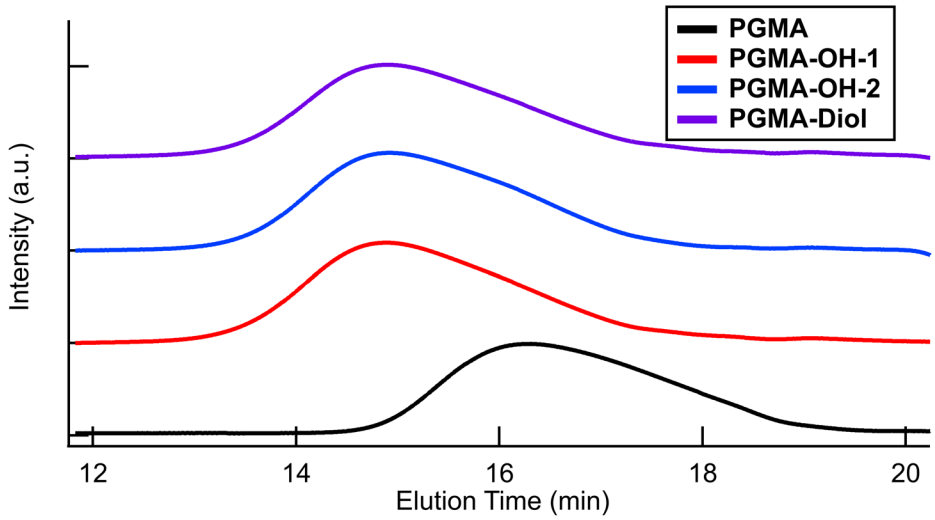

Figure S5.20: GPC (DMF) of **PGMA** series

5.6 REFERENCES

(1) Beyene, H. D.; Werkneh, A. A.; Ambaye, T. G. Current Updates on Waste to Energy (WtE) Technologies: A Review. *Renew. Energy Focus* **2018**, *24* (March), 1–11. https://doi.org/10.1016/j.ref.2017.11.001.

(2) Placke, T.; Kloepsch, R.; Dühnen, S.; Winter, M. Lithium Ion, Lithium Metal, and Alternative Rechargeable Battery Technologies: The Odyssey for High Energy Density. *J. Solid State Electrochem.* **2017**, *21* (7), 1939–1964. https://doi.org/10.1007/s10008-017-3610-7.

(3) Shi, Y.; Eze, C.; Xiong, B.; He, W.; Zhang, H.; Lim, T. M.; Ukil, A.; Zhao, J. Recent Development of Membrane for Vanadium Redox Flow Battery Applications: A Review. *Appl. Energy* **2019**, *238* (December 2018), 202–224. https://doi.org/10.1016/j.apenergy.2018.12.087.

(4) Kim, H. C.; Mun, S.; Ko, H. U.; Zhai, L.; Kafy, A.; Kim, J. Renewable Smart Materials. *Smart Mater. Struct.* **2016**, *25* (7). https://doi.org/10.1088/0964-1726/25/7/073001.

(5) Ellabban, O.; Abu-Rub, H.; Blaabjerg, F. Renewable Energy Resources: Current Status, Future Prospects and Their Enabling Technology. *Renew. Sustain. Energy Rev.* **2014**, *39*, 748–764. https://doi.org/10.1016/j.rser.2014.07.113.

(6) Hallinan, D. T.; Balsara, N. P. Polymer Electrolytes. *Annu. Rev. Mater. Res.* **2013**, *43*, 503–525. https://doi.org/10.1146/annurev-matsci-071312-121705.

(7) Bet-Moushoul, E.; Mansourpanah, Y.; Farhadi, K.; Tabatabaei, M. TiO2 Nanocomposite Based Polymeric Membranes: A Review on Performance Improvement for Various Applications in Chemical Engineering Processes. *Chem. Eng. J.* **2016**, *283*, 29–46. https://doi.org/10.1016/j.cej.2015.06.124.

(8) Manuel Stephan, A.; Nahm, K. S. Review on Composite Polymer Electrolytes for Lithium Batteries. *Polymer (Guildf).* **2006**, *47* (16), 5952–5964. https://doi.org/10.1016/j.polymer.2006.05.069.

(9) Kim, D. J.; Jo, M. J.; Nam, S. Y. A Review of Polymer-Nanocomposite Electrolyte Membranes for Fuel Cell Application. *J. Ind. Eng. Chem.* **2015**, *21*, 36–52. https://doi.org/10.1016/j.jiec.2014.04.030.

(10) Boaretto, N.; Meabe, L.; Martinez-Ibañez, M.; Armand, M.; Zhang, H. Review—Polymer Electrolytes for Rechargeable Batteries: From Nanocomposite to Nanohybrid. *J. Electrochem. Soc.* **2020**, *167* (7), 070524. https://doi.org/10.1149/1945-7111/ab7221.

(11) Kim, J. W.; Ji, K. S.; Lee, J. P.; Park, J. W. Electrochemical Characteristics of Two Types of PEO-Based Composite Electrolyte with Functional SiO2. *J. Power Sources* **2003**, *119–121*, 415–421. https://doi.org/10.1016/S0378-7753(03)00263-5.

(12) Qian, X.; Gu, N.; Cheng, Z.; Yang, X.; Wang, E.; Dong, S. Impedance Study of (PEO)10LiClO4-Al2O3 Composite Polymer Electrolyte with Blocking Electrodes. *Electrochim. Acta* **2001**, *46* (12), 1829–1836. https://doi.org/10.1016/S0013-4686(00)00723-4.

(13) Wang, Y. J.; Pan, Y.; Kim, D. Conductivity Studies on Ceramic Li1.3Al0.3Ti1.7(PO4) 3-Filled PEO-Based Solid Composite Polymer Electrolytes. *J. Power Sources* **2006**, *159* (1 SPEC. ISS.), 690–701. https://doi.org/10.1016/j.jpowsour.2005.10.104.

(14) Liu, W.; Liu, N.; Sun, J.; Hsu, P. C.; Li, Y.; Lee, H. W.; Cui, Y. Ionic Conductivity Enhancement of Polymer Electrolytes with Ceramic Nanowire Fillers. *Nano Lett.* **2015**, *15* (4), 2740–2745. https://doi.org/10.1021/acs.nanolett.5b00600.

(15) Liu, W.; Lin, D.; Sun, J.; Zhou, G.; Cui, Y. Improved Lithium Ionic Conductivity in Composite Polymer Electrolytes with Oxide-Ion Conducting Nanowires. *ACS Nano* **2016**, *10* (12), 11407–11413. https://doi.org/10.1021/acsnano.6b06797.

(16) Liu, W.; Lee, S. W.; Lin, D.; Shi, F.; Wang, S.; Sendek, A. D.; Cui, Y. Enhancing Ionic Conductivity in Composite Polymer Electrolytes with Well-Aligned Ceramic Nanowires. *Nat. Energy* **2017**, *2* (5), 1–7. https://doi.org/10.1038/nenergy.2017.35.

(17) Mariano, M.; El Kissi, N.; Dufresne, A. Cellulose Nanocrystals and Related Nanocomposites: Review of Some Properties and Challenges. *J. Polym. Sci. Part B Polym. Phys.* **2014**, *52* (12), 791–806. https://doi.org/10.1002/polb.23490.

(18) Eichhorn, S. J.; Dufresne, A.; Aranguren, M.; Marcovich, N. E.; Capadona, J. R.; Rowan, S. J.; Weder, C.; Thielemans, W.; Roman, M.; Renneckar, S.; Gindl, W.; Veigel, S.; Keckes, J.; Yano, H.; Abe, K.; Nogi, M.; Nakagaito, A. N.; Mangalam, A.; Simonsen, J.; Benight, A. S.; Bismarck, A.; Berglund, L. A.; Peijs, T. Review: Current International Research into Cellulose Nanofibres and Nanocomposites. *J. Mater. Sci.* **2010**, *45* (1), 1–33. https://doi.org/10.1007/s10853-009-3874-0.

(19) Calvino, C.; Macke, N.; Kato, R.; Rowan, S. J. Development, Processing and Applications of Bio-Sourced Cellulose Nanocrystal Composites. *Progress in Polymer Science*. 2020, pp 1–21. https://doi.org/10.1016/j.progpolymsci.2020.101221.

(20) Capadona, J. R.; Van Den Berg, O.; Capadona, L. A.; Schroeter, M.; Rowan, S. J.; Tyler, D. J.; Weder, C.; Berg, O. V. a N. D. E. N. A Versatile Approach for the Processing of Polymer Nanocomposites with Self-Assembled Nanofibre Templates. *Nat. Nanotechnol.* **2007**, *2* (12), 765–769. https://doi.org/10.1038/nnano.2007.379.

(21) Dagnon, K. L.; Way, A. E.; Carson, S. O.; Silva, J.; Maia, J.; Rowan, S. J. Controlling the Rate of Water-Induced Switching in Mechanically Dynamic Cellulose Nanocrystal Composites. *Macromolecules* **2013**, *46* (20), 8203–8212. https://doi.org/10.1021/ma4008187.

(22) Cudjoe, E.; Hunsen, M.; Xue, Z.; Way, A. E.; Barrios, E.; Olson, R. A.; Hore, M. J. A.; Rowan, S. J. Miscanthus Giganteus: A Commercially Viable Sustainable Source of Cellulose Nanocrystals. *Carbohydr. Polym.* **2017**, *155*, 230–241. https://doi.org/10.1016/j.carbpol.2016.08.049.

(23) Morandi, G.; Heath, L.; Thielemans, W. Cellulose Nanocrystals Grafted with Polystyrene Chains through Surface-Initiated Atom Transfer Radical Polymerization (SI-ATRP). *Langmuir* **2009**, *25* (14), 8280–8286. https://doi.org/10.1021/la900452a.

(24) Wohlhauser, S.; Delepierre, G.; Labet, M.; Morandi, G.; Thielemans, W.; Weder, C.;

Zoppe, J. O. Grafting Polymers from Cellulose Nanocrystals: Synthesis, Properties, and Applications. *Macromolecules* **2018**, *51* (16), 6157–6189. https://doi.org/10.1021/acs.macromol.8b00733.

(25) Gadim, T. D. O.; Vilela, C.; Loureiro, F. J. A.; Silvestre, A. J. D.; Freire, C. S. R.; Figueiredo, F. M. L. Nafion® and Nanocellulose: A Partnership for Greener Polymer Electrolyte Membranes. *Ind. Crops Prod.* **2016**, *93*, 212–218. https://doi.org/10.1016/j.indcrop.2016.01.028.

(26) Cheng, X.; Wang, J.; Liao, Y.; Li, C.; Wei, Z. Enhanced Conductivity of Anion-Exchange Membrane by Incorporation of Quaternized Cellulose Nanocrystal. *ACS Appl. Mater. Interfaces* **2018**, *10* (28), 23774–23782. https://doi.org/10.1021/acsami.8b05298.

(27) Jabbour, L.; Bongiovanni, R.; Beneventi, D. Cellulose-Based Li-Ion Batteries : A Review. *Cellulose* **2013**, No. 20, 1523–1545. https://doi.org/10.1007/s10570-013-9973-8.

(28) Kreuer, K. D. Ion Conducting Membranes for Fuel Cells and Other Electrochemical Devices. *Chem. Mater.* **2014**, *26* (1), 361–380. https://doi.org/10.1021/cm402742u.

(29) Rincón-Iglesias, M.; Lizundia, E.; Costa, C. M.; Lanceros-Méndez, S. Tailoring Electrical and Mechanical Properties of All-Natural Polymer Composites for Environmentally Friendlier Electronics. *ACS Appl. Polym. Mater.* **2020**, *2* (4), 1448–1457. https://doi.org/10.1021/acsapm.9b01098.

(30) Lettow, J. H.; Kaplan, R. Y.; Nealey, P. F.; Rowan, S. J. Enhanced Ion Conductivity through Hydrated, Polyelectrolyte-Grafted Cellulose Nanocrystal Films. *Macromolecules* **2021**, *54* (14), 6925–6936. https://doi.org/10.1021/acs.macromol.1c01155.

(31) Salvatore, D. A.; Gabardo, C. M.; Reyes, A.; O'Brien, C. P.; Holdcroft, S.; Pintauro, P.; Bahar, B.; Hickner, M.; Bae, C.; Sinton, D.; Sargent, E. H.; Berlinguette, C. P. Designing Anion Exchange Membranes for CO2 Electrolysers. *Nat. Energy* **2021**, *6* (4), 339–348. https://doi.org/10.1038/s41560-020-00761-x.

(32) Xue, Z.; He, D.; Xie, X. Poly(Ethylene Oxide)-Based Electrolytes for Lithium-Ion Batteries. *J. Mater. Chem. A* **2015**, *3* (38), 19218–19253. https://doi.org/10.1039/c5ta03471j.

(33) Chen, C.; Tse, Y. L. S.; Lindberg, G. E.; Knight, C.; Voth, G. A. Hydroxide Solvation and Transport in Anion Exchange Membranes. *J. Am. Chem. Soc.* **2016**, *138* (3), 991–1000. https://doi.org/10.1021/jacs.5b11951.

(34) Chu, W.; Webb, M. A.; Deng, C.; Colon, Y. J.; Kambe, Y.; Krishnan, S.; Nealey, P. F.; de Pablo, J. J. Understanding Ion Mobility in P2VP/NMP+I − Polymer Electrolytes: A Combined Simulation and Experimental Study. *Macromolecules* **2020**, *53* (8), 2783–2792. https://doi.org/10.1021/acs.macromol.9b02329.

(35) Sharon, D.; Bennington, P.; Liu, C.; Kambe, Y.; Dong, B. X.; Burnett, V. F.; Dolejsi, M.; Grocke, G.; Patel, S. N.; Nealey, P. F. Interrogation of Electrochemical Properties of Polymer Electrolyte Thin Films with Interdigitated Electrodes. *J. Electrochem. Soc.* **2018**, *165* (16), H1028–H1039. https://doi.org/10.1149/2.0291816jes.

(36) Arges, C. G.; Kambe, Y.; Suh, H. S.; Ocola, L. E.; Nealey, P. F. Perpendicularly Aligned, Anion Conducting Nanochannels in Block Copolymer Electrolyte Films. *Chem. Mater.* **2016**, *28* (5), 1377–1389. https://doi.org/10.1021/acs.chemmater.5b04452.

(37) Dong, B. X.; Bennington, P.; Kambe, Y.; Sharon, D.; Dolejsi, M.; Strzalka, J.; Burnett, V. F.; Nealey, P. F.; Patel, S. N. Nanothin Film Conductivity Measurements Reveal Interfacial Influence on Ion Transport in Polymer Electrolytes. *Mol. Syst. Des. Eng.* **2019**, *4* (3), 597–608. https://doi.org/10.1039/c9me00011a.

(38) Yuan, H.; Nishiyama, Y.; Wada, M.; Kuga, S. Surface Acylation of Cellulose Whiskers by Drying Aqueous Emulsion. *Biomacromolecules* **2006**, *7* (3), 696–700. https://doi.org/10.1021/bm050828j.

(39) Miao, C.; Hamad, W. Y. Alkenylation of Cellulose Nanocrystals (CNC) and Their Applications. *Polymer (Guildf).* **2016**, *101*, 338–346. https://doi.org/10.1016/j.polymer.2016.08.099.

(40) In, I.; La, Y. H.; Park, S. M.; Nealey, P. F.; Gopalan, P. Side-Chain-Grafted Random Copolymer Brushes as Neutral Surfaces for Controlling the Orientation of Block Copolymer Microdomains in Thin Films. *Langmuir* **2006**, *22* (18), 7855–7860. https://doi.org/10.1021/la060748g.

(41) Han, E.; Stuen, K. O.; La, Y. H.; Nealey, P. F.; Gopalan, P. Effect of Composition of Substrate-Modifying Random Copolymers on the Orientation of Symmetric and Asymmetric Diblock Copolymer Domains. *Macromolecules* **2008**, *41* (23), 9090–9097. https://doi.org/10.1021/ma8018393.

(42) Chu, W.; Webb, M. A.; Deng, C.; Colón, Y. J.; Kambe, Y.; Krishnan, S.; Nealey, P. F.; De Pablo, J. J. Understanding Ion Mobility in P2VP/NMP+I- Polymer Electrolytes: A Combined Simulation and Experimental Study. *Macromolecules* **2020**. https://doi.org/10.1021/acs.macromol.9b02329.